Hunting for PeV proton accelerators in Galactic supernova remnants by γ-ray observations

Tomohiko Oka

Department of Physics, Graduate School of Science, Kyoto University
Kitashirakawa Oiwake-cho, Sakyo, Kyoto, Kyoto, 606-8502, Japan

oka.tomohiko.25n@st.kyoto-u.ac.jp

January 2023

Abstract

Although cosmic rays (CRs) are an important actor in the universe, their origin is not well understood. In particular, CRs up to PeV energies are believed to be produced by supernova remnants (SNRs) in our Galaxy, but there is no conclusive observational evidence for this. In this work, we analyze γ-ray observation data for the two SNRs, G106.3+2.7 and HB9, to reveal proton acceleration up to PeV in the SNRs.

SNR G106.3+2.7 is a promising candidate as the PeV protons accelerator since previous studies revealed γ rays above 100 TeV around this SNR. However, this contains a pulsar wind nebula (PWN) producing high-energy electrons, and the γ-ray origin is thus unknown. To identify the origin by spatially resolving the emission region, we performed the TeV γ-ray observations with better angular resolution (0.07–0.1°) than previous studies in the band by using the MAGIC telescope. We found significant emissions above 0.2 TeV spatially coinciding with the SNR radio shell, while emissions above 6 TeV are detected only far from the PWN. This fact suggests that the 100-TeV γ ray originates in the SNR rather than the PWN. Furthermore, spectral modeling results have shown that leptonic models cannot explain the energy spectrum, while a hadronic scenario works well and suggests proton acceleration up to $\sim$ PeV in this region.

Next, we tried to measure the time evolution of particle acceleration in SNRs with an aim to verify why γ-ray observations have found not many PeV proton accelerators. For this purpose, we proposed a new measurement method and applied it to the γ-ray data around SNR HB9. In this method, we expect that runaway CRs from the SNR illuminate the cloud and generate γ rays reflecting the particle distribution in the SNR at a specific epoch in the past, while the spectrum at the shell reflects the present distribution of particles. We can therefore quantify the evolution of the acceleration in the SNR by comparing the spectra at the SNR shell and nearby clouds observed simultaneously. Our *Fermi*-LAT analysis has revealed new γ-ray emissions spatially correlated with the molecular cloud as well as the SNR shell. We then succeeded in explaining these spectra with the scenario above, giving evidence for the CR acceleration by the SNR up to higher energies ($\gtrsim$ 10 TeV) in the past than that produced in the present shell (300 GeV). We also found that this kind of method allows for estimating the diffusion coefficient around SNRs with few uncertainties.

The model developed in this method is applied to the observations for SNRs G106.3+2.7 and G335.2+0.1. Using the obtained model parameters, we confirmed that the luminosity of CRs from SNRs is roughly consistent with that of the measurement at the Earth. Finally, we discuss the future prospect with the next-generation γ-ray observatories.

Contents

Chapter 1

Introduction

Many mysteries remain in the evolution of the universe and the formation of stars and galaxies. The origin of Cosmic Rays (CRs), which are the key to these mysteries (e.g., Padovani et al., 2020; Ohira & Murase, 2019), is, however, still unclear. CRs are charged particles (∼90% of these are protons) that travel through space, and were first discovered by Hess (1912). More than a century of observational research since then has revealed the following interesting features:

i. The highest energy of CR reaches $> 10^{20}$ eV (Bird et al., 1995), which is many orders of magnitude higher than the energy that can be produced on Earth (13.6×10^{12} eV; Large Hadron Collider in CERN[1]). Once we can identify an environment that produces such high energy, it could provide a venue for testing the standard theory (e.g., Mattingly, 2005; Aartsen et al., 2021a; Kephart & Weiler, 1996).

ii. With sufficient interaction with its surroundings, particle energies should follow a Maxwellian (thermal) distribution. However, this is not the case for CRs, which follow a power-law distribution (i.e., a non-thermal distribution), as shown in Fig. 1.1. This indicates that the CR "explosively" acquire energy and reach the Earth without sufficient interaction.

iii. The energy density of CRs is ~ 1 eV cm^{-3}, which agrees well with that of other components for the universe, as listed in Table 1.1. This confirms that, contrary to (ii), there are some interactions between CRs and the other components.

Still, the full picture of the CR origin - where and how they originate and are accelerated - remains unclear. An elucidation of their origin is thus one of the most essential issues in astrophysics.

1.1 Candidate for CR origin: Supernova Remnants

As shown in Fig. 1.1, the CR spectrum has multiple breaks, suggesting the existence of multiple origins. Interestingly, the shape resembles a human foot, and thus certain parts are called by the name of the foot (e.g., "Knee" at ∼ PeV, "Ankle" at ∼ EeV). As for candidates of the CR

[1] https://home.cern/science/accelerators/large-hadron-collider

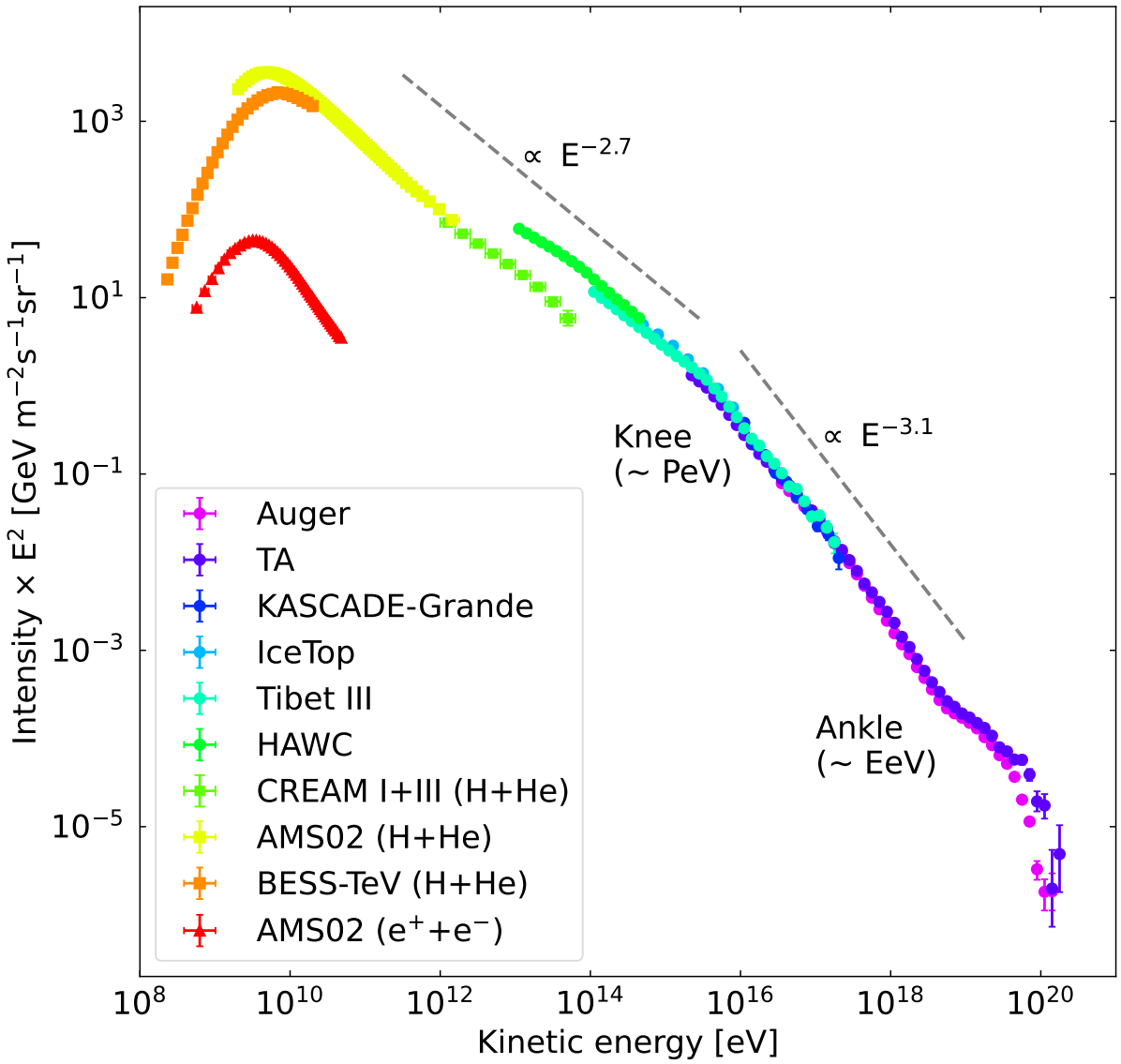

Figure 1.1: The CR spectrum observed in the Earth. The data for the all-particle flux are taken from Verzi (2020), Ivanov (2020), Apel et al. (2013), Aartsen et al. (2013), Amenomori et al. (2008), and Alfaro et al. (2017). In the lower band, the total flux of proton and helium (Yoon et al., 2017; Aguilar et al., 2015b,a; Shikaze et al., 2007) as well as electron and positron flux (Aguilar et al., 2018) are also shown.

Table 1.1: Energy densities in the Local interstellar medium (Draine, 2011).

Component	Energy density [eV cm^{-3}]
Cosmic microwave background ($T_{\rm CMB} = 2.725$ K)	0.26
Far-infrared radiation from dust	0.31
Starlight ($h\nu < 13.6$ eV)	0.54
Thermal kinetic energy $(3/2)nkT$	0.49
Turbulent kinetic energy $(1/2)\rho v^2$	0.22
Magnetic energy $B^2/8\pi$	0.89
Cosmic rays	1.39

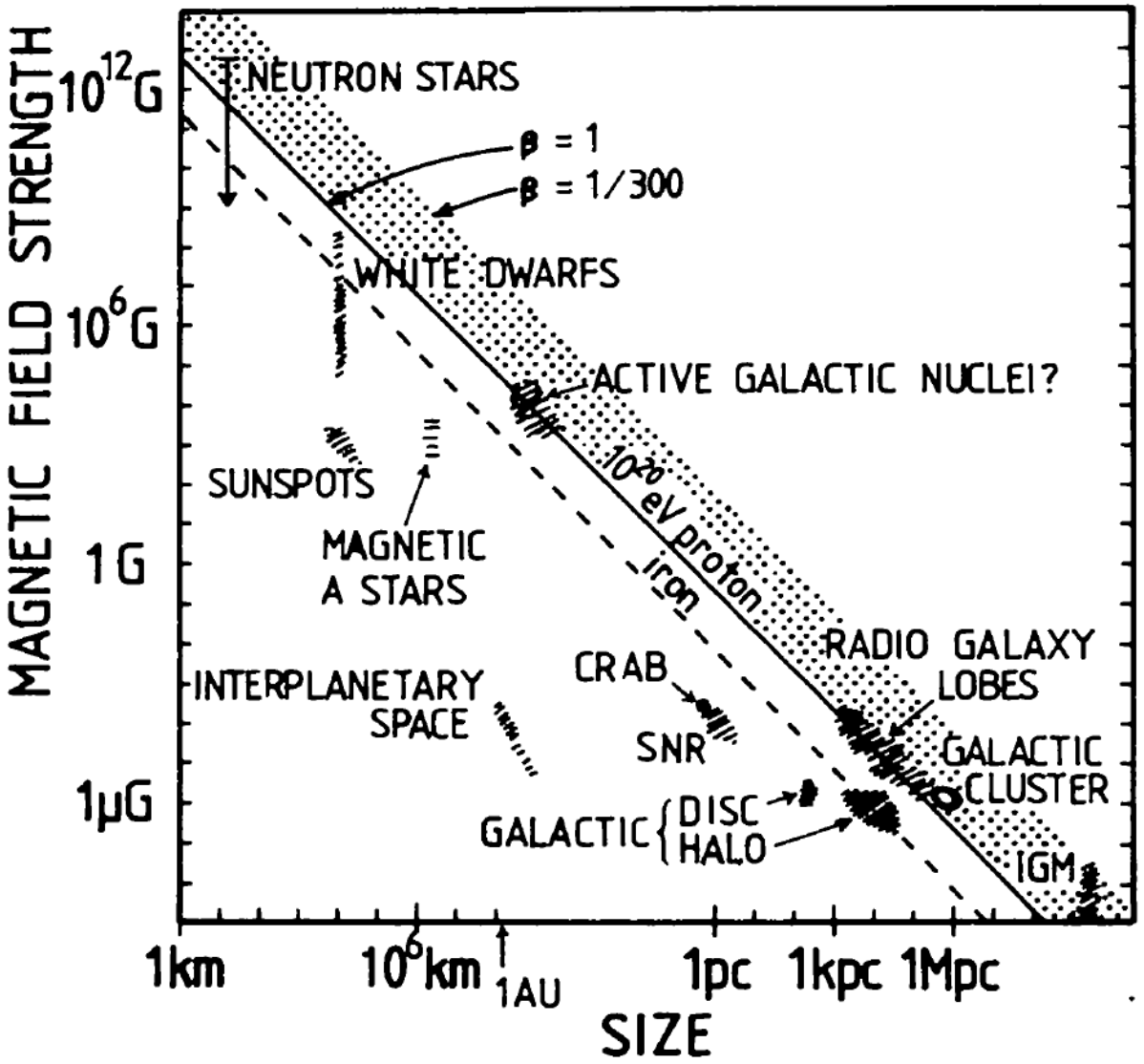

Figure 1.2: The predicted maximum energies as a function of the size and magnetic-field strength of systems (Hillas, 1984). This is called Hillas plot after the first person who created it.

origin, the bottom-up scenario (i.e., accelerations in multiple celestial species) has been expected, while the super heavy dark matter is also considered for the CRs at $\sim 10^{20}$ eV (Chung et al., 1998). In the bottom-up scenario, the Larmor radius formula can roughly predict the maximum acceleration energy for each object in terms of how high energy the system can confine. The maximum energy is hence evaluated as a function of the magnetic-field strength (B) and the size ($R_{\rm L}$) of the system, expressed as:

$$p_{\rm max} \lesssim \frac{ZeR_{\rm L}B}{c} = 1 \text{ PeV Z} \left(\frac{\rm B}{1\ \mu\rm G}\right)\left(\frac{\rm R_L}{1\ \rm pc}\right) \tag{1.1}$$

where Z is the atomic number, e is the elementary charge, and c is the speed of light. Fig. 1.2 shows a summary of the maximum acceleration energies for each object species based on Eq. 1.1.

1.1.1 The SNR paradigm

Among them, supernova remnants (SNRs) are believed to be a promising candidate for CR origin, especially up to PeV energies from the point of the Hillas plot. The following discussions regarding the explosion energy budget and elemental composition have also justified this possibility.

Energy budget in SNRs

Baade & Zwicky (1934) first proposed the possibility of SNRs as the CR source by considering the energy budget. The explosion energy of SN is typically $E_{\rm SN} \sim 10^{51}$ erg (e.g., Utrobin & Chugai, 2017), while the energy supply required to sustain CRs in the Galaxy is $L_{\rm CR} \sim 10^{41}$ erg s^{-1}. If assuming that SNs occur two or three times per 100 yr ($\sim$0.03 yr^{-1}; Tammann et al., 1994) and 10% of the energy can be used for the CR acceleration, the energy supply by SNR is found to be $L_{\rm SN} \sim 0.1 E_{\rm SN}/0.03$ yr $\sim 10^{41}$ erg s^{-1} $\sim$ L$_{\rm CR}$, which is compatible to the CR energy.

Elemental composition in SNRs

Hayakawa (1956) showed that the elemental abundances of CRs (especially from H to Ni) produced by SN explosions roughly reproduce observations assuming that CR origins are uniformly distributed in the Galaxy and travel through the interstellar medium (ISM) with a uniform density. By optimizing the contributions from SN Type I, Type II, and ISM, the observed elemental abundances were successfully reproduced within a deviation by a factor of 2.5 (Yanagita et al., 1990). Furthermore, the deviation can be reduced to a factor of 1.6 by additionally considering a contribution of Wolf-Rayet stars (Yanagita & Nomoto, 1999).

For these perspectives, the SNR is the leading candidate for the CR origin. Fig. 1.3 shows an example of the modelling for the CR spectrum assuming the multiple origins (Thoudam et al., 2016), which is based on Eq. 1.1. The modeling assumes that dominant CR origins are regular SNRs for $\lesssim$1 PeV, Wolf–Rayet SNe/SNRs for 1 PeV–1 EeV, and active galactic nuclei (AGNs) for $\gtrsim$1 EeV. It should be noted that the model can also reproduce the spectra of heavier nuclei, as well as protons.

1.1.2 SNR as a CR accelerator

Since SNRs change with age during their lifetimes, the period that an SNR can accelerate CRs is limited. SNRs are born when the blast of an explosion at the end of a star's life (supernova) sweeps up the ISM. The blast then compresses the ISM, creating a shock wave. The shock waves are expected to accelerate CRs, as we will describe the detail in the next section. The evolution of an SNR is separated into the following periods (e.g., Draine, 2011, and references therein).

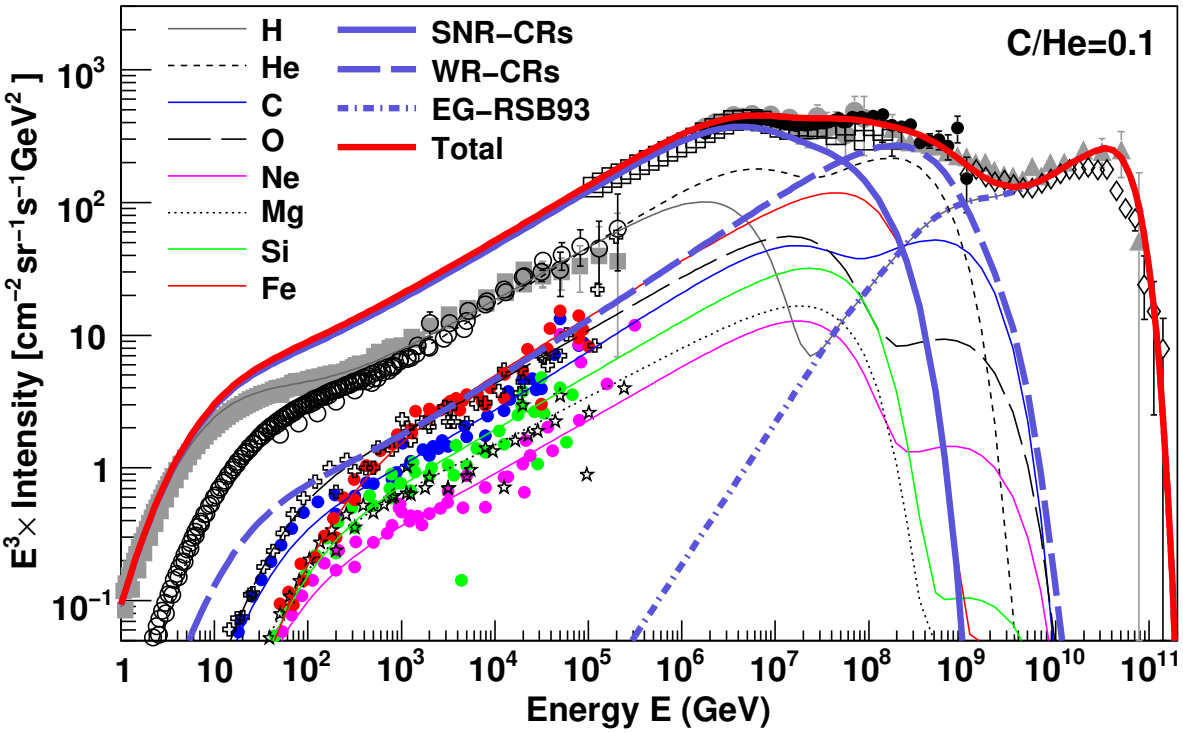

Figure 1.3: An example of the modelling result to the CR spectrum, taken from Thoudam et al. (2016). The thick lines represent the model emissions from SNRs (blue solid), Wolf-Rayet stars (blue dashed), extra-galactic sources (blue dash-dotted), and total (red solid).

(i) Free expansion phase

When the SNR age ($t_{\rm age}$) is younger than ∼1 kyr, the mass of the swept-up ISM ($M_{\rm ISM}$) is smaller than that of the ejecta ($M_{\rm ej}$), and thus the ejecta freely expands without a deceleration. The shock speed can be expressed as:

$$v_{\rm sh} = \sqrt{\frac{2E_{\rm SN}}{M_{\rm ej}}} \sim 10000 \text{ km s}^{-1} \left(\frac{\rm E_{SN}}{10^{51} \text{ erg}}\right)^{1/2} \left(\frac{\rm M_{ej}}{\rm M_{\odot}}\right)^{-1/2}, \tag{1.2}$$

where $E_{\rm SN}$ is the explosion energy.

(ii) Adiabatic expansion (Sedov) phase

Once $M_{\rm ISM}$ surpassed $M_{\rm ej}$, the shock decelerates due to the ISM. Assuming a point-like explosion in a uniform ISM and then using the self-similar solution (Sedov-Taylor solution), the shock velocity during this period is expressed as:

$$v_{\rm sh} = 490 \text{ km s}^{-1} \left(\frac{\rm t_{age}}{10 \text{ kyr}}\right)^{-3/5} \left(\frac{\rm E_{SN}}{10^{51} \text{ erg}}\right)^{1/5} \left(\frac{\rm n_{ISM}}{1 \text{ cm}^{-3}}\right)^{-1/5}, \tag{1.3}$$

where $n_{\rm ISM}$ is the density of the ISM.

(iii) Radiative cooling (Snowplow) phase

When $t_{\rm age}$ is older than 10 kyr, energy loss due to radiative cooling becomes significant. The shock velocity gradually slows with the relation:

$$v_{\rm sh} \propto t_{\rm age}^{-5/7}, \tag{1.4}$$

and finally, down to the speed of sound, by $t_{\rm age}$ reaches 100 kyr. The ejecta merges with the ISM, and then the shock compression declines. As a result, CR acceleration is no longer possible.

1.2 CR acceleration and diffusion

In this section, we describe the CR acceleration by shock waves (Sect. 1.2.1) and the diffusion of CRs (Sect. 1.2.2) toward an interpretation of the power-law form of the CR spectrum.

1.2.1 CR acceleration in an SNR

Diffusive Shock Acceleration (DSA) mechanism

Diffusive Shock Acceleration (DSA), developed by Blandford & Ostriker (1978) and Bell (1978), is the most fundamental theory for CR acceleration in SNRs. In this theory, we consider the case where CRs travel back and forth through the shock wave of the SNR many times, as shown in the conceptual diagram in Fig. 1.4. Here, the following conditions are imposed as the environment of the shock wave of SNR:

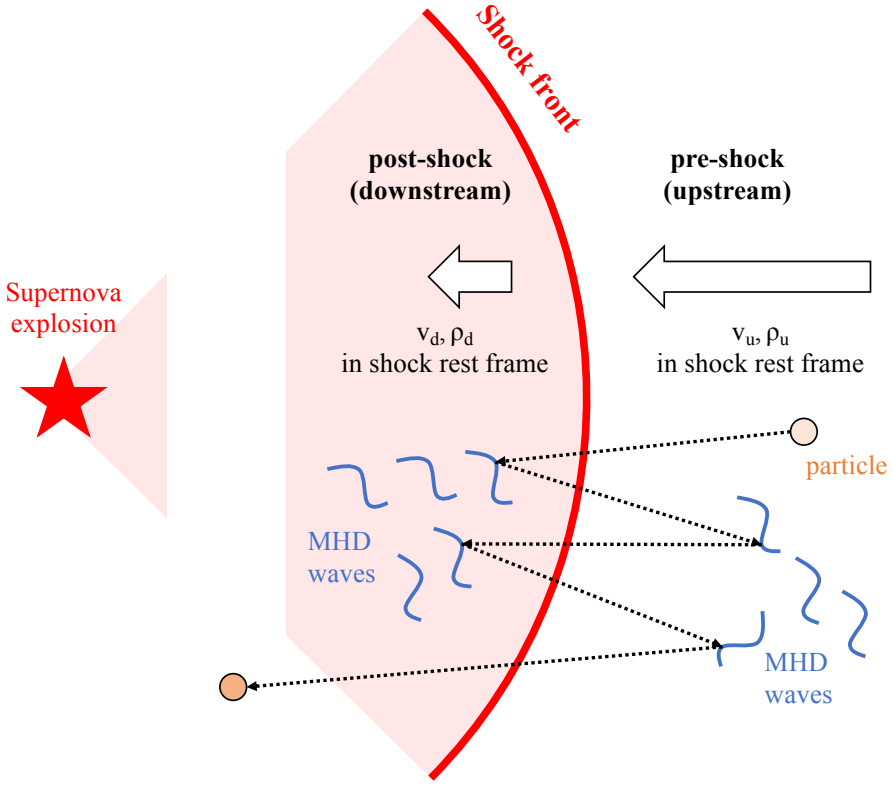

Figure 1.4: Schematic view of the DSA in an SNR. The physical quantities are discontinuous through the shock front.

a) The shock compresses the fluid downstream with a compression ratio of r ($= v_{\rm u}/v_{\rm d}$, where $v_{\rm u}$ and $v_{\rm d}$ are upstream and downstream velocities, respectively, in the shock rest frame).
b) There are no collisions among particles (commonly known as collision-less shock waves).
c) Particles are isotropically scattered by the Alfvén waves.
d) Conditions b and c allow particles to cross the shock front many times.
e) The shock front can be treated as a plane.
f) The velocity of the particle can be approximated to the speed of light, and sufficiently faster than the shock velocity.

Suppose first that a particle with an energy of E_1 crosses the shock wave plane at an angle of θ_1 from upstream to downstream. The energy of this particle in the rest system of downstream is:

$$E_1' = \Gamma E_1(1 - \beta\cos\theta_1), \tag{1.5}$$

where Γ is the Lorentz factor and β is the shock velocity normalized the speed of light ($\beta = \frac{v_{\rm u}-v_{\rm d}}{c}$). Once the particle is scattered by a Alfvén wave and crosses again the shock front at an angle of θ_2, the particle energy in the rest system of upstream is:

$$E_2 = \Gamma E_1'(1 + \beta\cos\theta_2). \tag{1.6}$$

Hence, the energy gained during one round trip on the shock wave is:

$$\Delta E = \frac{E_2}{E_1} = \Gamma^2(1 - \beta\cos\theta_1 + \beta\cos\theta_2 - \beta^2\cos\theta_1\cos\theta_2). \tag{1.7}$$

Next, we find the mean values for the two angles, θ_1 and θ_2. Eq. 1.7 is written by:

$$\Delta E = \Gamma^2(1 - \beta\langle\cos\theta_1\rangle + \beta\langle\cos\theta_2\rangle - \beta^2\langle\cos\theta_1\rangle\langle\cos\theta_2\rangle). \tag{1.8}$$

If a particle moves at an angle of θ with a velocity of v, the particle approach the shock wave surface at a speed of $v \times \cos\theta$, which corresponds to the probability of crossing the shock wave surface. Therefore, we can obtain the mean values by of weighting with $\cos\theta$. The mean values in Eq. 1.8 are found to be:

$$\langle\cos\theta_1\rangle = \frac{2 \times \int_{\pi/2}^{\pi} \cos^2\theta_1 \sin\theta_1 {\rm d}\theta}{2 \times \int_{\pi/2}^{\pi} \cos\theta_1 \sin\theta_1 {\rm d}\theta} = \frac{-2 \times \int_{-1}^{0} {\rm x}^2 {\rm dx}}{-2 \times \int_{-1}^{0} {\rm x dx}} = -\frac{2}{3} \tag{1.9}$$

$$\langle\cos\theta_2\rangle = \frac{2}{3}. \tag{1.10}$$

where the integration ranges for θ_1 and θ_2 are from $+\pi/2$ to $+3\pi/2$ and from $-\pi/2$ to $+\pi/2$, respectively. Using Eq. 1.9, Eq. 1.8 can be rewritten by

$$\Delta E = \Gamma^2(1 + \frac{4}{3}\beta + \frac{4}{9}\beta^2) \sim 1 + \frac{4}{3}\beta. \tag{1.11}$$

where we assume $\beta \ll 1$ and thus the second-order term and higher are ignored. If a particle with initial energy of E_1 makes n round trips on the shock wave, the total energy acquired is

therefore:

$$\frac{E_n}{E_1} \sim (1+\epsilon)^n \sim \exp(\epsilon \mathrm{n}) \text{ (for n} \to \infty). \tag{1.12}$$

where $\epsilon = \Delta E - 1 = 4\beta/3$.

In other words, the energy of the particles is amplified (reduced) due to the Lorentz boost when particles cross the shock wave from upstream (downstream) to downstream (upstream), resulting in the energy balance of the round trip being positive. This acceleration mechanism is called "Fermi first-order acceleration" because Fermi pioneered this concept (Fermi, 1949) and because the energy gained is proportional to the first order of the shock velocity.

This mechanism can explain the CR spectrum with the non-thermal distribution. To obtain the energy spectrum of particles escaping from this acceleration region, we evaluate the probability of particles escaping from downstream. Since the particle flux (F_d) escaping from downstream can be regarded as the amount of particles flowing along with the fluid of downstream, the flux can be written as:

$$F_\mathrm{d} \sim N_\mathrm{d} v_\mathrm{d}, \tag{1.13}$$

where N_d is the number density of particles in downstream. Regarding the flux of particles that back upstream, the number of particles is first reduced by half because the particles can back only with the absolute value of the angle between the direction and the shock wave should be less than 90 degrees. We also take a weighted average with $\cos\theta$, as in Equation 1.9. As a result, the flux is obtained as:

$$F_\mathrm{u} \sim N_\mathrm{d} \times \frac{1}{2} \times c \frac{2\int_0^{\pi/2} \cos\theta \sin\theta \mathrm{d}\theta}{2\int_0^{\pi/2} \sin\theta \mathrm{d}\theta} = \frac{N_0 c}{4}. \tag{1.14}$$

where we assume the velocity of particles can be approximate to the speed of light. Hence, the probability that particles escape from the acceleration region (P_esc) is found to be

$$P_\mathrm{esc} = \mathrm{F_u} F_\mathrm{d} = \frac{N_\mathrm{d} v_\mathrm{d}}{N_\mathrm{d} c/4} = \frac{4 v_\mathrm{d}}{c}. \tag{1.15}$$

The fraction of the particles that do not escape from the shock region during n round trip on the shock surface is:

$$S(n) = (1 - P_\mathrm{esc})^n \sim \exp(-\mathrm{P_{esc}n}) \text{ (for n} \to \infty) \tag{1.16}$$

Since n can be written by $ln(\Delta E)/ln(1+\epsilon)$ using Eq. 1.12, the $S(n)$ is rewritten by:

$$S(n) = \exp(-\mathrm{P_{esc}} \times \frac{\ln(\Delta \mathrm{E})}{\ln(1+\epsilon)}) \sim \Delta \mathrm{E}^{-\frac{\mathrm{P_{esc}}}{\epsilon}}, \tag{1.17}$$

where we use the approximation of $ln(1-\epsilon) \sim \epsilon$. Finally, the differential flux is written as follows:

$$\frac{dS}{dE} \propto \Delta E^{-\frac{P_\mathrm{esc}}{\epsilon}-1}. \tag{1.18}$$

In this way, we can reproduce the power-law form as in the CR spectrum. With the compression

ratio ($r = v_{\rm u}/v_{\rm d}$), the spectral index of particles (α) is written as:

$$\alpha = -\frac{P_{\rm esc}}{\epsilon} - 1 = -\frac{4u_{\rm d}}{c} \times \frac{3c}{4(v_{\rm u} - v_{\rm d})} - 1 = -\frac{r+2}{r-1}. \tag{1.19}$$

Rankine–Hugoniot equation

At the discontinuous boundary of the perpendicular shock, as shown in Fig. 1.4, the conservation of mass, momentum, and energy leads to the following relation (called "Rankine–Hugoniot relation"):

$$\rho_{\rm u} v_{\rm u} = \rho_{\rm d} v_{\rm d} \tag{1.20}$$

$$\rho_{\rm u} v_{\rm u}^2 + p_{\rm u} = \rho_{\rm d} v_{\rm d}^2 + p_{\rm d} \tag{1.21}$$

$$w_{\rm u} + \frac{1}{2} v_{\rm u}^2 = w_{\rm d} + \frac{1}{2} v_{\rm d}^2, \tag{1.22}$$

where ρ, v, p and w represent the density, velocity, pressure and enthalpy per unit volume, respectively. Assuming an ideal gas, the enthalpy can be written by

$$w = C_{\rm p} T = \frac{\gamma p}{(\gamma - 1)\rho}, \tag{1.23}$$

where $\gamma = c_{\rm p}/c_{\rm v}$ and $c_{\rm p}$ and $c_{\rm v}$ are the specific heat at constant pressure and the specific heat at constant volume, respectively. Assuming that the shock wave has a large Mach number, i.e., the upstream pressure is negligible relative to that of downstream ($p_{\rm u}/p_{\rm d} \ll 1$), the following relations is obtained:

$$\rho_{\rm d} = \frac{\gamma + 1}{\gamma - 1} \rho_{\rm u} \tag{1.24}$$

$$v_{\rm d} = \frac{\gamma - 1}{\gamma + 1} v_{\rm u} \tag{1.25}$$

The compression ratio (r) is then obtained as:

$$r \equiv \frac{v_{\rm u}}{v_{\rm d}} = \frac{\gamma + 1}{\gamma - 1} = 4 \ (\text{for } \gamma \ = \ 5/3) \tag{1.26}$$

where we consider the case of a monatomic gas and γ is thus 5/3. Substituting this into Eq 1.18, the spectral index of particles (α) is found to be -2.0.

Maximum acceleration energy by DSA

In Sect. 1.1, we evaluated the maximum acceleration energy determined by the Lorentz force using Eq. 1.40. Here, we again evaluate it by considering the timescale of CR escape under the environment of the shock region. The timescale of particle acceleration is written as:

$$t_{\rm acc} = \Delta T \times \epsilon, \tag{1.27}$$

where ΔT is the time taken for one round trip of the shock wave and can be estimated by adding up the time that particles stay in the upstream and downstream. Hence,

$$\Delta T = \frac{4D_{\rm u}}{v_{\rm u}c} + \frac{4D_{\rm d}}{v_{\rm d}c}, \tag{1.28}$$

where D is the diffusion coefficient and can be expressed as:

$$D = \frac{\lambda_{\rm mfp}c}{3}, \tag{1.29}$$

using the mean free path of the particle ($\lambda_{\rm mfp}$). The mean free path is determined by the magnetic field and can be expressed using the Larmor radius ($R_{\rm L}$) as:

$$\lambda_{\rm mfp} = \eta R_{\rm L}, \text{ with } \eta \equiv \left(\frac{\rm B}{\delta \rm B}\right)^2 \geq 1, \tag{1.30}$$

where η, called gyro-factor, is the parameter of strength of the magnetic field turbulence. Smaller η indicates stronger turbulence, especially the limit of $\eta \to 1$ is called the Bohm limit. Note that the gyro-factor of SNRs using X-ray observations is estimated to be 1–10 (Tanaka et al., 2020; Tsuji et al., 2021), indicating the particle acceleration in SNR is close to the Bohm limit. By assuming that $r = 4$ as in Eq. 1.26 and $D_{\rm u} = D_{\rm d}$, $t_{\rm acc}$ can be rewritten by:

$$t_{\rm acc} = \frac{20}{3}\frac{c\eta R_{\rm L}}{v_{\rm sh}^2}. \tag{1.31}$$

If the SNR shock radius can be approximated as $R \sim t_{\rm acc} \times v_{\rm sh}$, then the maximum acceleration energy is obtained as:

$$p_{\rm max} \sim 0.5 \text{ PeV } \frac{Z}{\eta}\left(\frac{v_{\rm sh}}{10^4 \text{ km s}^{-1}}\right)\left(\frac{B}{10\ \mu\text{G}}\right)\left(\frac{R}{10 \text{ pc}}\right). \tag{1.32}$$

The maximum energy is proportional to the shock velocity as well as the magnetic field strength and the source radius.

1.2.2 CR propagation in the Galaxy

The spectral index of CRs at SNRs is expected to be -2.0 as derived in Sect. 1.2.1, while that of CR spectrum observed on the Earth is -2.7. The difference in indices would be explained by considering the propagation effect in the Galaxy. In this section, we introduce the observation of energy dependency on the diffusion.

The steady-state transport equation can be written by:

$$\frac{\partial N_i}{\partial t} = (\text{Injection}) + (\text{Decay from heavier nuclei}) \tag{1.33}$$

$$- (\text{Loss due to collision}) - (\text{Loss due to decay}) \tag{1.34}$$

$$= Q_i + \frac{v\rho}{m_{\rm p}}\sum_{k>i}\sigma_{k\to i}N_k - \frac{v\rho\sigma_i}{m_{\rm p}}N_i - \frac{1}{\Gamma\tau_{\rm life}}N_i \tag{1.35}$$

where each parameter means the follows.

i, k: the particle species
N: the number density of CR particle
v: the velocity of CR particle
ρ: the matter density in the Galaxy
m_p: the rest mass of proton
$\sigma_{k\to i}$: the decay probability from heavier nuclei
σ: the cross section between the particle and the matter in the Galaxy
Γ: the Lorentz factor
$\tau_{\rm life}$: the lifetime of particle

Here, we assume that boron (B) is not elementally synthesized in space ($Q_B = 0$) and generated only by decay from carbon (C) and oxygen (O). We also assume that the lifetime of boron is sufficiently long to survive without decay during propagation (i.e. $1/(\Gamma\tau_{\rm life})N_i \sim 1$). Once the fraction of CR escaping from the Galaxy is written as $\exp(-{\rm t}/\tau_{\rm esc})$, Eq. 1.33 becomes:

$$\frac{N_{\rm B}}{\tau_{\rm esc}} = \frac{v\rho}{m_p}(\sigma_{\rm C\to B}N_{\rm C} + \sigma_{\rm O\to B}N_{\rm O}) \tag{1.36}$$

Furthermore, we can transform this equation using $N_{\rm O} \sim N_{\rm C}$:

$$\frac{N_{\rm B}}{N_{\rm C}} = \frac{\lambda_{\rm esc}}{1-\lambda_{\rm esc}/\lambda_{\rm B}}\frac{\sigma_{\rm C\to B}+\sigma_{\rm O\to B}}{m_p} \tag{1.37}$$

where $\lambda_{\rm B}(\equiv m_{\rm p}/\sigma_{\rm B})$ is the mean free path of the boron in space and $\lambda_{\rm esc}(\equiv v\rho\tau_{\rm esc})$ is the path length of escaping CR particles. In Eq. 1.37, $\lambda_{\rm B}$, $\sigma_{\rm C\to B}$, and $\sigma_{\rm O\to B}$ can be measured with ground-based experiments. $\lambda_{\rm esc}$ is expected to depend on the kinetic energy (velocity) of the particles, and follows a relation: $\lambda_{\rm esc} \propto E^{\delta}$. Once we can evaluate the energy dependence of $\lambda_{\rm esc}$, we can estimate the effect of CR diffusion on the observed CR spectrum. The observed energy dependence of the CR boron and carbon abundance ratios is shown in Fig. 1.5. The fitted result ($\lambda_{\rm esc} \propto E^{-0.6}$) indicates that the index is softened by $\sim$0.6 due to the CR diffusion (Garcia-Munoz et al., 1987). Consequently, the spectral index of CRs arriving from SNR to the Earth can be estimated to be: $\alpha + \delta \sim -2.6$, which is comparable to the observed spectrum.

The recent result from more precise observation of secondary-to-primary ratio (e.g., Boron-to-Carbon ratio) indicates a flatter slope of $\delta = -0.333 \pm 0.014_{\rm stat} \pm 0.005_{\rm syst}$ (Aguilar et al., 2016) than -0.6. This agrees well with expectation from the Kolmogorov turbulence theory, in which δ is asymptotically equal to $-1/3$ (Kolmogorov, 1991). However, this also suggests that the effect due to CR diffusion alone cannot explain the discrepancy in the spectral slope ($\sim$ 0.7) between the CR spectrum measured at the Earth ($\sim$ 2.7) and the injection spectrum at the CR source ($\sim$ 2.0; expected by DSA) as above stated. This discrepancy would imply an injection spectrum $\propto E^{-2.4}$, which is preferable from the point of view of anisotropy (Blasi & Amato, 2012). On the other hand, if considering spectral hardening observed in the the

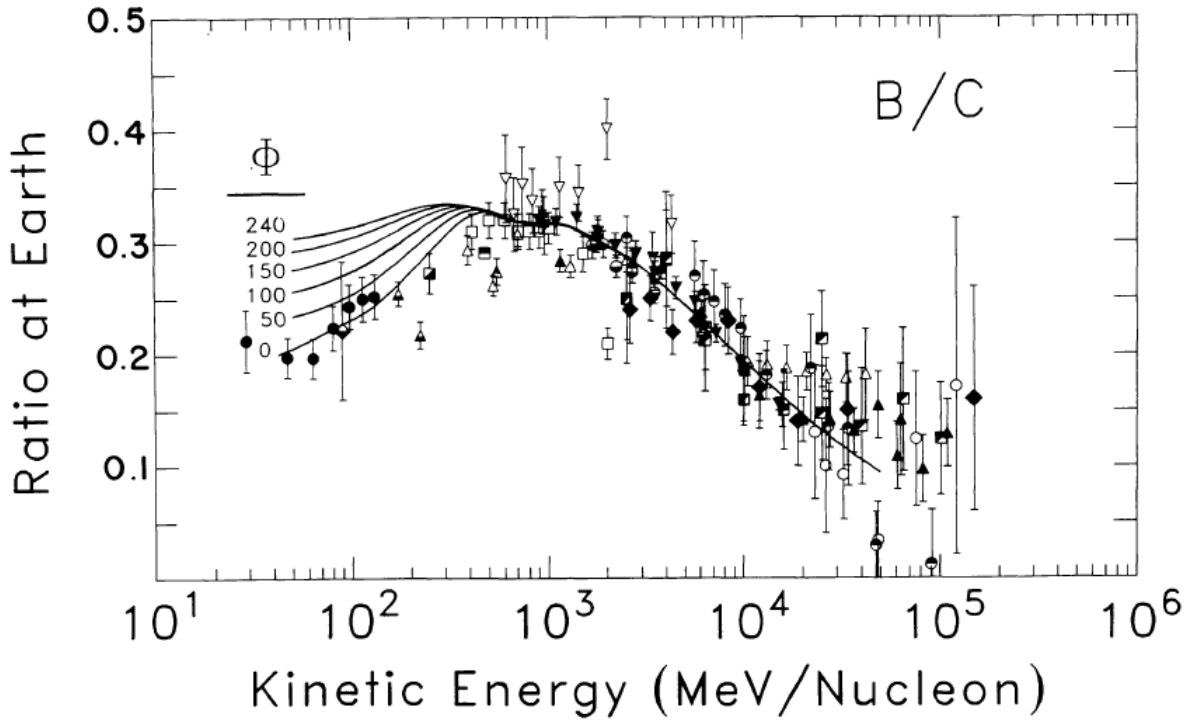

Figure 1.5: B/C ratio spectrum, taken from Garcia-Munoz et al. (1987). The black lines show the model curves (an exponential with $X_0 \propto E^{-0.6}$ for > 1 GeV) using different levels of solar modulation.

elemental spectra (Ahn et al., 2010) using the broken power-law function:

$$D(E) = D_0 \frac{E^{\delta}}{(1 + (E/E_{\rm b})^{\Delta\delta/s})^s}, \tag{1.38}$$

instead of

$$D(E) = D_0 E^{\delta}, \tag{1.39}$$

δ can be estimated to be 0.43–0.53 (Génolini et al., 2017, 2019), which relaxes the disagreement and is close to a Kraichnan turbulence spectrum ($\delta = -1/2$; Iroshnikov, 1964; Kraichnan, 1967). Such spectral hardening could be reproduced if assuming an additional CR source near the Earth (Kawanaka & Lee, 2021). However, it is still controversial and requires further investigation of CR diffusion, especially around SNRs.

1.3 Lights from CRs in SNRs

The interstellar magnetic field bends the pass of accelerated particles. The Larmor radius of a proton ($Z = 1$) with an energy of E is expressed with:

$$R_{\rm L} \sim 1 \text{ pc} \left(\frac{\rm E}{3 \times 10^{15} \text{ eV}} \right) \left(\frac{\rm B}{3 \ \mu\rm G} \right)^{-1}, \tag{1.40}$$

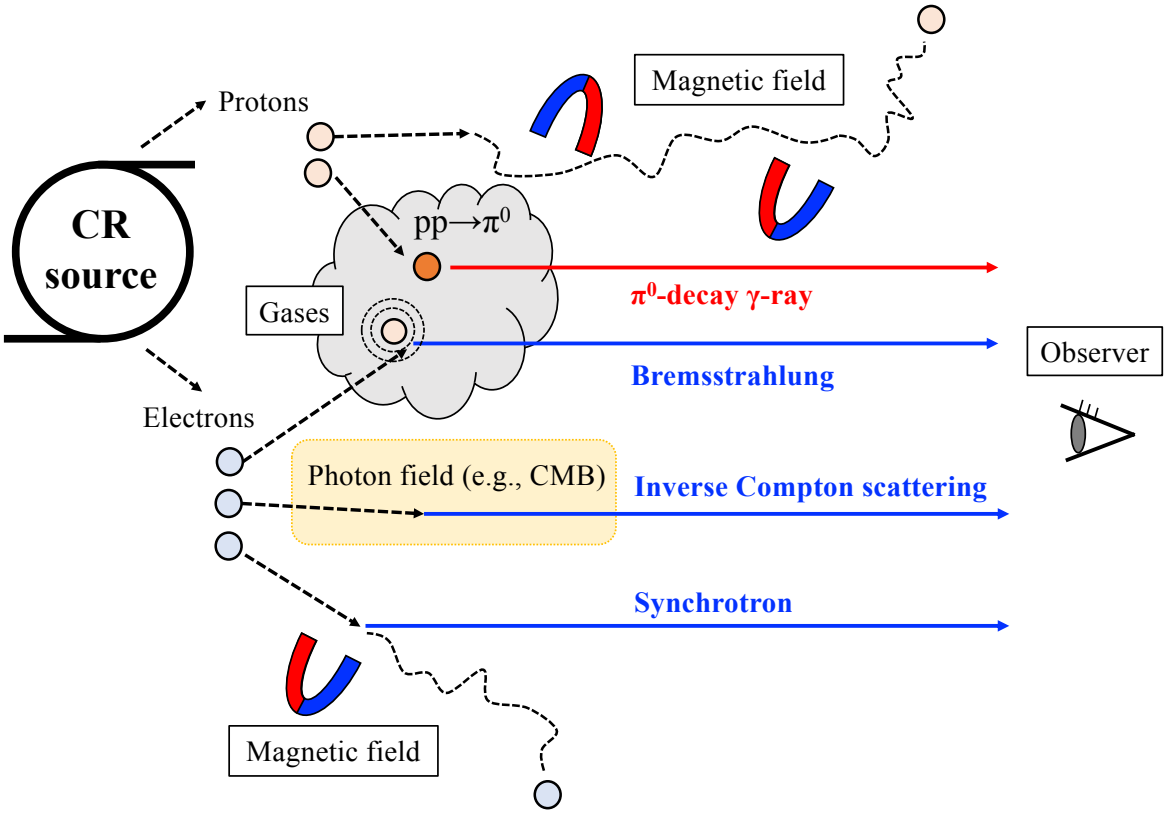

Figure 1.6: Illustration of the γ-ray emission processes around the CR source. Although CRs lose the information of their acceleration site, the γ-ray emissions would tell us them.

where B is the magnetic-field strength, normalized by the average interstellar value of 3 μG. This indicates that a PeV proton cannot travel straight for >1 pc without affections of the magnetic field and thus lose the information where they were accelerated. However, CRs also emit light via several processes as described in Sections 1.3.1 through 1.3.4 (see Fig. 1.6 for schematic illustration). Since light travels straight through space without affection by magnetic fields, its observation allows us to identify the acceleration site.

1.3.1 Neutral-pion decay

The protons collide with nuclei in the ISM, then produce π^0 as follows:

$$p + p \rightarrow p + p + \pi^0\pi^+\pi^-. \tag{1.41}$$

98% of π^0 decay accompany emitting a pair of γ rays as follows:

$$\pi^0 \rightarrow 2\gamma. \tag{1.42}$$

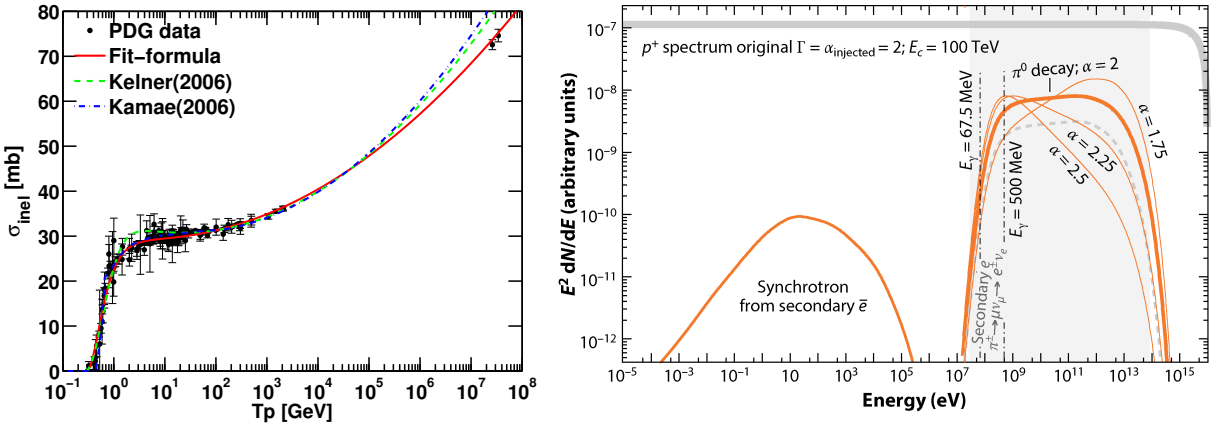

Figure 1.7: **Left**: Cross section for the proton-proton collisions (Kafexhiu et al., 2014). The abscissa is the kinetic energy of the proton in the laboratory frame. Black points indicate measured data and the red line shows the fitted curve for the points. **Right**: Example of the energy spectrum of γ-ray produced via the π^0-decay process (Funk, 2015). α means the assumed index of the differential proton spectrum.

The energy of γ-ray emission by this process can be written as:

$$E_\gamma = \frac{1}{2} m_\pi \Gamma_\pi (1 + \beta_\pi \cos\theta) \tag{1.43}$$

$$E_{\gamma,\ \mathrm{min}} = \frac{1}{2} E_\pi (1 - \beta_\pi),\ \ E_{\gamma,\ \mathrm{max}} = \frac{1}{2} E_\pi (1 + \beta_\pi), \tag{1.44}$$

where m_π is the rest mass of π^0 (~ 135 MeV), β_π is the velocity of π^0, Γ_π is the Lorentz factor, and θ is the angle between the direction of π^0 and the γ ray. The fraction of proton kinetic energy transferring to π^0 is $\kappa_{\pi^0} \sim 0.17$ (e.g., Funk, 2015), and then the energy fraction of γ-ray to proton is ~ 0.09 because the γ-ray energy should be half of π^0.

The energy loss rate of the π^0-decay process is given by

$$\left(\frac{dE}{dt}\right)_{\pi^0} \sim \frac{\Delta E}{\Delta t} = \frac{\kappa_{\pi^0} E_\mathrm{p}}{1/(cn\sigma_\mathrm{pp}^\mathrm{inel})} = \kappa_{\pi^0} E_\mathrm{p} cn \sigma_\mathrm{pp}^\mathrm{inel}, \tag{1.45}$$

where $\sigma_\mathrm{pp}^\mathrm{inel}$ is the inelastic proton-proton cross section, and n is the average density of target protons. Hence, the timescale of energy loss due to the neutral pion decay is

$$\tau_{\pi^0} = \frac{E}{dE/dt} \sim \frac{1}{\kappa_{\pi^0} cn \sigma_\mathrm{pp}^\mathrm{inel}} \sim 1.6 \times 10^8 \ \mathrm{yr} \left(\frac{\mathrm{n}}{1\ \mathrm{cm}^{-3}}\right)^{-1} \left(\frac{\sigma_\mathrm{pp}^\mathrm{inel}}{40\ \mathrm{mb}}\right)^{-1}. \tag{1.46}$$

The left panel of Fig. 1.7 shows $\sigma_\mathrm{pp}^\mathrm{inel}$ as a function of energy. The energy threshold of this γ-ray emission process is determined by the rest mass of π^0. Hence, the γ-ray spectrum has a characteristic cutoff at ~ 100 MeV. The right panel of Fig. 1.7 shows the energy spectrum of γ rays produced due to the proton-proton interaction. This spectrum has a "bump" structure in the energy band from 100 MeV to 1 GeV and its index after the bump is equal to that of proton.

Note that, CR protons can make not only π^0 and also the charged pions (π^+, π^-) by the interaction with nuclei in the ISM.

$$\mathrm{p} + \mathrm{p} \rightarrow \mathrm{p} + \mathrm{n} + \pi^+ \tag{1.47}$$

$$\mathrm{p} + \mathrm{p} \rightarrow \mathrm{n} + \mathrm{n} + 2\pi^+ \tag{1.48}$$

$$\mathrm{p} + {}^4\mathrm{He} \rightarrow 4\mathrm{p} + \mathrm{n} + \pi^-. \tag{1.49}$$

π^+ and π^- decay with a lifetime of 2.6×10^{-8} s, and the muon pairs (μ^+, μ^-) are produced. Furthermore, these muons then decay with a lifetime of 2.2×10^{-6} s, producing electron pairs (e^+, e^-). The Synchrotron emission (the detail of which will be described in 1.3.2) from these is shown in the right panel of Fig. 1.7.

1.3.2 Synchrotoron

Charged particles moving at relativistic speeds radiate electromagnetic waves when accelerated by magnetic filed. This radiation is called synchrotron radiation. The energy loss rate of charged particles, is expressed by

$$\left(\frac{dE}{dt}\right)_{\mathrm{sync}} = \frac{4}{3}\sigma_{\mathrm{T}} c \beta^2 \Gamma^2 U_{\mathrm{B}}, \tag{1.50}$$

where Γ is the Lorentz factor, $\sigma_{\mathrm{T}} = 8\pi r_0^2/3 = 0.665 \times 10^{-28}$ m^2 ($r_0 \equiv e^2/(m_{\mathrm{e}}c^2)$; classical electron radius) is the Thomson scattering cross section, and $U_{\mathrm{B}} = B^2/(8\pi)$ is the energy density of the magnetic field (B). Assuming they have the same energy (E) and substituting $\sigma_{\mathrm{T}} \propto 1/m^2$ and $\Gamma = E/(mc^2)$, the synchrotron radiation intensity ratio of electrons to protons is found to be

$$\frac{P_{\mathrm{p}}}{P_{\mathrm{e}}} = \left(\frac{m_{\mathrm{e}}}{m_{\mathrm{p}}}\right)^4 = 9 \times 10^{-14}. \tag{1.51}$$

Since the synchrotron radiation of protons is much lower than that of electrons, the energy loss due to its radiative cooling is small, indicating the protons can be accelerated to higher energy than electrons. Using Eq. 1.50, the timescale for synchrotron cooling can be written as

$$\tau_{\mathrm{sync}} = 1.25 \times 10^5 \text{ yr } \left(\frac{\mathrm{E_e}}{1 \text{ TeV}}\right)^{-1} \left(\frac{\mathrm{B}}{10\ \mu\mathrm{G}}\right)^{-2} \tag{1.52}$$

where E_{e} is the energy of electrons. In addition, the average energy of a photon from synchrotron radiation from a monochromatic electron can be written by

$$\epsilon \sim 2 \text{ keV } \left(\frac{\mathrm{E_e}}{100 \text{ TeV}}\right)^2 \left(\frac{\mathrm{B}}{10\ \mu\mathrm{G}}\right). \tag{1.53}$$

If the energy distribution of particles is represented by a power-law function $N(E) \propto E^{\alpha}$, then the photon spectrum can also be represented by a power-law function of

$$\epsilon \frac{dn}{d\epsilon} \propto \epsilon^{(\alpha-1)/2}. \tag{1.54}$$

Substituting $\alpha = 2$ expected by the DSA into Eq. 1.54, we can obtain the photon index of 0.5. This value agrees well with the observations of SNRs in the radio band (Reynolds et al., 2012).

1.3.3 Inverse Compton scattering

High-energy electrons produce γ rays by passing energy when they collide with light. This process is called inverse Compton scattering (ICs). The energy loss of charged particles due to ICs, is expressed by

$$\left(\frac{dE_{\rm e}}{dt}\right)_{\rm IC} = \frac{4}{3}\sigma_{\rm T} c \Gamma^2 \beta^2 U_{\rm photon}, \tag{1.55}$$

where $U_{\rm photon}$ represents the energy density of the radiation field. Thus, the cooling time scale due to IC is written by

$$\tau_{\rm IC} = 3.1 \times 10^5 \text{ yr} \left(\frac{\rm E_e}{1 \text{ TeV}}\right)^{-1} \left(\frac{\rm U_{photon}}{1 \text{ eV cm}^{-3}}\right)^{-1}. \tag{1.56}$$

1.3.4 Bremssthlung

Bremsstrahlung is the process by which γ rays are emitted when a charged particle is accelerated by the electric field of an atomic nucleus instead of magnetic field considered in the synchrotron process. The emission of bremsstrahlung by relativistic electrons ($E \gg m_{\rm e}c^2$) is expressed by

$$\left(\frac{dE_{\rm e}}{dt}\right)_{\rm Brems} = \frac{3}{2\pi}\sigma_T c \alpha Z(Z+1) n (ln\Gamma + 0.36) E_{\rm e}, \tag{1.57}$$

where α is the fine-structure constant (1/137.036), Z is the atomic number of the target particle, and n is its number density. Thus, assuming $Z = 1$, the cooling time scale due to the bremsstrahlung is found to be

$$\tau_{\rm Brems} \sim 2.8 \times 10^8 \text{ yr} \left(\frac{\rm n}{1 \text{ cm}^{-3}}\right)^{-1} \frac{1}{(\ln\Gamma + 0.36)}. \tag{1.58}$$

1.3.5 Contributions to γ-ray flux

Fig. 1.8 shows the comparison of the radiative cooling timescale. $U_{\rm photon}$ and B are set to 0.26 eV cm^{-3} and 3 μG, respectively, the former corresponding to the energy density of CMB and the latter to the average magnetic-field strength in the Galaxy. The dominant cooling process for TeV electrons in SNRs is expected to be synchrotron losses because the magnetic field should be amplified due to the compression by the shock wave.

The contribution to the γ-ray flux from each radiation process can be also compared using these cooling times scales. We first compare the fluxes at 1 TeV due to neutral pion decay (F_{π^0}) and IC ($F_{\rm IC}$). γ rays with an energy of $\sim$ 1 TeV are produced by electrons (protons) with an energy of $E_{\rm e} \sim 20$ TeV ($E_{\rm p} \sim 10$ TeV) in the IC process with CMB (neutral pion decay) (Gabici & Aharonian, 2016). The flux ratio can be then written as:

$$\frac{F_{\rm IC}}{F_{\pi^0}} = \frac{1/\tau_{\rm IC} \times K_{\rm ep}}{1/\tau_{\pi^0}} \sim 0.27 \left(\frac{U_{\rm photon}}{0.265 \text{ eV cm}^{-3}}\right) \left(\frac{n}{100 \text{ cm}^{-3}}\right)^{-1} \left(\frac{K_{\rm ep}}{0.01}\right), \tag{1.59}$$

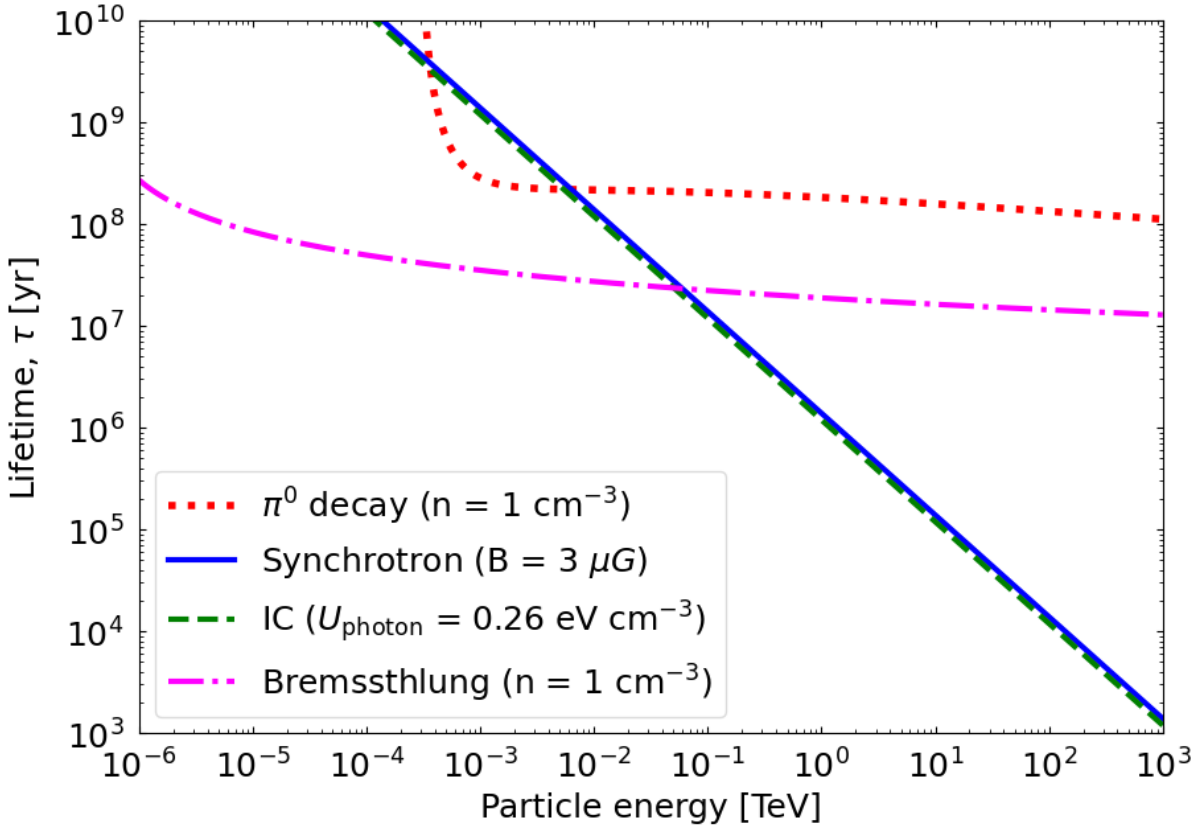

Figure 1.8: The typical cooling timescale due to π^0-decay (red dotted), Synchrotron (blue solid), IC (green dashed), and Bremssthlung (magenta dot-dashed).

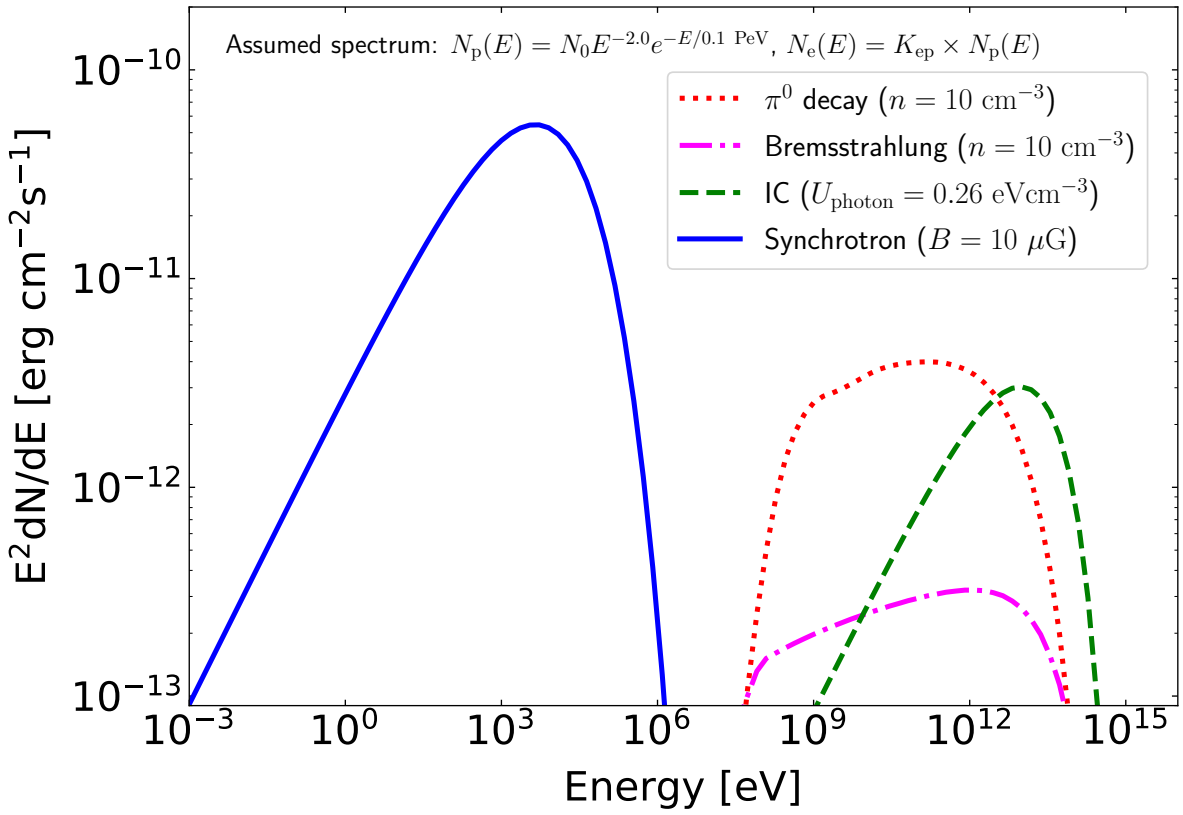

Figure 1.9: An example of the non-thermal emissions from an SNR. The red dotted, blue solid, green dashed, and magenta dot-dashed lines represent the emissions from π^0-decay, Synchrotron, IC, and Bremssthlung, respectively.

where $K_{\rm ep}$ is the electron-to-proton flux ratio and set to 1%, corresponding to the measured ratio of CRs at the Earth (Aguilar et al., 2015b, 2018). Eq. 1.59 implies that the π^0-decay radiation is dominant compared to IC at dense gas regions (e.g., molecular cloud). We also compare the flux from Bremssthlung with π^0-decay emission. As with Eq. 1.59, using Eq. 1.46 and 1.58, the Bremssthlung-to-π^0 flux ratio can be written as:

$$\frac{F_{\rm Brems}}{F_{\pi^0}} \sim 0.1 \left(\frac{K_{\rm ep}}{0.01} \right). \tag{1.60}$$

This does not depend on the gas density but only on the electron-to-proton flux ratio ($K_{\rm ep}$).

We calculate possible non-thermal emission spectra by primary particles accelerated at an SNR using the *naima* package (Zabalza, 2015), as shown in Fig. 1.9. Here we assume that the proton spectrum follows the power law with exponential cutoff function, and the electron spectrum has the same index and cutoff as the proton, with only normalization scaled by $K_{\rm ep}$ of 1%.

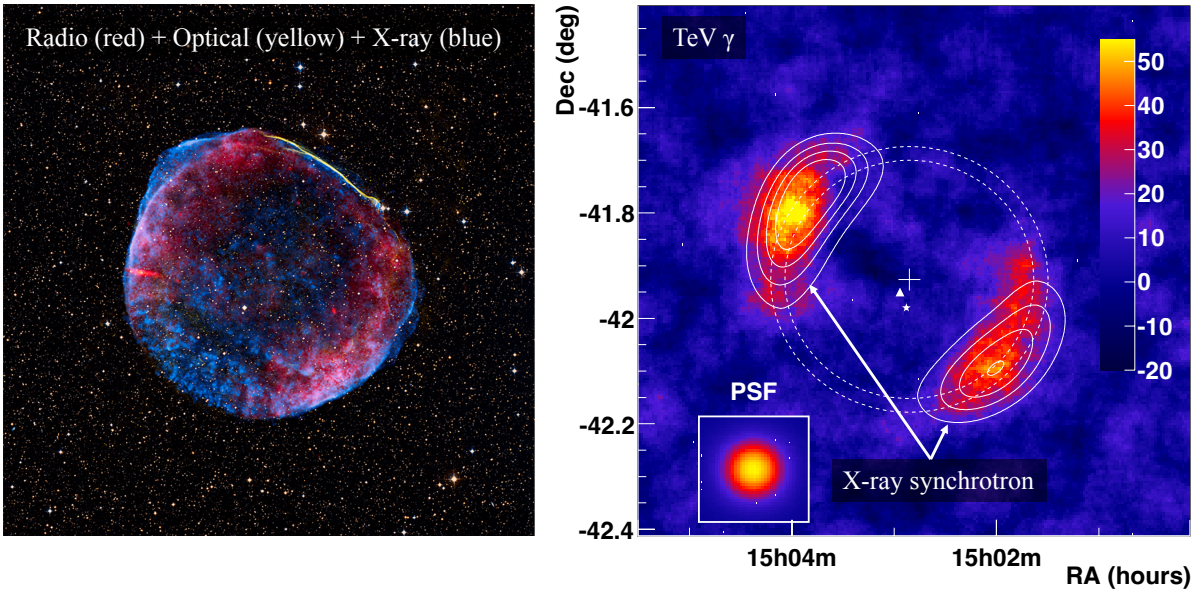

Figure 1.10: The sky image of SN 1006. **Left**: Composite view of the remnant of supernova SN 1006, including X-ray data in blue from the Chandra Observatory, optical data in yellowish hues, and radio image data in red. Image Credit: NASA, ESA, Zolt Levay (STScI). **Right**: TeV γ-ray image of SN 1006 (Acero et al., 2010). The white contours correspond to a constant 2–4.5 keV X-ray intensity as derived from the XMM-Newton flux map and smoothed to the H.E.S.S. point spread function, enclosing respectively 80%, 60%, 40% and 20% of the X-ray emission.

1.4 Overview of the SNR observations and PeVatron search

To elucidate the CR origin, search for the PeV proton accelerator "PeVatron" has been conducted thus far (see, e.g., Cristofari, 2021, for a review). This section describes the overview of SNR observations (Sect. 1.4.1) and 100-TeV γ-ray observations (Sect. 1.4.2) for the PeVatron search.

1.4.1 Observations for SNRs

In the history of SNR observations, Koyama et al. (1995) first discovered the synchrotron X-ray (non-thermal) emission in an SNR named SN1006. The follow-up observation detected TeV γ rays emitted from the same region as the synchrotron emission (Acero et al., 2010). These suggest an electron acceleration up to $\gtrsim$ 10 TeV in an SNR. Fig. 1.10 shows the skymaps of SN1006. The non-thermal emission (i.e., γ rays and synchrotron X-rays) regions spatially coincide with the shock front of the SNR, indicating that an efficient CR acceleration occurs there. In addition, the detailed observations of SN 1006 have revealed a filament structure with a width of $<$ pc of SNR shock waves (Bamba et al., 2003). Using the filament size and the magnetic-field strength derived by the X-ray observation, the maximum energy of electrons is estimated to be 37^{+4}_{-7} TeV.

The GeV γ-ray observations of SNRs IC 443, W44, and W51C with AGILE/Fermi-LAT revealed a bump structure that appears only in the π^0-decay spectrum (Fig. 1.11), providing

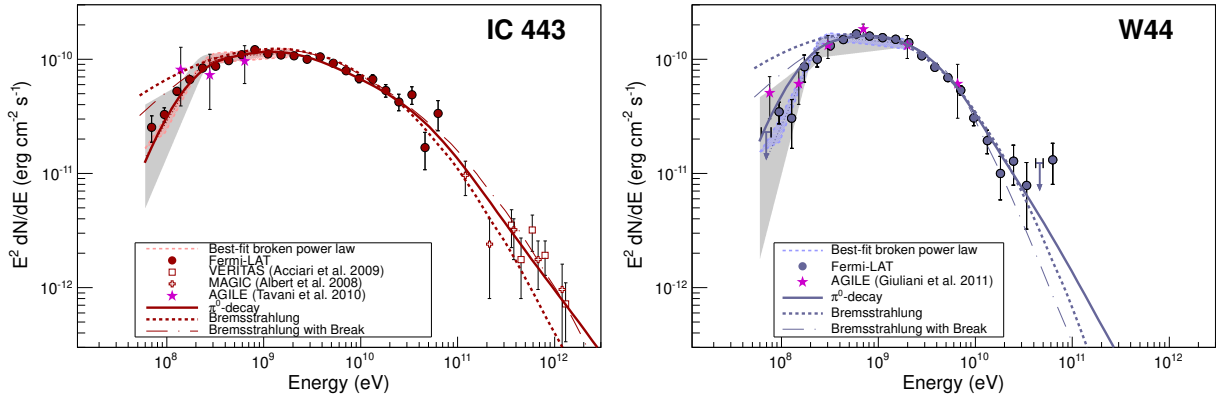

Figure 1.11: Gamma-ray spectra of IC443 (Left) and W44 (Right). Taken from Ackermann et al. (2013). In each panel, the solid line represents the π^0-decay emission, while the dashed and dash-dotted lines represent the electron bremsstrahlung emissions without/with the low-energy break at 300 MeV in the electron spectrum.

evidence for proton acceleration in the SNR (Ackermann et al., 2013; Jogler & Funk, 2016; Giuliani et al., 2011; Cardillo et al., 2016).

TeV γ rays have already been detected at $\gtrsim$ 20 SNRs[2], and these observations can give a lower or upper limit to maximum particle energy at SNRs. However, as mentioned in Sect. 1.3, there are multiple mechanisms for γ rays, thus we first need to identify the parent particle (i.e., electron or proton) and its emission mechanism. This identification can be approached by using γ-ray morphology. The fluxes of hadronic and electron bremsstrahlung emissions are proportional to the proton density, while IC does not depend on it (see Sect. 1.3). Hence, We can distinguish whether the radiation process is IC with the spatial correlation between the dense gas and the γ-ray emission. Moreover, once we assume $K_{\rm ep} = 1\%$ (corresponding to the measurement near Earth), we can consider that hadronic emission is dominant rather than Bremsstrahlung, as in Eq. 1.60.

Such spatial correlation between dense gas and γ-ray emission has been reported in several SNRs. For example, TeV emissions have been found from molecular clouds around SNR W28 (Aharonian, 2008a), as shown in Fig. 1.12. Since such middle-aged SNR with an age of 20–30 kyr is not expected to accelerate CRs efficiently, the TeV emissions are interpreted by considering re-acceleration due to shock-cloud interaction and/or CRs escaped from SNRs in the past (Uchiyama et al., 2010; Cui et al., 2018). Spatial correlations between dense gas and TeV γ rays have been found also in the young SNRs (e.g., Fukui et al., 2012; Sano et al., 2019), but the angular resolution of γ-ray observations is still insufficient to spatially separate the emissions from the shell and the dense gas. (e.g., Abdalla et al., 2018a). The latest research using the three-dimensional likelihood analysis of energy and morphology found the possibility of separating them (Fukui et al., 2021), and the next-generation TeV observatory is expected to give more reliable results (Acero et al., 2017). However, its maximum particle energy is at most $\lesssim$ 100 TeV in any cases and the existence of PeV protons in the SNR has not been confirmed.

[2] http://tevcat.uchicago.edu/

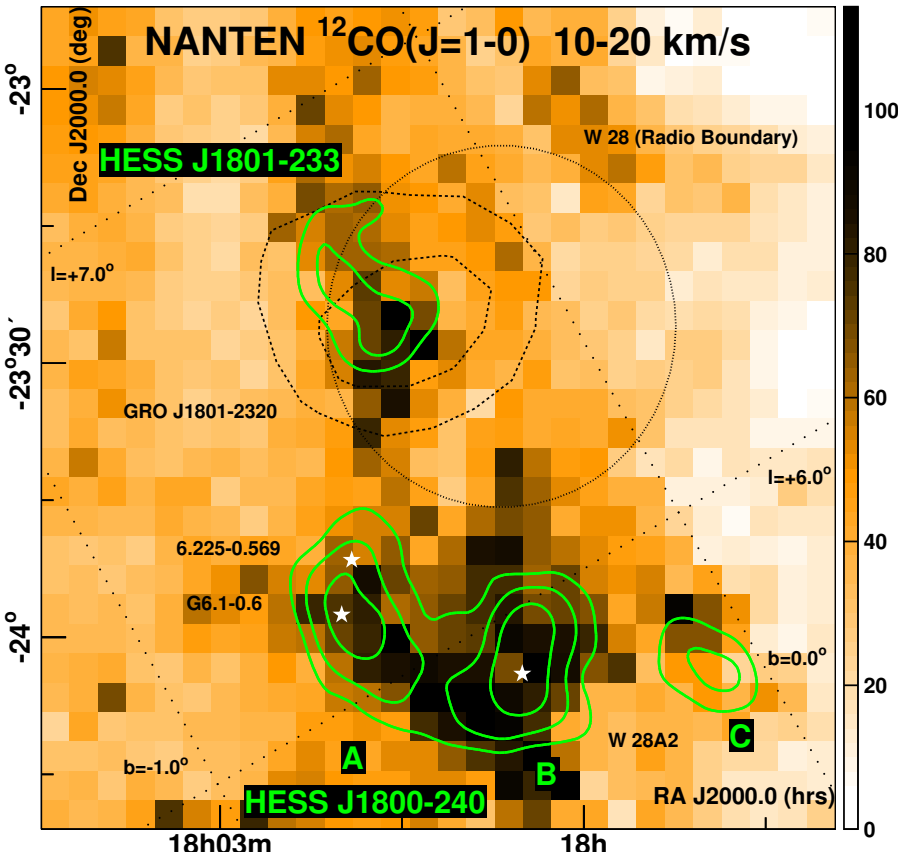

Figure 1.12: Skymap of molecular clouds measured with ^{12}CO ($J = 1 - 0$) line emission in the vicinity of SNR W28, overlaid with green counters of the TeV emissions (Aharonian, 2008a). The thin-dashed black circle represents the approximate radio boundary of the SNR.

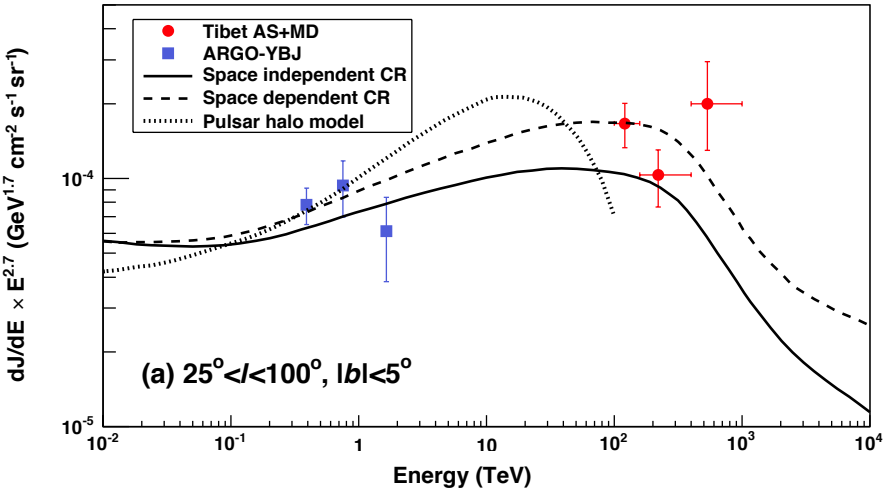

Figure 1.13: Energy spectrum of the diffuse γ rays from the Galactic plane in the region of $|b| < 5°, 25° < l < 100°$ (Amenomori et al., 2021a). The solid and dashed curves show the predicted hadronic emissions from local CR sources with the space-independent and space-dependent models (Lipari & Vernetto, 2018). The dotted curve shows the predicted leptonic emission from PWNe (Linden & Buckman, 2018).

1.4.2 Sub-PeV γ-ray observations

An observation of γ rays above 100 TeV is a reliable (actually only reliable when emission is proven to be hadronic) method to confirm the potential PeVatron. The recent detection of the diffuse sub-PeV γ rays from the Galactic diffuse plane suggests the presence of PeVatron in the Galaxy (Amenomori et al., 2021a). Fig. 1.13 shows the energy spectrum of the Galactic diffuse emission, which suggests the sub-PeV flux can be reproduced with the hadronic emission of local CR sources rather than leptonic emissions from PWNe[3]. Another recent observations with the LHAASO experiment have revealed 12 sources emitting a sub-PeV γ-ray emission (Cao et al., 2021), as tabulated in Table 1.2. However, the almost sources are possibly originated in a pulsar wind nebula (PWN) rather than an SNR.

PWNe are generated by the interaction between the circumstellar material and the electron-positron pair wind driven by the pulsar, which composes of a high density, a strong magnetic field, and high rotation speeds. Its shock wave is considered to accelerate mainly electrons and positrons served by the pulsar, whereas it can also accelerate protons theoretically (e.g., Nagataki, 2004). At present, no hint of proton acceleration has yet been obtained, and the latest Crab Nebula observation with LHAASO did not see it (Cao et al., 2021).

1.5 Research objectives and thesis structure

From the standpoint of believing the paradigm that SNRs are PeVatrons, we can interpret why a PeVatron has not been discovered yet, with the following two scenarios:

[3]Fang & Murase (2021) argued that the leptonic emissions from PWNe still can reproduce the observed sub-PeV γ-ray spectrum.

Table 1.2: The 100-TeV γ-ray sources detected with LHAASO (Cao et al., 2021).

Name	Possible Origin	Type	$E_{\rm max}$ [PeV]
J0534+2202	PSR J0534+2200	PSR	$0.88^{+0.11}_{-0.11}$
J1825−1326	PSR J1826−1334	PSR	$0.42^{+0.16}_{-0.16}$
	PSR J1826−1256	PSR	
J1839−0545	PSR J1837−0604	PSR	$0.21^{+0.05}_{-0.05}$
	PSR J1838−0537	PSR	
J1843−0338	SNR G28.6−0.1	SNR	$0.26^{+0.16}_{-0.10}$
J1849−0003	PSR J1849−0001	PSR	$0.35^{+0.07}_{-0.07}$
	W43	YMC	
J1908+0621	SNR G40.5−0.5	SNR	$0.44^{+0.05}_{-0.05}$
	PSR J1907+0602	PSR	
	PSR J1907+0631	PSR	
J1929+1745	PSR J1928+1746	PSR	$0.71^{+0.16}_{-0.07}$
	PSR J1930+1852	PSR	
	SNR G54.1+0.3	SNR	
J1956+2845	PSR J1958+2846	PSR	$0.42^{+0.03}_{-0.03}$
	SNR G66.0−0.0	SNR	
J2018+3651	PSR J2021+3651	PSR	$0.27^{+0.02}_{-0.02}$
	Sh 2−104	HII/YMC	
J2032+4102	Cygnus OB2	YMC	$1.42^{+0.13}_{-0.13}$
	PSR J2032+4127	PSR	
	SNR G79.8+1.2	SNR candidate	
J2108+5157	–	–	$0.43^{+0.05}_{-0.05}$
J2226+6057	SNR G106.3+2.7	SNR	$0.57^{+0.19}_{-0.19}$
	PSR J2229+6114	PSR	

(1) Some sources in Table 1.2 have not yet been identified well with a counterpart of the 100-TeV emission, and they thus may be SNR PeVatrons. Precise γ-ray observations will play an essential role in identifying γ-ray origins, leading to the discovery of SNR PeVatrons.

(2) We can consider the scenario as follows. An SNR is capable of accelerating particles up to PeV only when it is younger than 10^3 yr (Ptuskin & Zirakashvili, 2003, 2005), while such high-energy particles will escape from the SNR at an early stage (Gabici & Aharonian, 2007), reducing the opportunity of discovery of PeVatron. To validate this scenario, we need to measure the time evolution of the maximum acceleration energy at SNR.

In this thesis we explore the possibilities of the two scenarios described above. For the first point, we focus on LHAASO J2226+6057, which is expected to associate with the SNR G106.3+2.7 and thus one of the most promising PeVatron candidates. This SNR has a cometary shape which can be divided into a head and a tail region with different physical conditions. However, it is not identified in which region the 100 TeV emission is produced due to the limited position accuracy and/or angular resolution of existing observational data. Additionally, it remains unclear whether the origin of the γ-ray emission is leptonic or hadronic. We therefore carry out new observation for this source using the MAGIC telescopes, which is capable of observing γ rays with a better angular resolution than previous studies. The MAGIC telescope used for the observations is introduced in Chapter 2, and the MAGIC data analysis for SNR G106.3+2.7 are described in Chapter 3. The origin of the γ-ray emission is discussed in Chapter 4. For the second point, we propose a new way to measure the time evolution of the SNR, as described in Chapter 5, and apply this method to observed data. We select SNR HB9 as the first sample since this SNR has some advantages for this test, which we will mention in Chapter 5. We finally discuss the feasibility of the SNR paradigm in Chapter 6 based on these results, and summarize this work in Chapter 7.

Chapter 2

The MAGIC γ-ray telescope

To identify the γ-ray origin of PeVatron candidate SNR G106.3+2.7, further γ-ray observations with better angular resolution than the previous studies are required, as mentioned in the previous chapter. In this work, we observe this source with the MAGIC (Major Atmospheric Gamma Imaging Cherenkov) telescope, which is one of the Imaging Atmospheric Cherenkov Telescopes (IACTs) and achieves the highest sensitivity and better angular resolution than 0.1° at the TeV energy band. This chapter first introduces the Imaging Atmospheric Cherenkov technique used in the MAGIC telescope and describes in detail the configuration of the MAGIC telescope and the analysis method.

2.1 Imaging Atmospheric Cherenkov Telescope (IACT)

2.1.1 Air shower phenomena

Light in the ultraviolet and higher bands cannot be directly observed on the ground due to absorption by the atmosphere of the Earth. Basically, the observations in their bands are therefore carried out using telescopes onboard satellites. However, detecting high-energy γ rays requires a large effective area (because of the infrequent arrival), which is challenging to achieve

Figure 2.1: The two MAGIC telescopes. Image credits: Daniel Lopez/IAC

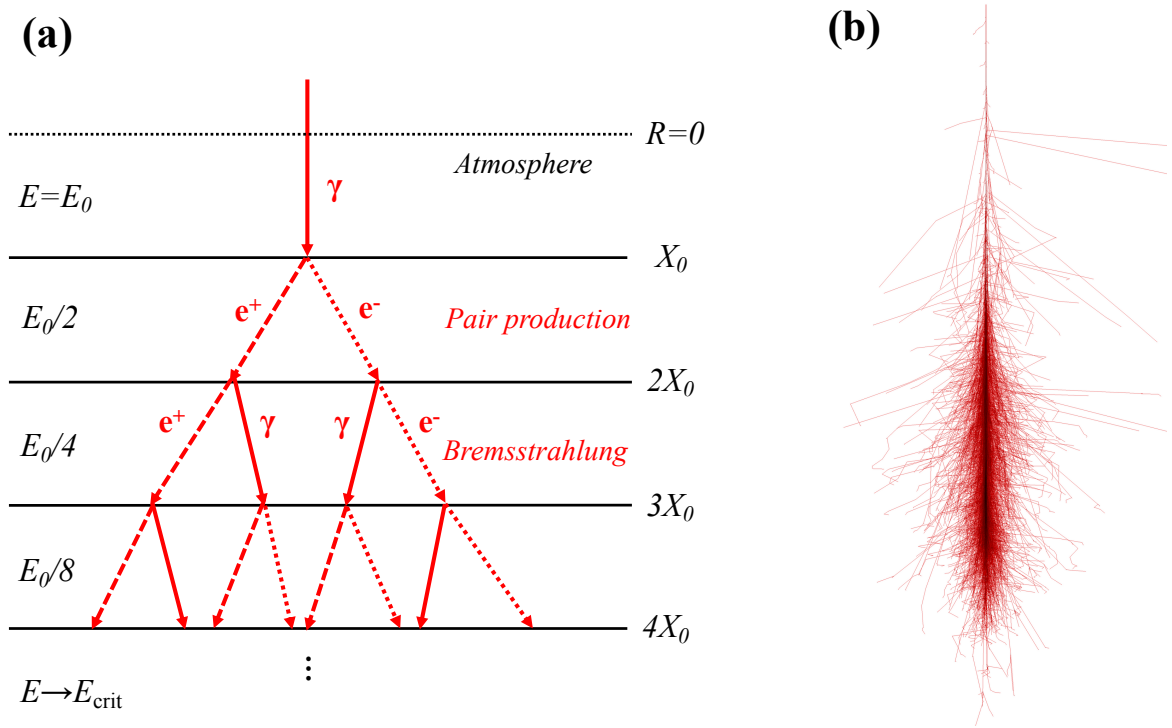

Figure 2.2: **(a)** Sketch of the electromagnetic shower phenomenon. E represents mean energies of particle or photon. X_0 is the radiation length of electron and positron, or a mean free path of a γ ray, with a dimension of the length. **(b)** CORSICA simulation of an electromagnetic air shower, initiated by a γ ray of 100 GeV (https://www.iap.kit.edu/corsika/). Image credit: Fabian Schmidt (University of Leeds, UK).

with a detector small enough onboard satellites. To observe such high-energy light, an innovative method was then proposed to use the atmosphere as a detector.

Once γ rays enter the atmosphere, the electron pair production occurs. The electrons then cause bremsstrahlung, producing γ rays, which causes again the pair production. The sequence of electron pair production and bremsstrahlung is repeated with the energy losses until the electron energy reaches the critical energy of $E_{\rm crit} \sim 83$ MeV, where electrons cannot cause another bremsstrahlung due to ionisation losses (see Fig. 2.2 for a sketch). This phenomenon is called an electromagnetic air shower. The longitudinal development of electromagnetic air showers approximately follows the semi-empirical model proposed by Greisen (1956), and is expressed with the so-called shower age (s) parameter. The shower age is defined as:

$$s = \frac{3t}{t + 2y} \text{ with } \mathrm{y} = \ln\frac{\mathrm{E_0}}{\mathrm{E_{crit}}}, \tag{2.1}$$

where E_0 is the primary energy and t is the shower depth in units of radiation length ($X_0 \sim 36.7$ g cm^{-2} for a dry air). The shower development begins at $s = 0$, reaches a maximum at $s = 1$ (i.e., $t = y$), and then decays. The average number of electron pairs above the critical

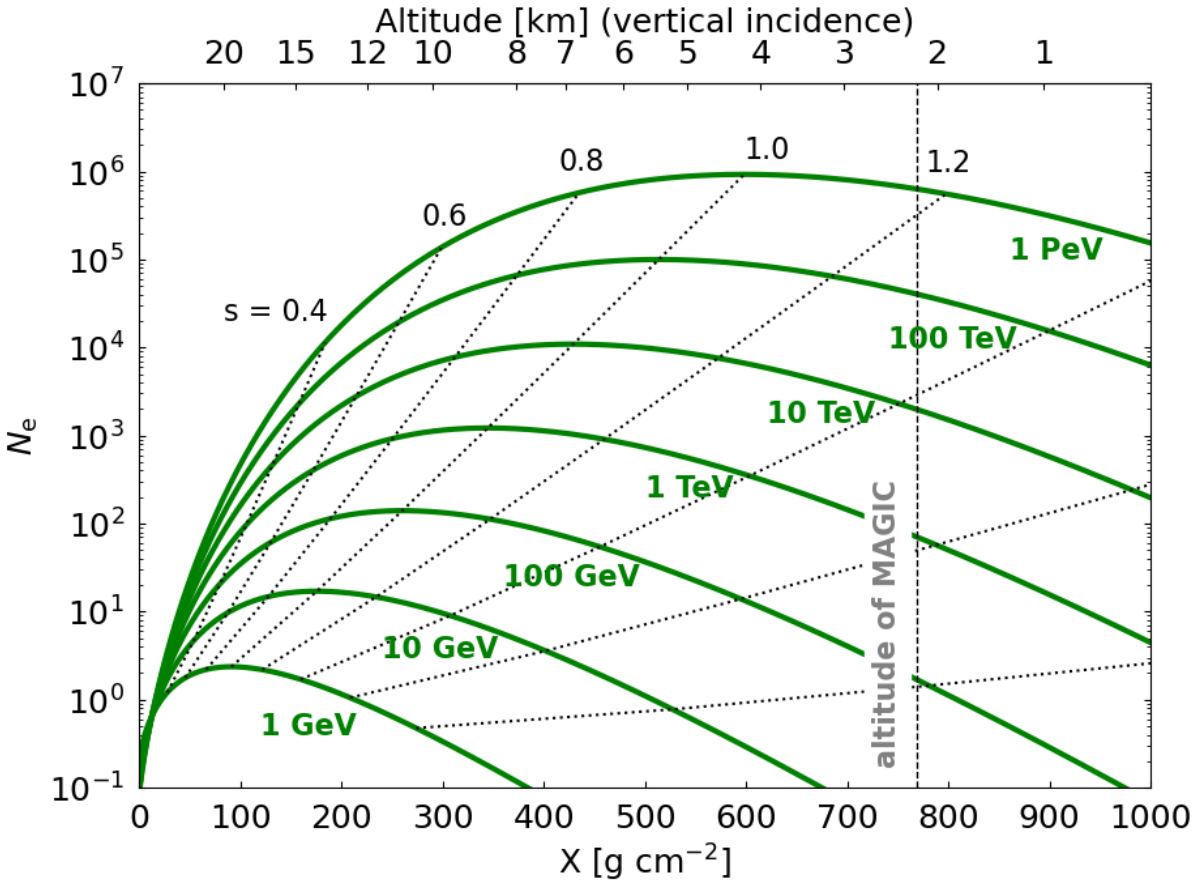

Figure 2.3: Longitudinal development of an electromagnetic air shower in a hydrostatic, isothermal atmosphere, following the Greisen semi-empirical model (Greisen, 1956). The shower size, characterized by the number of secondary electrons in the shower (N_e), is plotted as function of depth. The dashed lines corresponds to equal-age curves. The dashed lines corresponds to equal-age curves.

energy (E_{crit}) in the shower can be approximated by

$$N_e(t, E_0) = \frac{0.31}{\sqrt{y}} e^{t-1.5t\ln(s)}. \tag{2.2}$$

Figure 2.3 shows the longitudinal development of the γ-ray initiated air shower calculated using Eq. 2.2. For the IACT observations, it is necessary to capture the longitudinal development in the FoV. Therefore, an altitude of several thousand kilometers is suitable for the location of the telescope observing TeV γ rays.

2.1.2 Cherenkov emission

Once a charged particle travels faster than the speed of light in that medium, the medium is polarized and makes dipole radiation, as shown in the left panel in Figure 2.4. By Huygens' principle, the phases of the electromagnetic wave are aligned, resulting in a forward-beamed emission called "Cherenkov Radiation". Following this, electron pairs in an air shower emit the

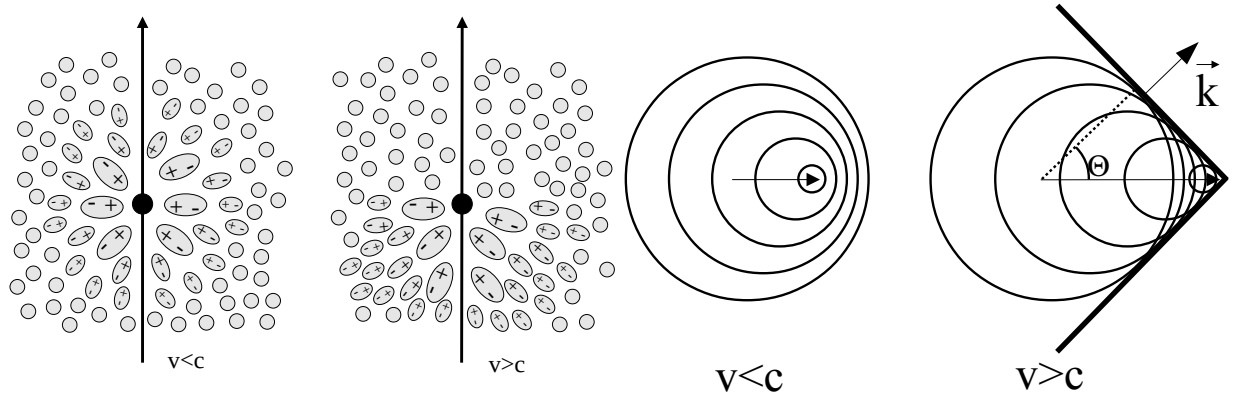

Figure 2.4: Illustration of the polarization of the medium induced by the crossing of a relativistic particle (Left) and Construction of Cherenkov wave-front (Right), which are taken from de Naurois & Mazin (2015).

Cherenkov light.

The radiation angle of the Cherenkov light (θ) depends on the velocity of the charged particle and the refractive index of the medium (n), and can be written by:

$$cos\theta = \frac{1}{\beta n} \text{ (for } \beta n \geq 1). \tag{2.3}$$

The typical refractive index of the atmosphere is $n \sim 1.0003$, and then $\theta \sim 1.4°$. With the overlapping of the Cherenkov lights from an air shower, its shape reproduces the longitudinal development of the shower.

The number of Cherenkov photons ($N_{\rm ph}$) per unit pass length and unit wavelength can be expressed as:

$$\frac{d^2 N_{\rm ph}}{dx d\lambda} = \frac{2\pi\alpha Z^2}{\lambda^2}(1 - \frac{1}{\beta^2 n^2}), \tag{2.4}$$

where α is the fine structure constant and Z is the atomic number of the incident particle. On the other hand, the photon spectrum will be affected by absorption in the air. Absorption is mainly due to O_3, O_2, and N_2 for the ultraviolet band (< 300 nm) and rotational or vibrational transition lines of H_2O and CO_2 for the infrared band. The resultant observable spectrum is shown in Figure 2.5 (Benn & Ellison, 1998; Bonardi et al., 2014), which peaks at 300–400 nm.

The density distribution of the Cherenkov light is expected to be uniform within the so-called light pool, the radius ($R_{\rm C}$) of which can be expressed as a product of the maximum height of air shower and θ. Thus, the radius for a γ ray of 100 GeV is estimated to be $R_{\rm C} = 10$ km $\times$ $1.0° \sim$ 110 m. In reality, however, the structure is broader than $R_{\rm C}$ due to the multiple scattering effect in the atmosphere. Fig. 2.6 shows simulations of Cherenkov photon density. Cherenkov photon densities are almost flat within $\sim$ 100 m, decreasing at large core distances. In addition, the density of Cherenkov photons increases at high altitudes, as with the air shower (Fig. 2.3). At higher altitudes, the telescopes are closer to the emission region, resulting in a larger density of photons over a smaller area on the ground. Hence, the energy thresholds of IACTs would be lower. On the other hand, there are several concerns with observations at high altitudes (e.g.,

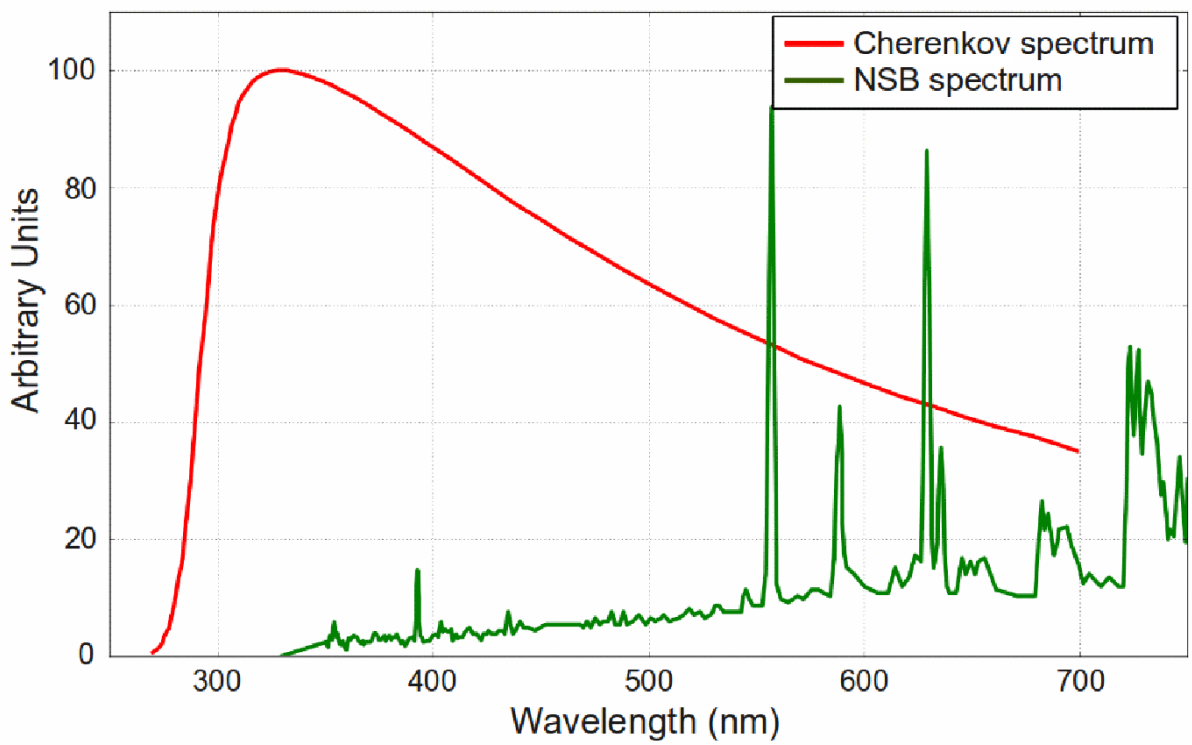

Figure 2.5: Cherenkov light and night sky background (NSB) spectra in La Palma (Canary Islands, Spain) at an altitude of 2200 m (Benn & Ellison, 1998; Bonardi et al., 2014).

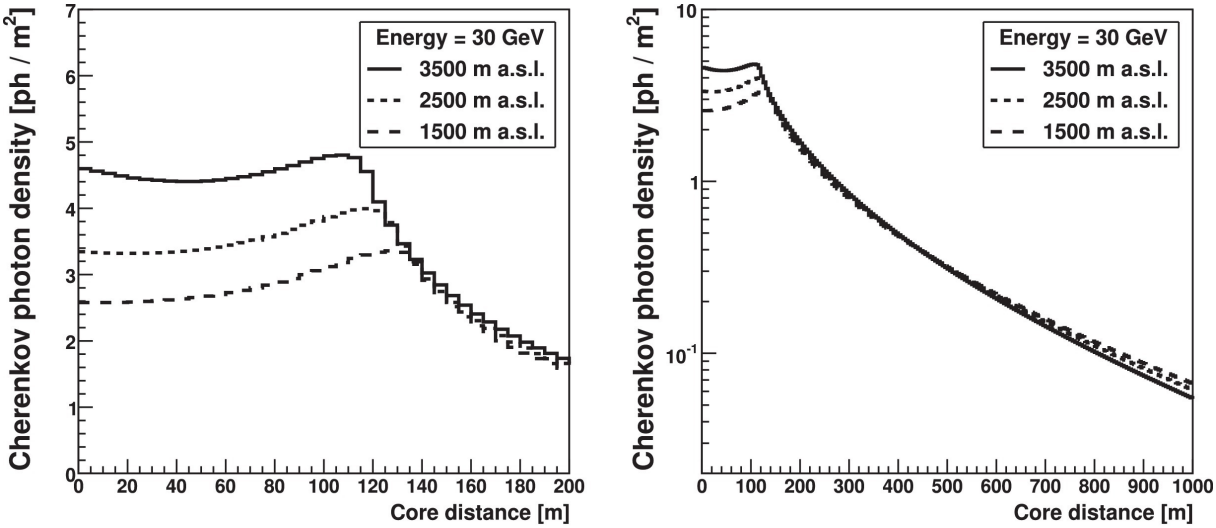

Figure 2.6: Lateral distributions of Cherenkov photon density for wavelengths from 300 to 600 nm (Hassan et al., 2017). The solid, dotted, and dashed lines represent results at an altitude of 3500, 2500, and 1500 m, respectively. **Left:** Cherenkov photon density in linear scale close to the core position. **Right:** Broader core distance ranges and logarithmic scale.

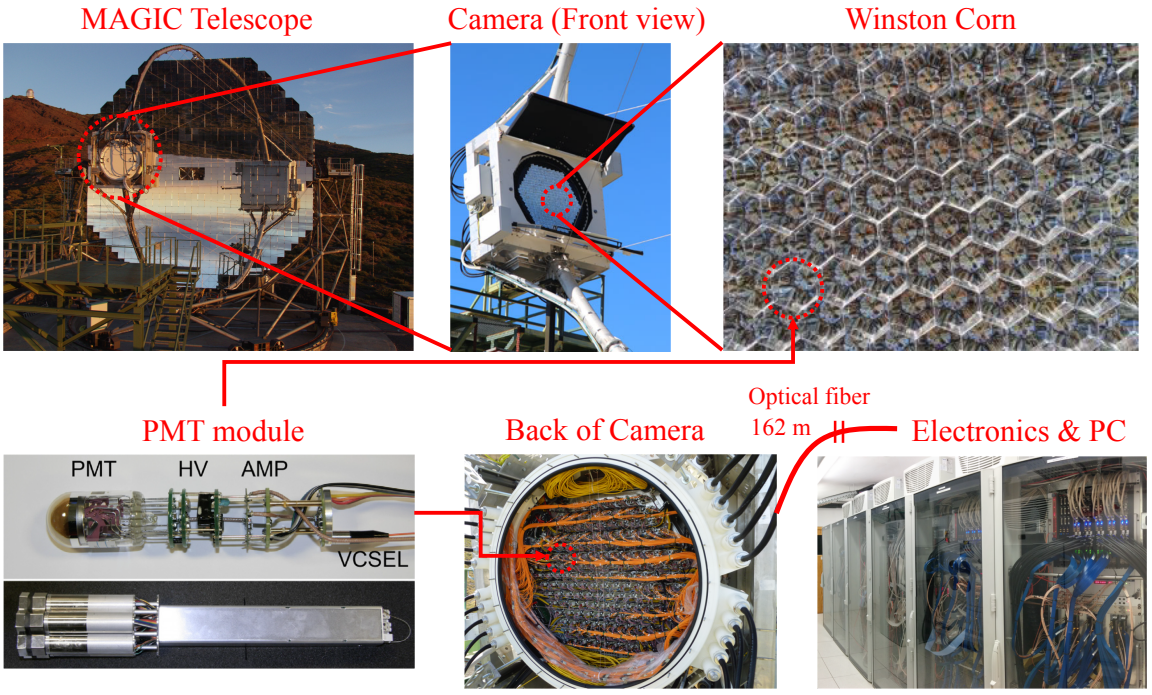

Figure 2.7: The focal plane camera of MAGIC telescope. The bottom-left and bottom-right pictures are taken from Aleksić et al. (2016). The other pictures are taken from https://magic.mpp.mpg.de.

Hassan et al., 2017). First, IACTs at high altitude will see larger fluctuations in the shower images because of random particles penetrating down to or close to ground level, which worsens the determination accuracy of the shower parameters. Also, the shower image tends to leak from the FoV of the telescope due to the larger angular difference between the shower axis and the pointing axis. Thus, the angular resolution and energy estimation accuracy worsen in this case. As a consequence of these effect, it is better to install the telescopes at the high altitude to achieve the lower energy threshold, or at the low altitude to improve the telescope performance regardless of the energy threshold.

2.2 The MAGIC system

In this section, we introduce the MAGIC telescopes used in this study. The MAGIC telescope is located at 2200 m altitude above sea level at the Observatorio del Roque de los Muchachos on the Canary island La Palma, Spain (28.76° N; 17.89° W). As shown in Figure 2.7 for the schematic view, the flow of the Cherenkov signal at the MAGIC telescope is as follows: (i) the MAGIC system focuses Cherenkov lights using parabolic mirrors with a diameter of 17 m to the focal plane camera, (ii) which converts into charge information and transmits them to the readout boards in the electronic room via optical fiber with lengths of 162 m. We describe the detail for (i) and for (ii) in sub-sections 2.2.1 and 2.2.2, respectively.

2.2.1 Optics

In order to detect low-energy γ rays as well as high energies, the MAGIC system focuses Cherenkov lights using a parabolic mirror with a relatively large diameter of 17 m. A parabolic mirror can suppress the arrival time dispersion of reflected photons and thus can provide a better signal-to-noise ratio, resulting in the achievement of the lower energy threshold[1]. The mirror dishes consist of 250- and 247-segmented mirrors for MAGIC-I and II, the area of which is ~ 240 m^2. The small deformations of the mirror dish due to a change of observation zenith angle can be corrected using the Active Mirror Control system (Biland et al., 2007). The total reflectivity of the mirrors is maintained at $\sim 85\%$ (Doro et al., 2008).

In addition, the hexagonal shape Winston cones are attached to the front of each photo-multiplier tubes (PMTs) of the focal plane camera to minimize dead space between PMTs and to exclude NSB from wide angles to the focal plane.

2.2.2 Photo-sensor and the readout system

Photo-multiplier tubes (PMTs)

Each MAGIC focal plane camera uses 1039 PMTs (R10408 from Hamamatsu Photonics), which has a hemispherical photo-cathode with a diameter of 1 inch. Fig. 2.8 shows the quantum efficiencies (QEs) of PMTs installed in the cameras. The maximum QEs are 30–35% in the wavelength range of 300–450 nm, corresponding to the peak of the Cherenkov light spectrum shown in Fig 2.5.

The average of the PMT gains is 3.0×10^4 with the high voltage (HV) of 850 V, but the distribution has a spread within (1.0–6.0) $\times 10^4$. Such a spread in the gains is unavoidable during the manufacturing process, but would make biases in the trigger production and the analysis. We, therefore, align the gains of each pixel by adjusting the applied voltage of each PMT and using attenuators for those with high gains. This process is called flat-fielding. The left and right panels in Fig. 2.9 show the distribution of the HVs applied to PMTs and the charge distribution of the calibration pulses in the MAGIC cameras after the HV flat-fielding procedure, respectively. The latter distribution is in good agreement between the MAGIC-I and II, leading the less systematic uncertainties on the energy and flux estimation than 8%. We also find two pixels in MAGIC-II that could not be flat-fielded well, because the gain is too low even at the maximum HV. The signal-to-noise ratio of these two pixels are worse than others but they can still be used in the analysis.

Readout system

The amplified analog signals from the PMTs are converted into optical signal with VCSELs, and then transmitted to the electronics room via optical fibers. The high sampling frequency of $\sim$1 GHz for the analog-to-digital conversion is required to acquire the waveform data of

[1] One disadvantage of parabolic mirrors is that they have a large coma aberration, yielding a narrow FoV of telescopes. For example, VERITAS and H.E.S.S. adopt the Davies-Cotton telescope (which can reduce coma aberration) to achieve a wide FoV instead of a low energy threshold.

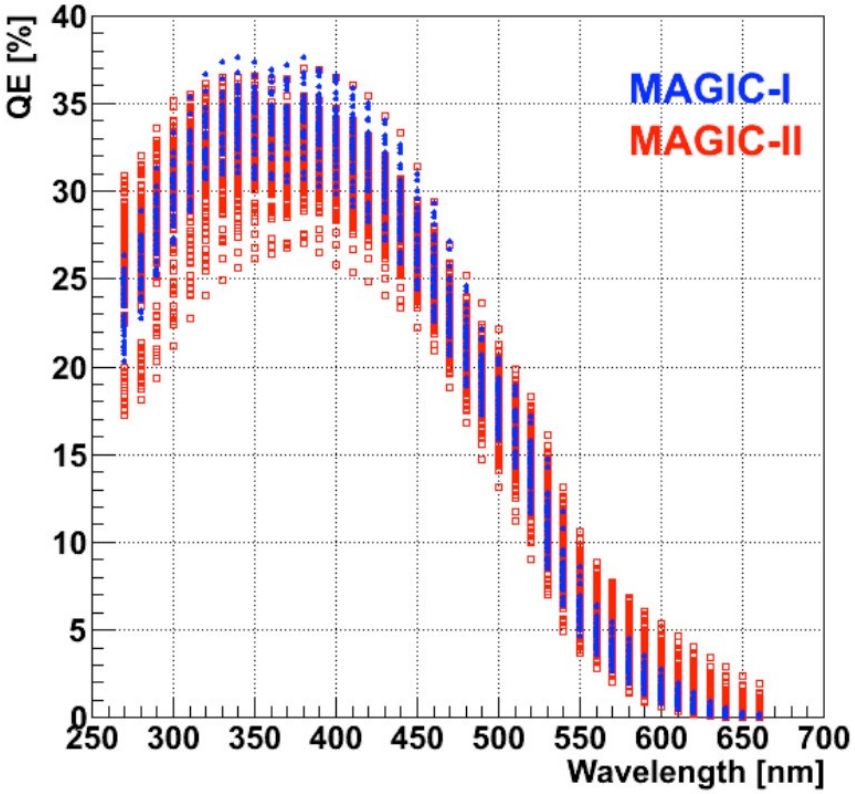

Figure 2.8: Quantum efficiency of PMTs for the MAGIC telescopes as function of wavelength (Nakajima, 2013).

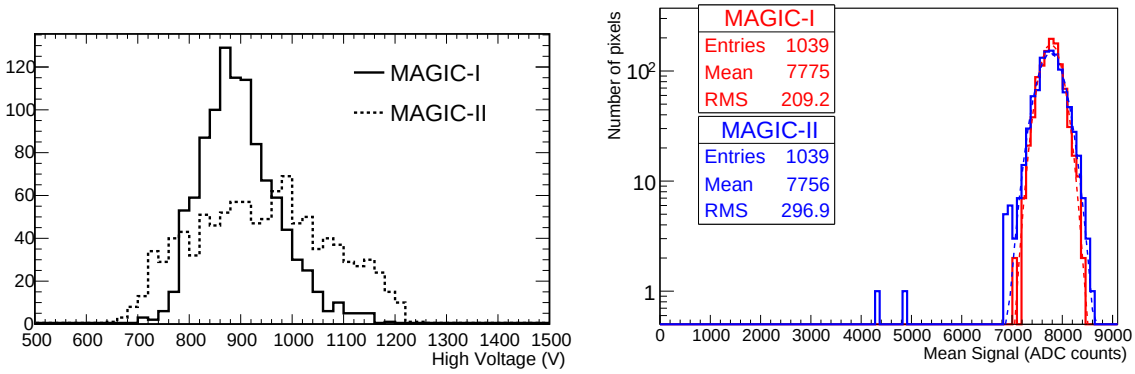

Figure 2.9: The distributions of the applied HVs for the MAGIC PMTs and of charges of the calibration pulses after the flat-fielding procedure (Aleksić et al., 2016). **Left**: The solid and dashed lines show the distributions in MAGIC-I and MAGIC-II cameras, respectively. The highest voltage that can be applied to the PMTs is 1250 V. **Right**: The red and blue data show the results of MAGIC-I and MAGIC-II cameras, respectively.

Cherenkov light with a time width of a few ns. Such high-speed sampling can also allow to reduce the NSB contamination with an arrival frequency of 10–100 MHz. For this requirement, the MAGIC system uses the Domino Ring Sampler version 4 (DRS4)[2] as well as the ADC (14 bit resolution), achieving a sampling frequency of 2.05 GHz. The DRS is an ASIC using a switched capacitor array, which can store charge information in thousands of capacitors in sequence and allow the relatively low-speed (32.5 MHz used in MAGIC) digitization with ADC at the latter part. The DRS was originally developed for the MEG experiment (Ritt et al., 2010), but is currently used in many experiments (e.g., Anderson et al., 2016; Nozaki et al., 2020) because DRS enable us to operate with lower power consumption compared to Flash ADC. The calibration method for DRS4 in the MAGIC telescope was established by Sitarek et al. (2013).

Trigger system

In the trigger generation process at the DAQ system, the MAGIC telescopes make signals in three stages (Aleksić et al., 2016), aiming to avoid accidental noise data and reduce the dead time. First, discriminators find pixels in which the amount of charge exceeds the criteria. Once the three or more pixel-wise triggers are generated simultaneously at neighboring pixels, the individual telescope trigger is generated. Finally, the stereo trigger is generated by finding the coincidence event between the individual telescope triggers of MAGIC-I and II within a 100 ns time window. The typical rate of the stereo trigger is set to be 250–300 Hz for normal operations. Figure 2.10 shows the block diagram of the readout and trigger chain.

In-Situ calibration of the PMT camera

Since the PMT gain varies with temperature, it is desirable to calibrate their response during observations. We perform in-situ calibration using a technique called the "F-Factor" method (Mirzoyan, 1997; Schweizer et al., 2002). This principle is as follows (Bencheikh et al., 1992). The relation between the average of the output ($Q_{\rm out}$) and input charges ($Q_{\rm in}$) can be written as:

$$\langle Q_{\rm out}\rangle = \langle G\rangle\langle Q_{\rm in}\rangle + P, \tag{2.5}$$

where G is the PMT gain and P is the pedestal noise. In the case of a perfect detector, i.e., where the detector response is one-to-one correspondence between input and output, the standard deviation of the output charge is determined only by the statistical uncertainty of the input charge, and thus:

$$\sigma_{Q_{\rm out}} = G\sqrt{Q_{\rm in}}. \tag{2.6}$$

By considering the uncertainty on the detector response, the observed variance will be

$$\sigma^2_{Q_{\rm out}} = \langle G\rangle^2\langle Q_{\rm in}\rangle + \langle G\rangle^2\langle Q_{\rm in}\rangle \left(\frac{\sigma_{Q_{\rm 1p.e.}}}{Q_{\rm 1p.e.}}\right)^2 + \sigma^2_{\rm elec}, \tag{2.7}$$

[2] https://www.psi.ch/en/drs

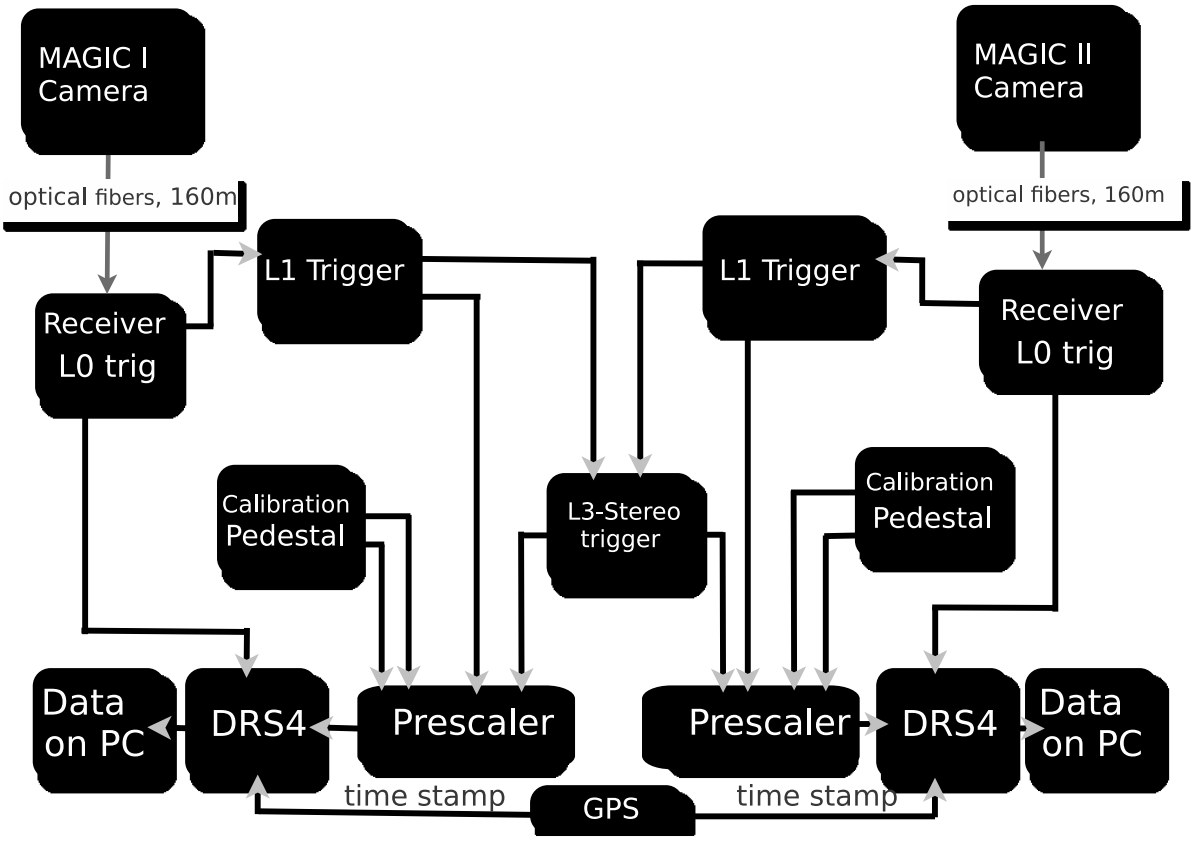

Figure 2.10: Schematic view of the readout and trigger chain of the MAGIC telescopes (Sitarek et al., 2013). The pixel-wise trigger, the individual telescope trigger, and the stereo trigger are named L0, L1, and L3, respectively.

where the $Q_{\rm 1p.e.}$ is the output charge for a single electron in PMT, $\sigma_{Q_{\rm 1p.e.}}$ is its standard deviation, and $\sigma_{\rm elec}$ is the combination of the detector, amplifiers and ADC electronics noise. Once $\langle G\rangle\langle Q_{\rm in}\rangle$ is large enough than the pedestal noise, the terms of P and $\sigma_{\rm elec}$ can be neglected from Eq. 2.5 and 2.7, respectively. Hence, we obtain the following relation:

$$\sigma^2_{Q_{\rm out}} = \langle G\rangle(1+\frac{\sigma^2_{Q_{\rm 1p.e.}}}{Q^2_{\rm 1p.e.}})\langle Q_{\rm out}\rangle. \tag{2.8}$$

Finally, the PMT gain can be written as:

$$\langle G\rangle = \frac{\sigma^2_{Q_{\rm out}}}{F^2\langle Q_{\rm out}\rangle}, \text{ with F} = \sqrt{1+\frac{\sigma^2_{\rm Q_{1p.e.}}}{\rm Q^2_{1p.e.}}}, \tag{2.9}$$

where F is the so-called F factor (also called excess-noise factor). In Eq. 2.9, $Q_{\rm 1p.e.}$ and $\sigma_{Q_{\rm 1p.e.}}$ can be measured in the laboratory before inserted in the telescopes. As a consequence, we can estimate the PMT gain using the pulse data uniformly illuminated over the entire camera with a higher amplitude than the noise. In the MAGIC operation, the pulse evens generated by the calibration box, installed the center part of the mirror dish, are taken simultaneously during the observations of air shower events. The calibration box has a Nd:YAG laser that produces pulses of 0.4 ns FWHM with a wavelength of 355 nm. This can illuminate light pulses onto the PMT camera uniformly with a fluctuation of less than 2% (Aleksić et al., 2016). This system are also used to perform the flat-fielding procedure.

2.2.3 Atmospheric monitoring

As mentioned in Sect. 2.1, the air shower depends on the thickness of the atmosphere, i.e., not only altitude and zenith angles and also the atmospheric transmission. Since the atmosphere changes from moment to moment, it is necessary to monitor it during observations. For the monitoring, we use Light Detection And Ranging (LIDAR; Fruck et al., 2014). The LIDAR system shoots a laser signal (wavelength: 532 nm, pulse width: 0.5 ns) to the air and measures the reflected laser light. The atmospheric transmission can then be estimated by measuring the time interval between the emission of the laser and the arrival of the reflected light. If a measured transmission is worse than $\sim 80\%$, we need to consider the additional systematic uncertainty of the energy estimation and/or the correction factor (Fruck et al., 2014; Hahn et al., 2014).

2.2.4 Drive system

The mount of the MAGIC telescope consists of a space frame of carbon-fiber reinforced plastic tubes, achieving the comparatively low weight of 72 tons per telescope. This allows a fast movement of 180° (360°) in azimuth within 20 s (33 s) (Bretz et al., 2009). The systematic uncertainty on the reconstructed source position is estimated to be less than 0.02° (Aleksić et al., 2016), and thus would not affect analysis results.

Table 2.1: The main Hillas parameters.

Name	Description
size	Total charge of selected pixels
width	length in the minor axis of the shower ellipse
length	length in the major axis of the shower ellipse
wl	*width* over *length*
CoG	Center of Gravity in the shower image
CONC	Fraction of the image concentrated in the brightest pixels.
time gradient	slope of the arrival time projection along the major axis
leakage	Charge contained in the outer edge pixel of the camera
MaxHeight	Height of the shower maximum point from the ground
impact	Crossing point of shower axis on the ground.
Number of islands	Number of non-connected pixels that survived the image cleaning.

2.3 Event reconstruction

As the name implies, the data analysis of IACT uses Cherenkov images for event reconstruction. In the imaging process, the signal is extracted using a sliding window algorithm (Albert et al., 2008a) by finding six consecutive cells (corresponding to 3 ns) selected to be maximized within the readout window. Also, NSB is removed by taking coincidence within 2–4 neighboring pixels. We then parameterize features of the images with the so-called Hillas parameters (Hillas, 1985). The main Hillas parameters are summarized in Table 2.1, some of which are shown in Fig. 2.11, overlaid on the electromagnetic shower image. Using these parameters, we estimate the energy, flux, and arrival direction of incident γ rays (Sect. 2.3.1 and 2.3.2) and remove background events (Sect. 2.3.3). These data analyses are performed with the MAGIC standard analysis package (Zanin, 2013).

2.3.1 γ-ray energy and flux

As shown in Figure 2.3, γ rays with higher energies make a large air shower, yielding a larger amount of charge in the shower (*size* parameter). Fig. 2.12 shows the correlation between the mean size of a γ-ray event and its energy, obtained with MC simulations. However, the energy estimation also depends on the incident angle of γ rays and the distance from telescope (corresponding to *impact*), which thus should be taken into account. We, therefore, estimate the energy of observed γ rays by evaluating the Hillas parameters with MC data. The evaluation is performed using machine learning, specifically, the Random Forest (RF) method (Breiman, 2001), which has been implemented into the MAGIC analysis by (Albert et al., 2008b).

Figure 2.13 shows the energy resolution and energy bias evaluated with MC simulations. The energy resolution has been estimated to be 15–25% for the range of 60 GeV–20 TeV, indicating that the estimated energy spectrum may be biased. We therefore compute the response function using MC simulation data and then derive a true energy by unfolding with the results. The relation between the distribution of the estimated energy (S) and the true energy (Y) is expressed

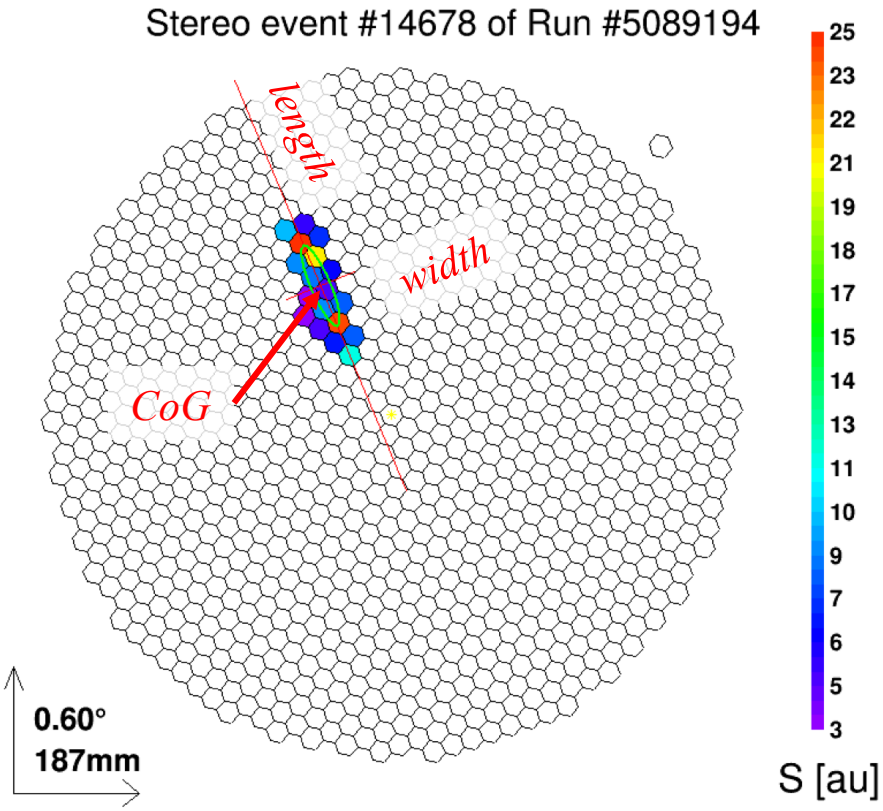

Figure 2.11: Cherenkov image of an electromagnetic air shower, overlaid with the several Hillas parameters (see Tab. 2.1 for detail).

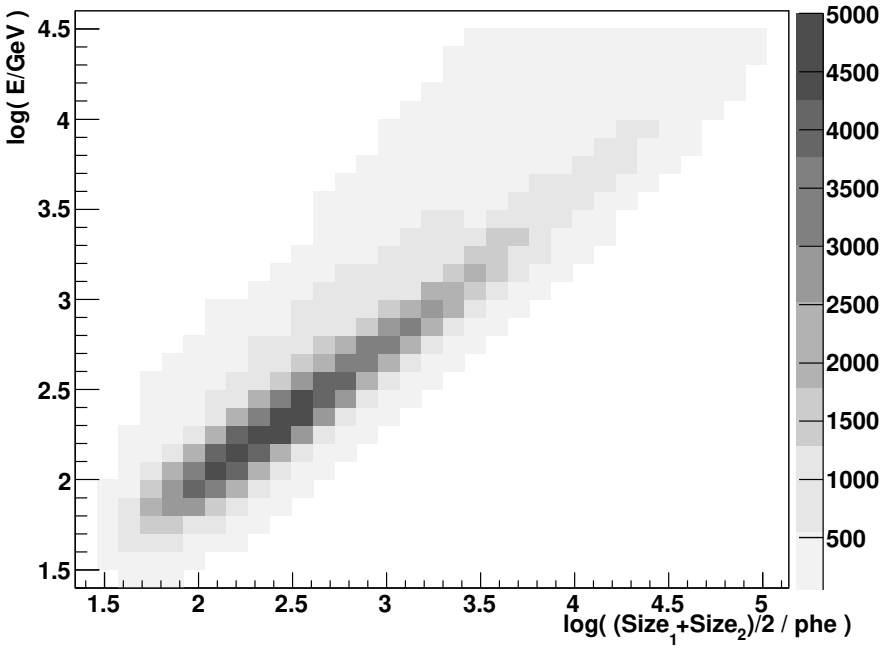

Figure 2.12: Correlation between the mean size of a γ-ray event and its energy obtained with MC simulations (Aleksic et al., 2012).

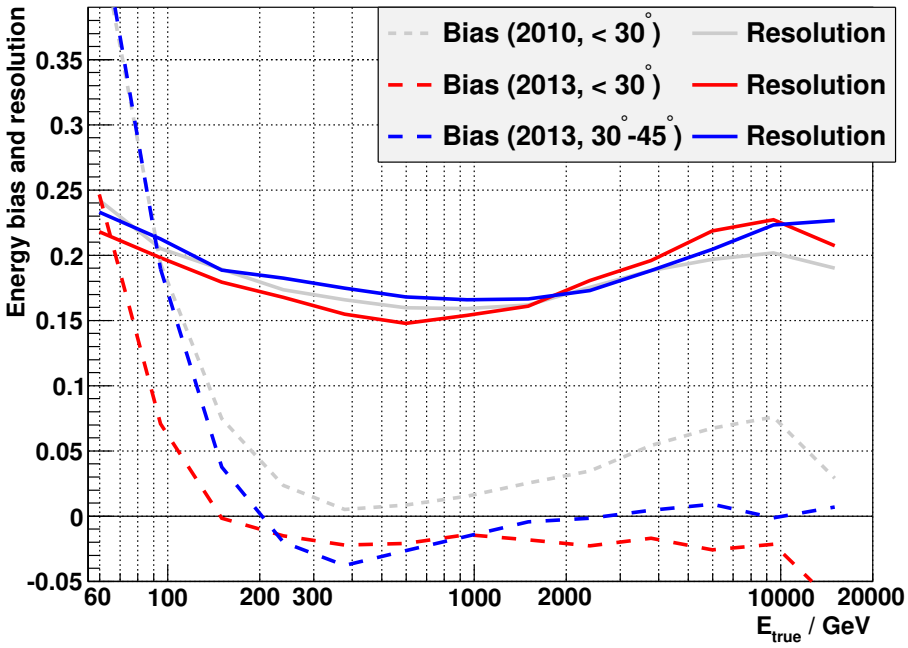

Figure 2.13: Energy resolution and energy bias of the MAGIC telescope (Aleksić et al., 2016).

using the transfer matrix (M) as follows

$$Y_i = \sum_j M_{ij} \cdot S_j \ (i = 1, ..., n). \tag{2.10}$$

Furthermore, we perform a regularization to suppress the effect of the systematic uncertainty in the unfolding. Although there are several regularization methods (Albert et al., 2007), the difference in the results of the spectral index among the methods is estimated to be less than 0.1 (Aleksic et al., 2012). The final results in this thesis are those obtained with the Tikonov method.

The differential γ-ray flux is defined as:

$$\frac{dF}{dE} = \frac{dN_\gamma}{dE dt_{\rm obs} dA_{\rm eff}} \tag{2.11}$$

where N_γ is the number of γ-ray events, $t_{\rm obs}$ is the observation time, and $A_{\rm eff}$ is the effective area. The effective area is actually obtained by integrating the detection efficiency with azimuthal direction (Az) and the *impact* parameter (P_{impact}), and is defined as:

$$A_{\rm eff} = \int_0^{2\pi} dAz \int dP_{impact} \ \epsilon(E, Zd, Az, P_{impact}) \times P_{impact}, \tag{2.12}$$

Note that ϵ depends on the energy and zenith angle (Zd) as well as P_{impact} and Az. Using the MC simulation data of γ rays, the effective area can be also computed as follows:

$$A_{\rm eff} = \frac{N_{\rm survived}}{N_{\rm input}} A_{\rm MC}, \tag{2.13}$$

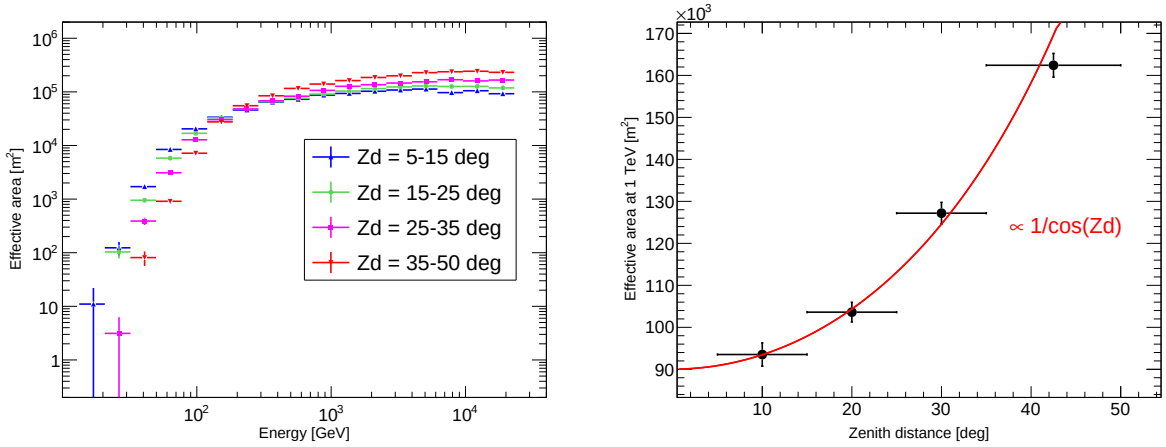

Figure 2.14: **Left**: Effective area of the MAGIC telescope as a function of energy. **Right**: Effective area at 1 TeV as a function of zenith angle. The red curve shows the fit function of $1/cos(Zd)$.

where N_{input} and N_{survived} are the number of a total simulation events and the survived events after the analysis cut, respectively, and A_{MC} is the geometrical are used in the simulation.

Fig. 2.14 shows the effective area for point sources derived with the MC simulation. The zenith dependence of the effective area follows a relation between relative air mass and zenith and then $A_{\text{eff}} \propto 1/cos(Zd)$ (the right panel of Fig. 2.14). In observations at the larger zenith angle, the energy threshold become higher[3] but the effective area can be increased, enabling us to observe higher energy photons.

2.3.2 Arrival direction

In the case of stereo observations (observations with two or more telescopes), the arrival direction of incoming γ rays can be geometrically determined from the crossing point of the major axes of the Hillas ellipse. Although this estimation method has been used conventionally, it may fail if the Hillas parameters are not determined well (e.g., in the case of low-energy events). In the MAGIC data analysis, the arrival direction is therefore estimated with the DISP RF method (Aleksić et al., 2016), which takes into account the *time gradient* parameter. As shown in Fig. 2.15, the DISP RF method estimates the arrival position as follows:

1 Two estimated points per telescope are obtained using the time gradient parameter.
2 We then find the combination of the estimated positions between MAGIC-I and II so that the distance is the shortest
3 We take the average of the two points by weighting the number of pixels in the image.

The estimated angular resolution can be evaluated with MC simulation data or the real observation data of a point-like source. Fig. 2.16 shows the angular resolution of the MAGIC

[3]Fig. 2.14 indicates that an effective area in larger zenith observation is smaller than the lower ones at the low energy band. We usually set a safety energy threshold to consider the deterioration of the signal-to-background ratio due to this effect. The analysis threshold can be approximated by an empirical formula: $74 \times cos(Zd)^{-2.3}$ GeV (Aleksić et al., 2016).

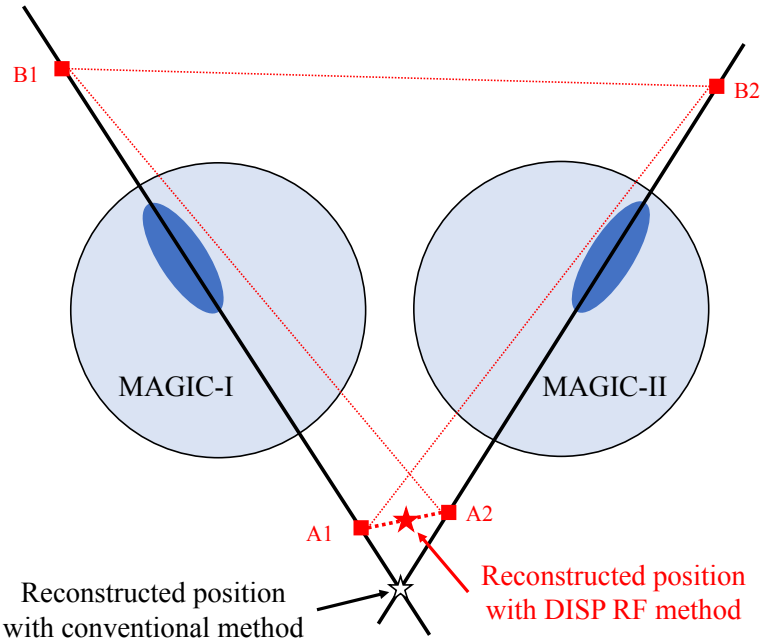

Figure 2.15: Schematic view of the DISP RF method. The main axes of the Hillas ellipses are shown with solid black lines. The red squares represent the estimated positions using the time gradient parameter. The black and red stars represent the reconstructed position with the conventional and DISP RF methods, respectively.

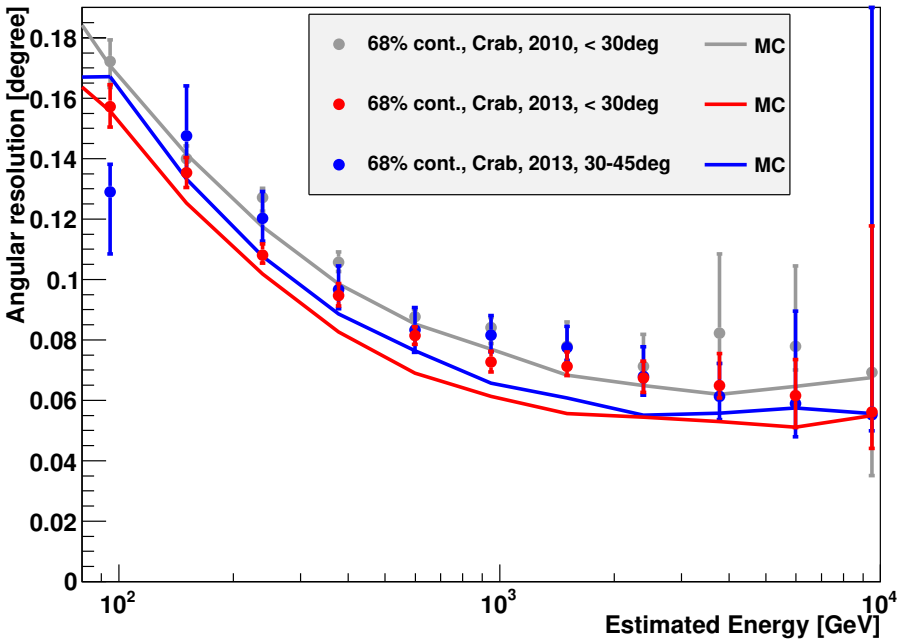

Figure 2.16: Angular resolution of the MAGIC telescopes as a function of the estimated energy obtained with the Crab Nebula data sample (points) and MC simulations (solid lines) (Aleksić et al., 2016). Red (blue) points show the low (medium) zenith angle sample. For comparison the low zenith angle pre-upgrade angular resolution is shown as gray points (Aleksic et al., 2012).

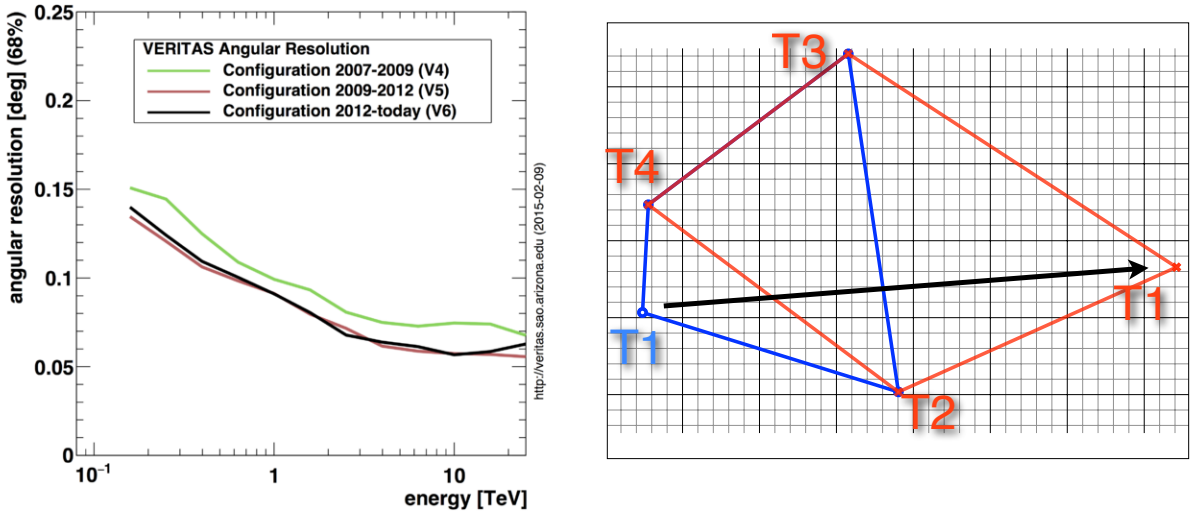

Figure 2.17: **Left**: Angular resolution of the VERITAS telescopes as a function of the energy (https://veritas.sao.arizona.edu/about-veritas/veritas-specifications). **Right**: Schematic of the VERITAS telescopes as viewed from directly overhead (Perkins & Maier, 2009). The blue lines are for the original array layout, while the red lines are for the new array layout. The black arrow indicates the relocation of Telescope-1. The small grid squares are 5 m on a side.

telescopes as a function of an estimated energy. In the lower energy band than $\sim$ 1 TeV, the angular resolution is determined by the accuracy of the Hillas parameters and, thus, improves with energy since γ rays with higher energies produce more explicit shower images. At higher energies above 1 TeV, the pixel size of PMTs determine the resolution limit.

In addition, the resolution is also correlated with the number of telescopes ($N_{\rm tel}$) that can observe simultaneously, and roughly proportional to $N_{\rm tel}^{-0.5}$ (Funk & Hinton, 2009). While $N_{\rm tel}$ of the MAGIC system is half of VERITAS, the used pixel size is small compared to VERITAS. The resultant current angular resolution of both telescopes is comparable. Note that the angular resolution in the previous study with the VERITAS telescopes for SNR G106.3+2.7 (Acciari et al., 2009) is 10–25% worse than the current performance due to the constructed location of the telescopes. The left panel in Fig. 2.17 shows the angular resolution of the VERITAS telescope for the several periods. After the previous study, the angular resolution has been improved by moving the telescope (Perkins & Maier, 2009), as shown in the right panel of Fig. 2.17.

2.3.3 Background estimation

The hadron-initiated air shower

A main background in the shower image analysis is the hadron-initiated shower. CRs arriving at the Earth produce pions due to their strong interaction with atmospheric nuclei, according to Eq. 1.41:

$$p + p \rightarrow p + p + \pi^0\pi^+\pi^-. \qquad (1.41)$$

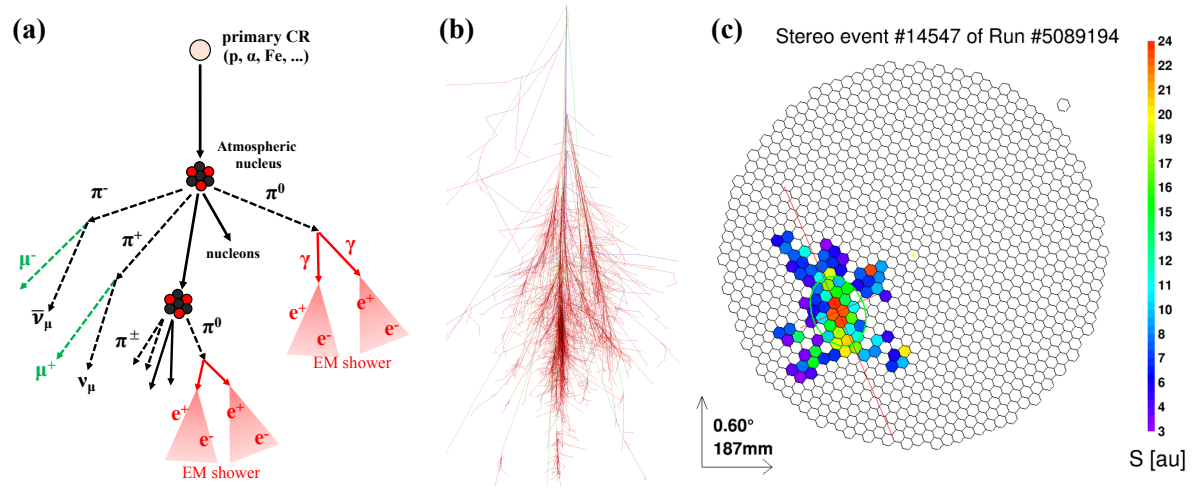

Figure 2.18: **(a)** Schematic view of a hadron-initiated air shower. **(b)** Longitudinal development of the hadron-initiated showers obtained with CORSICA simulations. (Image credit: Fabian Schmidt, University of Leeds; https://www.iap.kit.edu/corsika/). **(c)** Cherenkov image of a hadron-initiated shower obtained with the MAGIC telescope.

The cross section can be written as:

$$\sigma_{\mathrm{AA}}\ [\mathrm{mb}] \sim 65(\mathrm{A}_{\mathrm{in}}^{1/3} + \mathrm{A}_{\mathrm{air}}^{1/3} + 1.12)^2, \tag{2.14}$$

where A_{in} and A_{air} indicate the mass number of the incident CR and the atmosphere, respectively, the latter of which is $A_{\mathrm{air}} \sim 14.5$. In this process, π^0, π^+, and π^- are generated at a ratio of $1:1:1$, respectively. π^+ and π^- then decay due to the weak interaction as follows:

$$\begin{aligned} \pi^+ &\rightarrow \mu^+ + \nu_\mu \\ \pi^- &\rightarrow \mu^- + \overline{\nu_\mu}, \end{aligned} \tag{2.15}$$

and 98% of π^0 decays according to Eq. 1.42:

$$\pi^0 \rightarrow 2\gamma. \tag{1.42}$$

The γ rays may produce electromagnetic air showers as described in Sect. 2.1.1. As a result, the CR hadrons can cause air shower phenomena similar to the γ-initiated showers (see Fig. 2.18). Since the number of the γ-initiated events is much less than the hadron ones (even for bright sources, e.g., Crab Nebula, the fraction is $\sim 10^{-3}$), it is necessary to distinguish whether the observed air shower is initiated by hadrons or γ rays.

The main differences between showers initiated by γ rays and hadrons are as follows:

1. In the case of a γ-initiated shower, all the energy of incoming γ rays is converted into shower development, while most energy of a hadron-initiated shower is lost due to μ and ν produced by Eq. 2.15. Consequently, the charge in the Cherenkov image (*size*) of hadron-initiated showers will be less than that of γ rays with the same energy.

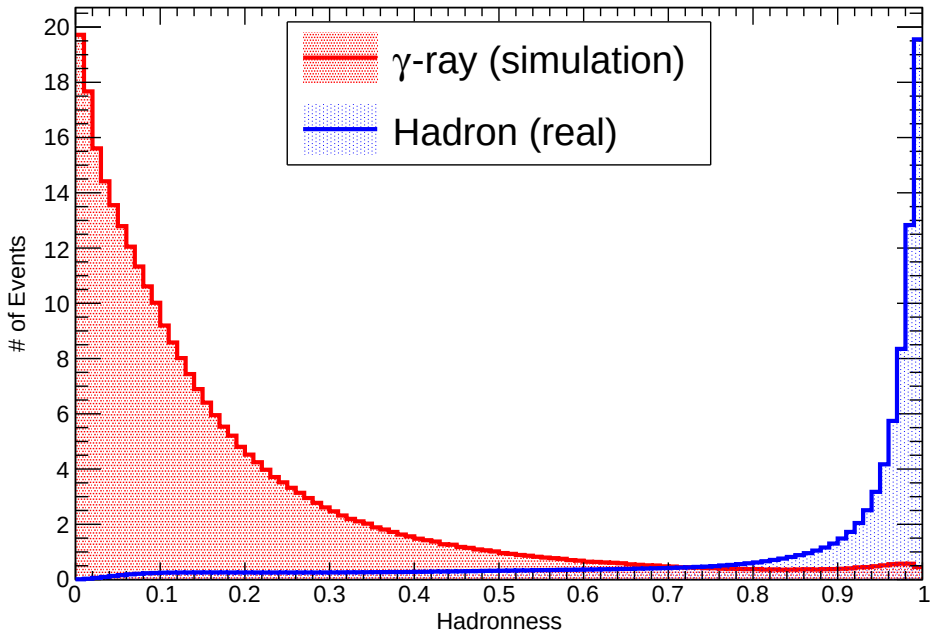

Figure 2.19: The *hadronness* distributions of γ-ray data generated with the MC simulation and the hadron data obtained with the real observation.

2 Because of the momentum of the π^0 at the production, the shower spreads significantly not only in the longitude but also in the lateral direction. The structure of the shower may be asymmetric or have sub-cores within it.

Simulated image of the hadron-initiated shower are shown in the right panel of Fig. 2.18, in which the difference from the γ-initiated shower (Fig. 2.11) appears well. This difference is also evident in the Hillas parameters. For example, the hadron-initiated showers have a larger *width* and *wl* (*width* over *length*) than those of γ-ray showers. Furthermore, the *CONC* parameter tends to be large for γ-initiated showers. Thus, we can distinguish between hadron and γ-initiated shower, by evaluating the Hillas parameters. γ/hadron separation is made by the so-called "*hadronness*" parameter, which takes a value close to 1 (0) when identified as a hadron(γ)-initiated shower. As with the estimation of γ-ray energy (Sect. 2.3.1) and arrival direction (Sect. 2.3.2), we use the Random Forest method (Albert et al., 2007) to obtain the *hadronness* parameter. The training data for the machine learning are γ-ray data obtained with MC simulations and hadron data obtained from actual observations. Figure 2.19 shows the *hadronness* distributions of γ-ray data generated with MC simulation and hadron data obtained with actual observations. It indicates that the hadron and γ-ray events can be distinguished well, and thus the event selection using *hadronness* will be efficient.

Note that, there is a trade-off between reducing the hadron background events and increasing the gamma-ray statistics. In this work, we select *hadronness* cut value so that 90% of gamma-ray events remain for each energy bin by finding with MC simulations.

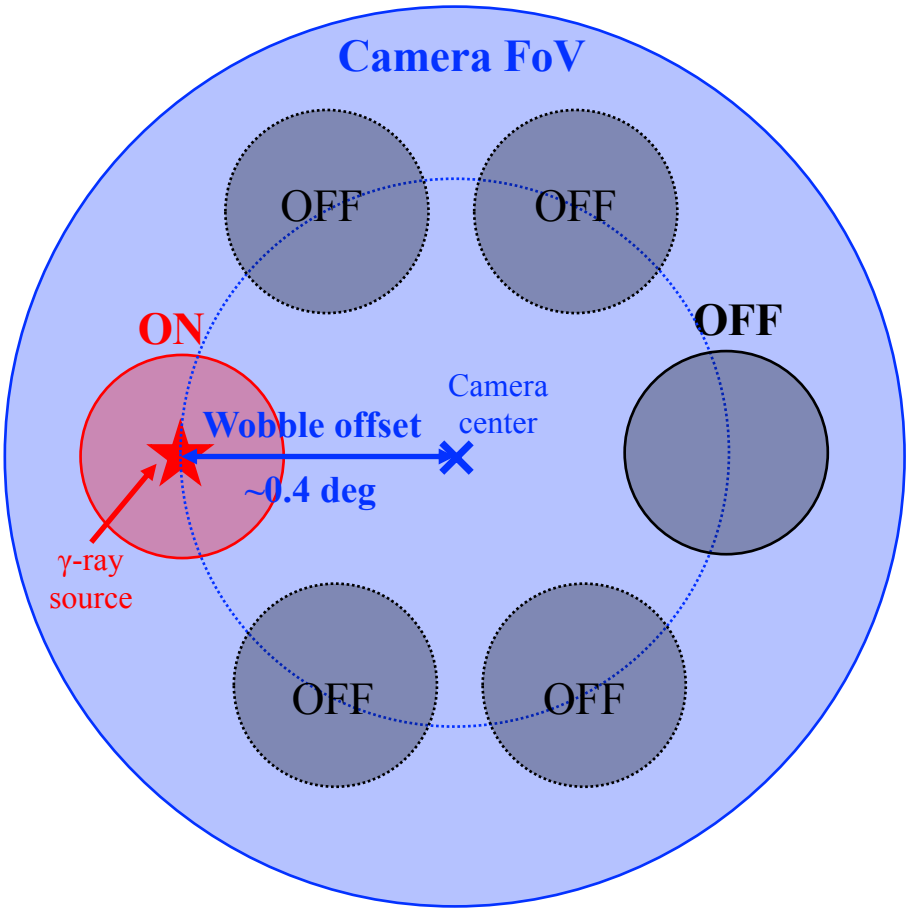

Figure 2.20: The ON (red circle) and OFF (black circle) regions in the Camera FoV.

The wobble-mode observation

As mentioned above, the hadron-initiated shower event is a main background in the IACT observation. The background reduction using the *Hadronness* parameter is very useful, but as shown in Figure 2.19, it cannot eliminate them completely. In addition, electron-initiated showers can also be a background event, which also cannot be classified with the *Hadronness* cut. Therefore, we estimate the background rate after the *Hadronness* cut by selecting the OFF region without including γ-ray sources from the Camera FoV. However, since the sensitivity in the FoV depends on the distance from the camera center (Aleksić et al., 2016), it is necessary to choose a location from which the distance is the same. In addition, it is desirable to observe the ON and OFF regions simultaneously to consider time variations in weather and NSB. For this reason, we perform IACT observations with the wobble mode (Fomin et al., 1994), in which the center of the γ-ray source is shifted from the camera center. Fig. 2.20 shows the schematic view of the ON and OFF regions in the wobble mode. The distance between the camera center and the γ-ray source is named wobble offset and is typically set to 0.4° (a larger wobble offset may be adapted for extended sources).

Table 2.2: Summary of Systematic uncertainties in the MAGIC observations (Aleksic et al., 2012). ES, FN, and SL are abbreviations for the energy scale, flux normalization, and spectral slope, respectively.

Part	Uncertainty
F-Factor	10% ES
atmospheric transmission	$\lesssim$ 10% ES
mirror reflectively	8% ES
PMT electron collection efficiency	5% ES
Light collection in a Winston Cone	5% ES
PMT quantum efficiency	4% ES
Signal extraction	3% ES
Temperature dependence of gains	2% ES
Charge flat-fielding	2–8% ES FN
Analysis and MC discrepancies	$\lesssim$10–15% FN
Background subtraction	1–8% FN
Broken channels/pixels	3% FN
Mispointing	1–4% FN
NSB	1–4% FN
Trigger	1% FN
Unfolding of energy spectra	0.1 SL
Non-linearity of readout	0.04 SL

2.4 Systematic uncertainties

The systematic uncertainties due to each component are summarized in Table 2.2. The total effect on the energy spectrum parameters will be also described in Sect. 2.4.1 through 2.4.3.

2.4.1 Flux normalization

The systematic uncertainty for the flux normalization are mainly due to the charge flat-fielding of the camera, analysis and MC discrepancy, and background subtraction (Aleksic et al., 2012). The uncertainty can be described as:

$$\sigma_{\mathrm{norm}} = \sqrt{\sigma_{\mathrm{A}}^2 + \sigma_{\mathrm{SBR}}^2}, \tag{2.16}$$

where σ_{A} and σ_{SBR} are the uncertainties dut to the effective area and signal-to-background ratio (SBR), respectively. σ_{A} has been estimated to be 18% at the low energies ($<$ 100 GeV), 11% at the medium energies, and 16% at the high energies ($\gtrsim$ 1 TeV) (Aleksić et al., 2016). σ_{SBR} is described as:

$$\sigma_{\mathrm{SBR}} = \frac{0.015}{SBR}. \tag{2.17}$$

If the SBR is worse than 1.5%, the uncertainty exceeds 100%.

Table 2.3: Parameters of the existing IACTs.

Telescope	location	latitude	Height [m]	Mirror Diameter [m]	FoV [deg]
MAGIC	La Palma (Spain)	28.76°N	2200 m	17 m × 2	3.5
VERITAS	Arizona (USA)	31.68°N	1268 m	12 m × 4	3.5
H.E.S.S	Namibia	23.27°S	1800 m	28 m × 1 + 12 m × 4	3.2, 5.0†

† The former is of the 28-m telescope, while the latter is of the 12-m telescope.

2.4.2 Energy scale

The estimate of an energy scale highly depends on the accuracy of the PMT calibration (F-Factor method, see Sect. 2.2.2) and the atmospheric transmission (see Sect. 2.2.3). This uncertainty is estimated at 17% at low energies and 11% on the high energies.

2.4.3 Spectral slope

The uncertainty for the energy slope mainly comes from the unfolding accuracy of energy spectra and non-linearity of readout. This uncertainty is estimated to be ± 0.15, while in the faint source (e.g., SNR < 0.25), this increases with the SBR as follows:

$$\Delta\alpha_{\mathrm{SBR}} = 2 \times \frac{\sqrt{(1\%/SBR_{\mathrm{LE}})^2 + (1\%/SBR_{\mathrm{HE}})^2}}{\ln(\mathrm{E_{max}}/\mathrm{E_{min}})}. \tag{2.18}$$

2.5 Comparison in the performance of IACTs

In 1989, the Whipple telescope first succeed the detection of γ-ray emission from the Crab Nebula (Weekes et al., 1989). Subsequently, HEGRA made the first successful observation with a stereo system (Daum et al., 1997), while TeV γ-ray observations of the southern sky were initiated by CANGAROO (Tanimori et al., 1994). The MAGIC, VERITAS, and H.E.S.S telescopes are currently in operation. IACTs have many upgrades over the 30-year operation. The comparison in the performance of existing IACTs are summarized in Table 2.5. With the end of the operation of CANGAROO in 2011, only H.E.S.S. is currently installed in the Southern Hemisphere.

The sensitivity curves of the gamma-ray telescopes are shown in Fig 2.21. MAGIC, H.E.S.S., and VERITAS have comparable sensitivity in the TeV band, while the MAGIC can observe the lower energies since the stereo system has telescopes with a larger diameter. Note that the sensitivity of MAGIC depends on the zenith angle, but there is little difference in sensitivity between the low and medium zenith observations. Furthermore, the next generation project CTA, which will have sensitivity about one order of magnitude better than the existing IACTs, is underway.

The highest sensitivity in the GeV band is provided by *Fermi* -LAT, which directly detects primary γ rays with a telescope onboard a satellite (the detail will be described in Sect. 5.2). In the energy band above 10 TeV, LHAASO provides the highest sensitivity. LHAASO observes γ rays by detecting the secondary particles rather than the Cherenkov radiation from them.

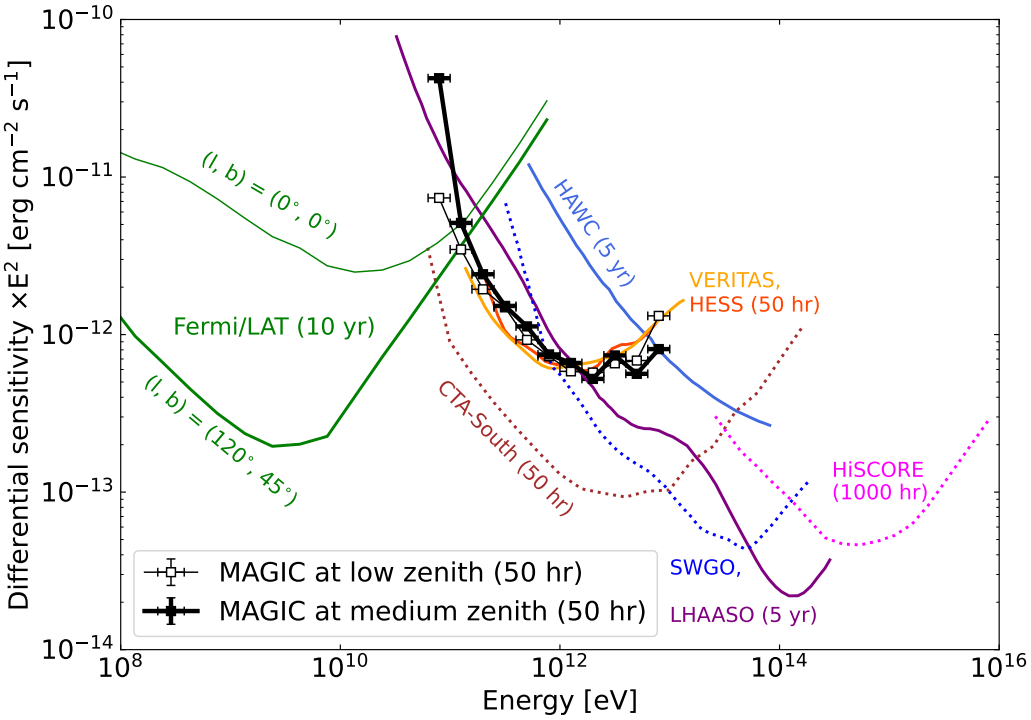

Figure 2.21: Differential 5σ sensitivity of gamma-ray telescopes. Black open and filled squares represent the post-upgraded MAGIC sensitivity for 50 hr at low ($< 30°$) or medium ($30°$–$45°$) zenith angle (Aleksić et al., 2016), respectively. Future instruments (CTA: Bernlöhr et al. (2013), SWGO: Albert et al. (2019), and HiSCORE: Tluczykont et al. (2014)) are shown as dotted lines and existing instruments (*Fermi*-LAT: https://www.slac.stanford.edu/exp/glast/groups/canda/lat_Performance.htm, VERITAS: https://veritas.sao.arizona.edu/about-veritas/veritas-specifications, H.E.S.S.: Holler et al. (2016), HAWC: Abeysekara et al. (2017), and LHAASO: Addazi et al. (2022)) are shown as solid lines.

Although the resultant angular resolution is inferior to IACTs, the system can achieve a large effective area. While the IACT can work only at night, this type of detector, the so-called air shower array, can observe gamma rays throughout the day, benefiting the high-duty cycle.

Chapter 3

MAGIC observation in the vicinity of SNR G106.3+2.7

3.1 PeVatron candidate: SNR G106.3+2.7

One of the 100-TeV γ-ray sources, LHAASO J2226+6057, is spatially consistent with SNR G106.3+2.7 (Cao et al., 2021), and thus this SNR is the most promising PeVatron candidate. However, previous studies have shown that this region is very complex.

This region consists of the PWN named "Boomerang" as well as the SNR G106.3+2.7, the latter of which was first discovered by the radio observations (Joncas & Higgs, 1990). As shown in Fig. 3.1 (a), the SNR has a comet-shaped morphology, where the bright circle and fainter extended parts were labeled "head" and "tail", respectively. The spectral indices of the head and tail regions are $\alpha = 0.49 \pm 0.05$ and 0.70 ± 0.07 (Pineault & Joncas, 2000), respectively, which are in rough agreement with the typical value (~ 0.5) in SNRs (Reynolds et al., 2012). Although the origin of this comet-shaped structure is not well understood, the HI line observations suggested that it was formed due to the surrounding gas distribution (Kothes et al., 2001). Under the assumption that the SN occurred in the head region, its shock wave can be expected to have grown in the southeast direction, where the HI density is relatively low (see Fig. 3.1 b). The Boomerang PWN is located at the north of the head region. This is driven by an energetic pulsar PSR J2229+6114, whose spin-down luminosity and the characteristic age are 2.2×10^{37} erg s^{-1} and ~ 10 kyr, respectively (Halpern et al., 2001a). The spectrum of the PWN shows a spectral break at 4.3 GHz attributed to synchrotron cooling, suggesting that its age is ~ 3.9 kyr (Kothes et al., 2006). Association of HI and molecular clouds with SNR G106.3+2.7 suggests that the distance is 800 pc (Kothes et al., 2001), while the estimation from X-ray absorption indicates that it is 3 kpc (Halpern et al., 2001b).

In this region, non-thermal X-ray emissions have been found not only in the compact region of the PWN and also in the entire SNR, i.e., both the head and tail regions (Ge et al., 2021; Fujita et al., 2021). Fujita et al. (2021) claims that the emission in both regions is generated by electrons originating in the PWN, while Ge et al. (2021) argue that the tail emission is more likely due to the electrons accelerated in the shock of the SNR.

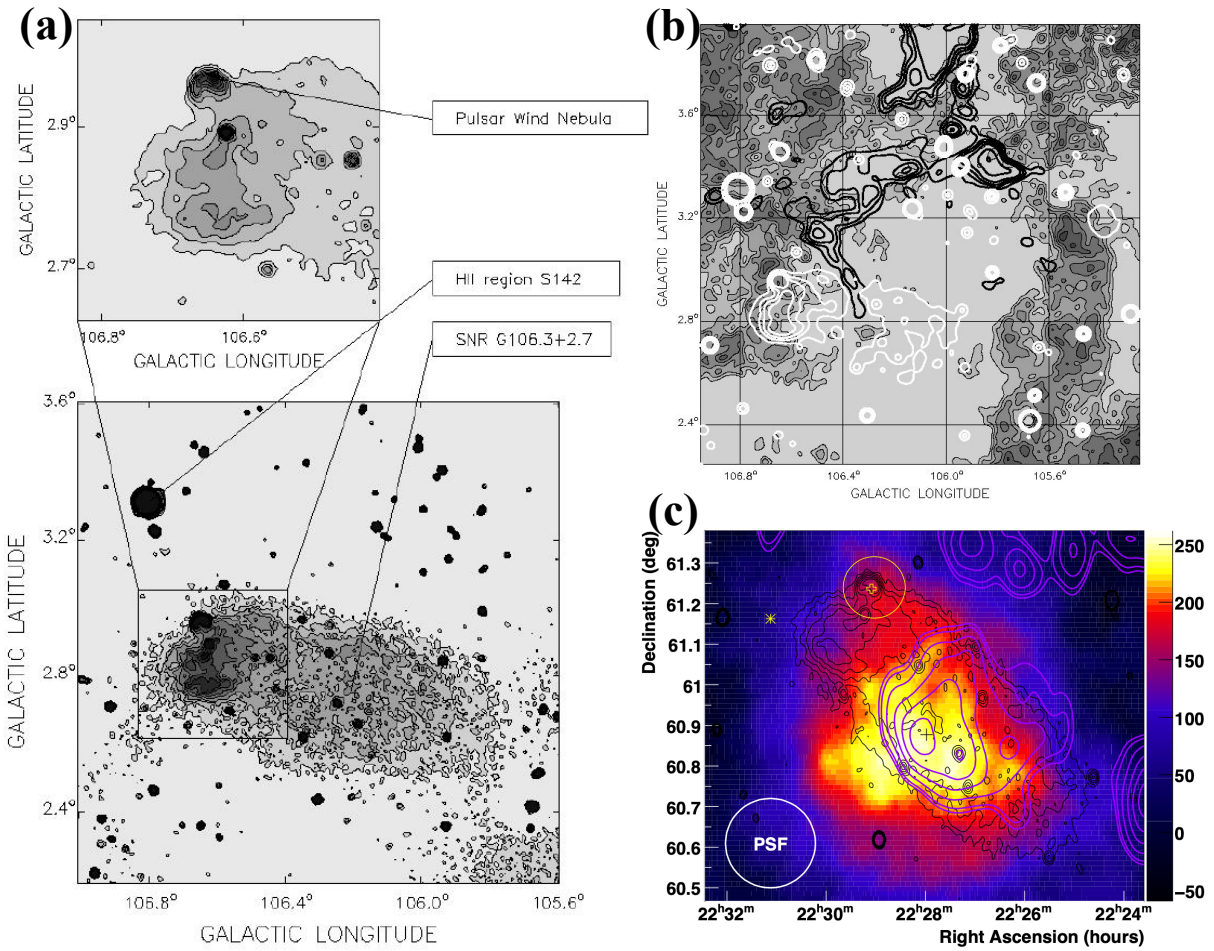

Figure 3.1: Skymaps in the vicinity of SNR G106.3+2.7. **(a)** Radio continuum intensity map at 1420 MHz. **(b)** HI line intensity map overlaid with the contours of ^{12}CO ($J = 1 - 0$) line (thick black line) as well as radio continuum emission at 1420 MHz (thick white line). Panels (a, b) are taken from Kothes et al. (2001). **(c)** TeV γ-ray excess event map obtained with the VERITAS observation (Acciari et al., 2009). The black and magenta contours represent the radio continuum and CO line emissions, respectively. The yellow open cross represents the location of PSR J2229+6114.

Many observations in γ-ray bands have also been performed for this region. The *Fermi*-LAT and EGRET observations have revealed a pulsed GeV emission from the pulsar (Abdo et al., 2009a; Hartman et al., 1999) and a steady emission above 3 GeV (Xin et al., 2019; Fang et al., 2022). The emission region of the latter is close to the SNR tail ($\sim 0.4^\circ$ away from the position of PSR J2229+6114) and was better described with a 0.25° radius disk than a point-like source (Xin et al., 2019). The steady emission was also detected with the VERITAS telescope in the TeV band (Acciari et al., 2009) and labeled VER J2227+608 (Fig. 3.1 c). The shape of the TeV emission region can be characterized with an elongated two-dimensional Gaussian with 0.27 ± 0.05 $(0.18 \pm 0.03)^\circ$ extent in the major (minor) axis. In addition, γ rays above 10 TeV from this region were first detected with the Milagro experiment (Abdo et al., 2007, 2009b) and also observed with HAWC (Albert et al., 2020), Tibet ASγ (Amenomori et al., 2021b), and LHAASO experiments (Cao et al., 2021). The HAWC and Tibet ASγ results suggest a power law spectrum without a cutoff and the spectral indices are $2.25 \pm 0.23_{\rm stat}$ and $3.17 \pm 0.63_{\rm stat}$, respectively. This emission above tens of TeV provides a lower limit on the maximum energy of the particles accelerated in this object. If the emission process is leptonic, an exponential cutoff energy of the electron must be higher than 270 TeV (Albert et al., 2020) or 190 TeV (Amenomori et al., 2021b), while if it is hadronic, the maximum proton energy should be higher than 800 TeV (Albert et al., 2020) or 500 TeV (Amenomori et al., 2021b).

However, it is still inclusive whether parent particles are accelerated in the SNR blast wave or the PWN complex due to the limited angular resolution of the γ-ray observations. The spatial coincidence between the molecular clouds and the γ-ray emission supports a hadronic origin of γ rays (e.g., Acciari et al., 2009), while the leptonic scenario for the origin is not ruled out (Fujita et al., 2021). Therefore, further precise γ-ray observations with a better angular resolution than that of previous studies are needed to resolve its origin.

3.2 Observation and data analysis

For this purpose, we observed SNR G106.3+2.7 using the MAGIC telescopes between May 2017 and August 2019 for 183.7 hr. To estimate the background simultaneously, all observations were performed in wobble mode (see Sect. 2.3.3) at three positions (RA = 336.31°, DEC = 61.40°; RA = 338.25°, DEC = 61.06°; RA = 336.66°, DEC = 60.42°) with an offset of 0.57° from the position (RA = 337.05°, DEC = 60.96°), which is close to the center of VER J2227+608 (RA = 337.0°, DEC = 60.8°). The left panel of Fig. 3.2 shows the zenith angle distribution during the observations. For the event reconstruction, we also use hadron (real observations) and γ-ray (MC simulation) data at approximately the same zenith angle as the SNR observations, as shown on the left of Fig. 3.2. We estimate the analysis energy threshold with the MC simulation data by assuming the energy distribution follows a simple power-law function with an index of 2.0 (the right panel in Fig. 3.2). Since the peak of this histogram can be defined as the analysis energy threshold for IACT observations, we conservatively set to 200 GeV for this work.

The MAGIC angular resolution, characterized by the point spread function (PSF), for this analysis was estimated to be 0.084° (68% containment radius) at $E > 0.2$ TeV and 0.072° at

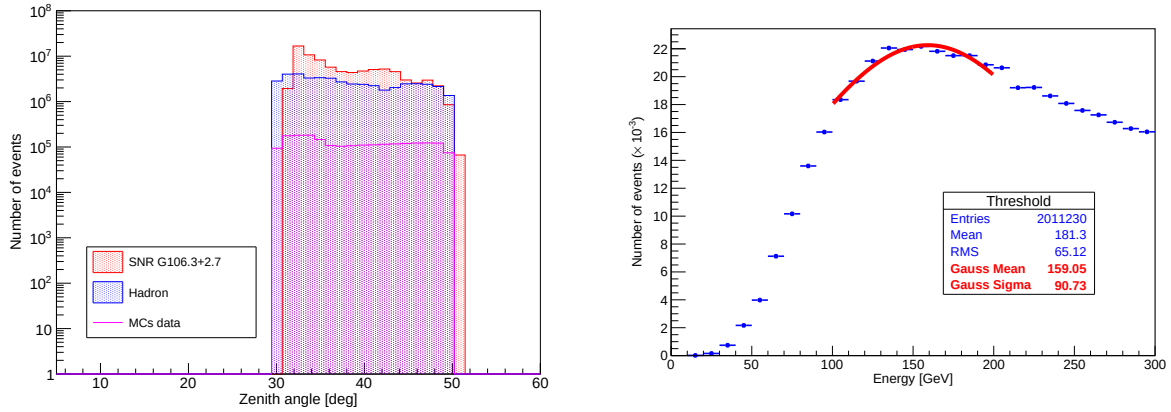

Figure 3.2: **Left:** Zenith angle distribution in the MAGIC observations for SNR G106.3+2.7 (red). Also shown the blue and magenta histograms represent the hadron (real observations) and the γ-ray (MC simulation) data. **Right:** Energy distributions of the MC simulation data, the peak energy of which corresponds the analysis threshold.

Table 3.1: Comparison of the conditions in the observations for SNR G106.3+2.7 between MAGIC (this work) and VERITAS (Acciari et al., 2009)

	VERITAS (Acciari et al., 2009)	MAGIC (This work)
Observation period	2009	2017–2019
Observation time	33 hr	122 hr
Energy threshold	0.63 TeV	0.20 TeV
Angular resolution (68%-containment radius)	0.11°	0.084° ($>$ 0.2 TeV) 0.070° ($>$ 1.0 TeV)

$E > 1$ TeV, which is the best angular resolution among the previous γ-ray observations for this object (e.g. 68% containment radius of the observation with the VERITAS telescope performed in 2009 is 0.11°).

The data analysis was performed with the MAGIC standard analysis package (Zanin, 2013). The data selection was based mainly on the transmission of the atmosphere monitored with a LIDAR system (Fruck et al., 2014). In this analysis we only selected data with an atmospheric transmission above 85% of the optimum. After quality cuts, the total dead time corrected observation time is 121.7 hours. We used the wobble-map method (e.g., Vovk et al., 2018) for estimating backgrounds. To cross-check the results obtained with the MAGIC standard analysis package, we used the SkyPrism package (Vovk et al., 2018), which includes independent methods to compute the instrument response functions and estimate the energy spectra using a spatial, maximum likelihood fit. Both results are in good agreement, as we will mention in Section 3.4.2.

The comparison of the observation conditions between this work and the previous study with the VERITAS telescope (Acciari et al., 2009) is summarized in Table 3.1.

3.3 Results

3.3.1 Morphological study

Fig. 3.3 shows the pre-trial significance maps around SNR G106.3+2.7 in different energy bands. Panel (a) shows the morphology of the γ-ray emission above 0.2 TeV overlaid with the radio emission contours at 408 MHz measured by DRAO (Pineault & Joncas, 2000) and ^{12}CO ($J = 1 - 0$) emission contours (Taylor et al., 2003). γ-ray emission above 0.2 TeV from the direction of VER 2227+608 (shown in Fig. 3.1 c and Fig. 3.3 c) is clearly detected. We evaluate the statistical significance using Eq. 17 of Li & Ma (1983):

$$S = \sqrt{2\left(N_{\rm on}\ln\frac{1+\alpha}{\alpha}\frac{\rm N_{on}}{\rm N_{on}+N_{off}} + \rm N_{off}\ln(1+\alpha)\frac{N_{off}}{N_{on}+N_{off}},\right)}, \tag{3.1}$$

where $N_{\rm on}$ ($N_{\rm off}$) is the number of signal (background) events and α is a ratio between the observation time of the signal region and background regions[1]. Integrating the same area as VERITAS and using Eq. 3.1, the resultant statistical significance is found to be 8.9σ. It is extended and spatially coincident with the radio shell of the SNR, i.e., the emission region is extending from the SNR head region to the tail region. The emission at the tail coincides with strong ^{12}CO ($J = 1 - 0$) emission, but the overall emission profile does not follow well the CO distribution. The emission at the head is in fact seen where ^{12}CO ($J = 1 - 0$) emission is not observed. It should be noted that ^{12}CO ($J = 1 - 0$) does not trace all existing interstellar gas as will be discussed in Sect. 4.2.

The panels (b), (c) and (d) of Fig. 3.3 show the maps at 0.2 to 1.1 TeV, 1.1 to 6.0 TeV and 6.0 to 30 TeV, respectively. The morphology of the detected γ-ray emission clearly changes with energy. By fitting with a symmetric Gaussian function, the center position of the γ-ray emission in the highest energy band of 6.0–30 TeV is estimated to be (RA, DEC) = (336.66 $\pm$ 0.05°, +60.87 $\pm$ 0.02°) (J2000), which is offset from the location of PSR J2229+6114 by 0.47 $\pm$ 0.03° (Panel d). On the other hand, the lower energy emission extends close to the pulsar position (Panels b and c). The centroid of the low energy emission for 0.2–1.1 TeV and its distance from the pulsar position are found to be (RA, DEC) = (336.99 $\pm$ 0.04°, +61.04 $\pm$ 0.02°) (J2000) and 0.24 $\pm$ 0.03°. The 1σ extension at 6.0–30 TeV, after removing the effect of PSF is 0.14 $\pm$ 0.09°, which is consistent with the value (0.24 $\pm$ 0.14°) reported by Tibet ASγ Amenomori et al. (2021b).

The spatial distribution in Fig. 3.3 (a) appears to have a more complex shape than the double symmetric Gaussian function, but current statistics allow fitting data with this function. The best-fit parameters are as in Table 3.2 for the center position, and 0.083° (0.087°) for the 1σ extension of head (tail). Fig. 3.4 shows the residual map after subtracting two Gaussian sources and its significance distribution of the residuals. The distribution is consistent with the null hypothesis, which indicates that, with the current statistics, the double Gaussian assumption is valid (i.e., the reduced chi-squared statistics of the fit is reasonably smaller than 1), though the

[1]The evaluation with this equation is valid even if the events is not followed to the Gaussian distribution and/or if the observation times in the signal and background regions are different.

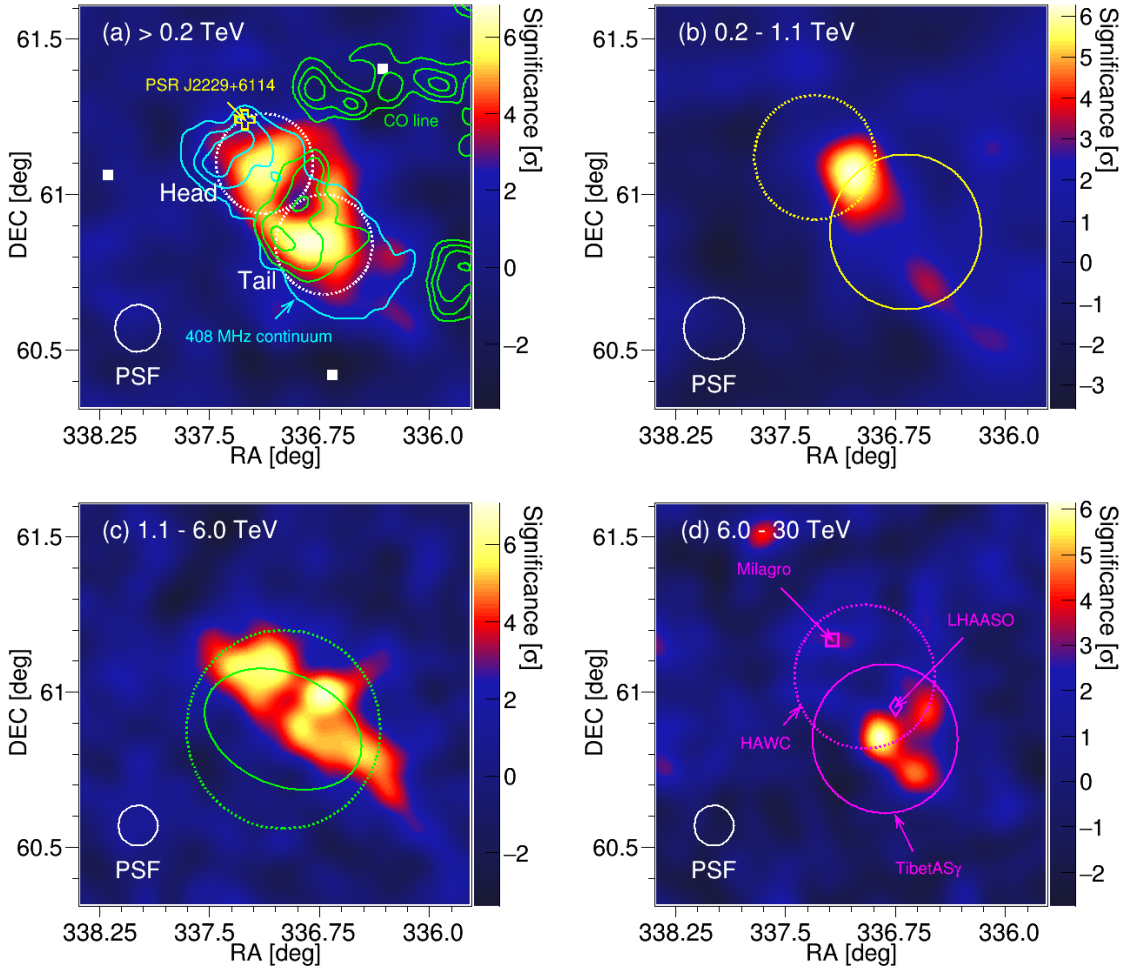

Figure 3.3: Energy-dependent pre-trial significance maps of SNR G106.3+2.7 observed with the MAGIC telescopes. **(a)** The map above 0.2 TeV. The white circle labeled "PSF" represents the 0.075° size of a Gaussian kernel (corresponding to the MAGIC γ-ray point spread function) for this analysis. The position of PSR J2229.0+6114 is marked with the open yellow cross. The cyan contours show the radio emission of SNR G106.3+2.7 at 408 MHz by DRAO (Pineault & Joncas, 2000). The green contours represent ^{12}CO ($J = 1 - 0$) line intensity integrated over the velocity range from -6.41 to -3.94 km s^{-1}. The white dotted circles show θ^2 cut regions of the head and tail regions, respectively, as shown in Table 3.2. Also shown by white squares are the pointing positions used in the observations. **(b)** The map at 0.2–1.1 TeV. The white circle labeled "PSF" represents the 0.100° size of a Gaussian kernel as the panel (a). The yellow solid and dotted circle represent the extension and location of the *Fermi*-LAT source (Xin et al., 2019) and the analysis region for the head region used in Liu et al. (2020), respectively. **(c)** The map at 1.1-6.0 TeV. The white circle labeled "PSF" represents the 0.065° size of a Gaussian kernel as the panel (b). The green ellipse and dotted circle represent the extended TeV γ-ray emission of VER J2227+608 and θ^2 cut region used in the VERITAS paper (Acciari et al., 2009), respectively. **(d)** The map at 6.0 - 30 TeV. The white circle labeled "PSF" represents the 0.065° size of a Gaussian kernel as the panel (c). The magenta solid and dotted circle represent the extended γ-ray emission above 10 TeV observed with Tibet ASγ (Amenomori et al., 2021b) and the upper limit at 90% confidence level of the Gaussian extension of HAWC J2227+610 (Albert et al., 2020). The open square and diamond show the centroid of the VHE γ-ray emission detected with Milagro (Abdo et al., 2009b) and LHAASO (Cao et al., 2021), respectively.

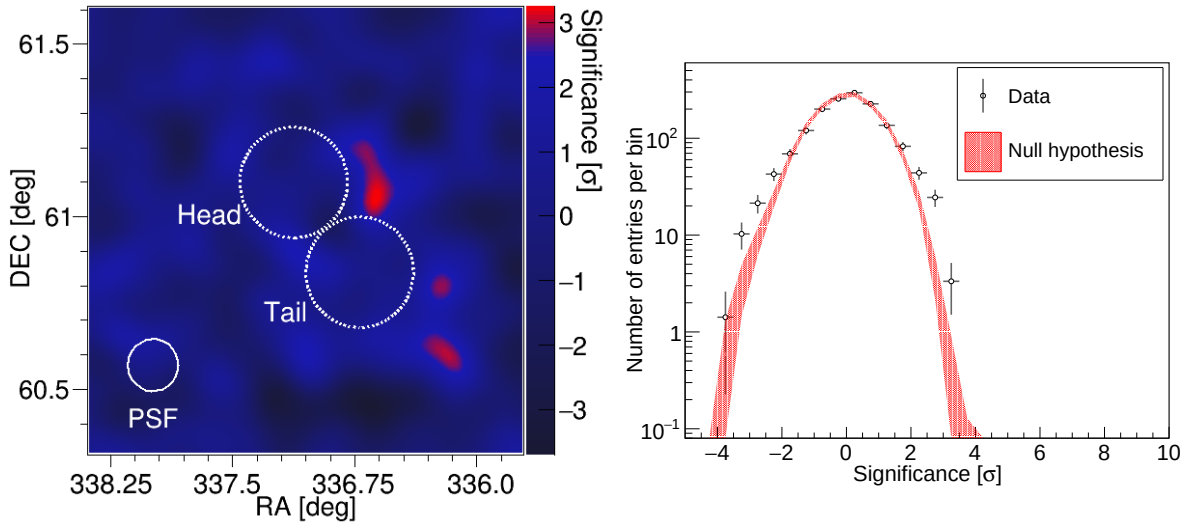

Figure 3.4: Top: The residual map after subtracting two Gaussian sources in the energy range above 0.2 TeV. As for the Gaussian parameters, the locations are the same as the definition of head and tail and each 1σ extension radius is 0.085°. Bottom: Pre-trial significance distribution of the residual map.

Table 3.2: Regions considered in this work for the analysis of MAGIC data and their modelling.

Source	RA	DEC	Radius
head region	337.°13	61.°10	0.°16
tail region	336.°72	60.°84	0.°16

true γ-ray source morphology may be more complex.

To understand the emission mechanism better, we study the γ-ray spectra at the head and the tail regions. The parameters for the two regions are defined in Table 3.2 and also shown in Fig. 3.3 (a). The centers of these regions are adapted from a fit to the γ-ray map above 0.2 TeV with a double symmetric Gaussian. The position of the tail emission is in good agreement with the peak position observed with VERITAS/Tibet (Acciari et al., 2009; Amenomori et al., 2021b) and included within the upper limit at 90% confidence level of the Gaussian extension of HAWC J2227+610 (Albert et al., 2020). The radii of these areas are chosen to be the same for both regions and of maximum length without the regions overlapping.

Fig. 3.5 shows the so-called θ^2 distributions of the two regions, where θ is the opening angle between the center of the region and the event arrival direction. The excesses are detected from the head and tail regions above 0.2 TeV with statistical significance of 6.2σ and 6.9σ, respectively, evaluated using Eq. 17 of Li & Ma (1983). Fig. 3.6 shows the energy-dependent θ^2 plots, in which the energy range is the same as in Fig. 3.3. The significances for 0.2–1.1 TeV are 4.8σ at head and 2.8σ at tail, while for 6.0–30 TeV they are 6.5σ at the tail, and only 2.4σ at the head, indicating that the magnitude ratio of the head and the tail emissions flips between the low and high energy bands.

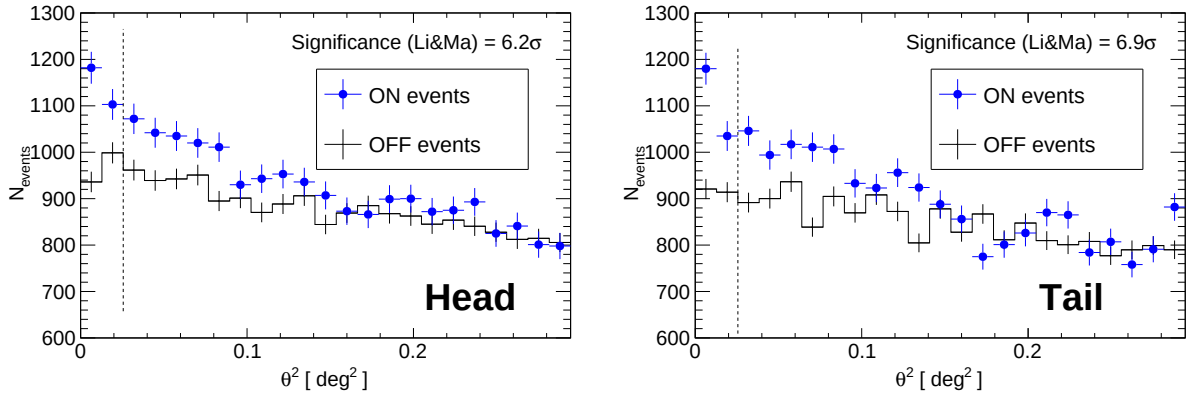

Figure 3.5: θ^2 distributions of ON (blue circles) and OFF (black line) events above 0.2 TeV toward the center of the head region (left) and that of the tail region (right). The region between zero and the vertical dashed line (at $\theta^2 = 0.0256$ deg^2) has been used to estimate ON and OFF events. The OFF data represents the average of six regions rotated by 120 and 240 deg with respect to each wobble center from the ON region.

3.3.2 Energy spectrum

Fig. 3.7 and 3.8 show the γ-ray spectra of the two regions defined in Table 3.2 and the extraction region of VER J2227+608 (Acciari et al., 2009), respectively. Using the forward-folding method (Aleksić et al., 2016), the spectra are fitted with a power-law function:

$$\frac{dN}{dE} = N_0 \left(\frac{E}{3 \text{ TeV}} \right)^{-\Gamma} . \tag{3.2}$$

The best-fit parameters are summarized in Table 3.3. The γ-ray spectrum in the tail region has a higher flux and a marginally harder index than that of the head region. For the VER J2227+608, using the same integration region as VERITAS, our results are consistent with theirs (Acciari et al., 2009) within the statistical uncertainties in both the index and the normalization at 3 TeV. The apparent discrepancy seen in Fig. 3.8 between the MAGIC results and the Tibet ASγ measurement at the 6–20 TeV range, amounts to only 1.4σ statistical uncertainty. Considering the source extension of VER J2227+608 and the MAGIC PSF, the flux derived in this work may correspond to $\sim 60\%$ of the whole region estimated with the other experiments. If this loss is considered, the discrepancy between MAGIC and Tibet ASγ relaxes from 1.4σ to 1.1σ. In addition, if the systematic uncertainties are taken into account, both results agree within 1σ.

3.4 Systematic uncertainties in the extended source analysis

3.4.1 Estimation of the effective area

The effective area used in the spectral analysis is estimated by assuming a source radius. In Sect. 3.3.2, we assumed 0.16° as the radii of head and tail. However, as mentioned in Sect. 3.3.1, the actual radii and morphology of the γ-ray emissions are unknown. Here, we evaluate the

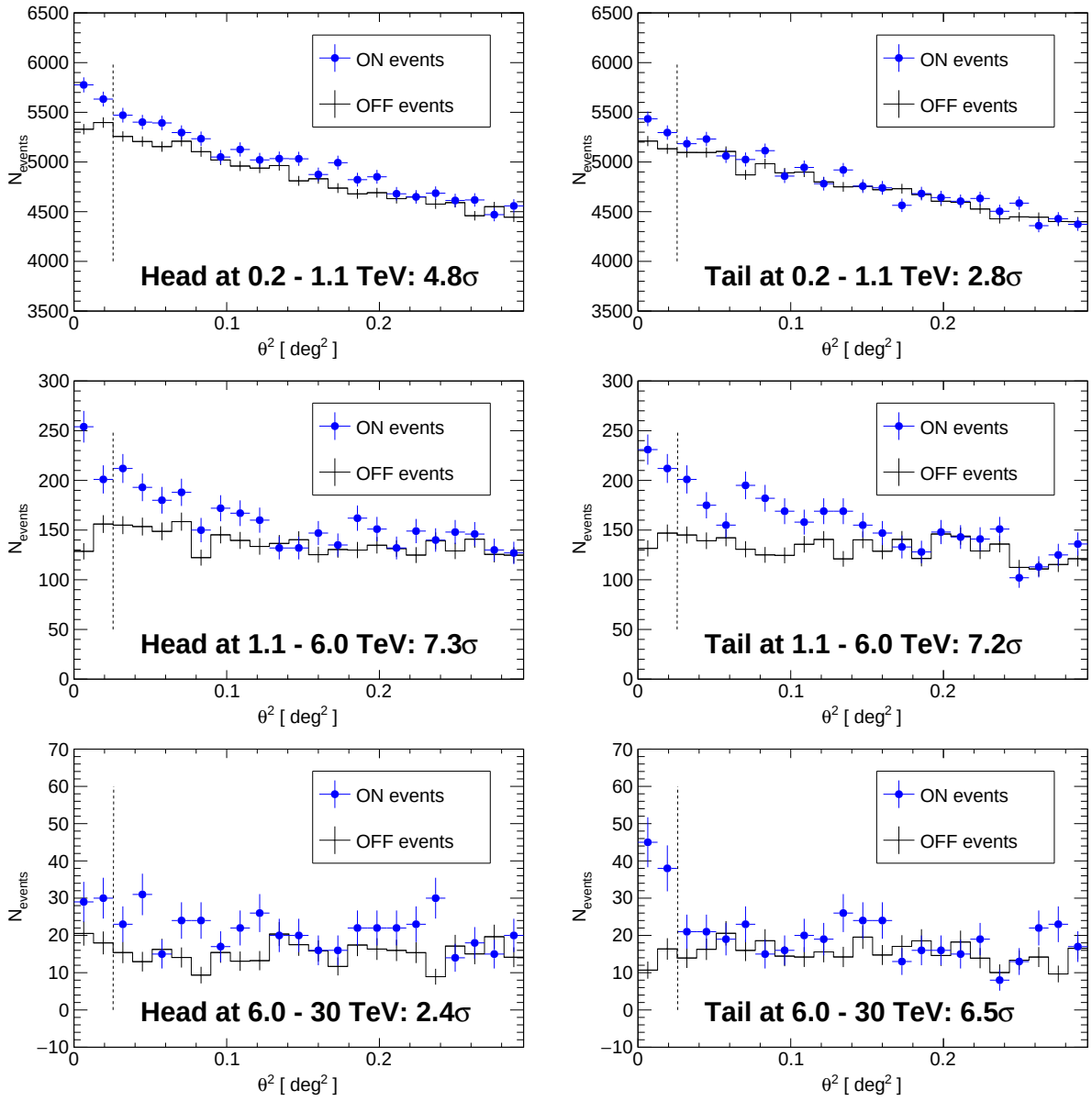

Figure 3.6: The same as in Fig. 3.5 but for the energy of 0.2–1.1 TeV (top), 1.1–6.0 TeV (middle), and 6.0–30 TeV (bottom).

Table 3.3: Comparison of the spectral parameters between this MAGIC results reported here and the VERITAS ones (Acciari et al., 2009). All sources were fitted with the power-law function of Eq. 3.2, using a forward-folding method (Aleksić et al., 2016). The systematic uncertainties are estimated based on as in Sect. 2.4.

Source	N_0 at 3 TeV (10^{-14} cm^{-2} s^{-1} TeV^{-1})	Γ	χ^2/ndf
head	$3.8 \pm 0.7_{\rm stat} \pm 0.7_{\rm sys}$	$2.12 \pm 0.12_{\rm stat} \pm 0.15_{\rm sys}$	5.5/6
tail	$6.0 \pm 0.7_{\rm stat} \pm 1.0_{\rm sys}$	$1.83 \pm 0.10_{\rm stat} \pm 0.15_{\rm sys}$	2.6/6
VER J2227+608 (MAGIC)	$13.1 \pm 1.1_{\rm stat} \pm 2.1_{\rm sys}$	$1.91 \pm 0.07_{\rm stat} \pm 0.15_{\rm sys}$	7.1/6
VER J2227+608 (VERITAS†)	$11.5 \pm 2.7_{\rm stat} \pm 3.5_{\rm sys}$	$2.3 \pm 0.33_{\rm stat} \pm 0.30_{\rm sys}$	-

† Ref: Acciari et al. (2009).

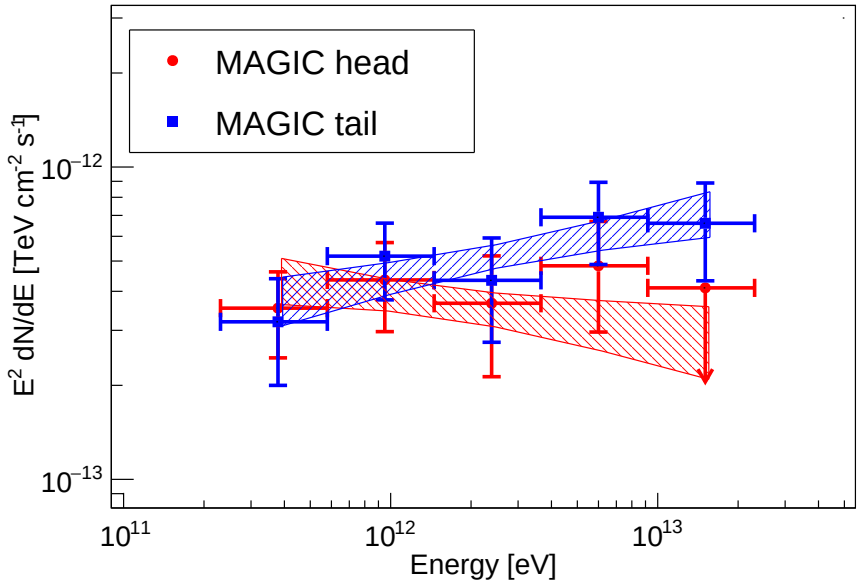

Figure 3.7: Energy spectra of the head and tail regions. Red and blue data represent the spectra of the head and tail, respectively. The color bow-tie areas show the result of fitting with a simple power-law function and 1σ statistical uncertainties.

Table 3.4: Details of the Crab nebula data.

Observation period	Oct. 2016 – Mar. 2018
Observation time	23.0 hr
Zenith angle	30–50°
Wobble angle	35°, 215°
Offset angle	0.4°
Analysis energy threshold	100 GeV

impact of different assumptions in the source model on estimating the effective area, as an additional systematic uncertainty. We investigate the effects of (I) assumed source extension and (II) assumed center position, using the observation data of the Crab Nebula, whose morphology is well known. The data set used in this study is summarized in Table 3.4.

(I) Uncertainty of the source extension

We examine the difference of the computed effective area and the energy spectrum due to the assumed radius of the γ-ray source (see Fig. 3.9 a for a schematic view). For this, we prepare the MC simulation data shown in Figure 3.10, in which the radii are set 0.05, 0.1, 0.15, and 0.2°.

Figure 3.11 shows the dependence of the effective area on the assumed source radius. The ratio to the point source data is also shown in the lower part of Fig. 3.11. The resultant discrepancy between the assumptions is found to be at most 5% at the energy band higher than the analysis threshold of 100 GeV. The energy spectrum of Crab Nebula is fitted with a

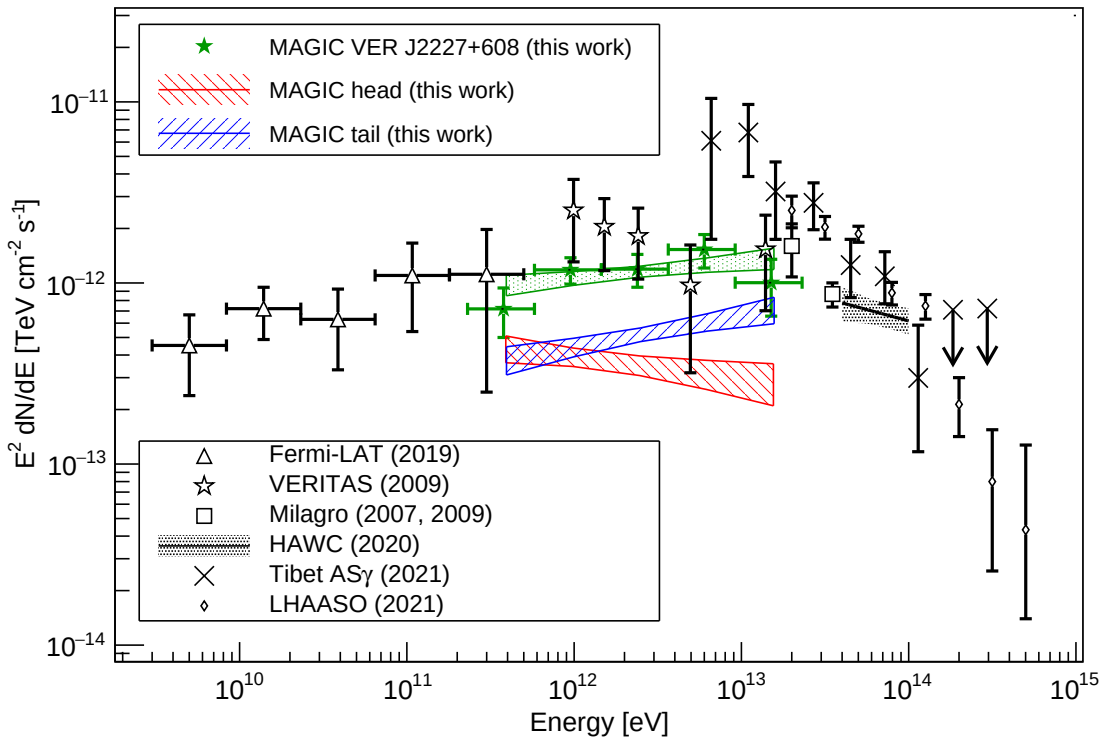

Figure 3.8: Spectral energy distribution of the whole region of SNR G106.3+2.7. Green data represents the spectrum of VER J2227+608 region as measured with the MAGIC telescopes. Also shown as the shaded blue and red regions are the same as in Fig. 3.7. The open triangles, open stars, open squares, x marks, and open diamonds show the *Fermi*-LAT (Xin et al., 2019), VERITAS (Acciari et al., 2009), Milagro Abdo et al. (2007, 2009b), Tibet ASγ (Amenomori et al., 2021b), and LHAASO measurements (Cao et al., 2021), respectively. The black bow-tie area shows a power-law fit and 1σ statistical errors measured by HAWC (Albert et al., 2020).

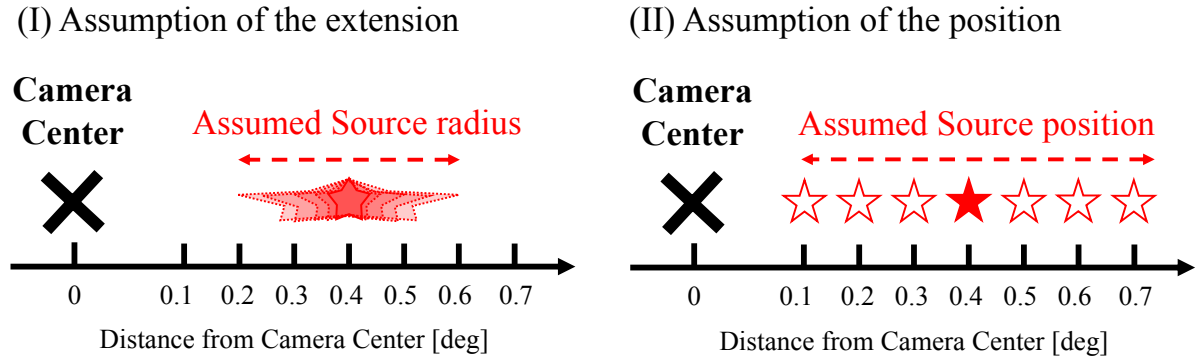

Figure 3.9: Schematic diagram in the calculation of systematic uncertainties due to the assumption of (I) the extension and (II) the center position of a γ-ray source.

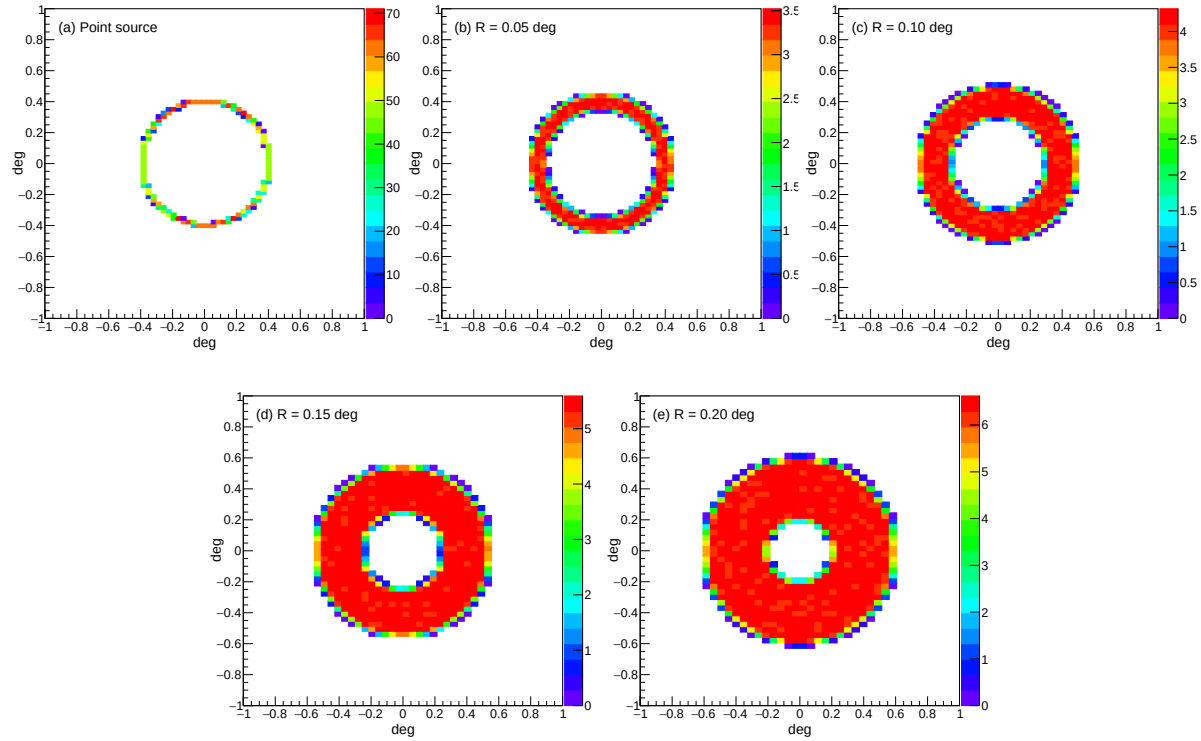

Figure 3.10: Distributions of MC simulation data used for the estimation of the systematic uncertainties (in the camera coordinate). Panel a shows the data distribution for a point source, while Panels b–e show those for extended sources with a radius of 0.05–0.2°.

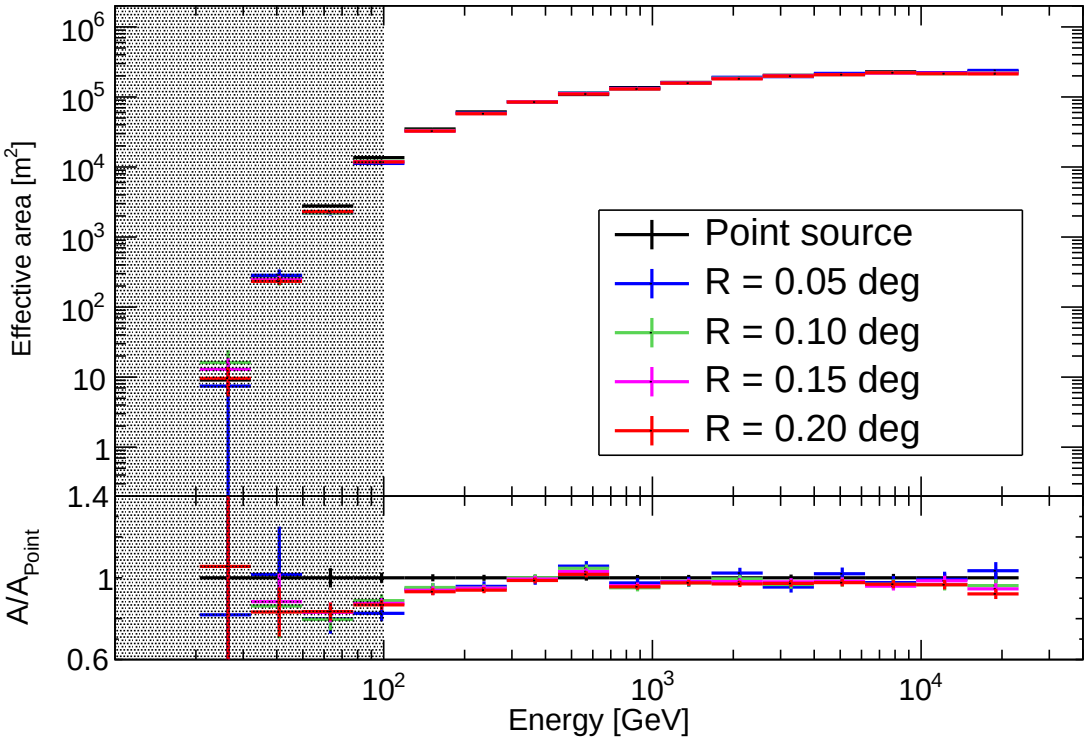

Figure 3.11: The effective areas as a function of an estimated energy. The black data show the result of the point source MC data. The blue, green, magenta, and red data show the result of assuming the source radius of 0.05°, 0.10°, 0.15°, and 0.20°, respectively. The lower panel shows the ratio to that of the point source model. The gray shaded area indicates the lower energy band than the analysis threshold.

single-power law function as follows:

$$\frac{dF}{dE} = N_0 \left(\frac{E}{1 \text{ TeV}} \right)^{-\Gamma}. \tag{3.3}$$

The best-fit parameters for the case of using the point source MC are $N_0 = (2.78 \pm 0.04_{\text{stat}}) \times 10^{-11}$ cm^{-2}s^{-1}TeV^{-1} and $\Gamma = 2.48 \pm 0.01_{\text{stat}}$, respectively. We then compare the fitting parameters with those derived using the other MC data and show the result in Fig. 3.12. The systematic differences are at most 3% for the normalization flux and 1% for the spectral index, respectively.

(II) Uncertainty of the source location

Next, we investigate the effect due to the assumed source position, as shown in the panel b of Fig. 3.9. While the wobble offset (D) of 0.4° is correct, we prepare the MC data with the wobble offset from 0.1 to 0.7° shown in Fig. 3.13. Note that the source radius is assumed to be 0.05°.

Fig. 3.11 and Fig. 3.12 show the effective areas computed with MC data of Fig. 3.13 and the comparison of the spectral fitting results, respectively. The difference from the case with

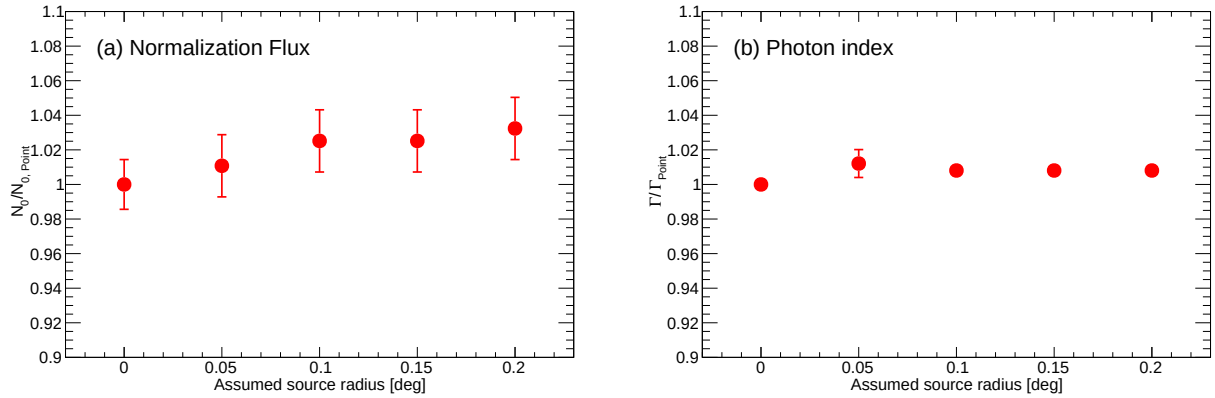

Figure 3.12: Assumed source radius dependence of normalization flux (a) and spectral index (b). A source radius of 0° corresponds to the point source of MC simulation data.

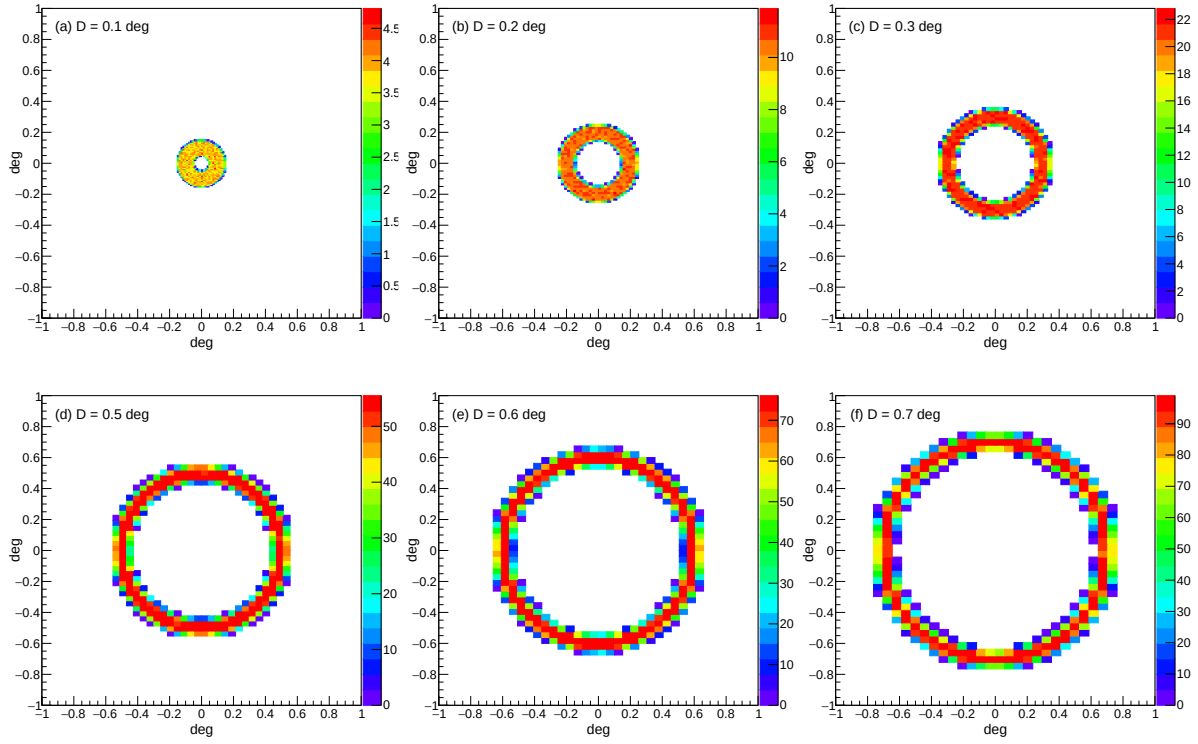

Figure 3.13: Distributions of MC simulation data, which is used to investigate the systematic uncertainties due to the assumption of the source position (in the camera coordinate). In Panels a–f, the assumed distance from the camera center is changed from $D = 0.1°$ to 0.7° in 0.1° increments.

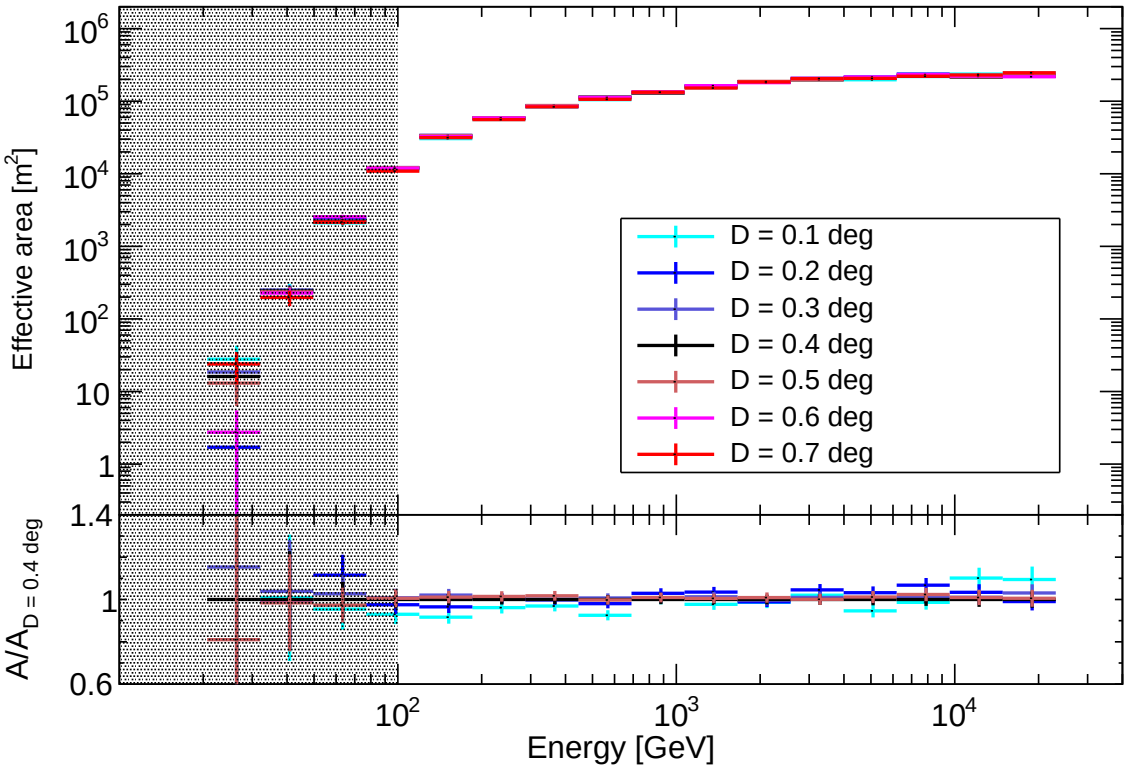

Figure 3.14: Same as Fig. 3.11, but the results with the other MC data of Fig. 3.13.

the correct wobble offset ($D = 0.4°$) appears to increase in correlation with the absolute value of $D - 0.4°$. Even if the assumed center position is wrong by 0.2° (which is larger than PSF), the systematic discrepancies in the fitting parameters (flux and index) are still less than 1%.

(III) Dependency on the offset angle

As mentioned in Sect. 2.3.3, the camera sensitivity depends on the wobble offset (Aleksić et al., 2016). This may affect the investigation of this systematic uncertainty on the effective area. In particular, the distance between the assumed source position and the pointing position in the SNR G106.3+2.7 observation is 0.42–0.78°, which is different from the Crab Nebula observation ($D = 0.4°$). Fig. 3.16 shows the offset angle dependence of the effective area at 1 TeV. The computed effective area decreases as the offset angle increases, and its slope steepens after 0.55°. The systematic uncertainty of the effective area would increase following the change in slope, i.e., a factor of ~ 1.9.

The total effect due the uncertainty of the source assumption can be evaluated by:

$$\begin{aligned}&\text{(Systematic uncertainty due to the MC source model)}\\ &\quad = \text{(Offset angle factor)} \times \sqrt{(\text{extension uncertainty})^2 + (\text{position uncertainty})^2}. \quad (3.4)\end{aligned}$$

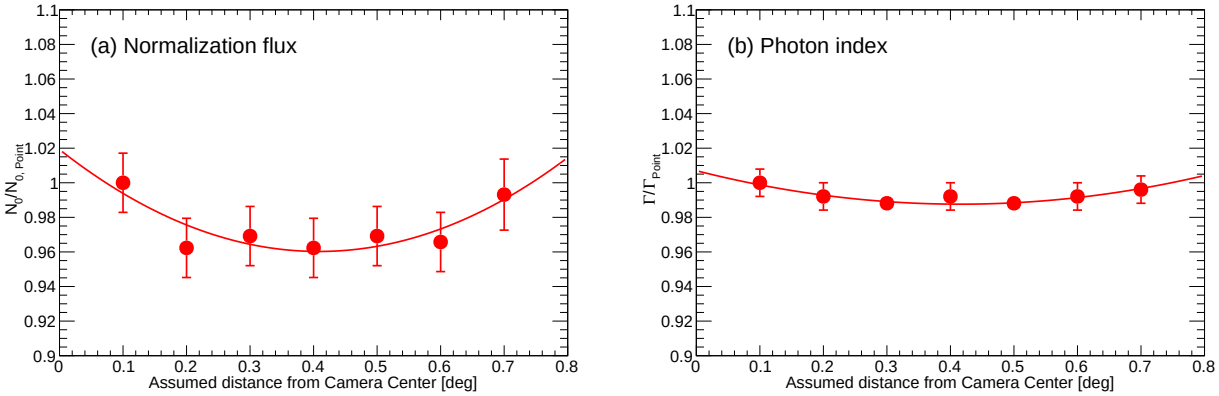

Figure 3.15: Assumed source location dependence of the fitting parameters, normalization flux (a) and spectral index (b). Also shown with the red line is the fit result with a quadratic function.

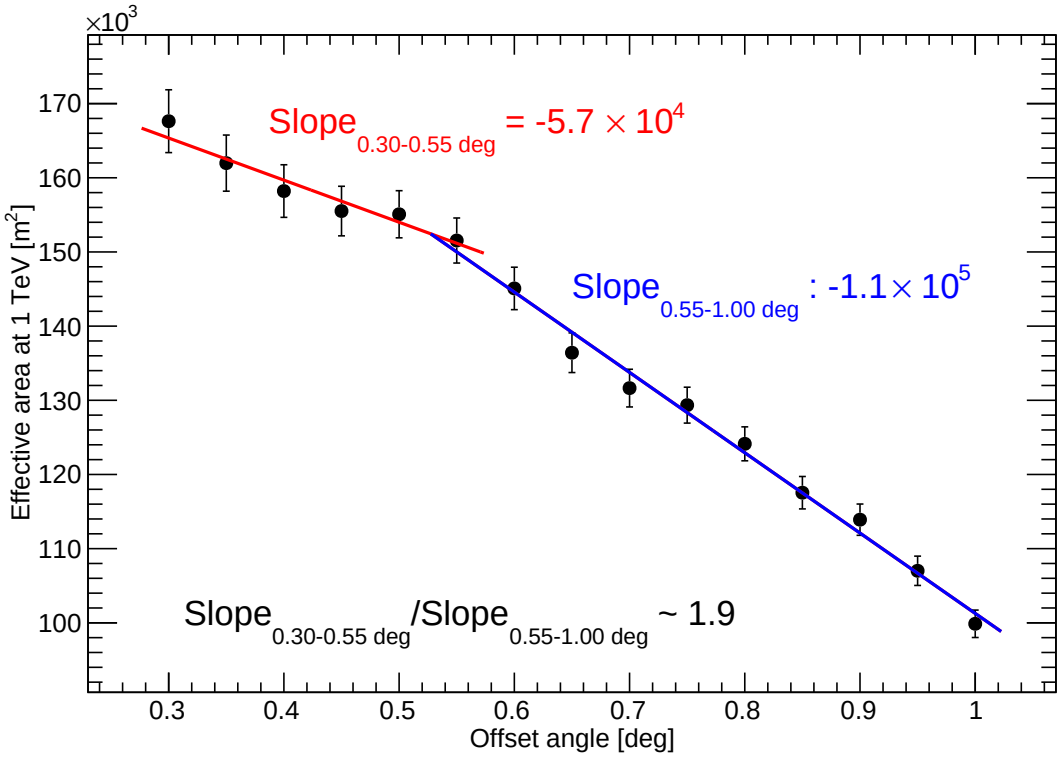

Figure 3.16: Effective area at 1 TeV as a function of the offset angle. The solid lines show the fit result with a linear function to the data of 0.3–0.55° (red) and 0.55–1.0° (blue).

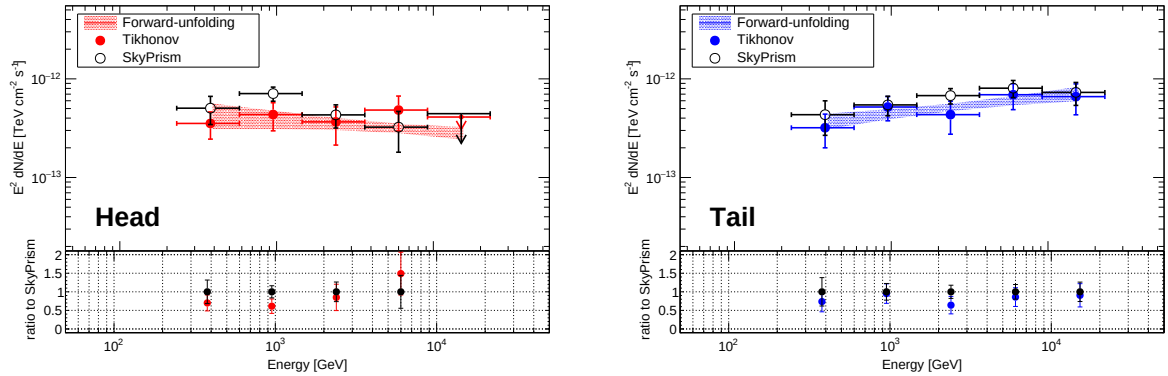

Figure 3.17: Comparison in energy spectra between the results of Sect. 3.3.2 and the SkyPrism analysis.

Hence, the effects on the normalization and slope are estimated as:

$$\sigma_{\mathrm{norm}} \lesssim 6.0\% \tag{3.5}$$

$$\sigma_{\mathrm{index}} \lesssim 2.7\%, \tag{3.6}$$

respectively. As a result, the systematic uncertainty due to differences in the models used in the extended source analysis are found to be smaller than the systematic uncertainties in the standard MAGIC analysis (15–20%) and thus be negligible.

3.4.2 Effect due to θ^2 cut

Although we cannot claim the proper source shape of the head and tail components from the present statistics, under the assumption that the source has Gaussian-like extension with 1σ of 0.085° (after removing the effect of PSF), the loss and contamination rate from the θ^2 cut are estimated to be 23.5% and 2.7%, respectively.

Another concern is leakage from the θ^2 cut region due to the limitation of angular resolution. In the SkyPrism analysis (Vovk et al., 2018), we can calculate the effective area for a given spatial source model, considering the energy dependence of PSF. We use the disk model with a radius of 0.16° as a spatial model. The comparison in energy spectra is shown in Fig. 3.17. The spectra derived with the SkyPrism method are in good agreement with the result derived in Sect. 3.3, and the residual of each energy bin is lower than the statistical 1σ uncertainties.

Chapter 4

Spectral modeling and implication to the γ-ray origin of SNR G106.3+2.7

The spatial coincidence of the MAGIC γ-ray emission and the 408 MHz radio continuum shown in Fig. 3.3 (a) indicates that the VHE γ-ray emission is associated with the radio SNR G106.3+2.7. On the other hand, the emission above 6 TeV is detected only in the tail region but not in the head region, suggesting that the γ-ray origin is not the same for both regions, as well as, the emission up to 100 TeV observed in previous studies (Abdo et al., 2009b; Albert et al., 2020; Amenomori et al., 2021b; Cao et al., 2021) comes mainly from the tail region.

Here, we attempt to model the γ-ray emission mechanism of the head and the tail region individually, while the previous studies (e.g., Liu et al., 2020; Ge et al., 2021; Bao & Chen, 2021) discussed the origin of γ rays using the spectrum up to 100 TeV of the whole region of this object. The possible mechanisms of γ-ray radiation are electron bremsstrahlung, inverse Compton (IC) scattering, and hadronic emission, as described in Chapter 1. Considering the three cases where each emission process dominates, we search for model parameters that reproduce the observed data in each case and try to identify the origin of the head and tail emission.

4.1 Modeling

As mentioned above, we consider three cases: (i) bremsstrahlung-dominated, (ii) IC-dominated model, and (iii) hadronic-dominated model. The electron synchrotron emitting in the radio-to-X-ray band is also considered. The model emissions are computed with the naima framework (Zabalza, 2015).

The radio data for the head and tail regions are taken from Pineault & Joncas (2000). The X-ray spectra for the head and tail regions are taken from results of the "East" and "West" regions from Fujita et al. (2021), respectively, multiplying the intensity by the area of a circle with a radius of 0.16° used in the MAGIC analysis. In this study, we do not consider the direct contributions from the compact Boomerang nebula, whose angular diameter is $\sim 0.05°$, because the γ-ray flux of the region is estimated to be $\sim 10\%$ or less of the head region from the radio and X-ray flux (Liu et al., 2020). At GeV range, Xin et al. (2019) and Liu et al. (2020) reported

the spectral points and upper limits assuming that the sources have a disk shape. They obtained the radii of 0.20° and 0.25° for the disks. We scaled down their measurements by $(0.16/0.20)^2$ for the head and $(0.16/0.25)^2$ for the tail. We also assume that the emission above 10 TeV measured with the air shower experiments (Abdo et al., 2009b; Albert et al., 2020; Amenomori et al., 2021b; Cao et al., 2021) is only from the tail region, since the extracted spectra, shown in Fig. 3.8, suggest that the head contribution to the total flux above 10 TeV is less than 37.1% (2σ upper limit).

The chi-squared statistic for each model is calculated to confirm that model is statistically acceptable. Since the results in the X-ray band (Fujita et al., 2021) and HAWC (Albert et al., 2020) have been given as a fitted power-law function, the flux and statistical uncertainty only at the normalization energy of the fit are considered in the calculation of chi-squared statistic. Several experiments have given measurement results in the γ-ray band, each of which differs beyond statistical error, and thus the influence of systematic error cannot be ignored. This calculation also takes into account systematic as well as statistical errors for γ-ray data. As the systematic errors for the *Fermi*-LAT and LHAASO results were not estimated in the previous papers for this source, we estimate those of *Fermi*-LAT and LHAASO with the uncertainties of the effective area[1] and absolute energy scale (Aharonian et al., 2021), respectively.

In this modeling, the distance to the SNR G106.3+2.7 from the Earth is assumed to be 0.8 kpc, as estimated by the radio observations (Kothes et al., 2001), rather than 3 kpc, as estimated by the X-ray observations (Halpern et al., 2001b). We note that this difference in assumptions slightly affects the estimations of the SNR radius and the total energy of CRs by a factor of $(3/0.8\ \mathrm{kpc}) \sim 4$ and $(3/0.8\ \mathrm{kpc})^2 \sim 14$, respectively, but not critically.

4.1.1 Bremsstrahlung-dominated model

The energy spectra of electrons are assumed to follow a power-law function with an exponential cutoff. The target gas density of each region is estimated using the radio line data of HI and ^{12}CO ($J = 1 - 0$) (see Appendix A). As a result, we adopted $n_{\mathrm{HI}} + n_{\mathrm{CO}} \sim 100\,\mathrm{cm}^{-3}$ for the head region and $n_{\mathrm{HI}} + n_{\mathrm{CO}} \sim 200\,\mathrm{cm}^{-3}$ for the tail region. The following procedure obtained the model parameters: the total amount of electrons is determined to reproduce the γ-ray data with the given target gas density, and the magnetic field strength and electron cutoff energy are determined such that the synchrotron reproduces the radio and X-ray data, respectively.

The top panels of Fig. 4.1 show the modeling results for the head (left) and tail (right). Parameters for the modeling are summarized in Table 4.1. For both regions, models that can reproduce X-ray data fails to reproduce γ-ray data. While the electron cutoff energy of $\sim$ 300 TeV is required to explain the γ-ray data with the bremsstrahlung emission, the synchrotron spectrum computed with the cutoff parameter is in contradiction with the observed X-ray flux.

[1] https://fermi.gsfc.nasa.gov/ssc/data/analysis/scitools/Aeff_Systematics.html

4.1.2 IC-dominated model

As for the seed photon fields in the IC process, the cosmic microwave background, a galactic near-infrared (NIR) radiation field, and a galactic far-infrared (FIR) radiation field are considered. Using the model in the GALPROP package (Porter et al., 2008), the energy density of NIR and FIR are estimated to be 0.1 eV cm^{-3} at T = 30 K and 0.3 eV cm^{-3} at T = 3000 K, respectively. We do not consider the synchrotron self-Compton emission because its flux is about two orders of magnitude lower than the IC emissions with the other seed photons. The electron distribution and the magnetic-field strength are determined in the same manner as in the bremsstrahlung-dominated model.

The modeling results is shown in the middle panels of Fig. 4.1 and the parameters are tabulated in Table 4.1. The broad-band spectrum of the head region can be explained well with the leptonic model (χ^2/ndf = 5.0/7). In the case of the tail region, the leptonic model can reproduce the observed data only in the radio, X-ray, *Fermi*-LAT and MAGIC band (χ^2/ndf = 9.3/13), but fails when including air-shower experiments (χ^2/ndf = 103.1/31). To explain the γ-ray emission above 10 TeV measured by air shower experiments, a high cutoff energy of electrons of $\sim$1200 TeV is required. However, the synchrotron spectrum produced with such high cutoff energy is excluded by the observed X-ray flux. The χ^2/ndf for the model with the high cutoff energy is found to be $\gg 1$ when considering the X-ray data.

4.1.3 Hadronic-dominated model

For the hadronic model, the γ-ray emission results from the decay of neutral pions produced by inelastic pp-collisions. The energy spectra of protons are assumed to follow a power-law function with an exponential cutoff. The target gas density of each region is set to 100 cm^{-3} for the head region and 200 cm^{-3} for the head region, as in the bremsstrahlung-dominated model. The proton spectrum (flux and energy cutoff) is determined to reproduce the γ-ray data, while the electron spectrum is given such that the synchrotron radiation reproduces the radio and X-ray data assuming a magnetic-field strength of 10 μG.

The modeling results show that the γ-ray spectra of both the head and the tail region can be reproduced assuming a proton maximum energy of 35 TeV and 1 PeV, respectively (χ^2/ndf = 5.3/7 and 39.9/31). The parent electron distribution should follow a power-law spectrum different from the ones of protons (parameters shown in Table 4.1).

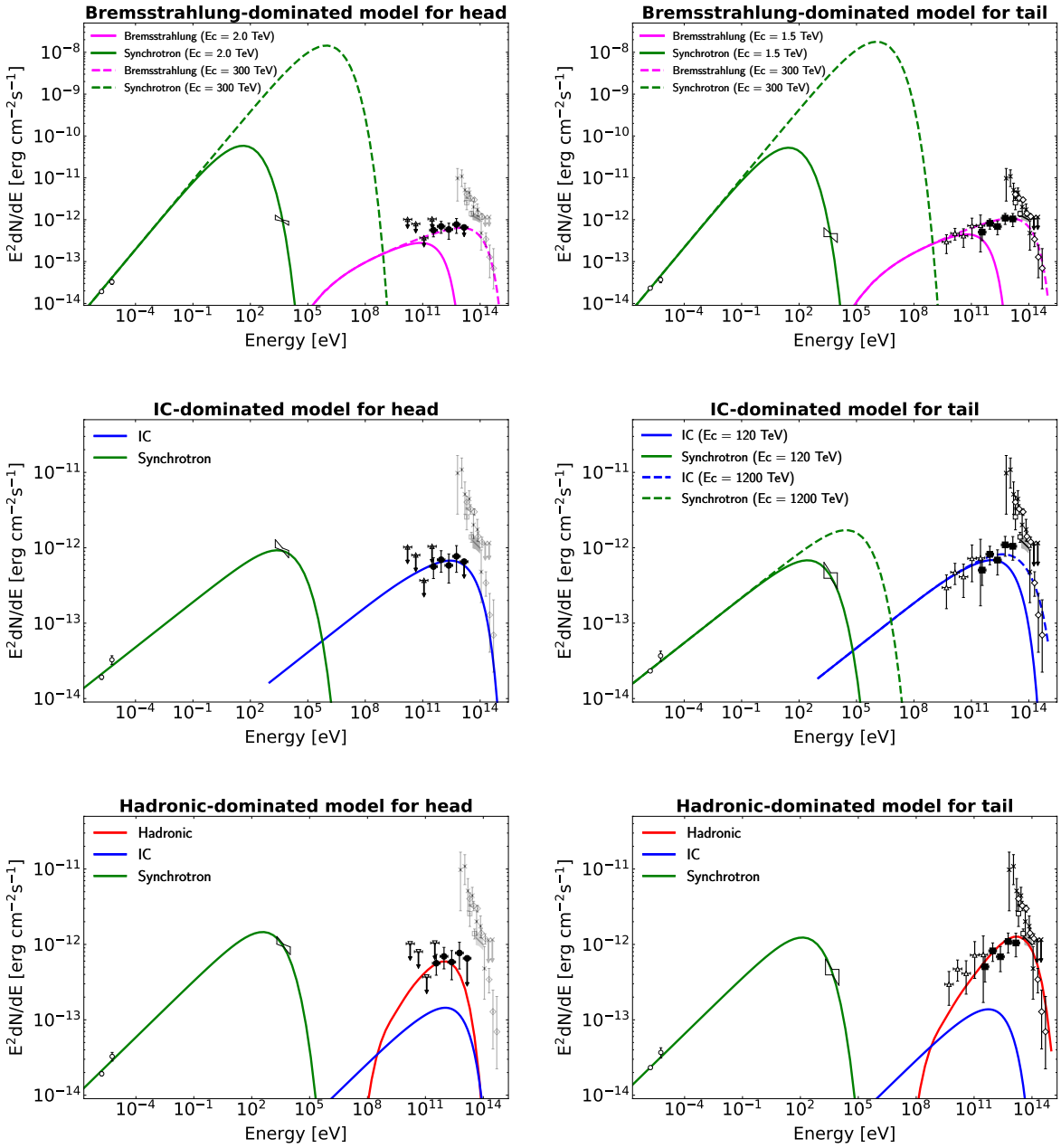

Figure 4.1: Modeling of the SED of SNR G106.3+2.7. The left and right panels show the results of the head and the tail, respectively. The top, middle, and bottom panels show the results of the Bremsstrahlung- and IC- and hadronic-dominated models, respectively. The white circles show the radio flux of each region (Pineault & Joncas, 2000). The black bow-tie area shows a power-law fit and 1σ statistical errors measured by Suzaku (Fujita et al., 2021). The open triangles show the *Fermi*-LAT measurements (Xin et al., 2019; Liu et al., 2020). The markers in the TeV γ-ray band are the same as in Fig. 3.8, but those corresponding to the MAGIC data are shown in black here. The red, magenta, blue and green lines show the hadronic, Bremsstrahlung, IC, and synchrotron emission. The model parameters of each panel are summarized in Table 4.1. In the top two and middle-right panels, the solid and dashed lines show the emissions with the electron cutoff energy indicated in each legend.

Table 4.1: Model parameters for reproducing the observed spectra. α and E_c are the power-law index and the cutoff energy of the particle spectrum, respectively. W is the total energy of particles with energy above 1 GeV. The subscript e and p denote electrons and protons. B is the magnetic-field strength in unit of μG. N_{gas} is the gas density in unit of cm^{-3}.

Model	Source	α_e	$E_{c,e}$ [TeV]	W_e [erg]	B [μG]	α_p	$E_{c,p}$ [TeV]	W_p [erg]	N_{gas} [cm^{-3}]	χ^2/ndf
Bremsstrahlung dominated	head	1.9	2.0 (300)†	7.4×10^{44} (1.7×10^{45})†	190	-	-	-	100	25.3/7 ($\gg 1$)†
	tail	1.9	1.5 (300)†	5.9×10^{44} (1.4×10^{45})†	230	-	-	-	200	148.7/31 ($\gg 1$)†
IC-dominated	head	2.6	360	1.4×10^{47}	3	-	-	-	-	5.0/7
	tail	2.6	120 (1200)†	1.6×10^{47}	3	-	-	-	-	103.1/31 ($\gg 1$)†
Hadronic dominated	head	2.5	60	1.8×10^{46}	10	1.7	60	8.9×10^{45}	100	5.3/7
	tail	2.5	35	2.0×10^{46}	10	1.7	1000	8.2×10^{45}	200	39.9/31

† In the top-right panel of Fig. 4.1, the model curve using the value in the parentheses is shown with the dashed line.

4.2 Interpretation of the γ-ray origin

4.2.1 head region

The X-ray emission in the head region exhibits a softening of the spectral index with distance from the pulsar, suggesting the emission originates in electrons accelerated in and propagated from the shock of the PWN (Ge et al., 2021). Our modeling result shows that X-ray and gamma-ray fluxes can be explained with IC-dominated model from the same electron population. It thus implies that the γ-ray emission can originates in the PWN. Assuming the electron cutoff energy ($E_{\rm c,e}$) and the magnetic-field strength (B) used in the leptonic model for the head region, the electron lifetime due to synchrotron losses is given by: ~ 3.9 kyr $(E_{\rm c,e}/360\ {\rm TeV})^{-1}({\rm B}/3\ \mu{\rm G})^{-2}$, which is consistent with the age of the SNR estimated to be 3.9 kyr from the spectral break in the radio spectrum of the PWN (Kothes et al., 2006) or 10 kyr from the pulsar spin-down age (Halpern et al., 2001a). With the spin-down luminosity of $L_{\rm sd} = 2.2 \times 10^{37}$ ergs^{-1}, the total electron energy from the PWN can be roughly approximated to be $L_{\rm sd} \times t_{\rm age} = 2.8 \times 10^{48}$ erg ($\rm t_{age}$/4 kyr), which is sufficiently larger than the current model parameter ($W_{\rm e} = 1.4 \times 10^{47}$ erg).

The hadronic-dominated model also works for the head. The protons accelerated up to 60 TeV can explain the VHE γ-ray emission detected by MAGIC, given the presence of dense HI clouds in the head region pointed out by Kothes et al. (2001). Although CO emission is not prominent, the total intensity of HI and CO line emissions suggests the presence of gases with a total proton density of ~ 100 cm^{-3}, which is sufficient for the pp emission, as derived in Appendix A. Still electrons with a largely different spectral index are needed to explain the radio and X-ray emission. One of the simplest explanation would be that electrons are mainly from the PWN, while the protons were accelerated in the shell. While SNRs can accelerate CRs only for the limited periods (see Sect. 1.1.2), the shock wave of an SNR with an age of ~ 4 kyr is sufficient to produce protons up to 60 TeV (Ptuskin & Zirakashvili, 2003, 2005), which is required by the modeling result.

4.2.2 tail region

The modeling described in the previous section suggests that it is difficult to explain the tail emission with the Bremsstrahlung- and IC-dominated models. On the other hand, the hadronic-dominated model worked well. The γ-ray spectrum of the tail region can be reproduced assuming a proton maximum energy of 1 PeV (χ^2/ndf = 39.9/31). Generally speaking, acceleration up to 1 PeV can only be achieved at the early stages of the SNR evolution (~ 0.1 kyr) (Ptuskin & Zirakashvili, 2003, 2005). However, as mentioned in Sect. 4.2.1, the age of this SNR has been estimated to be 3.9 kyr from the spectral break in the radio spectrum of the PWN (Kothes et al., 2006) or 10 kyr from the pulsar spin-down age (Halpern et al., 2001a). This discrepancy in the SNR age can be solved assuming a CR-escape scenario (e.g. Aharonian & Atoyan, 1996; Gabici & Aharonian, 2007). In this scenario, protons accelerated up to $\sim$ PeV energies at a young SNR escape from acceleration regions and illuminate nearby clouds, which produce "delayed" γ-ray emission. This scenario can also explain a proton index of 1.8, harder than 2.0 expected from

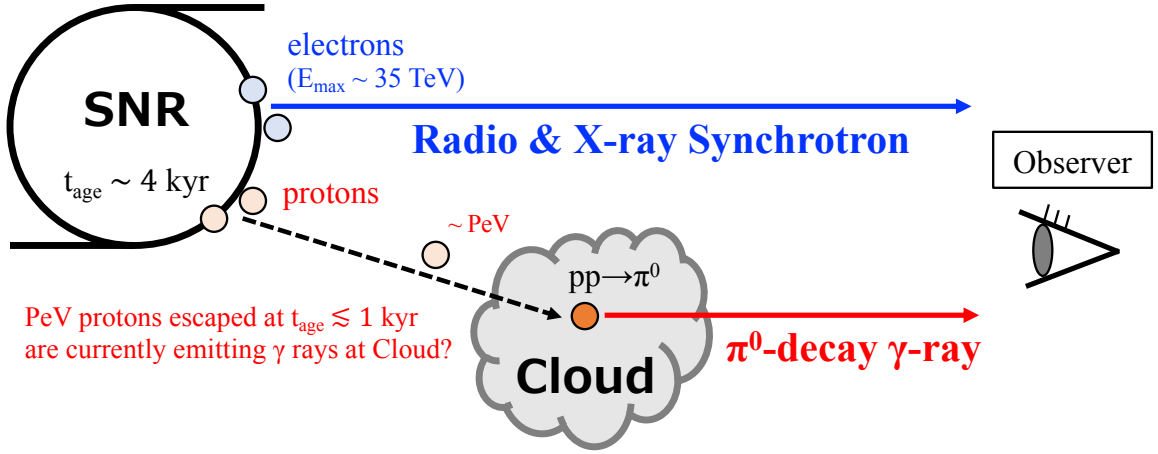

Figure 4.2: Schematic view of the interpretation of the non-thermal emissions from the tail region. $t_{\rm age}$ indicates the age of SNR (i.e., the time interval after the SN explosion).

the DSA theory, as described in Sect. 1.2.1. On the other hand, it requires high density clouds spatially coinciding with the γ-ray morphology. Using the CGPS data of HI and ^{12}CO ($J = 1-0$) (see Appendix A), we confirmed a coincidence of the γ-ray emission with CO line emission in the velocity range -6.41 to -3.94 km s^{-1} in the tail region, which was already pointed out by Kothes et al. (2001) and Acciari et al. (2009). This supports the CR-escape scenario in the tail region. Moreover, the scenario is consistent with the interpretation given in Albert et al. (2020), Fujita et al. (2021), and Amenomori et al. (2021b). The authors estimated the diffusion length of CRs using the relation: $l_{\rm diff} = \sqrt{Dt}$, where D is the diffusion coefficient, and t is the diffusion time. They then found, even assuming a small diffusion coefficient ($D \sim 10^{26}$ cm^{2}s^{-1} at GeV), that the diffusion length for CRs with an energy of $\mathcal{O}$(100 TeV) in 5–10 kyr is larger (40–60 pc) than the size of the SNR ($\sim$ 6 pc) and thus suggested the CRs are not confined in the SNR.

Electrons may also escape in the same way as protons but be affected by radiative cooling, which is not considered in the modeling. However, the change in the spectral index due to the cooling effect is estimated to be at most 0.1–0.4 (Diesing & Caprioli, 2019), suggesting that the difference ($\sim$ 0.7) between the proton and electron indices cannot be explained even by considering it. This fact implies that leptonic and hadronic emissions may happen at different locations and thus under different physical conditions. For example, as shown in the schematic view in Fig. 4.2, lepton emissions come from the SNR shell and hadron emissions come from interstellar gas spatially separated from the SNR. This assumption can allow the unusual ratio of the total energy of CRs ($W_{\rm p} \lesssim W_{\rm e}$) because only the hadronic emission is affected by the propagation effect (Gabici & Aharonian, 2007), and thus only $W_{\rm p}$ decreases.

The hard proton index found in the TeV band can also be explained with the SNR-cloud interactions (Inoue et al., 2012), as an alternative to the CR-escape scenario. The thermal instability due to the shock-cloud interaction is expected to generate a clumpy ISM, where the magnetic field may be amplified up to $B = 1$ mG. The penetration length of CRs in the clumpy ISM depends

on the energy and is given by $l_{\rm pd} = 0.1\eta^{1/2}(E/10\ {\rm TeV})^{1/2}({\rm B}/100\ \mu{\rm G})^{-1/2}({\rm t_{age}}/1\ {\rm kyr})^{1/2}$ pc, where η is the gyro factor ($\delta B^2/B^2$), E is the particle energy. Thus, it is acceptable that the proton index is $\lesssim 0.5$ harder than expected in DSA theory, as required in the modeling for the tail region. However, this model cannot explain the maximum energy of $\gtrsim$ PeV in SNRs older than 1 kyr and the differences in the distribution of electrons and protons as mentioned above (Diesing & Caprioli, 2019).

4.2.3 Remarks on the modeling

It should be noted that the data points of Milagro, HAWC, Tibet ASγ, and LHAASO, included in the modeling of the tail spectrum, are from extraction regions, which include the head. Hence, they are potentially contaminated if the head emits radiation $>$ 10 TeV. Based on the present data alone, we cannot strongly claim that the origins of the γ rays from the head and the tail are different. Thus, to accurately determine the emission mechanism, it is necessary to separate the extraction regions at the head and tail also for spectral points above 10 TeV. In addition, the integrated region of MAGIC-tail in this analysis may miss a fraction of the γ-ray emissions observed by air shower experiments. Using the Gaussian extension at $>$6 TeV derived with θ^2 plot around tail, the survival rate is estimated to be 73.9–94.5% (1σ uncertainties). We examined the effect on our model fit for the tail spectrum when using the scaled down flux of air shower experiments by 26.1%. In the leptonic model, χ^2/ndf changed (from 103.1/31 to 96.3/31.1) slightly, indicating the model is still inconsistent with the observed data. In the hadronic model, χ^2/ndf also changed (from 39.9/31 to 41.3/31), and the model still works. As a result, the underestimation of the flux due to the angular cut does not affect our conclusion.

In conclusion, the spectral modeling indicates an evidence that the 100-TeV γ ray originates from PeV proton accelerated by SNR G106.3+2.7. However, this conclusion is based on the qualitative interpretation by the CR-escape scenario, which has many uncertainties. To justify this interpretation, it would be necessary to pass two tests: whether the SNR can accelerate protons up to $\geq$ 1 PeV in the past and whether the observed spectrum can be reproduced by considering CR diffusion. These questions will be approached using the time-evolution measurement of the maximum energy in a single SNR, which will be attempted with SNR HB9 observations in Chapter 5. We will then revisit this interpretation for SNR G106.3+2.7 in Chapter 6.

Chapter 5

γ-ray observations of SNR HB9 toward the measurement of the DSA history

Although we have obtained an evidence that the SNR G106.3+2.7 examined in the previous chapters is almost certainly a PeVatron, the interpretation by the CR-escape scenario remains a qualitative discussion and requires a quantitative study. Also, a study of whether such SNRs are universal would require a measurement of the time evolution of the maximum acceleration energy within the above interpretation. In this chapter, we describe a method to measure the time evolution of maximum energy in SNRs and attempt to establish the new method by adapting it to the SNR HB9 observations.

5.1 A measurement method of the maximum energy evolution in an SNR

Systematic studies exploring the population of SNRs are expected to provide information on the evolution of the CR spectra of SNRs as a function of the SNR age (Ohira et al., 2011; Schure & Bell, 2013; Gaggero et al., 2018). Fig. 5.1 shows a correlation between γ-ray spectral cutoff ($E_{\rm cut}$)and the age of SNRs ($t_{\rm age}$). This correlation follows the power-law function:

$$E_{\rm cut} = 1.3^{+1.1}_{-0.63}\ {\rm TeV}\ \left(\frac{\rm t_{age}}{1\ {\rm kyr}}\right)^{-0.81\pm0.24}, \tag{5.1}$$

which suggests that an acceleration up to PeV is not possible even by young SNRs with an age of 100 yr (Suzuki et al., 2020, 2022). However, quantifying the evolution of DSA with this kind of method is challenging due to the large diversity of the surrounding environment of SNRs (e.g., Yasuda & Lee, 2019). This latter may affect the dominant radiative process for the gamma-ray emissions and the estimation of the maximum particle energy.

Another way to study the evolution of DSA is a simultaneous observation of a single SNR, specifically its shell part and nearby massive cloud regions. If a massive cloud exists in the

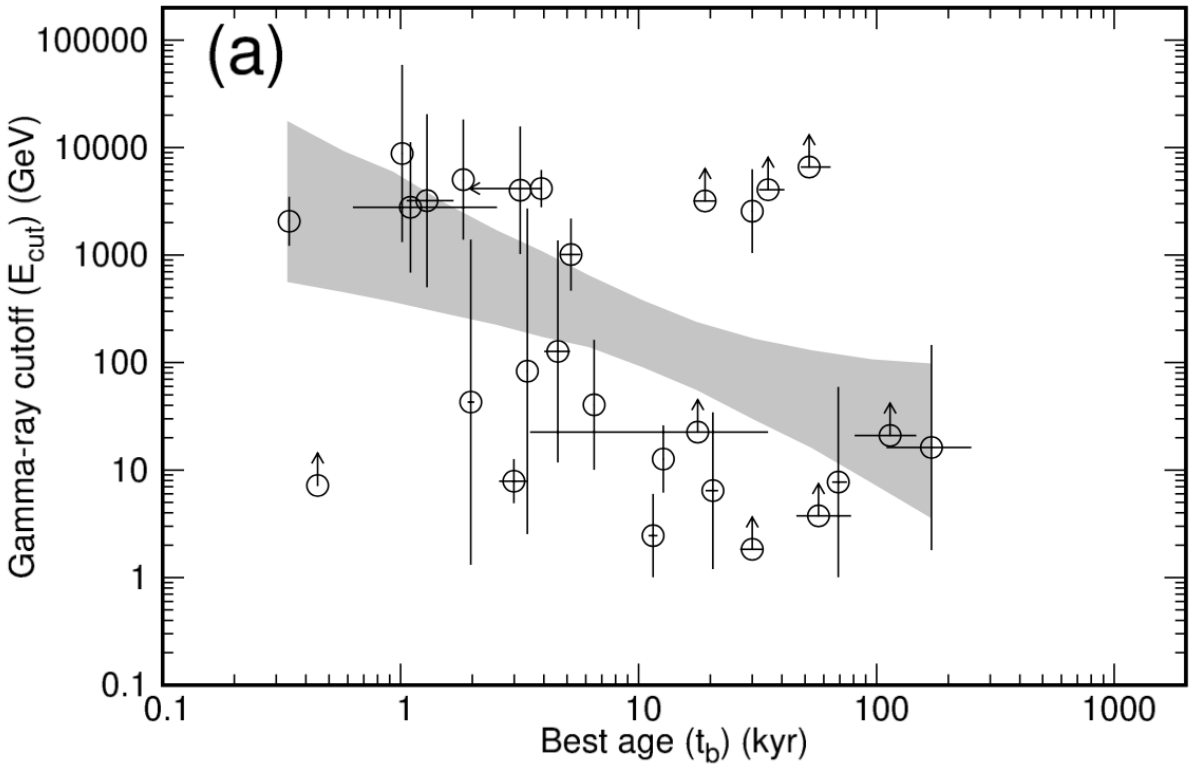

Figure 5.1: Cutoff energy of γ-ray spectra of SNRs as a function of an estimated age (Suzuki et al., 2022). The gray bow-tie area shows the fitting result with a simple power-law function.

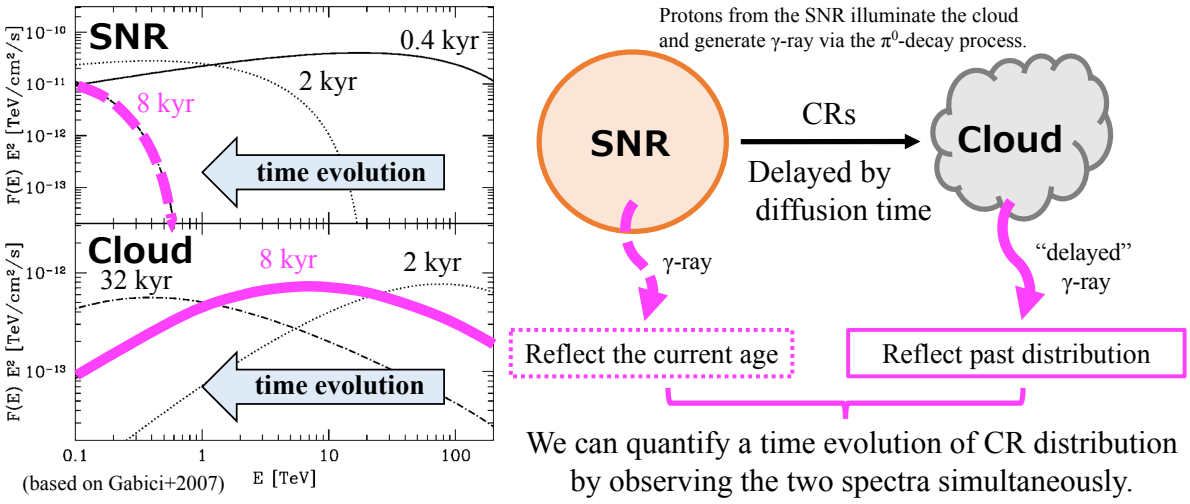

Figure 5.2: Schematic view of the measurement method for the time evolution of CR distribution in a single SNR.

vicinity of the SNR, protons that escaped the SNR illuminate the cloud and generate γ-ray emission via the π^0-decay process (Aharonian & Atoyan, 1996; Gabici & Aharonian, 2007). The delay of the timing of the γ-ray emission at the cloud region from that of the incident proton escape depends on the propagation time and accordingly reflects the particle distribution in the SNR at a specific epoch in the past. Fig. 5.2 shows (left) an example of time evolution in the energy spectra at the shell and cloud regions and (right) a schematic view for this measurement. A comparison of the spectra at the SNR shell and nearby clouds observed at roughly the same time enables us to quantify the evolution of the DSA in the SNR.

5.1.1 Previous observations of delayed γ-ray emission

In observations of SNR W28, such "delayed" γ-rays have been detected from three cloud regions with HESS and *Fermi*-LAT (Aharonian, 2008a; Hanabata et al., 2014). The observed γ-ray spectra from these cloud regions, however, do not differ significantly from one another, and hence the maximum energy with the DSA at W28 has never been successfully measured as a function of the SNR age. Since the angular distances from the SNR center to these individual clouds are almost the same in W28, the emissions from the clouds should originate in protons accelerated at a similar epoch. The γ-ray emission from another cloud (named HESS J1801−233) located to the north of W28 was suggested to originate in protons that have been re-accelerated by a shock-cloud interaction (Cui et al., 2018), in which case the γ-ray spectrum does not reflect the SNR age. Hanabata et al. (2014) reported detection of the fifth γ-ray emitting region, named source W, located at the western part of W28. Although there is a possibility that the emission is explained with protons escaping from the SNR, no cloud counterpart has been found. Thus far, it is impossible to quantify the particle distribution at multiple epochs with the available observations of W28.

One concern with the study using delayed γ-ray spectra is a large dependence on the diffusion coefficient of CRs. The diffusion coefficient may be modified in the vicinity of an SNR due to the effect of self-confinement and/or magnetic-field amplification caused by the generation of turbulent plasma waves (Wentzel, 1974; Fujita et al., 2011; D'Angelo et al., 2018). In this scenario, CRs traveling in the interstellar magnetic field generate plasma waves, which scatter the CRs and prevent their diffusion. Furthermore, the CR pressure may increase the density fluctuation of ISM, resulting in the growth of turbulence in the magnetic field. While delayed γ-ray emissions are detected in the vicinity of several SNRs (e.g., Uchiyama et al. (2012)), the derived diffusion coefficients had large uncertainty, and so did the estimated amount of particle acceleration at the SNR shell in the past. Fig. 5.3 shows the modeling result with the delayed γ-ray emission for the observed spectrum around SNR W44. Their model spectra are almost identical, even with diffusion coefficients that differ by one order of magnitude. This is mainly because the SNRs discussed so far are relatively old. For older SNRs, clouds and SNR shells often interact directly, and as a result, the observed data do not provide much information on the diffusion coefficient (Fig. 5.3). Furthermore, even if clouds are significantly separated from SNR shells, the delayed γ-ray spectra do not differ significantly from those of the current SNR shells, and thus the data are not of much help for restricting the diffusion coefficients (Uchiyama

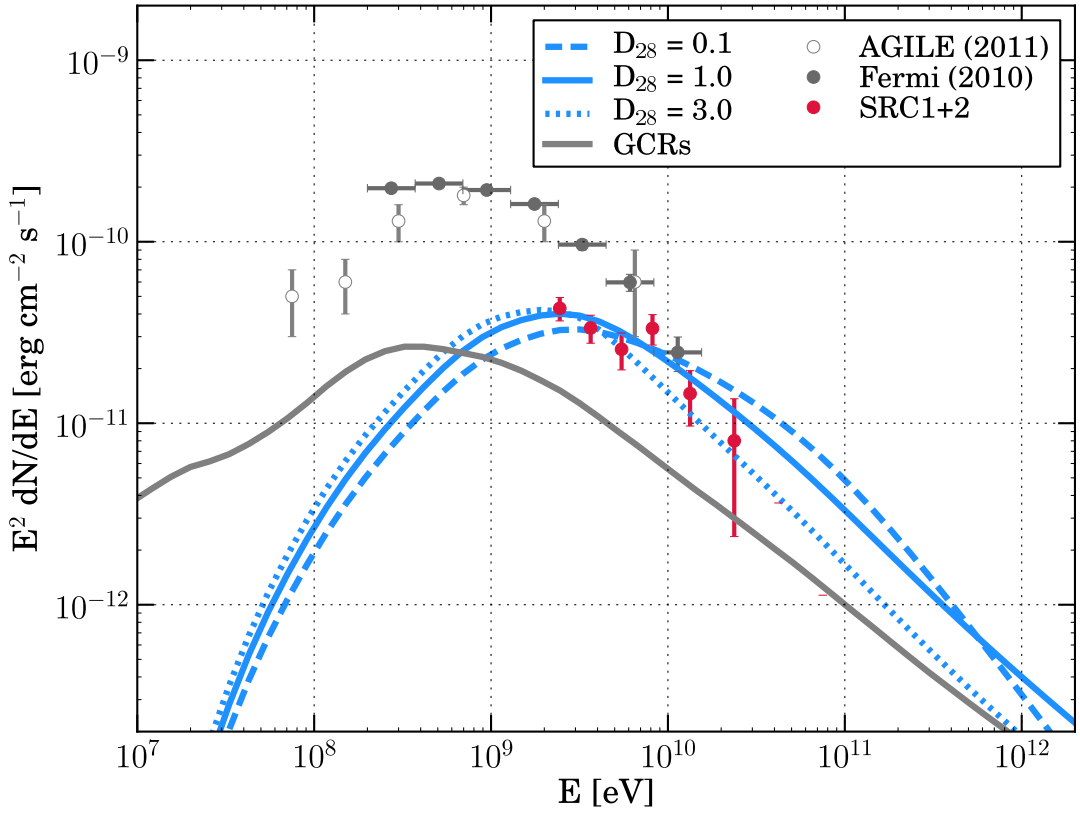

Figure 5.3: Modeling result to γ-ray emission from the cloud region around SNR W44 (Uchiyama et al., 2012). The red and grey data points represent the energy spectrum at the cloud and the shell region, respectively. The blue lines show the model of the delayed γ-ray emission with three cases of diffusion coefficient: $D = [0.1, 1.0, 3.0] \times 10^{28}$ cm^{2}s^{-1} (E/10 GeV)$^{0.6}$.

et al., 2012). This concern can be addressed by observing the spectral peak of the delayed γ-ray spectrum at cloud regions. Fig. 5.4 shows an example of the delayed γ-ray spectrum and the physical quantities associated with its features (i.e., spectral peak and index). The spectral peak mainly depends on the diffusion coefficient as well as the time evolution of $E_{\rm max}$ and the distance between the shell and cloud regions ($d_{\rm cl}$). The energy spectrum at the shell part and the two dimensional angular distance can give constraints on the evolution of $E_{\rm max}$ and $d_{\rm cl}$, respectively. Thus, if its spectral peak is observable, the diffusion coefficient can be estimated with few uncertainties by fitting the delayed γ-ray spectrum.

5.1.2 Introduction of SNR HB9

Here, we focus on SNR HB9 (G160.9+2.6), which is relatively young ($\sim 6.6 \times 10^3$ yr; Leahy & Tian (2007)) compared with other objects where delayed γ-rays have been observed. HB9 has two additional advantages for this type of study in the DSA evolution. Firstly, there are molecular clouds in the vicinity of this SNR, but their locations do not overlap with the SNR in the line of sight (Sezer et al., 2019), as shown in the left panel of Fig. 5.5. This allows to obtain

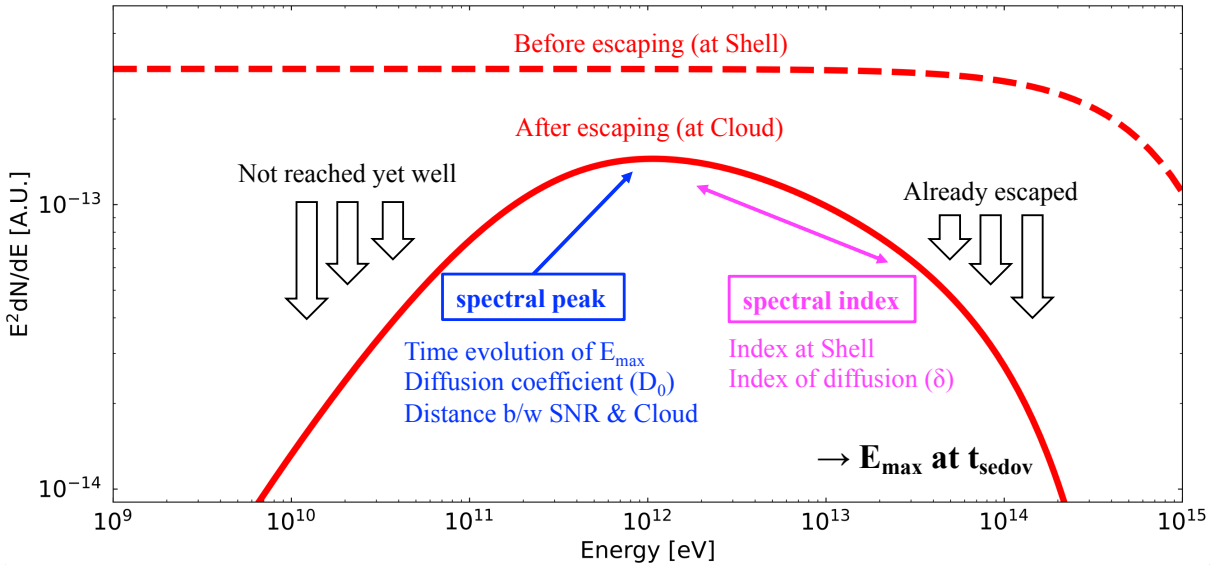

Figure 5.4: Example of the "delayed" γ-ray spectrum.

spatially-resolved spectra in the shell and cloud regions and to estimate the diffusion time using the angular distance between the SNR and clouds. Secondly, HB9 has observable γ-ray emission from the SNR shell (Araya, 2014), which is essential to estimate the current maximum energy of the accelerated particles at the SNR shock (the right panel in Fig. 5.5).

HB9 has a disk-like morphology with a radius of $\sim 1^\circ$ in the radio band (e.g., Leahy & Roger, 1991), and its spectral index is $\alpha = -0.47 \pm 0.06$ in frequencies between 408 and 1420 MHz (Leahy & Tian, 2007), which is consistent with the typical value ($\alpha = 0.5$) of SNRs (Reynolds et al., 2012). Its kinematic distance was estimated to be 0.8 ± 0.4 kpc from HI observations, yielding the dynamical age estimate of 6.6×10^3 yr (Leahy & Tian, 2007). Sezer et al. (2019) found an H$_{\rm I}$ shell expanding toward the SNR with a velocity ranging between -10.5 and $+1.8$ km s^{-1} and derived a kinematic distance to be 0.6 ± 0.3 kpc, which is consistent with the estimate by Leahy & Tian (2007). In the γ-ray band, spatially extended emission was detected from SNR HB9 along with its radio shell with the *Fermi*-LAT 5.5-year observations in the energy band above 0.2 GeV (Araya, 2014). The γ-ray spectrum was characterized by a power law with a photon index of 1.44 ± 0.25 accompanied by an exponential cutoff at 1.6 ± 0.6 GeV. The spectrum is explained with emission from inverse Compton (IC) scattering of electrons with a simple power-law energy spectrum with a differential index of 2 and maximum electron energy of 500 GeV. Furthermore, Sezer et al. (2019) analyzed the *Fermi*-LAT 10-year data in an energy range between 0.2 and 300 GeV and newly detected a point-like source near the SNR shell, named PS J0506.5+4546. The spectrum of the point source can be characterized by a simple power-law function with an index of 1.90 ± 0.19. The flux was $(6.59 \pm 3.47) \times 10^{-10}$ cm^{-2}s^{-1}. PS J0506.5+4546 was, however, suggested not to be related to the SNR shell, and its origin is unclear (Sezer et al., 2019).

In this work, we study the γ-ray morphology of SNR HB9 and the spectra of the SNR shell and the nearby cloud regions, using 12-year observations with the *Fermi*-LAT, to quantify the

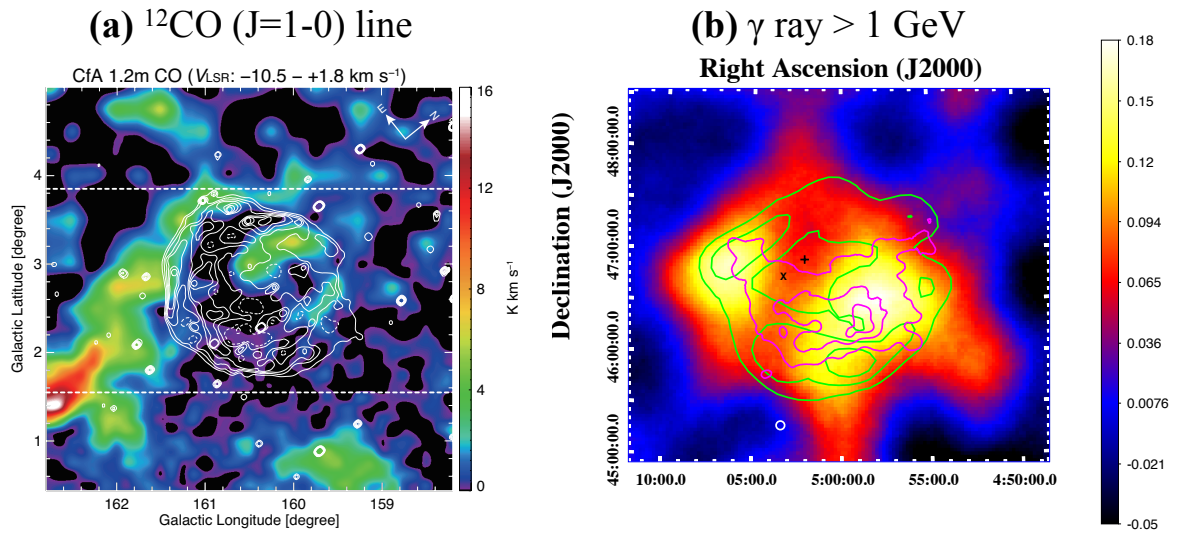

Figure 5.5: Skymaps in the vicinity of SNR HB9. **(a)** ^{12}CO ($J = 1-0$) line intensity map (Sezer et al., 2019). Also shown with white contours is the radio continuum emission at 4850 MHz. **(b)** GeV γ-ray map above 1 GeV (Araya, 2014). The green and magenta contours indicate the radio continuum at 4850 MHz and X-ray emissions, respectively.

evolution of DSA. In addition, since we suspect that the γ-ray emission from PS J0506.5+4546 originates in a molecular cloud located outside the radio shell, we search for spatial correlation between the ^{12}CO ($J = 1 - 0$) line and γ-ray emissions. In Section 5.2, we describe the *Fermi*-LAT observations and show the results of our analysis. We present the modeling study to interpret the origin of the observed γ-ray in Section 5.4.

5.2 Fermi-LAT observations in the vicinity of HB9

5.2.1 *Fermi*-LAT

The Large Area Telescope (LAT) onboard *Fermi* satellite, launched in 2008, is capable of detecting γ rays in an energy range from $\sim$ 200 MeV to $>$ 300 GeV (Atwood et al., 2009) and, as mentioned in Sect. 2.5 has better sensitivity at $<$ 10 GeV than the MAGIC telescopes. Furthermore, the wide field of view of 2.4 sr can provide abundant data over the entire sky, which is useful in investigating unknown γ-ray sources.

As shown in Fig. 5.6, the LAT detector consists of a tracker, a calorimeter, and an anti-coincidence detector, with a total size of 1.8 m $\times$ 1.8 m $\times$ 0.72 m. The detection principle of γ rays in the *Fermi*-LAT is similar to that of the IACT described in Chapter 2. In the LAT detector, an incoming γ ray causes pair production at the tungsten sheet of the tracker part, generating an electromagnetic shower in the calorimeter. The arrival direction of the gamma ray can be estimated by capturing the electron track of the first electron pair in the tracker, while its energy can be measured in the calorimeter. Each component is described below.

Tracker

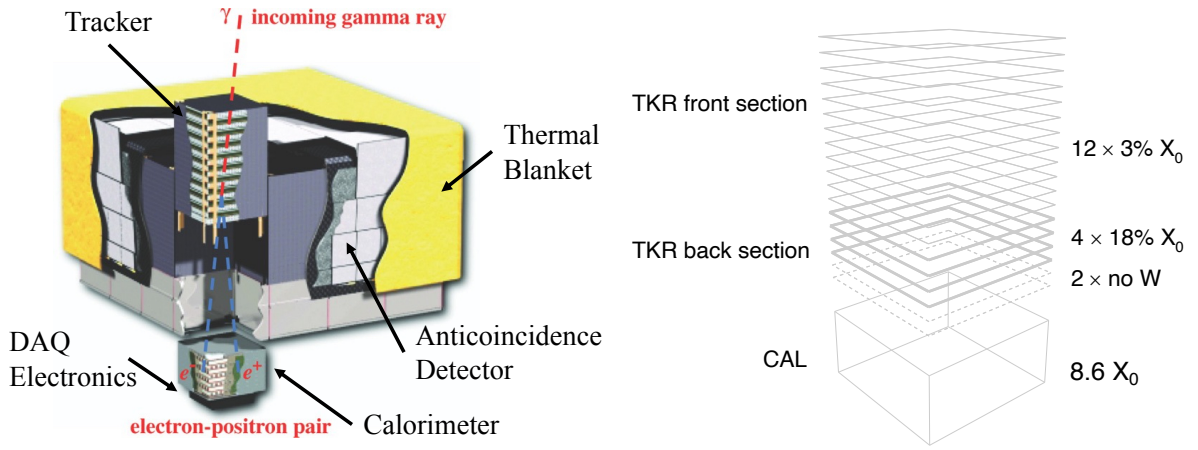

Figure 5.6: **Left:** Schematic view of the Fermi-LAT detector, based on Fig. 1 of Atwood et al. (2009). **Right:** Schematic diagram of the tracker and calorimeter within the LAT detector, adopted from (Ackermann et al., 2012b). X_0 indicates the radiation length.

The tracker consists of a total of 18 layers of silicon strip detectors and the tungsten sheets, the later of which are installed only at the front 16 layers. Since only events where electron pairs pass through three or more silicon strips are used for analysis, there are no tungsten sheets in the last two layers. The reason there are no tungsten sheets in the last two layers here is that only events in which electron pairs pass through three or more silicon sheets can be used in the analysis. The thicknesses of the tungsten sheets are 0.03 cm for the front 12 layers and 0.18 cm for the following 4 layers, which correspond to 3% and 18% of the γ-ray radiation length, respectively. The combination of the thicknesses has been determined by balancing the angular resolution and the effective area. When an incident γ ray causes pair production at the thin sheet, the multiple scattering effects of electrons are suppressed compared to the case of thick sheets and thus the arrival direction can be estimated with high accuracy. On the other hand, a thicker sheet provides a larger effective area, which helps to detect high-energy γ rays.

Calorimeter

The calorimeter uses 96 (12×8) CsI(Tl) crystals, the each size of which is 2.7 cm $\times$ 2.0 cm $\times$ 32.6 cm. Since we know which scintillator the shower particles pass through, we can reconstruct the electromagnetic shower and thus reduce the CR background events.

Anti-coincidence detector

Plastic scintillators cover the tracker and the calorimeter. They allow identifying the background events due to CRs passing through from the side of the detector.

Fig. 5.7 show the angular resolution of the LAT detector as a function of energy, the low energy part of which roughly follow with the relation of $E^{-0.8}$ (Ackermann et al., 2012b). It should be noted that the angular resolution in the front 12 thin layers is about twice better than that of the thick 4 layers in the back.

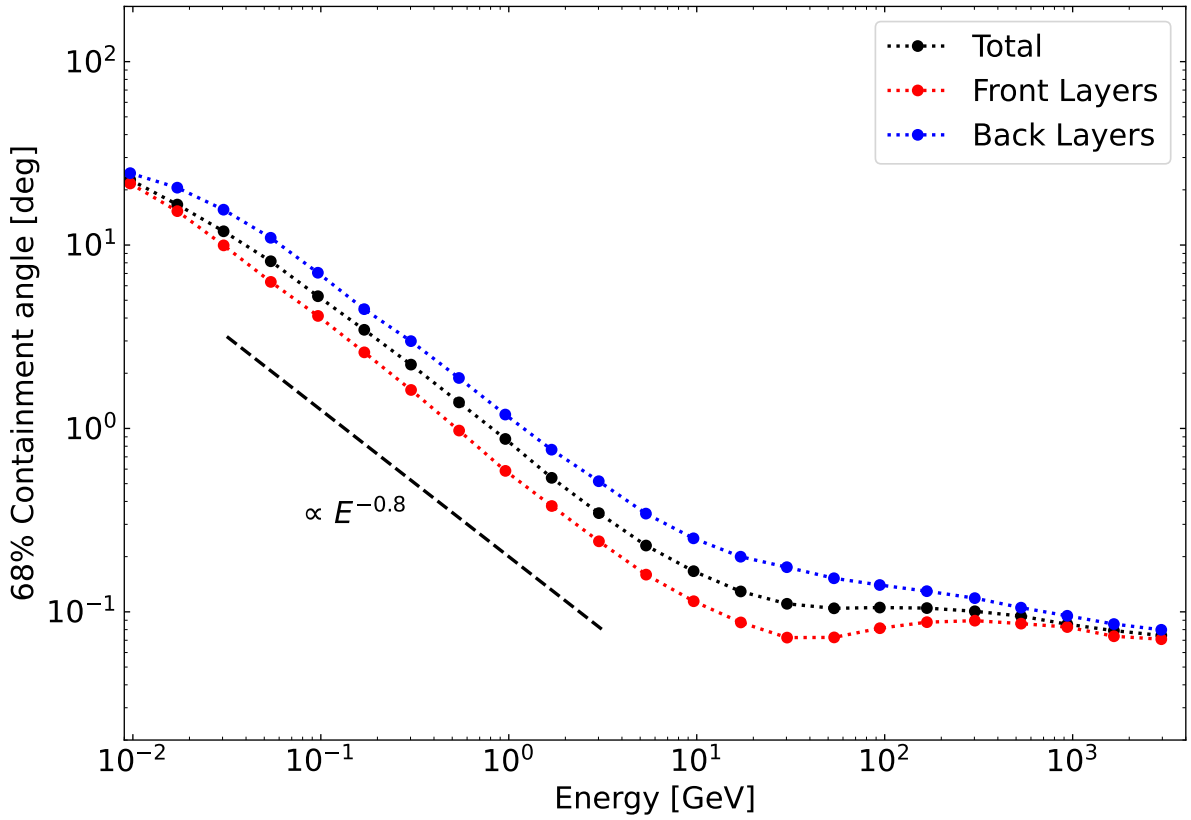

Figure 5.7: *Fermi*-LAT angular resolution as a function of energy (https://www.slac.stanford.edu/exp/glast/groups/canda/lat_Performance.htm). The black points represent the resolution for all events, while the red (blue) points represent the events where first pair production occurs in the front-thin (back-thick) layers of the tracker part.

5.2.2 Data selection and analysis

We analyze its 12-year data from 2008 August to 2020 August in the vicinity of SNR HB9. The standard analysis software, Science Tools (version v11r5p3[1]), is used. The "Source" selection criteria and instrument responses (`P8R2_SOURCE_V6`[2]) are chosen, considering a balance between the precision and photon-count statistics. The zenith-angle threshold is set to 90° to suppress the contamination of the background from the Earth rim. We employ the tool `gtlike` (in the binned mode), using a standard maximum likelihood method (Mattox et al., 1996), for spatial and spectral analyses. We choose a square region of 15° ×15° with the center coinciding with that of HB9 (Ra=75.25°, Dec=46.73°) as the region of interest (ROI) for the (binned) maximum likelihood analysis based on Poisson statistics. The pixel size is 0.1°.

The source spatial-distribution model includes all the sources in the fourth Fermi catalog (4FGL; Abdollahi et al., 2020) within the ROI and the two diffuse backgrounds, the Galactic (`gll_iem_v7.fits`) and extragalactic (`iso_P8R3_SOURCE_V2_v1.txt`) diffuse emissions. Regarding the emission of the SNR shell, Araya (2014) and Sezer et al. (2019) concluded that the radio template produced with the 4850 MHz radio continuum data from the Green Bank Telescope (Condon et al., 1994) is the best spatial model. Accordingly, we use the radio template provided in the Science Tools as the spatial model. In the fitting of the maximum likelihood analysis, all spectral parameters of HB9 SNR itself, 4FGL sources (Abdollahi et al., 2020) located within 5° from the center of HB9, and the two diffuse backgrounds are allowed to vary freely. We do not use the data below 1 GeV in this analysis since the fitting results of delayed γ-ray emission in this band suffer from the systematic uncertainty in the Galactic diffuse background model (Ackermann et al., 2012a). Note that the flux of the Galactic diffuse emission at the molecular cloud region is larger in this energy range than that of the delayed γ-ray emission from HB9, which will be estimated in Section 5.4.

The significance of a source is represented in this analysis by the Test Statistic (TS) defined as $-2\log(L_0/L)$, where L_0 and L are the maximum likelihood values for the null hypothesis and a model including additional sources, respectively (Mattox et al., 1996). The detection significance of the source can be approximated as $\sqrt{\mathrm{TS}}$ when the number of counts is sufficiently large.

5.3 Results

5.3.1 Morphology study

Figures 5.8 a and c show the background-subtracted γ-ray TS map created from the *Fermi*-LAT 12-year data above 1 GeV, where the background model consists of the Galactic and isotropic extragalactic emissions and the contributions from the known Fermi sources (see the previous subsection). The map is overlaid with cyan contours of the ^{12}CO ($J = 1 - 0$) line emission from the Dame survey data (Dame et al., 2001), which are integrated over a velocity range between

[1] https://fermi.gsfc.nasa.gov/ssc/data/analysis/software
[2] https://fermi.gsfc.nasa.gov/ssc/data/Cicerone/

-10.4 and $+2.6$ km s^{-1}, and also green contours of 1420 MHz radio continuum emission obtained from the CGPS survey with DRAO (Taylor et al., 2003). In Fig. 5.8 c, no significant emission from the SNR shell was found, which is consistent with the fact that the SNR spectrum has a cutoff below 10 GeV (Araya, 2014). Fig. 5.8 b is a similar γ-ray TS map to Fig. 5.8 a, but with the contribution from the SNR shell is additionally subtracted, for which we use the 4850 MHz radio-template model as a spatial model and assume a simple power-law spectrum. The γ-ray excess in Fig. 5.8 b and c appears to be more extended than the point source J0506.5+4546 reported in the previous study and rather spatially coincident with the CO line emission.

We test whether the γ-ray (> 1 GeV) spatial distribution is correlated with CO line emissions using the likelihood method. The ^{12}CO ($J = 1 - 0$) line image exhibits two distinctive regions (thus two molecular clouds), designated as R1 and R2 (Figure 5.8). For the test, we create a CO template for each of R1 and R2, which is made from the ^{12} CO ($J = 1-0$) line image (Dame et al., 2001) integrated over a velocity range between -10.4 and $+2.6$ km s^{-1} and cut with a threshold of > 4.5 K km s^{-1} (cyan thick-line contours in Figure 5.8). We assume the γ-ray spectra of the cloud regions and HB9 SNR shell to follow a simple power-law function of $dN/dE \propto E^{-\Gamma}$. Here, (i) the background model (the null hypothesis) consists of the radio template for the HB9 SNR shell as well as the Galactic and extragalactic diffuse emissions and 4FGL sources (Abdollahi et al., 2020). To compare spatial models, we use the Akaike information criterion (AIC; Akaike, 1974) defined as $2k - 2\log(L)$, where k is the number of the estimated parameters in the model. Consequently, we find that the model with the smaller AIC value is favored and that the better model gives a larger ΔAIC ($= (\mathrm{AIC})_0 - (\mathrm{AIC})_\mathrm{m}$), where $(\mathrm{AIC})_0$ and $(\mathrm{AIC})_\mathrm{m}$ are the AIC values for the null hypothesis and a model including additional sources, respectively. When we apply the CO template models to the two cloud regions (ii), ΔAIC is found to be 44.4, indicating a significant correlation between the γ-ray and ^{12} CO ($J = 1 - 0$) line emissions (Table 5.1). Since the γ-ray emission from R1 spatially coincides with PS J0506.5+4546 reported by Sezer et al. (2019), we also apply a point source model to the same position as PS J0506.5+4546, instead of the CO template model of R1 (iii). The resultant AIC is marginally (1.3σ level) improved from the case with the CO template. As a result, the γ-ray emission from R1 is consistent with PS J0506.5+4546, while R2 is newly detected with a statistical significance of 6.1σ in this study.

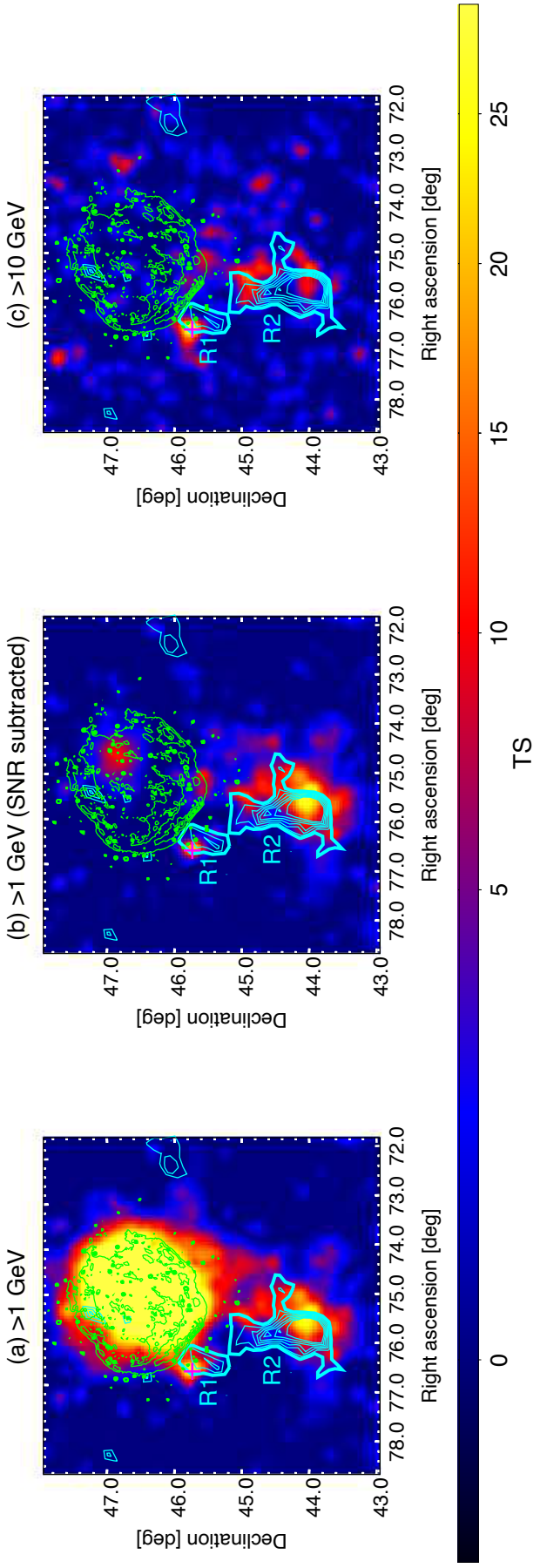

Figure 5.8: γ-ray TS maps in the vicinity of SNR HB9 observed with the *Fermi*-LAT. All maps are given with square bins of 0.05°, and Gaussian smoothing with a kernel $\sigma = 0.1°$ are applied. The energy ranges are (Panels a and b) 1 to 500 GeV and (c) 10 to 500 GeV. The subtracted background consists of (a and c) the Galactic and extragalactic diffuse emissions and known γ-ray source contribution and (b) additionally the estimated γ-ray emission from the HB9 SNR shell (see text for detail). Green contours show the radio emission of SNR HB9 at 1420 MHz with DRAO (Taylor et al., 2003) and are linearly spaced in increments of 0.5 K from 5.5 K to 10.0 K. Cyan contours show the ^{12}CO (J=1-0) line intensity integrated over a velocity range between -10.4 and $+2.6$ km s^{-1} and are linearly spaced in increments of 1.0 K km s^{-1} from 4.5 to 10.5 K km s^{-1}. The two apparent CO-emission regions (R1 and R2) are indicated. The magenta cross in each panel indicates the position of PS J0506.5+4546 (Sezer et al., 2019).

Table 5.1: Likelihood test results for spatial models and resultant spectral parameters of HB9 SNR shell and the two cloud regions, using the energy range of 1–500 GeV. The following three models are considered: (i) the background model (null hypothesis); (ii) additionally including γ-ray emission from R1 and R2 estimated by the CO template model (see text); and (iii) assuming a point-source model, where the position of the source is the same as PS J0506.5+4546 (Sezer et al., 2019), for R1 instead of the CO template model, while the CO template as in (ii) for R2. All sources of interest are fitted with a simple power-law function of $dN/dE \propto E^{-\Gamma}$. The "Flux" and "$\sqrt{\mathrm{TS}}$" columns refer to the integral flux in the energy band of 1–500 GeV in $10^{-10}\mathrm{cm}^{-2}\mathrm{s}^{-1}$ and the statistical significance (σ) of each source approximated as $\sqrt{\mathrm{TS}}$, respectively.

		R1			R2			HB9 SNR itself		
Model	ΔAIC	Flux	Γ	$\sqrt{\mathrm{TS}}$	Flux	Γ	$\sqrt{\mathrm{TS}}$	Flux	Γ	$\sqrt{\mathrm{TS}}$
(i)	0	-	-	-	-	-	-	24.9 ± 2.1	2.54 ± 0.06	13.2
(ii)	44.4	2.0 ± 0.8	1.84 ± 0.18	4.5	4.8 ± 1.2	1.84 ± 0.14	6.1	24.3 ± 2.1	2.55 ± 0.10	12.8
(iii)	58.2	1.3 ± 0.5	1.77 ± 0.18	5.8	4.8 ± 1.2	1.84 ± 0.14	6.1	24.5 ± 2.1	2.54 ± 0.10	13.0

5.3.2 Spectral results

We extract *Fermi*-LAT energy spectra from the radio SNR shell region and two regions R1 and R2, individually, using the CO template model for the cloud regions. Figure 5.9 shows the resultant spectra for an energy range between 1 and 500 GeV. We find that the obtained *Fermi*-LAT spectrum of the SNR shell is consistent with the γ-ray spectrum reported by Araya (2014) (Figure 5.9). The respective best-fit parameters are summarized in Table 5.1. Here, a potential concern about the spectrum of R1 is that our assumption of diffuse γ-ray spatial distribution may not be appropriate, given the spatial proximity with the already identified point source PS J0506.5+4546 (Figure 5.8). However, the discrepancy of the determined spectral properties (flux and index) between the results of the two spatial-distribution models is smaller than the 1σ uncertainty (Table 5.1). Therefore, we conclude that the difference in the results due to the difference between the assumed spatial distributions is not significant. We note that the power-law index of R1 is consistent with that of PS J0506.5+4546 reported by Sezer et al. (2019).

As mentioned in Sect. 5.2.2, the uncertainty of the Galactic diffuse background model may affect the spectral results. Here, we examine the spectral variations due to the background model parameters (normalization and index). We perform the likelihood fitting in the following four cases for the Galactic diffuse emission:

- both normalization and index are free parameters,
- only normalization is a free parameter,
- only index is a free parameter,
- both normalization and index are fixed.

Fig. 5.10 shows the energy spectra of the cloud regions obtained with those settings. The data point at 1 GeV fluctuates by a 1.5σ level of statistical error, while the rest of the points are not affected significantly. The resultant systematic variety of the spectral fitting results is at most a 1σ level of statistical error. Thus, we conclude that the systematic uncertainty on the background model is not critical in the modelling.

5.4 Spectral modelling and its implication

In this work, we explore the possibility that the R1 and R2 are attributed to the delayed γ-ray emission from molecular clouds illuminated by the CRs accelerated in HB9. In the following section, we calculate the delayed γ-ray spectra in the molecular cloud regions, R1 and R2, using the method described in Section 5.4.1, and try to fit the observed spectra of the cloud regions and the SNR shell simultaneously. According to Araya (2014), once the γ-ray spectrum of the SNR shell is modeled with the hadronic emission, it would require enormous explosion energy of supernova or a dense density of the interstellar medium (ISM). Hence, we assume that the γ-ray emission in the SNR shell originates mainly from the leptonic processes. On the other hand, we consider two cases for the origin of γ-ray emissions from the cloud regions: one where the leptonic emission dominates (Leptonic-dominated model), and the other where the hadronic

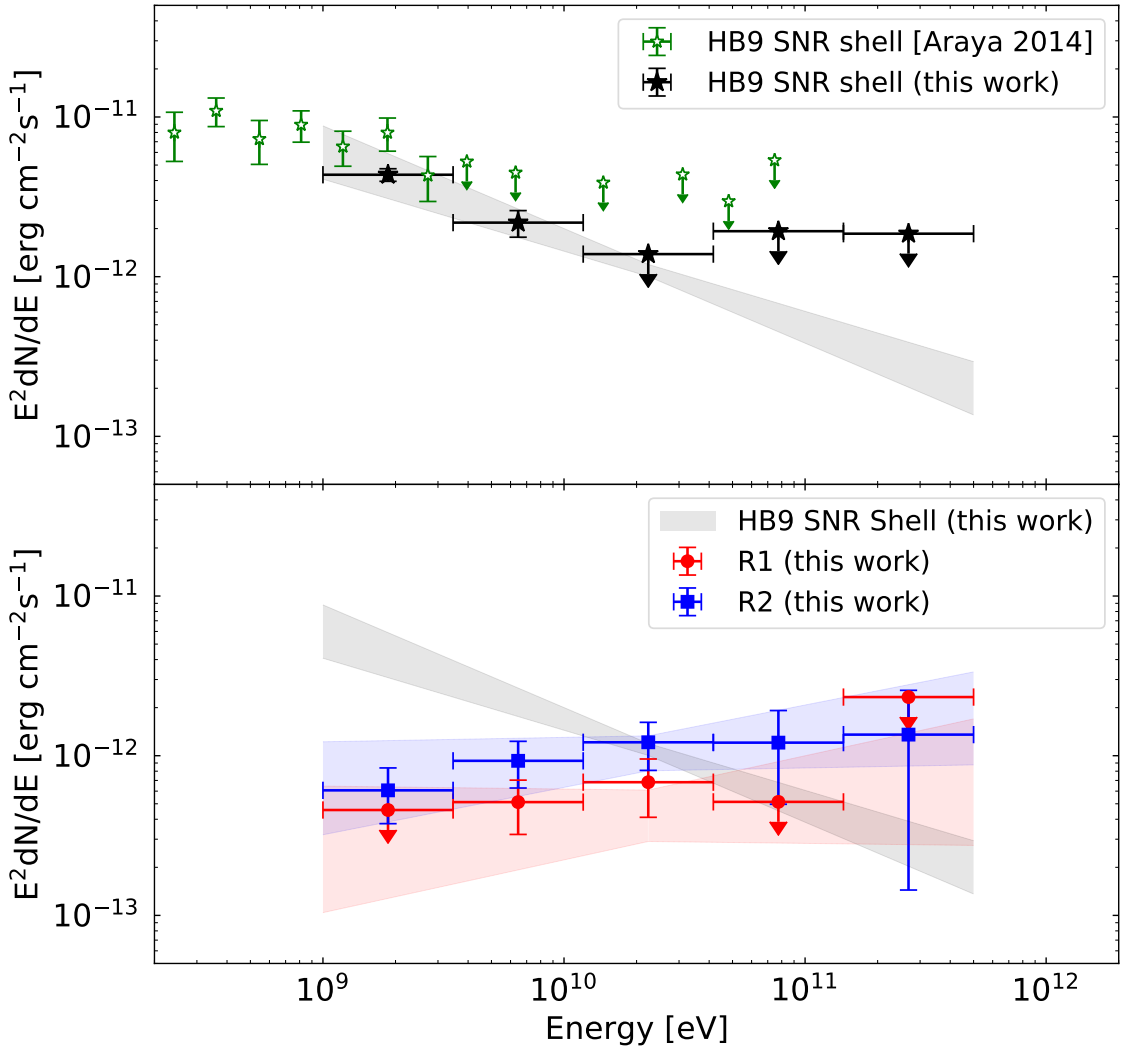

Figure 5.9: Spectral energy distributions measured with the *Fermi*-LAT (data points) and fit results in the γ-ray band. **Top**: Black and open green stars show the data of the SNR shell obtained in this work and Araya (2014), respectively. **Bottom**: Red and blue data represent the spectra of cloud regions R1 and R2, respectively. Also shown as the shaded black region is the fit result of the SNR shell.

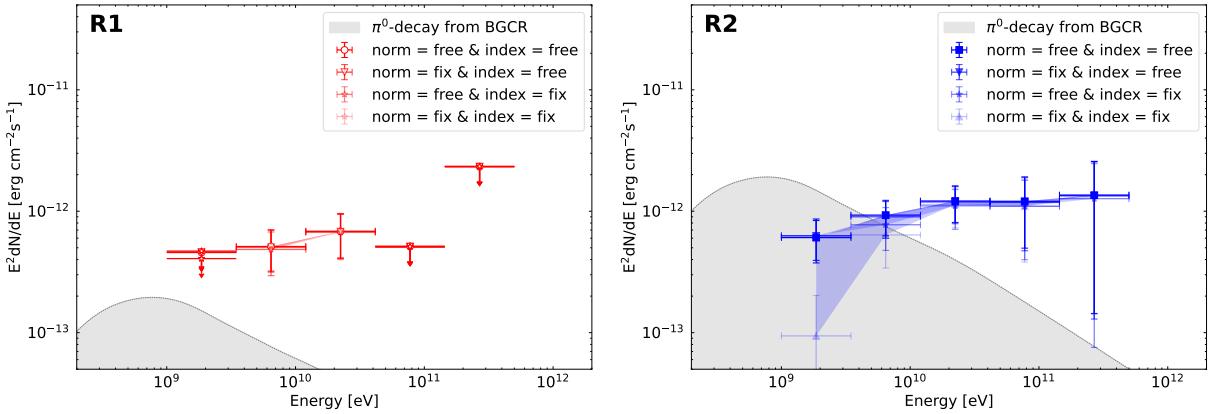

Figure 5.10: Comparison in energy spectra of the cloud regions obtained with several background model parameters. Also shown the gray shaded region is the hadronic emission from the background CRs, which will be derived in Sect. 5.4.

emission dominates (Hadronic-dominated model) in the GeV band. We present the results of the modeling in Sect. 5.4.2 and discuss implications on the model parameters in Sect. 5.4.3.

5.4.1 Modeling of delayed γ-ray emission

The energy spectra of the γ-ray emissions from the molecular clouds around HB9 are calculated following the method proposed by Gabici et al. (2009) and Ohira et al. (2011). They considered the escape process of the CR protons, which are accelerated by an SNR, from a shock front into interstellar space during the Sedov phase. Escaped CR protons emit high-energy γ-rays via π^0 production through pp collision in molecular clouds in the vicinity of the HB9 SNR. In addition, we also discuss the contribution from inverse Compton (IC) scattering and non-thermal bremsstrahlung from CR electrons escaping from the SNR. We evaluate later in this section the expected γ-ray fluxes from the R1 and R2 regions in conjunction with the energy spectra of the escaped CR protons and electrons.

The radio continuum contours (Figure 5.8) show a circular symmetric morphology of SNR HB9, suggesting it has probably maintained a spherically symmetric structure throughout its evolution. Therefore, we assume that the SNR shell itself and the escaped CR distribution are spherically symmetric. Based on X-ray observations, the energy of the supernova explosion ($E_{\rm SN}$) was estimated to be (0.15–0.30)$\times 10^{51}$ erg, and the relation between the explosion energy and the hydrogen density of ISM ($n_{\rm ISM}$) was also estimated as $(E_{\rm SN}/10^{51}\ {\rm erg})({\rm n_{ISM}}/1\ {\rm cm^{-3}})^{-1} = 5$ (Leahy & Tian, 2007). In this work, we adopt 0.3×10^{51} erg as the explosion energy, in which case the density is given as 0.06 cm^{-3}. If the initial velocity of the blast wave was $u_{\rm sh,0} = 10^9$ cm s^{-1}, HB9 entered the Sedov phase at the age $t_{\rm Sedov} = 3.6 \times 10^2$ yr when its radius was 3.6 pc. Given that the observed radius of HB9 is ~ 10 pc, which is larger than 3.6 pc, HB9 must be already in the Sedov phase. Leahy & Tian (2007) estimated the dynamical age of SNR HB9 to be 6.6×10^3 yr, which we adopt as the age of the SNR in this discussion.

First of all, let us model the energy spectrum of CR protons. During the Sedov phase, the maximum energy of the CR protons accelerated at the SNR shock is determined by the timescale

of escape from the acceleration region, and decreases with time (Ptuskin & Zirakashvili, 2005; Caprioli et al., 2009; Ohira et al., 2010). The temporal evolution of the maximum energy depends on non-linear processes, such as amplifying the magnetic field at the shock, which is still theoretically unclear. Thus, we adopt the phenomenological power-law dependence of the cutoff energy $E_{\rm esc}$ of the proton spectrum at the SNR shock on the age t of the SNR, as discussed by Gabici et al. (2009) and Ohira et al. (2010):

$$E_{\rm esc}(t) = E_{\rm max}\left(\frac{t}{t_{\rm Sedov}}\right)^{-\alpha}, \tag{5.2}$$

where $E_{\rm max}$ is the maximum energy of the CR protons at $t_{\rm Sedov}$ and is set to 3 PeV, and α is the power-law index that is determined so that the current maximum energy ($E_{\rm now}$) is equal to $E_{\rm esc}(t)$ at the current age $t_{\rm age} = 6.6 \times 10^3$ yr (Leahy & Tian, 2007). Here, we adopt $E_{\rm now} = 300$ GeV, which is the same value as that of the electrons at the SNR shell at present (see also Section 5.4.2). However, in general, the maximum energy of CRs in the SNR shell depends on the particle species and is determined by the balance between acceleration and escape from the shell or energy loss due to radiative cooling. Araya (2014), assuming that radiative cooling limits the maximum CR electron energy, estimated that the gyro factor would be a too large value of ~ 660 compared to the standard SNR value. In such a case, as shown in Ohira et al. (2012), the escape process determines both the highest energies of CR electrons and protons. Therefore, according to Ohira et al. (2012), we can assume that the current maximum energy of electrons is the same as that of the protons. The timescale for a particle with the energy E, $t_{\rm esc}(E)$, to escape into interstellar space from the supernova explosion, as a function of the particle energy E is given by

$$t_{\rm esc}(E) = t_{\rm Sedov}\left(\frac{E}{E_{\rm max}}\right)^{-1/\alpha}. \tag{5.3}$$

The distribution function $f_{p,\rm out}$ per unit energy per unit volume of the CR protons escaping into interstellar space can be obtained by solving the transport equation,

$$\frac{\partial f_{p,\rm out}}{\partial t}(t,r,E) - D_{\rm ISM}(E)\Delta f_{p,\rm out}(t,r,E) = q_{p,s}(t,r,E), \tag{5.4}$$

where t is the age of the SNR, r is the distance from the SNR center, $D_{\rm ISM}$ is the diffusion coefficient in the ISM, and $q_{p,s}$ is the injection rate of the CR protons from the SNR shock into interstellar space per unit energy, unit volume, and unit time. We adopt the following form of the diffusion coefficient $D_{\rm ISM}$:

$$D_{\rm ISM}(E) = D_0\left(\frac{E}{10\ {\rm GeV}}\right)^{\delta}, \tag{5.5}$$

where D_0 is the diffusion coefficient of CRs at $E = 10$ GeV. We assume $D_0 = 3 \times 10^{28}$ cm^2 s^{-1} and the index $\delta = 1/3$, the latter of which is consistent with the Galactic mean expected in the CR propagation model (e.g., Blasi & Amato, 2012). Following Ohira et al. (2011), we assume

that CRs with the energy E are injected from the SNR shell $R_{\rm esc} = u_{\rm sh,0} t_{\rm Sedov} (t_{\rm esc}(E)/t_{\rm Sedov})^{2/5}$ at $t = t_{\rm esc}(E)$. We also assume that the energy spectrum of the injected CRs is monochromatic with the energy E and that particles start to escape at any given time (see equation (5.3)). Taking account of these assumptions, the injection rate $q_{\rm s}$ is given by

$$q_{p,s} = \frac{N_{\rm esc}(E)}{4\pi r^2} \delta(r - R_{\rm esc}(E)) \delta\left(t - t_{\rm esc}(E)\right), \tag{5.6}$$

where r is the displacement from the center of the SNR, $N_{\rm esc}$ is the spectrum of all the CRs that have escaped from the SNR up to the present time. In this work, we assume that the total energy of the escaped CR protons is proportional to the explosion energy of the supernova explosion $E_{\rm SN}$, namely

$$\int_{E_{\rm now}}^{E_{\rm max}} E N_{\rm esc}(E) dE = \eta E_{\rm SN}, \tag{5.7}$$

where η is the acceleration efficiency coefficient. Here, we assume that $N_{\rm esc}$ is a power-law function of E with an index $p_{\rm esc}$. According to Ohira et al. (2010), it is shown that the index $p_{\rm esc}$ of CRs escaping from the SNR is steeper than the index $p_{\rm SNR}$ of CRs confined in the SNR shell. While the value of $p_{\rm esc}$ is determined by the time evolution of the maximum energy of CRs at the SNR shell and the CR production rate, we treat $p_{\rm esc}$ as a parameter. By assuming a power-law form of $N_{\rm esc}$, the integral of the equation (5.7) yields,

$$N_{\rm esc}(E) = \begin{cases} \frac{\eta(2-p_{\rm esc})E_{\rm SN}}{E_{\rm now}^2} \times \left[\left(\frac{E_{\rm max}}{E_{\rm now}} \right)^{2-p_{\rm esc}} - 1 \right]^{-1} \times \left(\frac{E}{E_{\rm now}} \right)^{-p_{\rm esc}} & p_{\rm esc} \neq 2 \\ \frac{\eta E_{\rm SN}}{\ln(E_{\rm max}/E_{\rm now})} E^{-2} & p_{\rm esc} = 2 \end{cases}. \tag{5.8}$$

The propagation models (Obermeier et al., 2012; Yuan et al., 2017) expect the spectral index of particles escaped from Galactic CR origin to be ~ 2.4, which is adopted as a fiducial parameter of $p_{\rm esc}$ in this modeling. The effect of this parameter on the modeling will be discussed in Section 5.4.3. The energy spectrum of the escaped CRs is obtained by combining the transport equation (5.4) and equations (5.6) and (5.8). Specifically, the solution of equation (5.4) for $E > E_{\rm esc}(t)$ is given by, according to Ohira et al. (2011)

$$f_{\rm p,out}(t, r, E) = \frac{N_{\rm esc}(E)}{4\pi^{3/2} r R_{\rm esc} R_{\rm d,p}} \left[\exp\left(-\frac{(r - R_{\rm esc})^2}{R_{\rm d,p}^2} \right) - \exp\left(-\frac{(r + R_{\rm esc})^2}{R_{\rm d,p}^2} \right) \right] \tag{5.9}$$

where $R_{\rm d,p}$ is the diffusion length of a CR proton with the energy E, defined as

$$R_{\rm d,p} \equiv \sqrt{4 D_{\rm ISM}(E) \left(t - t_{\rm esc}(E)\right)}. \tag{5.10}$$

In order to obtain the energy spectrum of CR electrons $f_{e,\rm out}$, it is required to solve the following transport equation with radiative cooling:

$$\frac{\partial f_{e,\rm out}}{\partial t}(t, r, E) - D_{\rm ISM}(E) \Delta f_{e,\rm out}(t, r, E) + \frac{\partial}{\partial E} \left(P(E) f_{e,\rm out}(t, r, E) \right) = q_{e,s}(t, r, E), \tag{5.11}$$

where $P(E)$ is an energy loss rate of CR electrons, and $q_{e,s}$ is an injection rate of CR electrons, which can be written as

$$q_{e,s} = K_{\rm ep} q_{p,s}, \tag{5.12}$$

where $K_{\rm ep}$ is the ratio of the total energy of CR electrons to CR protons. As a cooling process, we consider only the synchrotron radiation, which is the most dominant effect for electrons with energies above $\mathcal{O}$(GeV) (see Sect. 1.3).

The temporal evolution of the maximum energy of CR electrons in the SNR shell is different from that of protons due to radiative cooling. After entering the Sedov phase, the maximum energy of CR electrons is first determined by the balance between the radiative cooling and acceleration, and, after that, by the balance between acceleration and escape from the SNR shell, similar to the proton (Ohira et al., 2012). When these two phases switch, CR electrons start to escape from the SNR shell and be injected into the interstellar space. In this work, we parametrize this switching time t_e as follows:

$$t_e = \xi_e t_{\rm Sedov}, \tag{5.13}$$

where ξ_e is the time in the unit of $t_{\rm Sedov}$ at which the electron starts to escape, and in the limit of $\xi_e \to 1$, the injection is identical to that of the proton (see equation (5.6)). After t_e, since the time evolution of the maximum energy of electrons is expected same as that of the proton (Ohira et al., 2012), we use equations (5.2) and (5.3). Originally, ξ_e is given based on the assumed environment (Ohira et al., 2012), but we set $\xi_e = 1$ to consider the limit where the γ-ray flux of leptonic emissions is maximized in this modeling. The solution to equation (5.11) can be derived using the method described in Appendix B.1.

Considering only the synchrotron radiation as the cooling process (i.e. $P(E) = Q_{\rm syn}E^2$, see equation (B.7) of Appendix B.1 for details), the solution for $E_{\rm esc}(t) < E < E_{\rm esc}(t_e)$ can be written as:

$$f_{\rm e,out}(t, r, E) = \frac{K_{\rm ep} N_{\rm esc}(E_c)}{4\pi^{3/2} r R_{\rm c} R_{\rm d,e}} \frac{E_c^2}{E^2} \frac{1}{1 - Q_{\rm syn} t_c E_c/\alpha} \left[\exp\left(-\frac{(r - R_{\rm c})^2}{R_{\rm d,e}^2} \right) - \exp\left(-\frac{(r + R_{\rm c})^2}{R_{\rm d,e}^2} \right) \right]. \tag{5.14}$$

Once the energy spectrum of the CRs has been obtained, the flux of the γ-ray emission is calculated based on the neutral pion decay process in molecular clouds for CR protons, and inverse Compton scattering and the relativistic bremsstrahlung for CR electrons. Here we assume that the molecular cloud is "optically" thin for the CRs and that the cloud consists of a spatially uniform gas with the total mass $M_{\rm cl}$. For simplicity, we also assume that the molecular cloud is a sphere of radius $R_{\rm cl}$. The spectrum of CRs in the molecular cloud can be written as follows:

$$N_{\rm cl}(E) = \int_{d_{\rm cl} - R_{\rm cl}}^{d_{\rm cl} + R_{\rm cl}} \frac{\pi r}{d_{\rm cl}} \left(R_{\rm cl}^2 - (r - d_{\rm cl})^2 \right) f_{s,\rm out}(r) dr, \tag{5.15}$$

where $d_{\rm cl}$ is a distance to the center of the molecular cloud from the center of the SNR, and s is species (e=electron, p=proton). Note that, for the parameters used in this work, a spatial gradient of the CR distribution is not important, and only a few % difference occurs even if

Table 5.2: Fiducial parameters used to calculate the model spectra

SNR parameters	Symbol		
SN explosion energy	$E_{\rm SN}$	0.3×10^{51} erg	
Initial shock velocity	$u_{\rm sh}$	10^9 cm s^{-1}	
Age of the SNR	$t_{\rm age}$	6.6×10^3 yr	
Distance to the SNR		0.8 kpc	
Acceleration efficiency†	η	0.1 (0.003)	
Electron to proton flux ratio†	$K_{\rm ep}$	0.02 (1)	
Maximum CR energy at $t = t_{\rm Sedov}$	$E_{\rm max}$	3 PeV	
Current maximum energy of CRs	$E_{\rm now}$	300 GeV	
Magnetic field in the SNR	$B_{\rm SNR}$	8 μG	
Particle index in the SNR	$p_{\rm SNR}$	2.0	
Particle index after escaping from SNR	$p_{\rm esc}$	2.4	
ISM parameters	Symbol		
Number density	$n_{\rm ISM}$	0.06 cm^{-3}	
Diffusion coefficient at $E = 10$ GeV	D_0	3×10^{28} cm^2 s^{-1}	
Index of dependence on E of diffusion	δ	1/3	
Magnetic field in ISM	$B_{\rm ISM}$	3 μG	
Cloud parameters	Symbol	R1	R2
Distance to the cloud from SNR	$d_{\rm cl}$	17.8 pc	39.4 pc
Radius of the cloud	$R_{\rm cl}$	3.6 pc	7.0 pc
Average hydrogen number density†	$n_{\rm H}$	150 (1000) cm^{-3}	200 (1000) cm^{-3}
Mass of the cloud†	$M_{\rm cl}$	730 (4800) $M_\odot$	7100 (36000) $M_\odot$
Magnetic field in cloud	$B_{\rm cl}$	3 μG	

† The values in parentheses are used in the leptonic-dominated model.

$N_{\rm cl} \sim 4\pi R_{\rm cl}^3 f_{s,{\rm out}}(d_{\rm cl})/3$ is used.

The energy spectrum of CRs in the SNR shell, $N_{s,{\rm shell}}$, is calculated consistently with the distribution function of escaped particles. By using the normalization equation (5.7) same as equation (5.8), the spectra at $E < E_{\rm esc}$ of CR protons and electrons in the SNR shell can be written as

$$N_{p,{\rm shell}}(E) = N_{\rm esc}(E_{\rm now}) \left(\frac{E}{E_{\rm now}} \right)^{-p_{\rm SNR}}, \tag{5.16}$$

and

$$N_{e,{\rm shell}}(E) = K_{\rm ep} N_{\rm esc}(E_{\rm now}) \left(\frac{E}{E_{\rm now}} \right)^{-p_{\rm SNR}}, \tag{5.17}$$

respectively, where $p_{\rm SNR}$ is the index of CRs that have not yet escaped from the SNR shell. We fix $p_{\rm SNR} = 2$ in this work because the index $p_{\rm SNR}$ of HB9 has been well determined by observations of radio continuum (see Sect. 5.1.2).

To calculate the spectra of non-thermal emissions, we use the radiative code *naima* (Zabalza, 2015). As for the seed photon fields in the IC process, we assume the cosmic microwave background and Galactic far-infrared (FIR) radiation, the latter of which was not considered in the modeling of Araya (2014). The energy density of the FIR radiation is estimated to be 0.099 eV cm^{-3} at $T = 27$ K, using the model in the GALPROP package (Porter et al., 2008).

5.4.2 Application to the cloud regions around HB9

In order to calculate the γ-ray flux at the cloud regions, R1 and R2, the distance between the molecular clouds and SNR is required. By fitting the CO intensity map integrated over the velocity range between -10.4 and $+2.6$ km s^{-1} with a two-dimensional symmetric Gaussian, we determine the center positions of clouds R1 and R2 to be (l, b) = (161.8 $\pm$ 0.1°, 2.8 $\pm$ 0.1°) and (162.6 $\pm$ 0.1°, 1.6 $\pm$ 0.1°), respectively, in the galactic coordinates. Then, the projected distances between the centers of the SNR and clouds R1 and R2 are calculated to be 17.8 and 39.4 pc, respectively, using the distance to the SNR from the Earth of 0.8 kpc (Sect. 5.1.2 and Table 5.2). We treat these projected distances as the actual distances in our discussion, although they should be considered as the lower limit of the true distances in reality due to the uncertainty of their locations along the line of sight. We also obtain the radii of the molecular clouds from the standard deviation of the fitted Gaussian, which are 3.6 pc and 7.0 pc for R1 and R2, respectively.

For the spectral modeling, the data points in the radio band for the HB9 SNR shell are obtained from the literature (Dwarakanath et al., 1982; Reich et al., 2003; Leahy & Tian, 2007; Roger et al., 1999; Gao et al., 2011), while the radio flux of the mean local background including the cloud region at a frequency of 865 MHz (Reich et al., 2003) is used as an upper limit for the cloud regions. In the X-ray band, only the thermal emission from the hot gas inside the shell has been detected, while non-thermal emission has not been measured (e.g, Leahy & Aschenbach (1995); Sezer et al. (2019)). We adopt the 0.1–2.5 keV flux of the thermal emission from HB9 (Leahy & Aschenbach, 1995) as an upper limit for the non-thermal emission in the energy band.

We fit the spectra of R1 and R2 under two assumptions, the leptonic-dominated and hadronic-dominated models, and simultaneously reproduce the spectrum of the SNR shell with the leptonic emission. The electron to proton flux ratio, $K_{\rm ep}$, is assumed to be 1 and 0.02 for the leptonic-dominated and hadronic-dominated models, respectively, the latter of which is consistent with the ratio in the local CR abundance (e.g., Aguilar et al., 2016).

Figure 5.11 and 5.12 show the results of the leptonic-dominated and hadronic-dominated model, respectively. The total electron energy and the magnetic field in the SNR shell are in agreement with those estimated by Araya (2014), while the electron maximum energy at the shell (corresponding to $E_{\rm now}$) is determined to be 300 GeV. Our obtained value of $E_{\rm now}$ is slightly lower than that derived in the previous study (Araya, 2014) because the FIR radiation as a seed photon in the IC process is newly taken into account in this work. In the leptonic-dominated model, the γ-ray emissions via a bremsstrahlung process of relativistic electrons dominate in the cloud regions, and thus the delayed γ-ray spectra for 1–500 GeV have a hard index of $\sim$ 1.3, which contradicts the observed one at the cloud regions (Figure 5.11). In the hadronic-dominated model (Figure 5.12), the hadronic emission reproduces well the observed spectra even though the assumed parameters in the calculation are typical ones for an SNR and ISM (Table 2). We note that the γ-ray flux from the background CRs is lower than the observed data at higher energy than $\sim$ 3 GeV (see the middle and right panels of Figure 5.12). This is consistent with the fact that the systematic fluctuation due to the model parameters of the

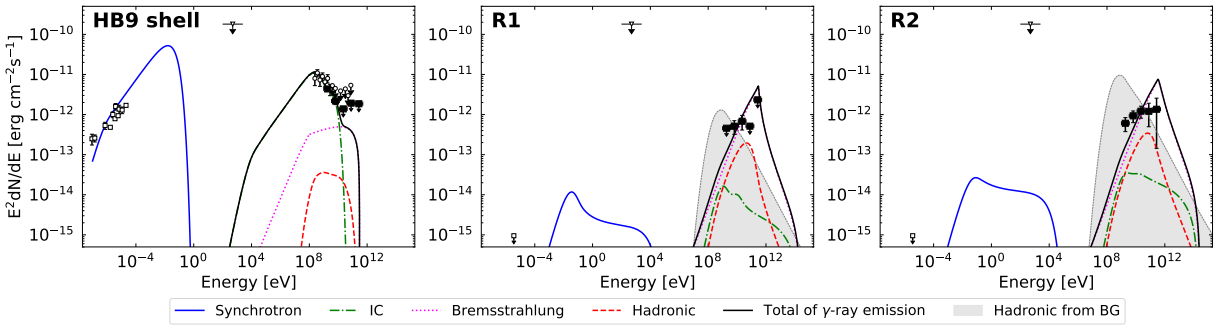

Figure 5.11: Broadband spectral energy distributions of the non-thermal emission from the HB9 shell and the cloud regions with the leptonic-dominated model, using the parameters tabulated in Table 5.2. The left, middle, and right panels show the results about the HB9 shell, R1 and R2, respectively. The radio and X-ray data are taken from Dwarakanath et al. (1982); Reich et al. (2003); Leahy & Tian (2007); Roger et al. (1999); Gao et al. (2011) and Leahy & Aschenbach (1995), respectively (see text for detail). The filled squares and open circles show the *Fermi*-LAT data derived in Section 5.3.2 and Araya (2014), respectively. The lines represent each component of the emission models: synchrotron (blue), electron bremsstrahlung (magenta), IC (green), neutral pion decay (red), and the total γ-ray emissions (black). In order to demonstrate how much of the Galactic diffuse background at the cloud regions, which may affect the systematic uncertainties in the *Fermi* analysis, we show the hadronic emission from the background CRs with the energy spectrum $J_{\rm CR}(E) = 2.2(E/{\rm GeV})^{-2.75}$ cm^{-2} s^{-1}GeV^{-1}sr^{-1} (e.g., Dermer, 1986) as the shaded grey region.

Galactic diffuse emission is small at $\gtrsim 3$ GeV, as shown in Fig. 5.10. By calculating the energy of the proton corresponding to the peak of photon spectra in each cloud region with the fiducial parameters, we estimate the epoch at which those protons escaped from the SNR shock by using equation (5.3). We then obtain $t_{\rm ref} \lesssim -5.8 \times 10^1$ yr for R1 and $\lesssim -6.3 \times 10^2$ yr for R2 dating back from now.

5.4.3 Accuracy of parameter determination

We investigate in the following procedure how the hadronic-dominated model curve varies depending on the input parameters and summarize the results in Figure 5.13. First, we evaluate

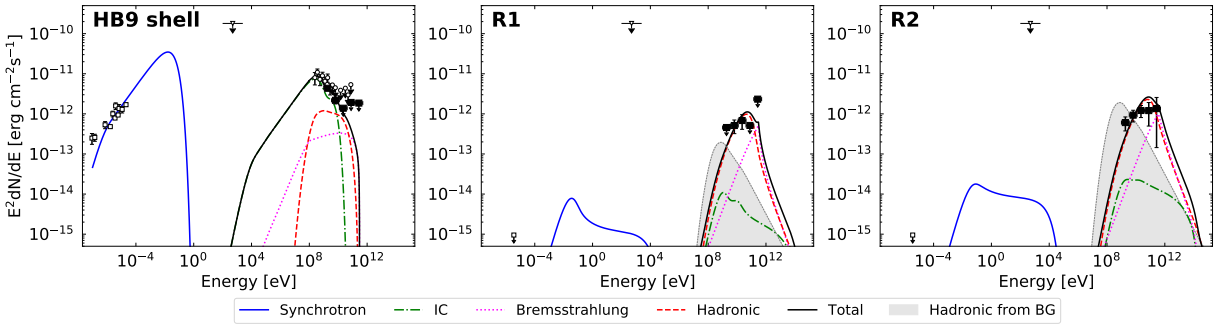

Figure 5.12: Same as Figure 5.11, but with the hadronic-dominated model.

the dependence of the model curve on D_0, which is the value of the diffusion coefficient at $E = 10$ GeV (Panels a and b in Fig. 5.13). The *Fermi*-LAT spectra obtained in this work are found to be well reproduced with the Galactic mean of $D_0 = 3 \times 10^{28}$ cm^2 s^{-1}. Orders of magnitude smaller D_0, in particular $D_0 = 3 \times 10^{26}$ cm^2 s^{-1}, however, clearly fail to reproduce the observed spectra. In the previous studies for other SNRs (e.g., Fujita et al., 2009), the estimated values of D_0 were ~ 10 times smaller than the Galactic mean, which were explained in conjunction with self-confinement caused by the generation of turbulent plasma waves (Wentzel, 1974; Fujita et al., 2011; D'Angelo et al., 2018). Our diffusion coefficient value, which is close to the Galactic mean, indicates that the excitation of such turbulent plasma waves at the distances to R1 and R2 is inefficient or that the wave damping has a significant effect. Second, we find that the model with either $\delta = 1/3$ or $1/2$ is preferred over that with $\delta = 0$ (Panels c and d in Fig. 5.13). Third, we also find that $E_{\rm max}$ above 10 TeV still explains the data points (Figures 5.13e and 5.13f). Given that there is a trend for a larger difference between the model curves in the higher energy band, future observations in the TeV band will provide results more sensitive to determine the δ and $E_{\rm max}$ parameters.

In order to verify that the Galactic mean value of the diffusion coefficient (D_0) is appropriate to explain the γ-ray spectra, we also try to model the γ-ray spectra, fixing D_0 at two orders of magnitude smaller $D_0 = 3 \times 10^{26}$ cm^2 s^{-1}. As can be seen in Figure 5.13(a, b), for smaller D_0, the spectrum shifts to the higher energy side. Also, as shown in Figure 5.13(e, f), the spectrum below $\mathcal{O}\left(10^{11}\right)$ eV does not depend much on $E_{\rm max}$. Therefore, the deviation of the spectrum in the lower energy band due to the small D_0 should be countered by δ dependence. Once we assume $\delta > 1.0$ while other parameters are kept the same as in Table 5.2, the model curves are roughly consistent with the observed γ-ray spectra (Figure 5.13(g, h)). However, $\delta > 1.0$ is inconsistent with the CR propagation model (e.g., Blasi & Amato, 2012). Thus, the small diffusion coefficient (i.e., $D_0 \sim 10^{26}$ cm^2 s^{-1}) is unlikely.

We have assumed $p_{\rm esc} = 2.4$ in the modeling so far, but the discussion on the diffusion coefficient may be affected by this parameter as well as δ. Here, we attempt to fit the observed spectra by considering two cases where a flatter ($p_{\rm esc} = 2.0$) or steeper ($p_{\rm esc} = 2.7$) index is assumed. Note that these assumptions are not favored by the propagation model as mentioned in Section 5.4.2. The results are shown in Figure 5.14 and 5.15. Although the model parameters except for $p_{\rm esc}$ and η are fixed at the values in Table 5.2, the observed spectra can be reproduced by giving a feasible value of $\eta = 0.3$ (0.05) for $p_{\rm esc} = 2.0$ (2.7) (Figure 5.14). Figure 5.15 shows the dependency on D_0 and δ for R2 as in Figure 5.13 (b) and (h). To explain the observed spectrum with the diffusion coefficient two orders of magnitude smaller $D_0 = 3 \times 10^{26}$ cm^2 s^{-1} than the Galactic mean, an unrealistic assumption that $\delta > 1.0$ is required for both cases of $p_{\rm esc} = 2.0$ and 2.7. This result is consistent with the case where $p_{\rm esc} = 2.4$, i.e., the diffusion coefficient of the Galactic mean value is preferred regardless of the assumption on $p_{\rm esc}$.

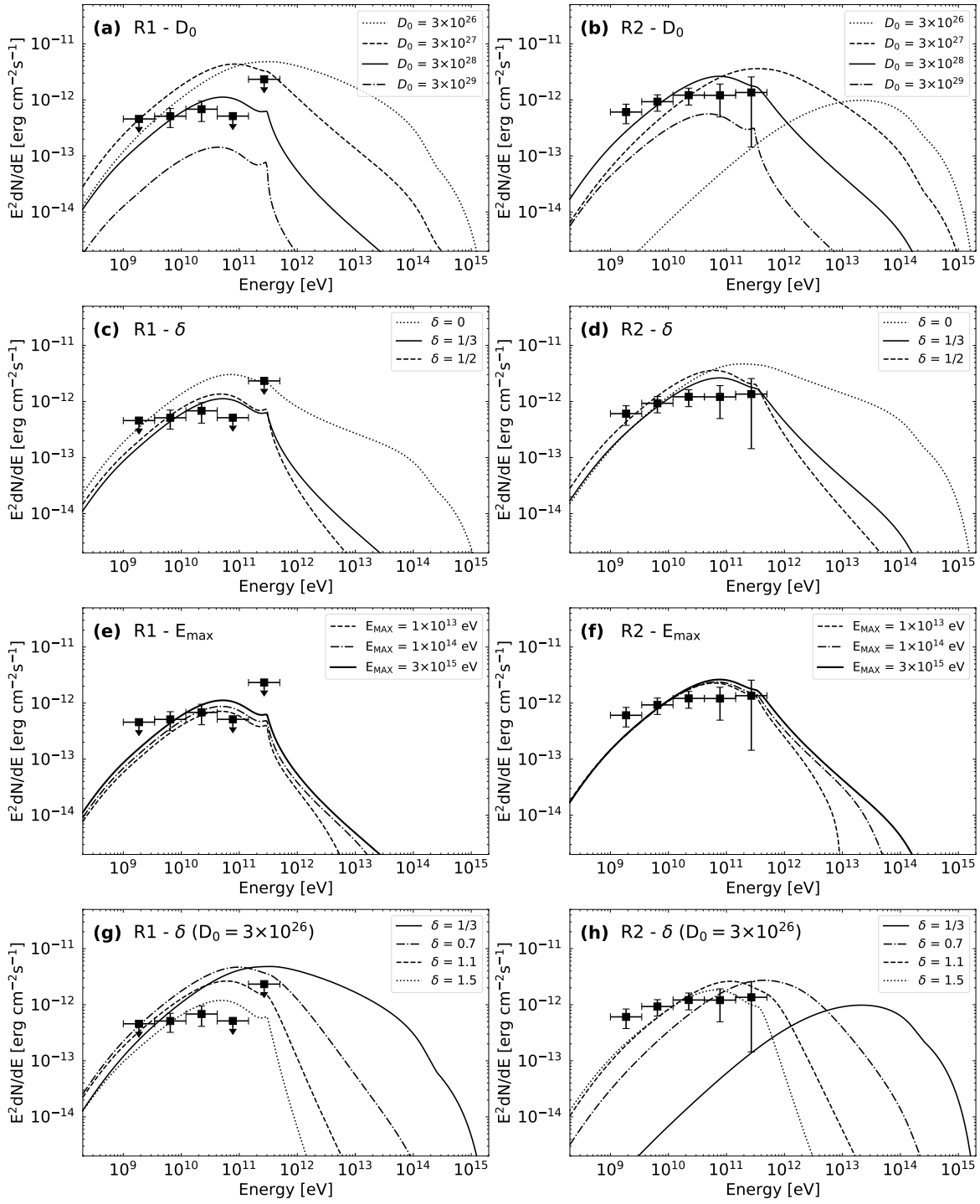

Figure 5.13: Input parameter dependency of the model. In panels (a–f), the left (a, c, e, g) and right (b, d, f, h) panels show the results about R1 and R2, respectively. **(a, b)** Dependency on D_0 (diffusion coefficient). Dotted, dashed, solid, and dot-dashed curves indicate the models with D_0 of 3×10^{26} cm^{2}s^{-1}, 3×10^{27} cm^{2}s^{-1}, 3×10^{28} cm^{2}s^{-1}, and 3×10^{29} cm^{2}s^{-1}, respectively. **(c, d)** Dependency on δ (degree of dependence of D_0 on the energy). Dashed, solid, and dot-dashed curves indicate the models with δ of 0, 1/3, and 1/2, respectively. **(e, f)** Dependency on $E_{\rm max}$ (maximum energy of the accelerated particles in the Sedov phase). Dashed, dot-dashed, and solid curves indicate the models with $E_{\rm max}$ of 1×10^{13} eV, 1×10^{14} eV, and 3×10^{15} eV, respectively. **(g, h)** Dependency on δ with D_0 of 3×10^{26} cm^{2}s^{-1}. Solid, dot-dashed, dashed, and dotted curves indicate the models with δ of 1/3, 0.7, 1.1, and 1.5, respectively.

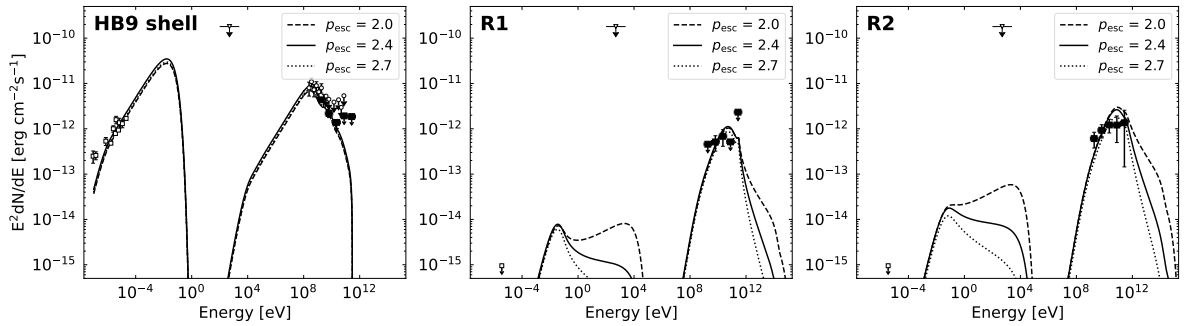

Figure 5.14: Energy spectra with the hadronic-dominated model under different assumptions on $p_{\rm esc}$. The dashed, solid, and dotted lines represent the model emissions with $p_{\rm esc}$ of 2.0, 2.4, and 2.7, respectively. The model with $p_{\rm esc} = 2.4$ is the same as in Figure 5.12, while for the models with $p_{\rm esc} = 2.0$ and 2.7, the acceleration efficiency is given to be $\eta = 0.3$ and 0.05, respectively.

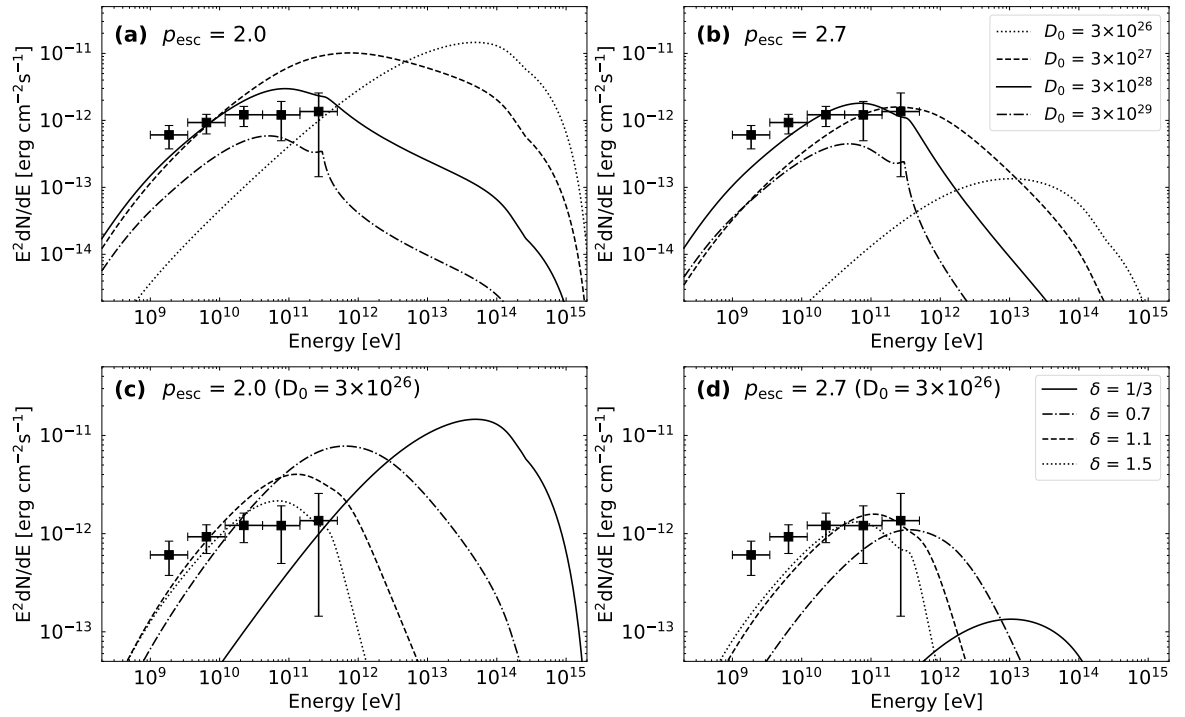

Figure 5.15: Input parameter dependency of the model in the R2 region when $p_{\rm esc} = 2.0$ (left) and 2.7 (right) are assumed. **(a, b)** Dependency on D_0 (diffusion coefficient). **(c, d)** Dependency on δ fixing at $D_0 = 3 \times 10^{26}$ cm^{2}s^{-1}.

Chapter 6

Discussion

With the delayed γ-ray emissions introduced in the previous chapter, we try to model the two SNRs: SNR G106.3+2.7 (Sect. 6.1) and G335.2+0.1 (Sect. 6.2). The modeling results in both cases will be discussed by comparing the results of HB9. In Sect. 6.3, we calculate the luminosity of CR escaped from SNRs using the parameters in the delayed γ-ray model and then compare the measurement at Earth. This provides one test of whether the SNR paradigm is still valid. Sect. 6.4 describes future prospects for γ-ray observations as well as neutrino observations.

6.1 Application of the delayed γ-ray model to SNR G106.3+2.7

The interpretation for the non-thermal emission from the tail region in SNR G106.3+2.7, as mentioned in Sect. 4.2.2, proposes that the γ rays come from the molecular cloud region, while the radio and X-ray emissions come from the SNR shell. We attempt to model the energy spectrum of the tail region derived in Sect. 3.3.2 again using the delayed gamma-ray model developed in Chapter 5, instead of the simple assumption used in Chapter 4. In this modeling, we expect that the tail spectrum is explained by the sum of emissions from the two components, the shell and cloud regions.

Fig. 6.1 shows the modeling result, and the given parameters are listed in Table 6.1. Combining the emissions from the two components mentioned above can explain all the observed data. Despite the expectation that the synchrotron emission from the shell part explains the radio and X-ray fluxes (see Fig. 4.2), the new result indicates that the leptonic emissions from the shell part reproduce the radio and GeV γ-ray fluxes while the emissions from the cloud explain the X-ray and TeV γ-ray data. Fig. 6.2 shows the sketch of the interpretation.

In addition, we find that the obtained model parameters are similar to the HB9 results except for the diffusion coefficient as shown in Table 6.1. Fig. 6.3 shows the difference in the model curve due to the assumption for (left) the diffusion coefficient and (right) the maximum energy at the beginning of the Sedov phase. The model reproducing the γ-ray spectrum at the tail requires a two orders of magnitude smaller diffusion coefficient (2×10^{26} cm^{2}s^{-1}) than those of the Galactic mean and HB9, as well as a cutoff energy of a few PeV.

Such the small diffusion coefficient can be explained with the effect of the CR-self confine-

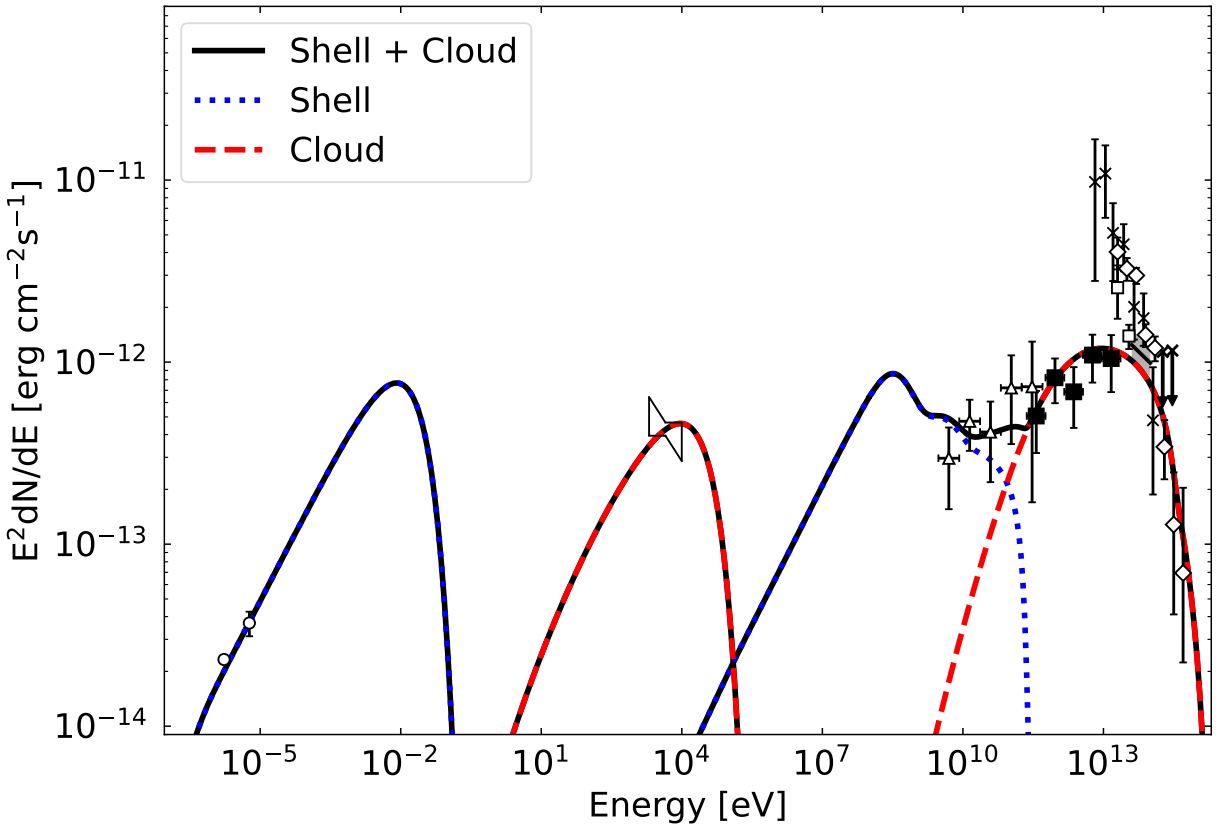

Figure 6.1: Modeling result to the tail spectrum of SNR G106.3+2.7 with the delayed γ-ray emission (red line) as well as the shell emission (blue line). The black line indicates the sum of the non-thermal emissions from the shell and cloud regions. The data points are the same as in Fig. 4.1.

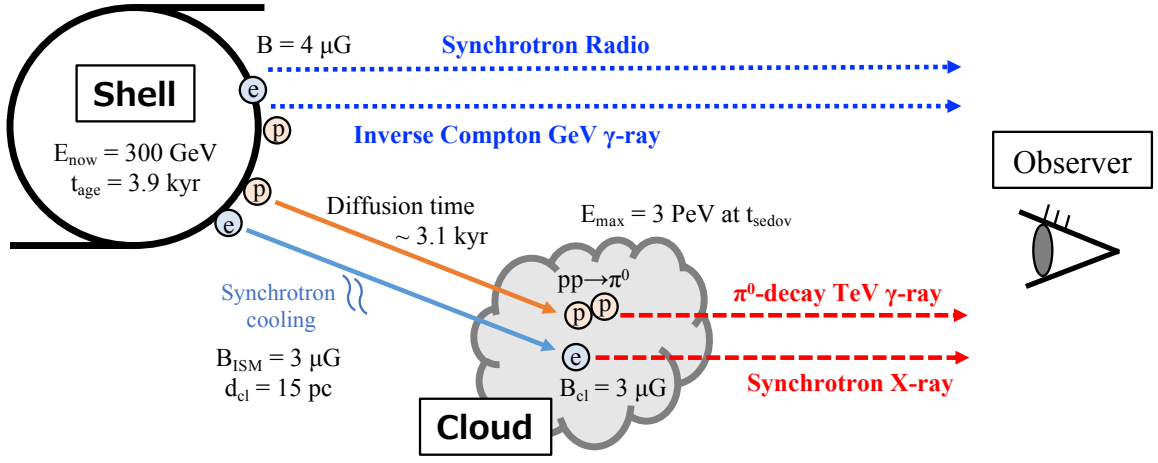

Figure 6.2: Schematic view of the new interpretation for the tail emissions in SNR G106.3+2.7. Some model parameters in Table 6.1 are also denoted.

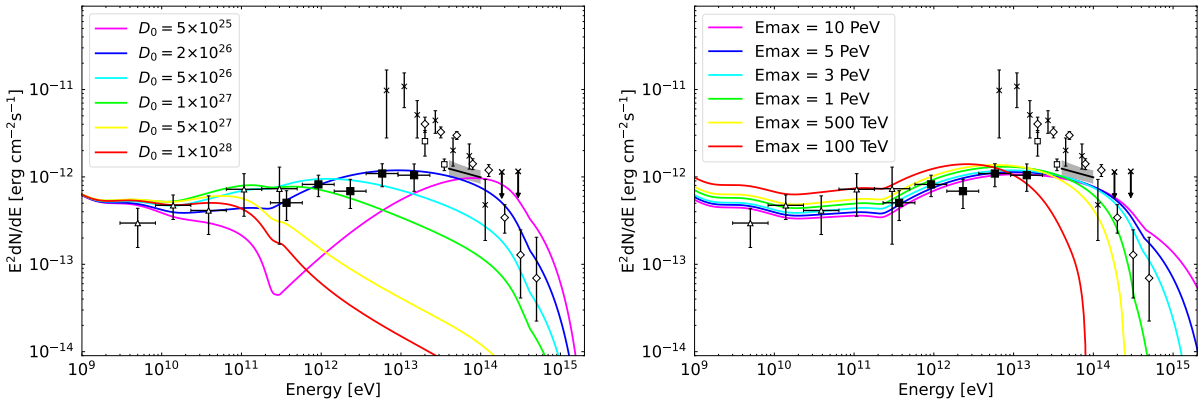

Figure 6.3: D_0 (left) and $E_{\rm max}$ (right) dependency of the delayed γ-ray spectrum at the SNR G106.3+2.7-tail. The data points are the same as in 4.1. In the left panel, the values in the legend indicate the diffusion constant at 10 GeV with units of cm^{2}s^{-1}.

ment (Wentzel, 1974; Fujita et al., 2011; D'Angelo et al., 2018). However, the difference in the obtained diffusion coefficients between SNR G106.3+2.7 and HB9 cannot be easily explained even by considering this effect. The diffusion coefficient is expected to depend on the strength of the surrounding magnetic field (Gabici et al., 2009; Fujita et al., 2009) and its direction (Malkov et al., 2013). In the latter case, the diffusion of CRs is considered to be asymmetric compared to the former. If we obtain the delayed gamma-ray spectra from two or more clouds around an SNR, we can investigate the isotropy of the CR diffusion to resolve the two scenarios above. Note that a large distance between the shell and the cloud may be assumed instead of the small diffusion coefficient but is not preferred here because the case yields a too large flux at the shell region compared to the cloud region.

6.2 Delayed γ-ray candidate: HESS J1626−490

HESS J1626−490 is one of the undefined TeV sources discovered by the HESS telescope. This source is located close to SNR G335.2+0.1 but does not overlap with any radio and X-ray sources in line of sight (Aharonian, 2008b). On contrary, *Fermi*-LAT observations revealed a GeV emission spatially coinciding with SNR G335.2+0.1, and two other point sources near the HESS emission (Abdollahi et al., 2020). Eger et al. (2011) have analyzed the HI and CO line data as well as the X-ray data and then found the spatially coincidence between the HESS source and the HI cloud associated with SNR G335.2+0.1, as shown in Fig. 6.4. The authors therefore suggested that the TeV γ-ray emission originates in the protons escaped from SNR G335.2+0.1. In this work we first attempt to model this unidentified TeV source with the delayed γ-ray emission.

We briefly describe here the physical quantity of SNR G335.2+0.1 estimated by previous studies. The angular diameter of this SNR is $\sim 0.33^\circ$ (Whiteoak & Green, 1996), while the spectral index is found to be $\alpha = -0.46$ (Clark et al., 1975). The distance from Earth is estimated to be about 1.8 kpc based on the HI observation (Eger et al., 2011). Therefore, the dynamical age is estimated to be ~ 1.1 kyr, indicating this SNR is young. Although the location

Table 6.1: Model parameters reproducing the observed spectra of MAGIC-tail in SNR G106.3+2.7, HESS J1626−490, and HB9. The parameters of HB9 was derived in Chapter 5.

SNR parameters	G106.3+2.7–Tail	G335.2+0.1	HB9–R2
SN explosion energy (10^{50} erg)	1.0	5.0	3.0
Initial shock velocity (10^9 cm s^{-1})	1.0	1.0	1.0
Age of the SNR, $t_{\rm age}$ (yr)	3.9×10^3	1.6×10^3	6.6×10^3
Distance to the SNR (kpc)	0.8	1.8	0.8
Acceleration efficiency	0.1	0.1	0.1
Electron to proton flux ratio	0.02	0.01	0.02
Maximum CR energy at $t_{\rm Sedov}$ (eV)	3×10^{15}	1×10^{15}	3×10^{15}
Maximum CR energy at $t_{\rm age}$, $E_{\rm max}$ (eV)	3×10^{11}	5×10^{10}	3×10^{11}
Temporal decay index of $E_{\rm cut}$, α	3.15	4.43	3.16
Magnetic field in the SNR (μG)	4	8	8
Particle index in the SNR	2.0	2.0	2.0
Particle index after escaping	2.0	2.4	2.4
ISM parameters	G106.3+2.7–Tail	G335.2+0.1	HB9–R2
Number density (cm^{-3})	0.1	1.0	0.06
Diffusion coefficient at 10 GeV, D_0 (cm^{2}s^{-1})	2×10^{26}	1×10^{27}	3×10^{28}
Energy slope of diffusion	1/3	1/3	1/3
Magnetic field in ISM (μG)	3	3	3
Cloud parameters	G106.3+2.7–Tail	G335.2+0.1	HB9–R2
Distance to the Cloud from SNR (pc)	15.0	13.6	39.4
Radius of the Cloud (pc)	2.2	7.5	7.0
Average hydrogen number density (cm^{-3})	300	200	200
Reflected SNR age (yr)	-3.1×10^3	-8.9×10^2	-6.3×10^2
Magnetic field in Cloud (μG)	3	3	3

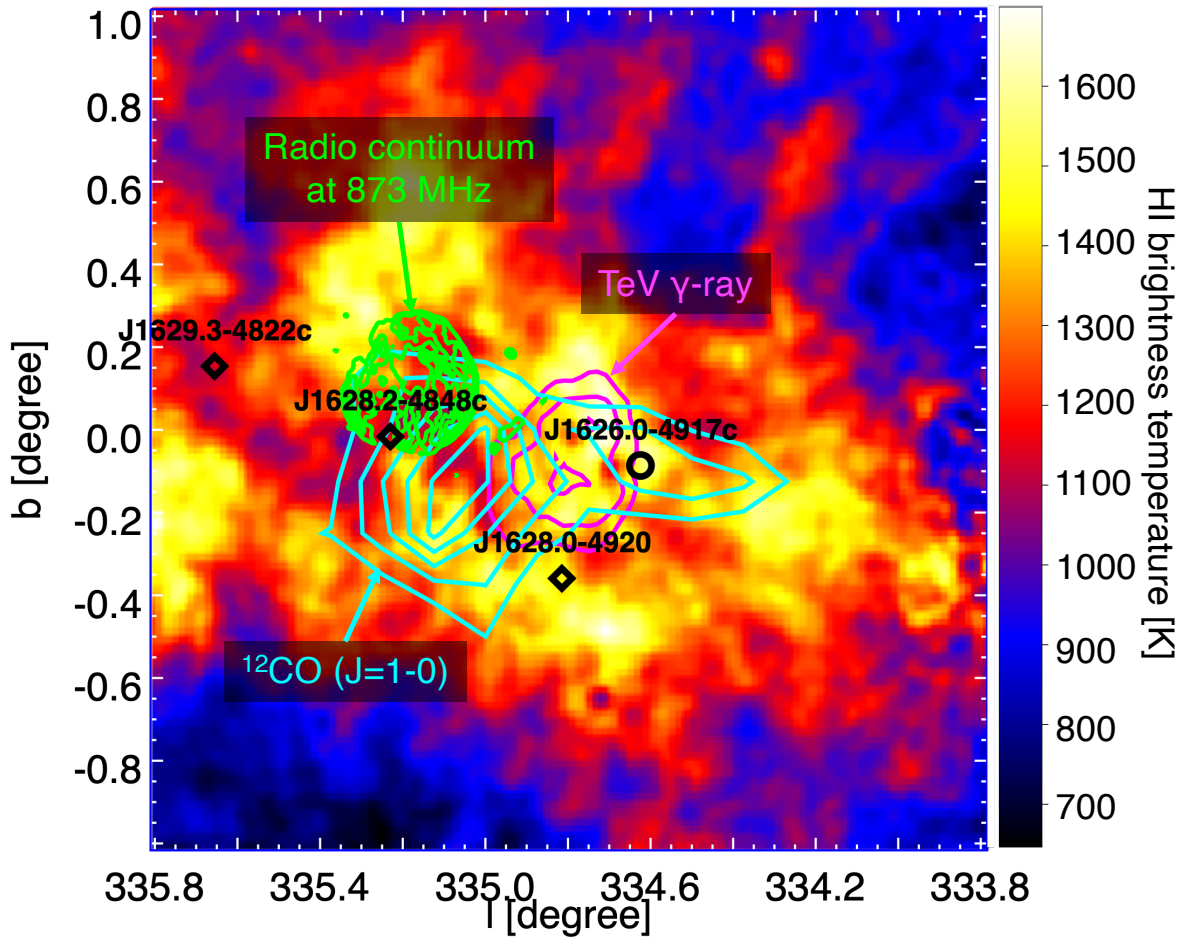

Figure 6.4: HI line intensity map in the vicinity of SNR G335.2+0.1 (McClure-Griffiths et al., 2005), which are integrated over a velocity range from -31 km s^{-1} to -18 km s^{-1} based on Eger et al. (2011). The green, cyan, and magenta contours represent the emissions of radio continuum at 843 MHz (http://snrcat.physics.umanitoba.ca/downloadFITS.php?location=FITS/radio/g335.2+00.1_8.73E08_MOST.fits), ^{12}CO ($J = 1 - 0$) line (Dame et al., 2001), and TeV γ rays (Abdalla et al., 2018b), respectively. The black markers indicate the positions of 4FGL sources (Abdollahi et al., 2020).

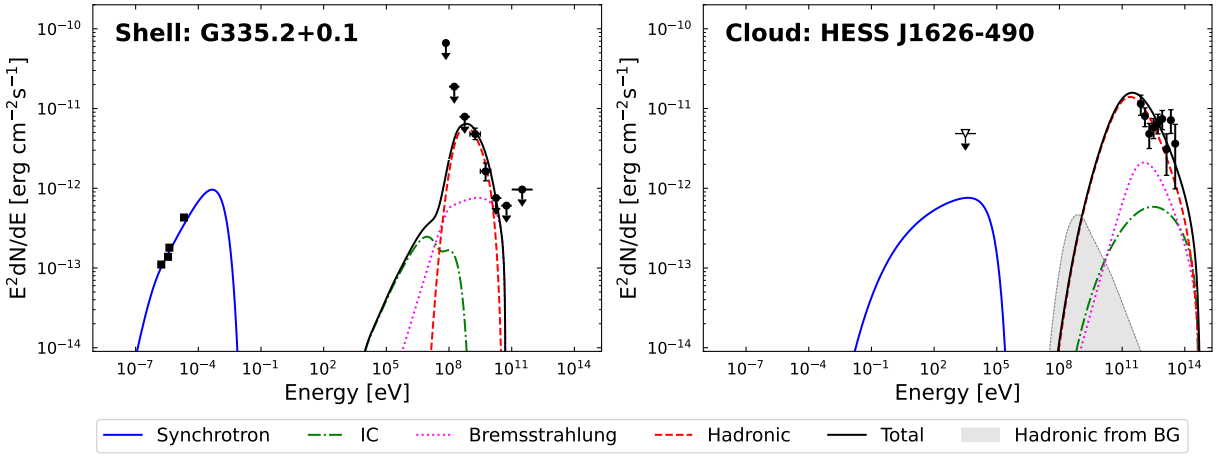

Figure 6.5: Modeling result to the energy spectra of the shell (left) and cloud regions (right) around SNR G335.2+0.1. The blue, green, magenta, and red lines represent the synchrotron, IC, electron bremsstrahlung, and π^0-decay emissions, respectively. The black line indicates the sum of the non-thermal emissions from the shell and cloud regions. Also shown with the grey shaded area is the hadronic emission from the background CRs. In the left panel, the data points in the radio and GeV band are taken from the literatures (Clark et al., 1975; Whiteoak & Green, 1996; Green, 1988) and Abdollahi et al. (2020), respectively. In the right panel, the flux upper limit in the X-ray band is taken from Eger et al. (2011), while the TeV spectrum is adopted from Aharonian (2008b).

of a pulsar PSR 1627−4845 is spatially consistent with SNR G335.2+0.1, its characteristic age (2.7 Myr) and estimated distance (6.8 kpc) significantly differ from those of the SNR mentioned above. Therefore, this pulsar is not considered to be associated with the SNR (Kaspi et al., 1996).

Here, we model the observed spectra at the SNR G335.2+0.1 (shell) and HESS J1626-490 (cloud), simultaneously, as with in Chapter 5. The radio data for the shell region are taken from Clark et al. (1975), Whiteoak & Green (1996), and Green (1988). The Fermi-LAT spectrum of 4FGL J1626−4848c (Abdollahi et al., 2020) is adopted as the shell emission. We also adopt the upper limit on the X-ray flux between 0.7 and 10.0 keV derived by Eger et al. (2011) as well as the TeV spectrum (Aharonian, 2008b), for the non-thermal emission from the HESS source (cloud) region. The energy density of seed photon for IC is estimated to be 0.25 eV cm^{-3} at 40 K using the model parameter in GALPROP (Porter et al., 2008). The cloud parameters (density, size, and location) for the HESS source region are adopted from the CO and HI observations (Eger et al., 2011).

Fig. 6.5 shows the modeling result to the energy spectra of G335.2+0.1 and HESS J1626−490. The model parameters used in the modeling are tabulated in Tab. 6.1. We find the hadronic emissions can reproduce both γ-ray spectra at the shell and cloud. Fig. 6.6 shows the model variations with diffusion coefficient and cutoff energy. The diffusion coefficient to reproduce the observed spectrum is found to be $D \sim 10^{27}$ cm^{2}s^{-1}, which is about one order smaller than the Galactic mean. As discussed in Sect. 6.1, the small diffusion constant can be explained by the effect of the CR-self confinement (e.g., Wentzel, 1974). The maximum energy at $t_{\rm sedov}$

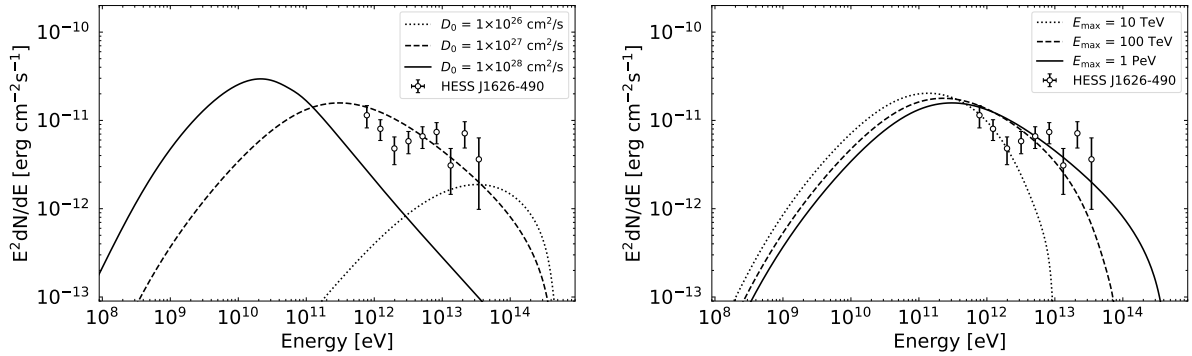

Figure 6.6: D_0 (left) and $E_{\rm max}$ (right) dependency of the delayed γ-ray model for HESS J1626−490. The data points are taken from Aharonian (2008b).

is estimated to be $\gtrsim$ 100 TeV. Although further observations with the *Fermi*-LAT or HESS telescopes are needed to better identify the counterpart of the γ-ray emissions, such observations would provide strong evidence that this SNR was a PeVatron in the past.

6.3 Discussion on the CR luminosity

The modeling results suggest that all three SNRs examined in this chapter are still allowed to accelerate protons up to $\gtrsim$ 1 PeV. Fig. 6.7 shows the time evolution of the maximum particle energy for each SNR based on Table 6.1. The obtained temporal decay index of the maximum energy (α = 3–4) is in good agreement with the phenomenological prediction (Ohira et al., 2011).

Here, we calculate intensities of the PeV CRs escaped from those SNRs and compare with the one observed at Earth. With the CR energy spectrum (Dermer, 1986)

$$J_{\rm CR} = 2.2(E/{\rm GeV})^{-2.75}\ {\rm cm}^{-2}{\rm s}^{-1}{\rm GeV}^{-1}{\rm sr}^{-1}, \tag{6.1}$$

the CR luminosity at Earth can be approximated as follows:

$$L_{\rm CR}(E) \sim \frac{W_{\rm CR}}{t_{\rm CR}} \sim \frac{4\pi}{c}\frac{V_{\rm Gal}}{t_{\rm CR}}E^2 J_{\rm CR}, \tag{6.2}$$

where $W_{\rm CR}$ is the total energy of CRs, $V_{\rm Gal}$ is the volume of the Galaxy, and $t_{\rm CR}$ is a diffusion timescale for CRs. Assuming that the shape of Galaxy is a cylinder, $V_{\rm Gal}$ can be approximated as follows

$$V_{\rm Gal} \sim 2\pi R^2 H = 2.09\times10^{68}\ {\rm cm}^3 \left(\frac{\rm R}{15\ {\rm kpc}}\right)^2 \left(\frac{\rm H}{7\ {\rm kpc}}\right), \tag{6.3}$$

where H is the halo size of Galaxy and R is the radius of the Galaxy disk. The diffusion timescale of CRs from the Galaxy can be estimated by

$$t_{\rm CR}(E) \sim \frac{H^2}{D(E)} \sim 1.15\times10^{16}\ {\rm s} \left(\frac{\rm H}{7\ {\rm kpc}}\right)^2 \left(\frac{\rm E}{1\ {\rm GeV}}\right)^{-\delta}, \tag{6.4}$$

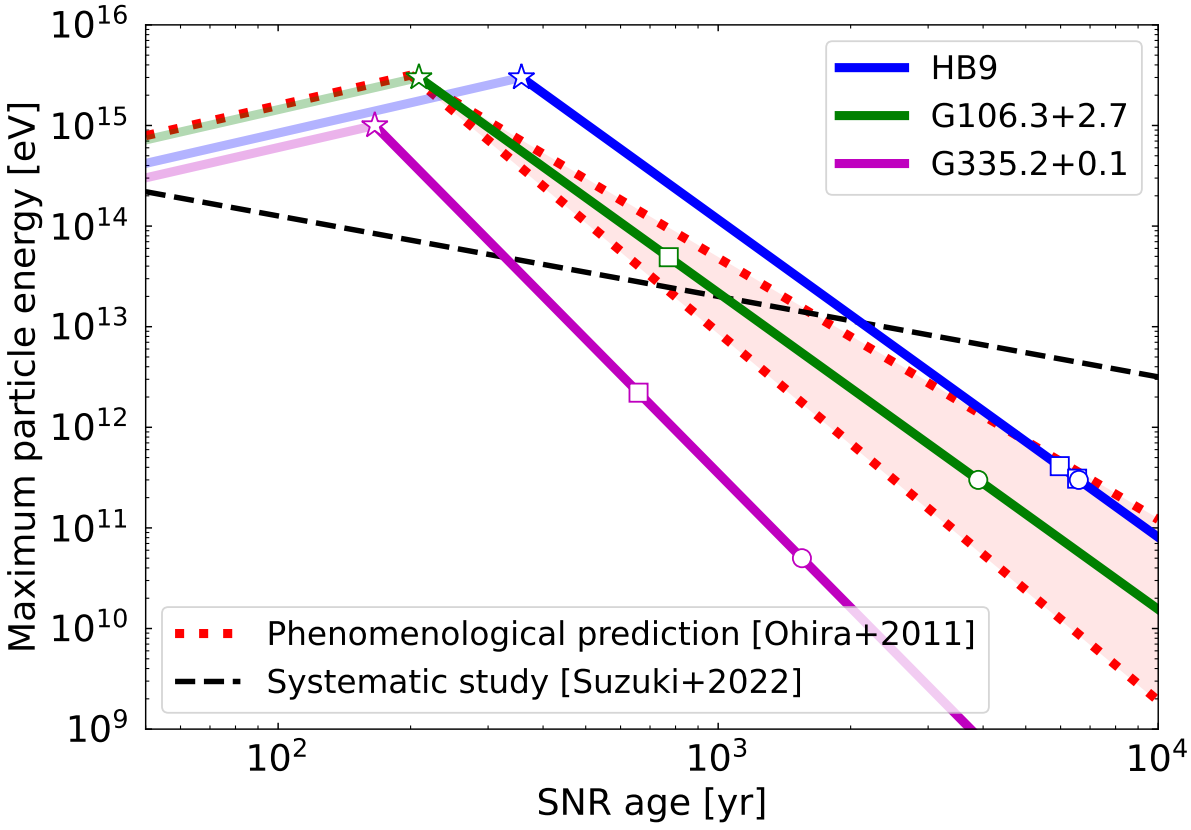

Figure 6.7: Maximum energy of accelerated particles in SNRs as a function of the age. The data points and solid lines represent the results obtained in this work. The circle and square markers indicate the maximum energies at the shell and cloud region, respectively. The star markers indicate the estimated time point ($t_{\rm Sedov}$) at entering the Sedov period. Although the model in this work does not consider the younger part than $t_{\rm Sedov}$, an extrapolation with $t_{\rm age}$ based on the theoretical expectation (e.g., Ohira et al., 2011) is shown for the sake of reference. The shaded area enclosed by the red dotted lines represent the phenomenological prediction based on Ohira et al. (2011), while the black dashed line represents the result derived by Suzuki et al. (2022).

Table 6.2: CR luminosity from SNRs computed with the model parameters of each SNR in Tab. 6.1.

Name	$L_{\rm SNR}(10\ {\rm TeV})$ [erg s^{-1}]	$L_{\rm SNR}/L_{\rm CR}$ at 10 TeV	$L_{\rm SNR}(1\ {\rm PeV})$ [erg s^{-1}]	$L_{\rm SNR}/L_{\rm CR}$ at 1 PeV
HB9	2.88×10^{39}	1.08	4.56×10^{38}	0.54
G106.3+2.7	1.03×10^{39}	0.39	1.03×10^{39}	1.22
G335.2+0.1	2.33×10^{39}	0.87	3.69×10^{38}	0.44

where D is the diffusion coefficient and adopted the results of the Boron-to-Carbon ratio (Yuan et al., 2017). Substituting Eq. 6.3 and 6.4 into Equation 6.2 yields

$$L_{\rm CR}(E) \sim 2.67 \times 10^{40}\ {\rm erg\ s^{-1}} \left(\frac{\rm E}{1\ {\rm GeV}}\right)^{-0.75+\delta} \left(\frac{\rm V_{Gal}}{2.1 \times 10^{68}\ {\rm cm^3}}\right), \tag{6.5}$$

where δ is the slope of the diffusion coefficient. In this calculation, we adopt the value ($\delta = 0.500$) estimated by Yuan et al. (2017). As a result, the CR luminosity is estimated to be $L_{\rm CR} = 2.67 \times 10^{39}$ erg s^{-1} at 10 TeV and 8.45×10^{38} erg s^{-1} at 1 PeV.

On the other hand, the luminosity of CRs escaped from SNRs can calculated as follows. First, the energy distribution of CRs escaped from an SNR is described by Eq. 5.8:

$$N_{\rm esc}(E) = \begin{cases} \frac{\eta(2-p_{\rm esc})E_{\rm SN}}{E_{\rm now}^2} \times \left[\left(\frac{E_{\rm max}}{E_{\rm now}}\right)^{2-p_{\rm esc}} - 1\right]^{-1} \times \left(\frac{E}{E_{\rm now}}\right)^{-p_{\rm esc}} & p_{\rm esc} \neq 2 \\ \frac{\eta E_{\rm SN}}{\ln(E_{\rm max}/E_{\rm now})} E^{-2} & p_{\rm esc} = 2 \end{cases} \tag{5.8}$$

The total luminosity from SNRs can be approximated by multiplying the birth rate of SNe:

$$L_{\rm SNR} \sim N_{\rm esc}(E) \times E^2 \times ({\rm SN\ rate}). \tag{6.6}$$

As for the SN rate, 0.03 yr^{-1} (Tammann et al., 1994) is adopted.

Using the best-fit parameters shown in Table 6.1, we calculate the contribution to the CR luminosity and summarize in Table 6.2. The calculated luminosity from SNRs ($L_{\rm SNR}$) varies by a factor of ~ 3 but is roughly consistent with the measurement at Earth ($L_{\rm CR}$).

6.4 Future prospect

6.4.1 Future γ-ray observations

As mentioned in Sect. 5.4.3, our work has suggested that further TeV γ-ray observations would give a crucial constraint on the model parameters. In particular, the parameter $E_{\rm max}$ should be estimated better to elucidate whether the SNR is a PeVatron. We simulate energy spectra at HB9-R2 expected to be obtained with the next generation γ-ray observatories, CTA-North (Bernlöhr et al., 2013) and LHAASO (Addazi et al., 2022). Since HB9-R2 is more extended ($\theta_{\rm src} = 0.36°$) than PSFs of these instruments ($\sim 0.05°$ for CTA-North and $\sim 0.30°$ for LHAASO), the sensitivities for a point source are scaled down by $\sqrt{(\theta_{\rm PSF}^2 + \theta_{\rm src}^2)/\theta_{\rm PSF}^2}$, to

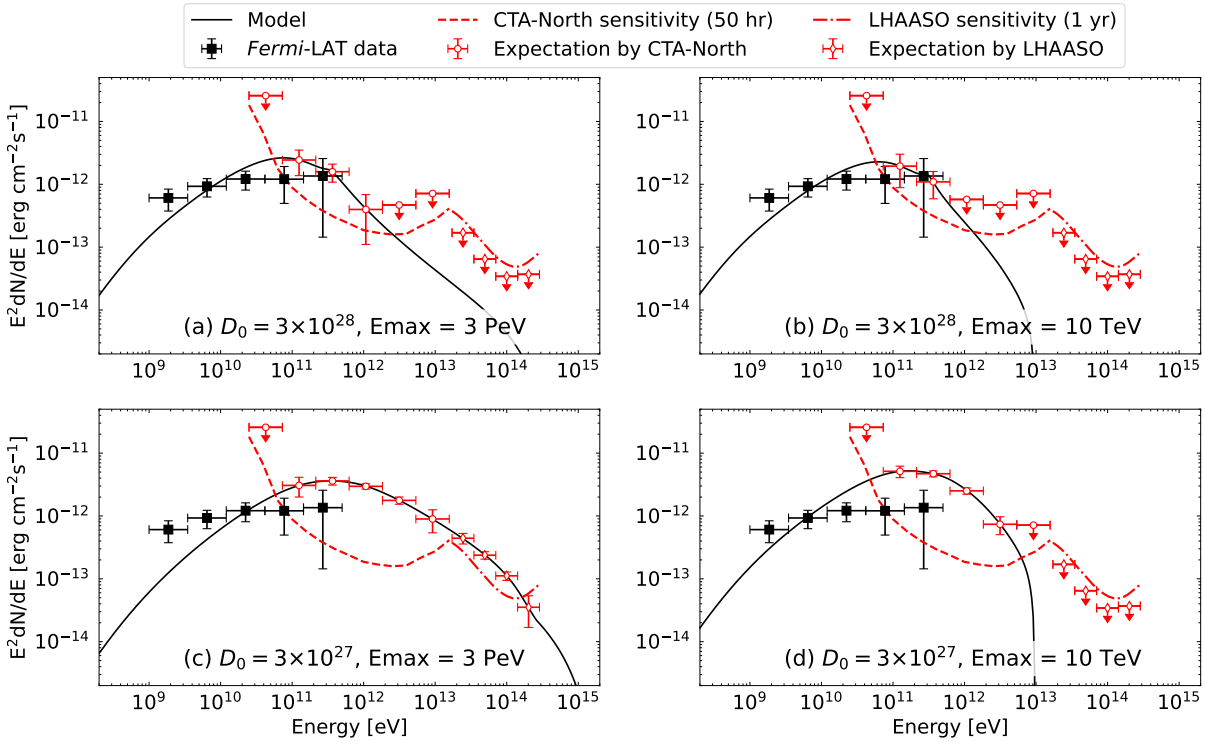

Figure 6.8: Energy spectra of HB9–R2 expected to be observed with the CTA (open circle) and LHAASO experiments (open diamond). The red dashed line shows the 5σ-detection sensitivity of the 50-hr CTA and 1-yr LHAASO observations. Black solid line shows the model emissions calculated using the parameters in Table 5.2 except for D_0 and $E_{\rm max}$, which are represented in each panel. The black points represent the *Fermi*-LAT data dervied in Sect. 5.3.2.

account for the deterioration of the signal-to-background ratio in the extended source analysis. Fig. 6.8 shows the expected energy spectra from a 50-hour observation by CTA-North and a one-year observation by LHAASO. Although four sets of model parameters that have not been ruled out in our study using the *Fermi*-LAT data are used for the simulation, the differences in the expected spectra can be found.

It should be noted that the model spectra at the TeV band may be affected by the assumption when electrons escape from the shock region. Under the assumption of Chapters 5 and 6, where the electron and proton begin to escape simultaneously, the amount of escaped electrons is maximized. Appendix B estimates the impact due to this assumption is at most a factor of ~ 2.

Once $E_{\rm max}$ is determined better, the temporal decay index (α) in the time evolution can be estimated with fewer uncertainties. The presently obtained value is $\alpha \sim 3.1$–4.4 for the three SNRs, which is steeper than that ($\alpha = 0.81 \pm 0.24$) obtained in the previous study with the systematic investigation of the gamma-ray spectra in many SNRs (Suzuki et al., 2022). As a result, our result supports that these SNRs were a PeVatron. While the future observations for HB9 in the northern sky are given here, future projects such as CTA-South (Bernlöhr et al., 2013), ALPACA (Asaba et al., 2018), and SWGO (Albert et al., 2019) are underway to observe γ-ray sources with better sensitivities in the southern sky, such as SNR G335.2+0.1. Observations with these future experiments would provide more precise results for the time evolution of DSA

in SNRs, which may find the difference between the types of SNe (e.g., Kamijima & Ohira, 2021, 2022).

6.4.2 Neutrino observations

Detection of neutrinos can strengthen the possibility of proton acceleration in SNRs. The IceCube experiment has achieved the highest sensitivity in modern neutrino observations, and its upgrade project, IceCube-Gen2, is also underway to improve the sensitivity by a factor of five or more (Aartsen et al., 2021b). Here we estimate the neutrino flux at the tail region of SNR G106.3+2.7 and compare it with the sensitivities of the IceCube and its future project.

Protons in SNRs generate π^+, π^-, and π^0 via p-p collision with a ratio of 1:1:1, as in Eq. 1.41. As in Eq. 1.42, π^0 then decays to 2γ, while $\pi^\pm$ decays to μ and ν_μ. Furthermore, μ decays to $e^\pm$ and ν_e. According to Ahlers & Murase (2014), the γ-ray flux and the neutrino fluxes for each flavor produced in this process is expressed as

$$E_\gamma J_\gamma(E_\gamma) \simeq \exp(-\mathrm{d}/\lambda_{\gamma\gamma}) \times \frac{1}{3} \sum_{\nu_\alpha} \mathrm{E}_\nu \mathrm{J}_{\nu_\alpha}(\mathrm{E}_\nu), \tag{6.7}$$

where E_γ (E_ν) is the γ-ray (neutrino) energy, J_γ (J_ν) is the differential flux for γ-rays (neutrinos), $\lambda_{\gamma\gamma}$ is the optical depth for the $\gamma\gamma$ absorption, and d is the distance from Earth. As for the effect of $\gamma\gamma$ absorption, we assume that it is negligible because d ($\sim$ 1 kpc) for SNR G106.3+2.7 is enough small. Since the energy of neutrinos is about one quarter of pions, $E_\gamma \simeq 2E_\nu$. At Earth, after the propagation, the neutrino fluxes for each flavor are almost the same due to neutrino oscillations (Cavasinni et al., 2006). Hence, Eq. 6.7 can be approximated as

$$E_\gamma J_\gamma(E_\gamma) \simeq 2E_\gamma J_\nu(2E_\gamma). \tag{6.8}$$

Using this relation between the γ-ray and neutrino flux, we estimate the energy spectrum of muon neutrino at the tail region of SNR G106.3+2.7 and show it in Fig. 6.9. The expected flux is lower than the sensitivities of the neutrino observations and is also consistent with the upper limit recently obtained by the IceCube experiment (Abbasi et al., 2022). Although 5σ detection of the neutrino emission from this region would be challenging even with IceCube-Gen2, Fig. 6.9 suggests the experiment may find the excess with 2–3σ significance at the range of 10–100 TeV.

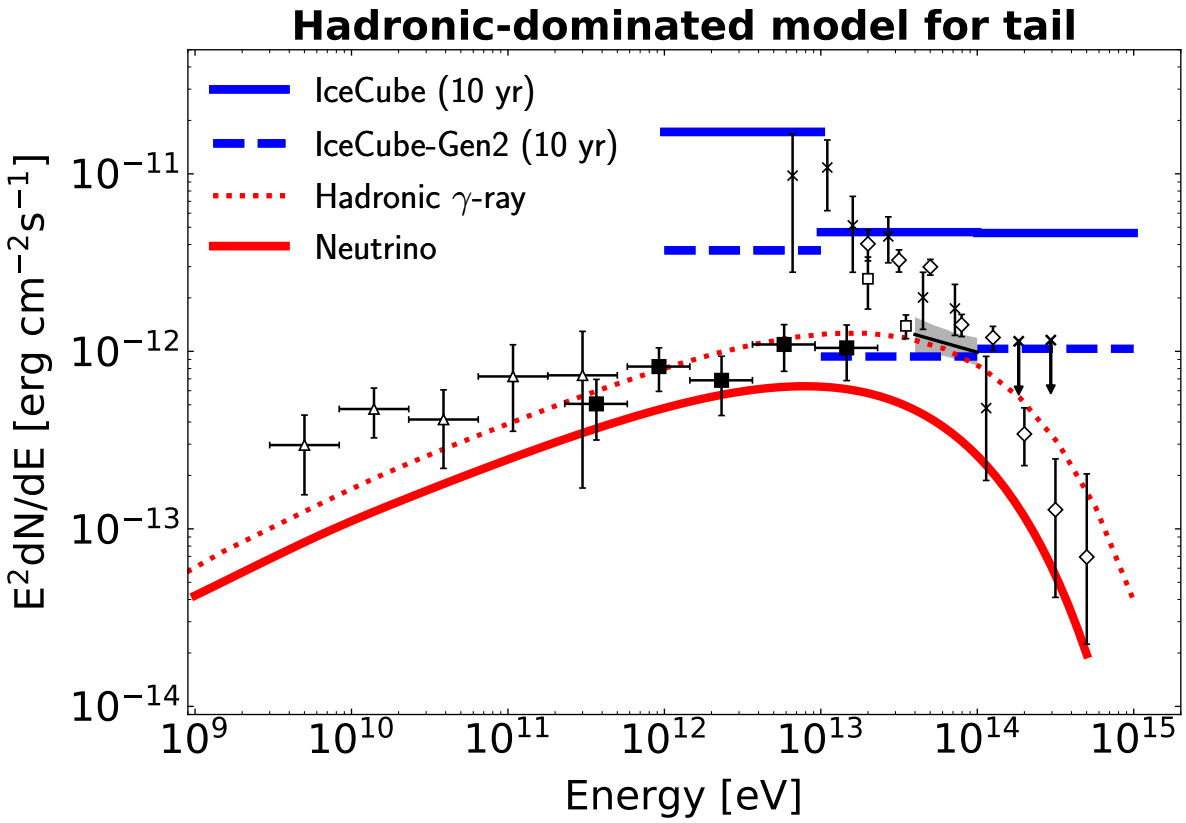

Figure 6.9: Expected energy spectra of muon neutrinos ($F_{\nu_\mu} + F_{\overline{\nu}_\mu}$; red solid) as well as the hadronic γ rays (red dotted) at the tail region of SNR G106.3+2.7. The blue solid (dashed) line represents the 5σ differential sensitivities of 10-yr IceCube (IceCube-Gen2) observations at the declination angle of 30° (Aartsen et al., 2021b).

Chapter 7

Summary

To elucidate the origin of CRs up to PeV, we investigated whether SNR PeVatrons (which accelerate particles up to PeV) exist in our Galaxy and whether SNRs can supply the total amount of PeV CRs measured at Earth, using γ-ray observations. For this purpose, we attempted to validate the time evolution scenario, in which the maximum acceleration energy in SNRs depends on the age and reaches PeV only for a limited period ($t_{\rm age} < 1$ kyr). Although theoretical works have expected this scenario, there was no conclusive observational evidence. We measured the time evolution of the maximum energy in a single SNR, for the first time, by simultaneously observing γ-ray spectra from the SNR shell (reflecting the present particle distribution) and the nearby clouds (reflecting the past particle distribution). This newly proposed method was applied to γ-ray observation data for the three SNRs, HB9, G106.3+2.7, and G335.2+0.1.

For the first application of this time-evolution measurement, we analyzed the GeV γ-ray data in the vicinity of SNR HB9, using 12-yr *Fermi*-LAT observations. We newly detected the γ-ray emissions spatially correlated with the cloud regions with a statistical significance of 6.1σ as well as the shell emission, the latter of which is consistent with previous studies. The γ-ray spectra at the cloud regions can be fitted with a power-law function with an index of < 2.0, which is the hardest spectrum ever observed at clouds around SNRs. The cloud spectra were successfully reproduced with the model of the time evolution scenario, in which CRs escaped from the shell in the past and now illuminate the cloud and generate the delayed γ-ray emissions. The results show that the SNR accelerated CRs up to higher energies ($\sim$ 3 PeV) in the past than the maximum energy at present (300 GeV).

Expecting that the SNR PeVatron may still be hidden in the 100-TeV sources detected by the LHAASO experiments, we focused on LHAASO J2226+6057/SNR G106.3+2.7 in this thesis. Since this region is a PWN/SNR complex, the origin of 100-TeV γ-ray emission from this source was not yet identified due to the limited angular resolution in previous studies. We observed it with the MAGIC telescopes, which achieve better angular resolution (0.07–0.1°) than the previous γ-ray observations for this source. We then found the extended TeV emissions ($> 6\sigma$) spatially coinciding with the radio shell, which consists of the head and tail regions. In particular, we detected the emission above 6 TeV only in the tail region but not in the head region, the latter of which contains the PWN. This fact suggests that the 100-TeV γ

rays originate in the SNR rather than the PWN. The spectral modeling in the two regions were performed. Both leptonic and hadronic emissions can reproduce the observed spectrum of the head region, while the leptonic model failed to reproduce the tail spectrum under the assumption that the observed emissions above 10 TeV come only from the tail region. We thus suggested that the γ-ray spectrum up to 100 TeV in the tail region originates in proton acceleration up to PeV in the SNR. Furthermore, we found that the time evolution scenario above explains the inconsistency between the proton cutoff energy of $\sim$ PeV and the SNR age of $\sim$ 4 kyr.

In addition, we performed the spectral modeling for HESS J1626$-$490/G335.2+0.1 with the time evolution scenario. The energy spectrum of the unidentified TeV source, HESS J1626$-$490, could be explained with the delayed γ-ray emissions by protons escaped from SNR G335.2+0.1.

The modeling results of the three SNRs yielded similar SNR parameters except for the diffusion coefficient, indicating that the time evolution scenario is general for SNRs. Moreover, the proton acceleration up to $\sim$ PeV is suggested in the all three SNRs. The amount of the escaped protons from SNRs calculated with these model parameters is in agreement with the CR flux observed at Earth within a factor of ~ 3. The results give compelling evidence supporting that Galactic SNRs are the origin of CRs up to PeV.

We also found this simultaneous model fitting to the shell and cloud regions allows for estimating the diffusion coefficient around SNRs with unprecedented accuracy. The diffusion coefficients around SNRs were theoretically expected to be smaller than the Galactic mean, but the results for each SNR varied by about two orders of magnitude, indicating a significant environmental dependence. Further observations with the future project were expected to estimate the above model parameters better. The luminosity frontier in TeV-PeV γ-ray observations will provide a unified picture of CR propagation and acceleration in SNRs, leading to the discovery of the CR origin.

Acknowledgements

First of all, I am deeply grateful to my supervisor, Prof. Hidetoshi Kubo, for his advice and continuous support. I would also like to express my gratitude to my research collaborators. Dr. Takayuki Saito and Dr. Marcel Strzys analyzed the MAGIC data for SNR G106.3+2.7 with me. Advice and comments given by the MAGIC Collaboration members, in particular Dr. Daniel Mazin and Dr. Marc Ribo, have been a great help in the MAGIC analysis. The MAGIC Collaboration is also acknowledged for allowing the use of proprietary observational data. Some MAGIC results presented in this thesis have not undergone the internal review procedure of MAGIC publications. Dr. Hidetoshi Sano, Dr. Tsuyoshi Inoue, and Dr. Yasuo Fukui have helped with the radio data analysis and its interpretation. Dr. Takaaki Tanaka gives insightful comments and suggestions for the *Fermi*-LAT data analysis. Dr. Wataru Ishizaki has provided the model calculation code and discussed with me the application to the observation data of SNR HB9. Special thanks to Dr. Toshihiro Fujii, Dr. Seiya Nozaki, and Kenta Terauchi for the fruitful discussions. Finally, I appreciate the support and encouragement of all the people in the Cosmic ray group at Kyoto University.

Appendices

Appendix A

Gas density in the vicinity of SNR G106.3+2.7

We calculate the gas density in the two regions of SNR G106.3+2.7 with the following outline. We use the data of HI line measured with the Dominion Radio Astronomy Observatory (DRAO) Synthesis Telescope (Landecker et al., 2000) and ^{12}CO ($J = 1 - 0$) line measured with the Five College Radio Astronomy Observatory (FCRAO; Heyer et al., 1998) from the Canadian Galactic Plane Survey (CGPS; Taylor et al., 2003) database. These observations were carried out with the velocity resolution of 0.824 km s^{-1} at HI line and 0.98 km s^{-1} at CO line. The following relationship is used to calculate the column density: $N_{\rm H}\,[{\rm cm}^{-2}] = X \int_{v_{\rm min}}^{v_{\rm max}} T(v) dv$, where v is the radial velocity, $T(v)$ is the observed brightness temperature (K) and X is the conversion factor (Dickey & Lockman, 1990). HI-to-N$_{\rm HI}$ and CO-to-N$_{\rm H_2}$ are given by $X_{\rm HI} = 1.823 \times 10^{18}$ (Dickey & Lockman, 1990) and $X_{\rm CO} = 2.0 \times 10^{20}$ (Bolatto et al., 2013). Fig. A.1 shows the radial profiles of HI and ^{12}CO ($J = 1 - 0$) line. There is a significant velocity dependence of the column density, especially in the CO data, which is a concern because the uncertainty of the velocity range affects the calculation of the gas density. Here, we consider two cases on the velocity ranges that associates with SNR G106.3+2.7: (i) -7.23 to -5.59 km s^{-1} suggested by Kothes et al. (2001) and (ii) -6.41 to -3.94 km s^{-1} suggested by Acciari et al. (2009); Albert et al. (2020). The clouds associated with the production of the observed γ-ray emission are assumed to be a spherical region around the emission center with a radius of 800 pc $\times$ tan(0.16°) $\sim$ 2.2 pc estimated from the MAGIC data as shown in Table3.2. The calculation results are summarized in Table A.1.

Table A.1: Gas densities of hydrogen atoms at the head and tail region. $n_{\rm HI}$ and $n_{\rm CO}$ are estimated with the HI line and ^{12}CO ($J = 1 - 0$) line data, respectively.

Velocity range [km s^{-1}]	-7.23 – -5.59	-6.41 – -3.94
$n_{\rm HI}$ at head [cm^{-3}]	42	59
$n_{\rm CO}$ at head [cm^{-3}]	73	66
$n_{\rm HI}$ at tail [cm^{-3}]	38	55
$n_{\rm CO}$ at tail [cm^{-3}]	137	191

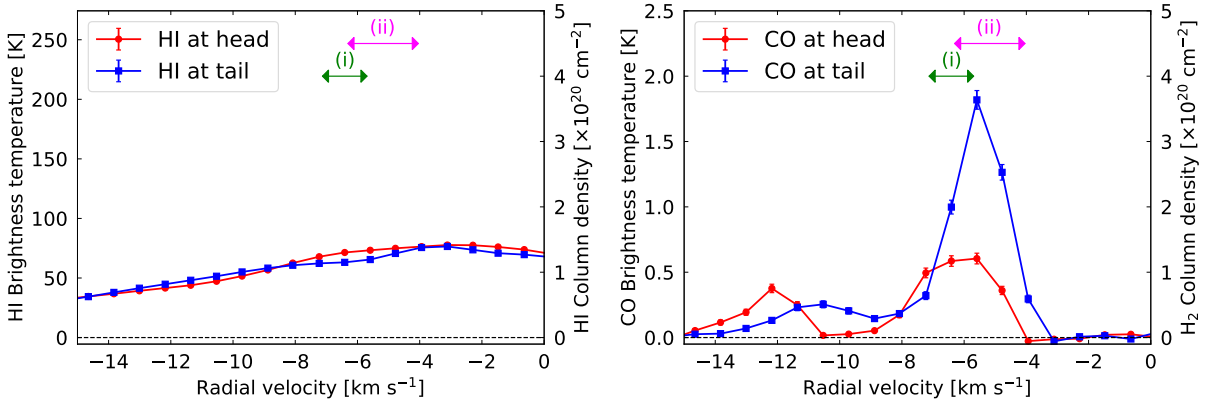

Figure A.1: The HI (left) and ^{12} CO ($J = 1 - 0$) (right) radial profile at the head and tail region. In both panel, red and blue data represent the profile of the head and tail regions. The green arrow labeled (i) indicates the velocity range pointed out by Kothes et al. (2001), while the magenta arrow labeled (ii) indicates the range used in Acciari et al. (2009) and Albert et al. (2020).

There is not big difference of the results between the integration velocity ranges. We use 100 cm^{-3} and 200 cm^{-3} as a gas density of head and tail regions for the modelling.

Appendix B

Electrons in the delayed γ-ray emission model

B.1 Derivation of the spectrum of CR electrons

The transport equation for CR electrons is written by

$$\frac{\partial f_{e,\mathrm{out}}}{\partial t}(t,r,E) - D_{\mathrm{ISM}}(E)\Delta f_{e,\mathrm{out}}(t,r,E) + \frac{\partial}{\partial E}\left(P(E) f_{e,\mathrm{out}}(t,r,E)\right) = q_{e,s}(t,r,E). \tag{B.1}$$

According to Atoyan et al. (1995), the Green function of equation (B.1) is

$$G(t,\mathbf{r},E;t_0,\mathbf{r}_0;E_0) = \frac{P\left(E_{t-t_0}\right)}{\pi^{3/2}P(E)r_{\mathrm{dif}}^3}\exp\left(-\frac{|\mathbf{r}-\mathbf{r}_0|^2}{r_{\mathrm{dif}}^2}\right)\delta\left(E_{t-t_0}-E_0\right), \tag{B.2}$$

where E_{t-t_0} is defined by the following implicit relation:

$$t - t_0 = \int_E^{E_{t-t_0}} \frac{dE'}{P(E')}, \tag{B.3}$$

$$r_{\mathrm{dif}} = \sqrt{4\Delta u}, \tag{B.4}$$

and

$$\Delta u = \int_E^{E_{t-t_0}} \frac{D_{\mathrm{ISM}}(E')}{P(E')} dE'. \tag{B.5}$$

From linearity, the solution to equation (B.1) can be calculated as follows:

$$f_{\mathrm{e,out}}(\mathrm{r},t,E) = \int dE_0 \int d^3\mathrm{r}_0 \int dt_0 G(t,\mathbf{r},E;t_0,\mathbf{r}_0;E_0) q_{e,s}\left(\mathbf{r_0},t_0,E_0\right). \tag{B.6}$$

In this work, only synchrotron radiation is considered as the most important process in radiative cooling. Thus, the cooling function $P(E)$ can be written as follows:

$$P(E) = \frac{4}{3}\sigma_T c\left(\frac{E}{m_e c^2}\right)^2 \frac{B_{\mathrm{ISM}}^2}{8\pi} \equiv Q_{\mathrm{syn}}E^2, \tag{B.7}$$

where σ_T is the Thomson scattering cross section, m_e is the electron mass, and $B_{\rm ISM}$ is a value of the magnetic field in the interstellar space. Evaluating equation (B.3) with using equation (B.7), we obtain

$$E_{t-t_0} = \frac{E}{1 - Q_{\rm syn} E (t - t_0)}. \tag{B.8}$$

For equation (B.5), we can calculate using equation (5.5) and (B.7) as follows:

$$\Delta u = \frac{r_{\rm dif}^2}{4} = \frac{D_{\rm ISM}(E)}{(1-\delta) Q_{\rm syn} E} \left[1 - \left(\frac{E}{E_{t-t_0}} \right)^{1-\delta} \right]. \tag{B.9}$$

By using equations (5.2), (5.6), (5.12), (B.2), (B.8), and (B.9) and performing the integration of equation (B.6), the solution to equation (B.1) can be obtained as follows:

$$f_{\rm e,out}(t, r, E) = \frac{K_{\rm ep} N_{\rm esc}(E_c)}{4\pi^{3/2} r R_{\rm c} R_{\rm d,e}} \frac{E_c^2}{E^2} \frac{1}{1 - Q_{\rm syn} t_c E_c / \alpha} \times \left[\exp\left(-\frac{(r - R_{\rm c})^2}{R_{\rm d,e}^2} \right) - \exp\left(-\frac{(r + R_{\rm c})^2}{R_{\rm d,e}^2} \right) \right],$$

where $t_c = t_c(t, E)$ is the time when the electron whose energy is E at the current time t is injected and determined as a solution to an algebraic equation $t_c = t_{\rm esc}(E_{t-t_c})$, or equivalently the below equation,

$$\frac{E}{1 - Q_{\rm syn} E (t - t_c)} = E_{\rm esc}(t_c), \tag{B.10}$$

$E_c(t, E) = E_{\rm esc}(t_c)$, $R_c(t, E) \equiv R_{\rm esc}(E_c)$, and $R_{\rm d,e}(t, E)$ is the diffusion length of CR electrons

$$R_{\rm d,e} = \sqrt{\frac{4 D_{\rm ISM}(E)}{(1-\delta) Q_{\rm syn} E} \left[1 - \left(\frac{E}{E_c} \right)^{1-\delta} \right]}. \tag{B.11}$$

Here, we have assumed that there is only one solution to equation (B.10), however this is not generally true. The condition for there to be only one solution can be written as follows:

$$t_{\rm Sedov} \geq t_{c,\rm crit} \equiv t_{\rm Sedov} \left[\frac{Q_{\rm syn} t_{\rm Sedov} E_{\rm max}}{\alpha} \right]^{1/(\alpha-1)} \tag{B.12}$$

For the range of parameters we use in this work, this condition is satisfied, and then the assumption of only one solution is consequently justified.

B.2 Impact of electron parameter to the delayed γ-ray model

We demonstrate the impact of assumed electron parameters to the γ-ray emission model. According to Ohira et al. (2012), the estimate of $\xi_{\rm e}$ $(= t/t_{\rm sedov})$ depends on the assumption of the environment of the magnetic field. The start time of escape of CR electrons is expressed by:

$$t_{\rm e} = \left(\frac{9 m_{\rm e}^2 c^{5/2} R_{\rm S}^2}{8 \eta_{\rm g,free} \eta_{\rm acc} e E_{\rm max}^{3/2}} \right)^{-2/(\alpha + 2\alpha_{\rm B} - 1)} t_{\rm sedov}^{(\alpha+2\alpha_{\rm B}+2)/(\alpha+2\alpha_{\rm B}-1)}, \tag{B.13}$$

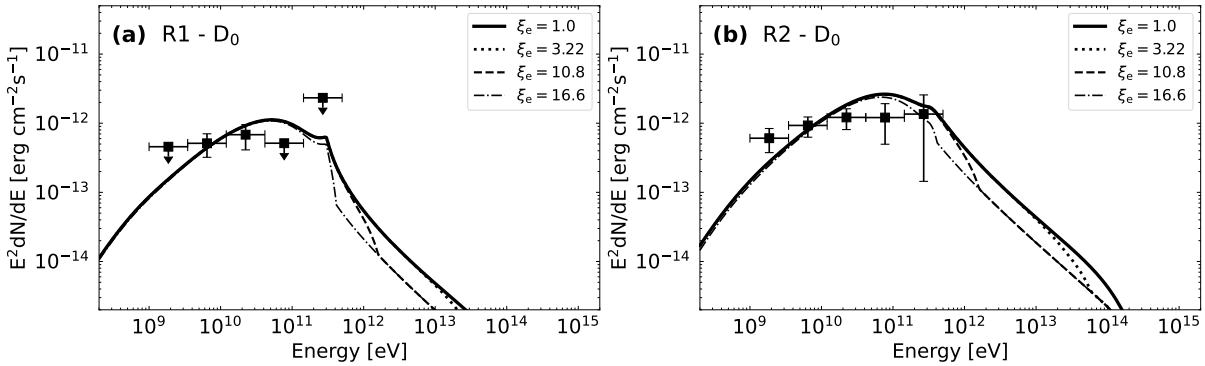

Figure B.1: ξ_e dependence of the delayed γ-ray model. Panels a and b show the energy spectra at the R1 and R2 cloud around SNR HB9. The data points are the same as in Fig. 5.13. The difference of the line type indicates the difference in the assumption of ξ_e.

where

$\eta_{g,free} \sim 1$: Gyrofactor during the free-expansion phase ($t_{age} < t_{sedov}$)
$\eta_{acc} \sim 10$: Numerical factor that depends on the shock compression ratio and the spatial dependence of the diffusion coefficient
R_S: SNR radius when $t_{age} = t_{sedov}$
α: Temporal decay index of the maximum energy of CR protons
α_B: Temporal decay index of the magnetic field

In particular, α_B depends on the environment of the magnetic field around SNRs, i.e., the assumption of the gyro-factor (η_g) and the shock velocity (v_{sh}) in the SNR. Ohira et al. (2012) assumed three magnetic field models and derived $\alpha_B = \alpha - 1$, 9/10, and 3/5. Once we substitute $\alpha = 3.16$, $t_{sedov} = 357$ yr, and $R_S = 3.65$ pc for the SNR HB9 (Sect. 5.4), ξ_e is estimated to be 3.22 for $\alpha_B = \alpha - 1$, 10.8 for $\alpha_B = 9/10$, and 16.6 for $\alpha_B = 3/5$. Fig. B.1 shows the model emissions computed with the parameters above. The TeV γ-ray fluxes computed with the larger ξ_e are (up to a factor of ~ 2) smaller than the case of $\xi_e = 1$ because of fewer escaped electrons.

Bibliography

M. G. Aartsen et al. (2013). 'Measurement of the cosmic ray energy spectrum with IceTop-73'. *Phys. Rev. D* **88**(4):042004.

M. G. Aartsen et al. (2021a). 'Detection of a particle shower at the Glashow resonance with IceCube'. *Nature* **591**(7849):220–224. [Erratum: Nature 592, E11 (2021)].

M. G. Aartsen et al. (2021b). 'IceCube-Gen2: the window to the extreme Universe'. *J. Phys. G* **48**(6):060501.

R. Abbasi et al. (2022). 'Searches for Neutrinos from LHAASO ultra-high-energy γ-ray sources using the IceCube Neutrino Observatory' .

H. Abdalla et al. (2018a). 'H.E.S.S. observations of RX J1713.7−3946 with improved angular and spectral resolution: Evidence for gamma-ray emission extending beyond the X-ray emitting shell'. *Astron. Astrophys.* **612**:A6.

H. Abdalla et al. (2018b). 'The H.E.S.S. Galactic plane survey'. *Astron. Astrophys.* **612**:A1.

A. Abdo et al. (2007). 'TeV Gamma-Ray Sources from a Survey of the Galactic Plane with Milagro'. *Astrophys. J.* **664**:L91–L94.

A. Abdo et al. (2009a). 'Fermi LAT detection of pulsed gamma-rays from the Vela-like pulsars PSR J1048-5832 and PSR J2229+6114'. *Astrophys. J.* **706**:1331–1340.

A. A. Abdo et al. (2009b). 'Milagro Observations of TeV Emission from Galactic Sources in the Fermi Bright Source List'. *Astrophys. J.* **700**:L127–L131. [Erratum: Astrophys. J.703,L185(2009)].

S. Abdollahi et al. (2020). '*Fermi* Large Area Telescope Fourth Source Catalog'. *Astrophys. J. Suppl.* **247**(1):33.

A. U. Abeysekara et al. (2017). 'Observation of the Crab Nebula with the HAWC Gamma-Ray Observatory'. *Astrophys. J.* **843**(1):39.

V. A. Acciari et al. (2009). 'Detection of Extended VHE Gamma Ray Emission from G106.3+2.7 with VERITAS'. *Astrophys. J.* **703**:L6–L9.

F. Acero et al. (2010). 'First detection of VHE gamma-rays from SN 1006 by H.E.S.S'. *Astron. Astrophys.* **516**:A62.

F. Acero et al. (2017). 'Prospects for Cherenkov Telescope Array Observations of the Young Supernova Remnant RX J1713.7−3946'. *Astrophys. J.* **840**(2):74.

M. Ackermann et al. (2012a). 'Fermi-LAT Observations of the Diffuse Gamma-Ray Emission: Implications for Cosmic Rays and the Interstellar Medium'. *Astrophys. J.* **750**:3.

M. Ackermann et al. (2012b). 'The Fermi Large Area Telescope On Orbit: Event Classification, Instrument Response Functions, and Calibration'. *Astrophys. J. Suppl.* **203**:4.

M. Ackermann et al. (2013). 'Detection of the Characteristic Pion-Decay Signature in Supernova Remnants'. *Science* **339**:807.

A. Addazi et al. (2022). 'The Large High Altitude Air Shower Observatory (LHAASO) Science Book (2021 Edition)'. *Chin. Phys. C* **46**:035001–035007.

M. Aguilar et al. (2015a). 'Precision Measurement of the Helium Flux in Primary Cosmic Rays of Rigidities 1.9 GV to 3 TV with the Alpha Magnetic Spectrometer on the International Space Station'. *Phys. Rev. Lett.* **115**(21):211101.

M. Aguilar et al. (2015b). 'Precision Measurement of the Proton Flux in Primary Cosmic Rays from Rigidity 1 GV to 1.8 TV with the Alpha Magnetic Spectrometer on the International Space Station'. *Phys. Rev. Lett.* **114**:171103.

M. Aguilar et al. (2016). 'Precision Measurement of the Boron to Carbon Flux Ratio in Cosmic Rays from 1.9 GV to 2.6 TV with the Alpha Magnetic Spectrometer on the International Space Station'. *Phys. Rev. Lett.* **117**(23):231102.

M. Aguilar et al. (2018). 'Observation of Complex Time Structures in the Cosmic-Ray Electron and Positron Fluxes with the Alpha Magnetic Spectrometer on the International Space Station'. *Phys. Rev. Lett.* **121**(5):051102.

F. Aharonian (2008a). 'Discovery of very high energy gamma-ray emission coincident with molecular clouds in the W28 (G6.4-0.1) field'. *Astron. Astrophys.* **481**:401.

F. Aharonian (2008b). 'HESS VHE Gamma-Ray Sources Without Identified Counterparts'. *Astron. Astrophys.* **477**:353–363.

F. Aharonian et al. (2021). 'Calibration of the air shower energy scale of the water and air Cherenkov techniques in the LHAASO experiment'. *Phys. Rev. D* **104**(6):062007.

F. A. Aharonian & A. M. Atoyan (1996). 'On the emissivity of $\pi\hat{0}\hat{}$decay gamma radiation in the vicinity of accelerators of galactic cosmic rays.'. *Astronomy and Astrophysics* **309**:917–928.

M. Ahlers & K. Murase (2014). 'Probing the Galactic Origin of the IceCube Excess with Gamma-Rays'. *Phys. Rev. D* **90**(2):023010.

H. S. Ahn et al. (2010). 'Discrepant hardening observed in cosmic-ray elemental spectra'. *Astrophys. J. Lett.* **714**:L89–L93.

H. Akaike (1974). 'A New Look at the Statistical Model Identification'. *IEEE Transactions on Automatic Control* **19**:716–723.

A. Albert et al. (2019). 'Science Case for a Wide Field-of-View Very-High-Energy Gamma-Ray Observatory in the Southern Hemisphere' .

A. Albert et al. (2020). 'HAWC J2227+610 and its association with G106.3+2.7, a new potential Galactic PeVatron'. *Astrophys. J. Lett.* **896**:L29.

J. Albert et al. (2007). 'Unfolding of differential energy spectra in the MAGIC experiment'. *Nucl. Instrum. Meth. A* **583**:494–506.

J. Albert et al. (2008a). 'FADC signal reconstruction for the MAGIC Telescope'. *Nucl. Instrum. Meth. A* **594**:407–419.

J. Albert et al. (2008b). 'Implementation of the Random Forest Method for the Imaging Atmospheric Cherenkov Telescope MAGIC'. *Nucl. Instrum. Meth. A* **588**:424–432.

J. Aleksic et al. (2012). 'Performance of the MAGIC stereo system obtained with Crab Nebula data'. *Astropart. Phys.* **35**:435–448.

J. Aleksić et al. (2016). 'The major upgrade of the MAGIC telescopes, Part I: The hardware improvements and the commissioning of the system'. *Astropart. Phys.* **72**:61–75.

J. Aleksić et al. (2016). 'The major upgrade of the MAGIC telescopes, Part II: A performance study using observations of the Crab Nebula'. *Astropart. Phys.* **72**:76–94.

R. Alfaro et al. (2017). 'All-particle cosmic ray energy spectrum measured by the HAWC experiment from 10 to 500 TeV'. *Phys. Rev. D* **96**(12):122001.

M. Amenomori et al. (2008). 'The All-particle spectrum of primary cosmic rays in the wide energy range from 10**14 eV to 10**17 eV observed with the Tibet-III air-shower array'. *Astrophys. J.* **678**:1165–1179.

M. Amenomori et al. (2021a). 'First Detection of sub-PeV Diffuse Gamma Rays from the Galactic Disk: Evidence for Ubiquitous Galactic Cosmic Rays beyond PeV Energies'. *Phys. Rev. Lett.* **126**(14):141101.

M. Amenomori et al. (2021b). 'Potential PeVatron supernova remnant G106.3+2.7 seen in the highest-energy gamma rays'. *Nature Astron.* **5**(5):460–464.

D. Anderson, et al. (2016). 'Precision timing calorimeter for high energy physics'. *Nucl. Instrum. Meth. A* **824**:670–673.

W. D. Apel et al. (2013). 'KASCADE-Grande measurements of energy spectra for elemental groups of cosmic rays'. *Astropart. Phys.* **47**:54–66.

M. Araya (2014). 'Fermi LAT Observation of Supernova Remnant HB9'. *Mon. Not. Roy. Astron. Soc.* **444**(1):860–865.

T. Asaba et al. (2018). 'The overview of the ALPACA Experiment'. *PoS* **ICRC2017**:827.

A. M. Atoyan, et al. (1995). 'Electrons and positrons in the galactic cosmic rays'. *Phys. Rev. D* **52**(6):3265–3275.

W. B. Atwood et al. (2009). 'The Large Area Telescope on the Fermi Gamma-ray Space Telescope Mission'. *Astrophys. J.* **697**:1071–1102.

W. Baade & F. Zwicky (1934). 'On Super-novae'. *Proceedings of the National Academy of Science* **20**(5):254–259.

A. Bamba, et al. (2003). 'Fine structures of shock of SN 1006 with the Chandra observation'. *Astrophys. J.* **589**:827.

Y. Bao & Y. Chen (2021). 'On the Hard Gamma-Ray Spectrum of the Potential PeVatron Supernova Remnant G106.3 + 2.7'. *Astrophys. J.* **919**(1):32.

A. R. Bell (1978). 'The Acceleration of cosmic rays in shock fronts. I'. *Mon. Not. Roy. Astron. Soc.* **182**:147–156.

B. Bencheikh, et al. (1992). 'A Simple light detector gain measurement technique'. *Nucl. Instrum. Meth. A* **315**:349–353.

C. Benn & S. Ellison (1998). 'Brightness of the night sky over La Palma'. *New Astronomy Reviews* **42**(6):503–507.

K. Bernlöhr et al. (2013). 'Monte Carlo design studies for the Cherenkov Telescope Array'. *Astropart. Phys.* **43**:171–188.

A. Biland, et al. (2007). 'The Active Mirror Control of the MAGIC Telescope'. In *30th International Cosmic Ray Conference*, vol. 3, pp. 1353–1356.

D. J. Bird et al. (1995). 'Detection of a cosmic ray with measured energy well beyond the expected spectral cutoff due to cosmic microwave radiation'. *Astrophys. J.* **441**:144–150.

R. Blandford & J. Ostriker (1978). 'Particle Acceleration by Astrophysical Shocks'. *Astrophys. J. Lett.* **221**:L29–L32.

P. Blasi & E. Amato (2012). 'Diffusive propagation of cosmic rays from supernova remnants in the Galaxy. II: anisotropy'. *JCAP* **01**:011.

A. D. Bolatto, et al. (2013). 'The CO-to-H_2 Conversion Factor'. *Ann. Rev. Astron. Astrophys.* **51**:207–268.

A. Bonardi, et al. (2014). 'A new solution for mirror coating in γ-ray Cherenkov Astronomy'. *Exper. Astron.* **38**(1-2):1–9.

L. Breiman (2001). 'Random Forests'. *Machine Learning* **45**(1):5–32.

T. Bretz, et al. (2009). 'The drive system of the Major Atmospheric Gamma-ray Imaging Cherenkov Telescope'. *Astropart. Phys.* **31**:92–101.

Z. Cao, et al. (2021). 'Ultrahigh-energy photons up to 1.4 petaelectronvolts from 12 γ-ray Galactic sources'. *Nature* **594**(7861):33–36.

Z. Cao et al. (2021). 'Peta–electron volt gamma-ray emission from the Crab Nebula'. *Science* **373**(6553):425–430.

D. Caprioli, et al. (2009). 'On the escape of particles from cosmic ray modified shocks'. *Mon. Not. Roy. Astron. Soc.* **396**:2065–2073.

M. Cardillo, et al. (2016). 'Supernova remnant W44: a case of cosmic-ray reacceleration'. *Astron. Astrophys.* **595**:A58.

V. Cavasinni, et al. (2006). 'TeV Neutrinos from SuperNova Remnants embedded in Giant Molecular Clouds'. *Astropart. Phys.* **26**:41–49.

D. J. H. Chung, et al. (1998). 'Superheavy dark matter'. *Phys. Rev. D* **59**:023501.

D. H. Clark, et al. (1975). '408 and 5000 MHz Observations of 28 New Galactic Supernova Remnants'. *Australian Journal of Physics Astrophysical Supplement* **37**:1–38.

J. J. Condon, et al. (1994). 'A 4.85 GHz Sky Survey. III. Epoch 1986 and Combined (1986-1987) Maps Covering 0degrees ¡ delta ¡+75degrees'. *The Astronomical Journal* **107**:1829.

P. Cristofari (2021). 'The Hunt for Pevatrons: The Case of Supernova Remnants'. *Universe* **7**(9):324.

Y. Cui, et al. (2018). 'Leaked GeV CRs from a Broken Shell: Explaining 9 Years of Fermi-LAT Data of SNR W28'. *Astrophys. J.* **860**(1):69.

T. M. Dame, et al. (2001). 'The Milky Way in molecular clouds: A New complete co survey'. *Astrophys. J.* **547**:792–813.

M. D'Angelo, et al. (2018). 'Diffuse gamma-ray emission from self-confined cosmic rays around Galactic sources'. *Mon. Not. Roy. Astron. Soc.* **474**(2):1944–1954.

A. Daum et al. (1997). 'First results on the performance of the HEGRA IACT array'. *Astropart. Phys.* **8**:1–11.

M. de Naurois & D. Mazin (2015). 'Ground-based detectors in very-high-energy gamma-ray astronomy'. *Comptes Rendus Physique* **16**:610–627.

C. D. Dermer (1986). 'Secondary production of neutral pi-mesons and the diffuse galactic gamma radiation'. *Astronomy and Astrophysics* **157**(2):223–229.

J. M. Dickey & F. J. Lockman (1990). 'HI in the galaxy'. *Ann. Rev. Astron. Astrophys.* **28**:215–261.

R. Diesing & D. Caprioli (2019). 'Spectrum of Electrons Accelerated in Supernova Remnants'. *Phys. Rev. Lett.* **123**(7):071101.

M. Doro et al. (2008). 'The reflective surface of the MAGIC telescope'. *Nucl. Instrum. Meth. A* **595**:200–203.

B. Draine (2011). 'Physics of the Interstellar and Intergalactic Medium'. *Physics of the Interstellar and Intergalactic Medium by Bruce T. Draine. Princeton University Press, 2011. ISBN: 978-0-691-12214-4* .

K. S. Dwarakanath, et al. (1982). 'Observations of the supernova remnants HB 9 and IC 443 at 34.5 MHz'. *Journal of Astrophysics and Astronomy* **3**:207–216.

P. Eger, et al. (2011). 'A multi-wavelength study of the unidentified TeV gamma-ray source HESS J1626-490'. *Astronomy and Astrophysics* **526**:A82.

K. Fang, et al. (2022). 'Evidence for PeV Proton Acceleration from Fermi-LAT Observations of SNR G106.3+2.7'. *Phys. Rev. Lett.* **129**(7):071101.

K. Fang & K. Murase (2021). 'Multimessenger Implications of Sub-PeV Diffuse Galactic Gamma-Ray Emission'. *Astrophys. J.* **919**(2):93.

E. Fermi (1949). 'On the Origin of the Cosmic Radiation'. *Physical Review* **75**(8):1169–1174.

V. Fomin, et al. (1994). 'New methods of atmospheric Cherenkov imaging for gamma-ray astronomy. 1: The False source method'. *Astropart. Phys.* **2**:137–150.

C. Fruck, et al. (2014). 'A novel LIDAR-based Atmospheric Calibration Method for Improving the Data Analysis of MAGIC'. In *Proceedings, 33rd International Cosmic Ray Conference (ICRC2013): Rio de Janeiro, Brazil, July 2-9, 2013*, p. 1054.

Y. Fujita, et al. (2021). 'X-Ray Emission from the PeVatron-candidate Supernova Remnant G106.3+2.7'. *The Astrophysical Journal* **912**(2):133.

Y. Fujita, et al. (2009). 'Molecular Clouds as a Probe of Cosmic-Ray Acceleration in a Supernova Remnant'. *Astrophys. J. Lett.* **707**:L179–L183.

Y. Fujita, et al. (2011). 'Alfven Wave Amplification and Self-Containment of Cosmic-Rays Escaping from a Supernova Remnant'. *Mon. Not. Roy. Astron. Soc.* **415**:3434.

Y. Fukui et al. (2012). 'A Detailed Study of the Molecular and Atomic Gas Toward the \gamma-ray SNR RX J1713.7-3946: Spatial TeV \gamma-ray and ISM Gas Correspondence'. *Astrophys. J.* **746**:82.

Y. Fukui, et al. (2021). 'Pursuing the origin of the gamma rays in RX J1713.7−3946 quantifying the hadronic and leptonic components' .

S. Funk (2015). 'Ground- and Space-Based Gamma-Ray Astronomy'. *Ann. Rev. Nucl. Part. Sci.* **65**:245–277.

S. Funk & J. A. Hinton (2009). 'Monte-Carlo studies of the angular resolution of a future Cherenkov gamma-ray telescope'. *AIP Conf. Proc.* **1085**(1):878–881.

S. Gabici & F. Aharonian (2016). 'Gamma-ray emission from young supernova remnants: hadronic or leptonic?'. *EPJ Web Conf.* **121**:04001.

S. Gabici & F. A. Aharonian (2007). 'Searching for galactic cosmic ray pevatrons with multi-TeV gamma rays and neutrinos'. *Astrophys. J. Lett.* **665**:L131.

S. Gabici, et al. (2009). 'Broad-band non-thermal emission from molecular clouds illuminated by cosmic rays from nearby supernova remnants'. *Monthly Notices of the Royal Astronomical Society* **396**(3):1629–1639.

D. Gaggero, et al. (2018). 'Time evolution of gamma rays from supernova remnants'. *Mon. Not. Roy. Astron. Soc.* **475**(4):5237–5245.

X. Y. Gao, et al. (2011). 'A Sino-German λ6 cm polarization survey of the Galactic plane. V. Large supernova remnants'. *Astronomy and Astrophysics* **529**:A159.

M. Garcia-Munoz, et al. (1987). 'Cosmic-Ray Propagation in the Galaxy and in the Heliosphere: The Path Length Distribution at Low Energy'. *The Astrophysical Journal Supplement Series* **64**:269.

C. Ge, et al. (2021). 'Revealing a peculiar supernova remnant G106.3+2.7 as a petaelectronvolt proton accelerator with X-ray observations'. *The Innovation* **2**:100118.

Y. Génolini et al. (2017). 'Indications for a high-rigidity break in the cosmic-ray diffusion coefficient'. *Phys. Rev. Lett.* **119**(24):241101.

Y. Génolini et al. (2019). 'Cosmic-ray transport from AMS-02 boron to carbon ratio data: Benchmark models and interpretation'. *Phys. Rev. D* **99**(12):123028.

A. Giuliani et al. (2011). 'Neutral pion emission from accelerated protons in the supernova remnant W44'. *Astrophys. J. Lett.* **742**:L30.

D. A. Green (1988). 'A Revised Reference Catalogue of Galactic Supernova Remnants'. *Astrophysics and Space Science* **148**(1):3–74.

K. Greisen (1956). *Progress in Cosmic Ray Physics, Vol. 3. ed. J. G. Wilson.* North-Holland, Amsterdam.

J. Hahn et al. (2014). 'Impact of aerosols and adverse atmospheric conditions on the data quality for spectral analysis of the H.E.S.S. telescopes'. *Astropart. Phys.* **54**:25–32.

J. Halpern, et al. (2001a). 'Psr j2229+6114: discovery of an energetic young pulsar in the error box of the egret source 3eg j2227+6122'. *Astrophys. J.* **552**:L125.

J. Halpern, et al. (2001b). 'A possible x-ray and radio counterpart of the high-energy gamma-ray source 3eg j2227+6122'. *Astrophys. J.* **547**:323.

Y. Hanabata et al. (2014). 'Detailed Investigation of the Gamma-Ray Emission in the Vicinity of SNR W28 with FERMI-LAT'. *Astrophys. J.* **786**:145.

R. Hartman et al. (1999). 'The Third EGRET catalog of high-energy gamma-ray sources'. *Astrophys. J. Suppl.* **123**:79.

T. Hassan et al. (2017). 'Monte Carlo Performance Studies for the Site Selection of the Cherenkov Telescope Array'. *Astropart. Phys.* **93**:76–85.

S. Hayakawa (1956). 'Supernova Origin of Cosmic Rays*)'. *Progress of Theoretical Physics* **15**(2):111–121.

V. F. Hess (1912). 'Über Beobachtungen der durchdringenden Strahlung bei sieben Freiballonfahrten'. *Phys. Z.* **13**:1084–1091.

M. H. Heyer, et al. (1998). 'The Five College Radio Astronomy Observatory CO Survey of the Outer Galaxy'. *The Astrophysical Journal Supplement Series* **115**(2):241–258.

A. M. Hillas (1984). 'The Origin of Ultra-High-Energy Cosmic Rays'. *Annual Review of Astronomy and Astrophysics* **22**:425–444.

A. M. Hillas (1985). 'Cerenkov Light Images of EAS Produced by Primary Gamma Rays and by Nuclei'. In *19th International Cosmic Ray Conference (ICRC19), Volume 3*, vol. 3 of *International Cosmic Ray Conference*, p. 445.

M. Holler et al. (2016). 'Observations of the Crab Nebula with H.E.S.S. Phase II'. *PoS* **ICRC2015**:847.

T. Inoue, et al. (2012). 'Toward Understanding the Cosmic-ray Acceleration at Young Supernova Remnants Interacting with Interstellar Clouds: Possible Applications to RX J1713.7-3946'. *Astrophys. J.* **744**:71.

P. S. Iroshnikov (1964). 'Turbulence of a Conducting Fluid in a Strong Magnetic Field'. *Soviet Astronomy* **7**:566.

D. Ivanov (2020). 'Energy Spectrum Measured by the Telescope Array'. *PoS* **ICRC2019**:298.

T. Jogler & S. Funk (2016). 'Revealing W51c as a Cosmic ray Source Using Fermi-lat Data'. *Astrophys. J.* **816**(2):100.

G. Joncas & L. A. Higgs (1990). 'The DRAO galactic-plane survey. II. Field at l= 105.'. *Astronomy and Astrophysics, Suppl. Ser.* **82**:113–144.

E. Kafexhiu, et al. (2014). 'Parametrization of gamma-ray production cross-sections for pp interactions in a broad proton energy range from the kinematic threshold to PeV energies'. *Phys. Rev. D* **90**(12):123014.

S. F. Kamijima & Y. Ohira (2021). 'Escape of cosmic rays from perpendicular shocks in the interstellar magnetic field' .

S. F. Kamijima & Y. Ohira (2022). 'Escape of cosmic rays from perpendicular shocks in the circumstellar magnetic field' .

V. M. Kaspi, et al. (1996). 'A Search for Radio Pulsars in Southern Supernova Remnants'. *The Astronomical Journal* **111**:2028.

N. Kawanaka & S.-H. Lee (2021). 'Origin of Spectral Hardening of Secondary Cosmic-Ray Nuclei'. *Astrophys. J.* **917**(2):61.

T. W. Kephart & T. J. Weiler (1996). 'Magnetic monopoles as the highest energy cosmic ray primaries'. *Astropart. Phys.* **4**:271–279.

A. N. Kolmogorov (1991). 'The Local Structure of Turbulence in Incompressible Viscous Fluid for Very Large Reynolds Numbers'. *Proceedings of the Royal Society of London Series A* **434**(1890):9–13.

R. Kothes, et al. (2006). 'The Boomerang PWN G106.6+2.9 and the Magnetic Field Structure in Pulsar Wind Nebulae'. *Astrophys. J.* **638**(1):225–233.

R. Kothes, et al. (2001). 'The Supernova Remnant G106.3+2.7 and Its Pulsar-Wind Nebula: Relics of Triggered Star Formation in a Complex Environment'. *The Astrophysical Journal* **560**(1):236–243.

K. Koyama, et al. (1995). 'Evidence for shock acceleration of high-energy electrons in the supernova remnant SN1006'. *Nature* **378**:255–258.

R. H. Kraichnan (1967). 'Inertial Ranges in Two-Dimensional Turbulence'. *Physics of Fluids* **10**(7):1417–1423.

T. L. Landecker et al. (2000). 'The synthesis telescope at the dominion radio astrophysical observatory'. *Astron. Astrophys. Suppl. Ser.* **145**:509.

D. A. Leahy & B. Aschenbach (1995). 'ROSAT X-ray observations of the supernova remnant HB 9.'. *Astronomy and Astrophysics* **293**:853–858.

D. A. Leahy & R. S. Roger (1991). 'Radio Emission from the Supernova Remnant G160.9+2.6 (HB9)'. *The Astronomical Journal* **101**:1033.

D. A. Leahy & W. Tian (2007). 'Radio Spectrum and Distance of the SNR HB9'. *Astron. Astrophys.* **461**:1013.

T.-P. Li & Y.-Q. Ma (1983). 'Analysis methods for results in gamma-ray astronomy'. *Astrophys. J.* **272**:317–324.

T. Linden & B. J. Buckman (2018). 'Pulsar TeV Halos Explain the Diffuse TeV Excess Observed by Milagro'. *Phys. Rev. Lett.* **120**(12):121101.

P. Lipari & S. Vernetto (2018). 'Diffuse Galactic gamma ray flux at very high energy'. *Phys. Rev. D* **98**(4):043003.

S. Liu, et al. (2020). 'Hadronic vs leptonic models for γ-ray emission from VER J2227+608'. *Astrophys. J.* **897**(2):L34.

M. A. Malkov, et al. (2013). 'Analytic Solution for Self-regulated Collective Escape of Cosmic Rays from their Acceleration Sites'. *Astrophys. J.* **768**:73.

D. Mattingly (2005). 'Modern tests of Lorentz invariance'. *Living Rev. Rel.* **8**:5.

J. R. Mattox et al. (1996). 'The Likelihood Analysis of EGRET Data'. *Astrophys. J.* **461**:396.

N. M. McClure-Griffiths, et al. (2005). 'The Southern Galactic Plane Survey: HI observations and analysis'. *Astrophys. J. Suppl.* **158**:178–187.

R. Mirzoyan (1997). 'On the Calibration Accuracy of Light Sensors in Atmospheric Cherenkov Fluorescence and Neutrino Experiments'. In *International Cosmic Ray Conference*, vol. 7 of *International Cosmic Ray Conference*, p. 265.

S. Nagataki (2004). 'High-energy neutrinos produced by interactions of relativistic protons in shocked pulsar winds'. *Astrophys. J.* **600**:883–904.

D. Nakajima (2013). 'New Imaging camera for the MAGIC-I Telescope'. In *33rd International Cosmic Ray Conference*, p. 0787.

S. Nozaki et al. (2020). 'Calibration and performance of the readout system based on switched capacitor arrays for the Large-Sized Telescope of the Cherenkov Telescope Array'. *Proc. SPIE Int. Soc. Opt. Eng.* **11447**:114470H.

A. Obermeier, et al. (2012). 'The boron-to-carbon abundance ratio and Galactic propagation of cosmic radiation'. *Astrophys. J.* **752**:69.

Y. Ohira & K. Murase (2019). 'Origin and Impacts of the First Cosmic Rays'. *Phys. Rev. D* **100**(6):061301.

Y. Ohira, et al. (2010). 'Escape-limited Model of Cosmic-ray Acceleration Revisited'. *Astron. Astrophys.* **513**:A17.

Y. Ohira, et al. (2011). 'Gamma-rays from molecular clouds illuminated by cosmic rays escaping from interacting supernova remnants'. *Monthly Notices of the Royal Astronomical Society* **410**(3):1577–1582.

Y. Ohira, et al. (2012). 'Escape of cosmic-ray electrons from supernova remnants'. *Mon. Not. Roy. Astron. Soc.* **427**:91.

M. Padovani, et al. (2020). 'Impact of Low-Energy Cosmic Rays on Star Formation'. *Space Sci. Rev.* **216**(2):29.

J. S. Perkins & G. Maier (2009). 'VERITAS Telescope 1 Relocation: Details and Improvements' .

S. Pineault & G. Joncas (2000). 'G106.3+2.7: A Supernova Remnant in a Late Stage of Evolution'. *The Astronomical Journal* **120**(6):3218–3225.

T. A. Porter, et al. (2008). 'Inverse Compton Origin of the Hard X-Ray and Soft Gamma-Ray Emission from the Galactic Ridge'. *Astrophys. J.* **682**:400–407.

V. S. Ptuskin & V. N. Zirakashvili (2003). 'Limits on diffusive shock acceleration in supernova remnants in the presence of cosmic-ray streaming instability and wave dissipation'. *Astron. Astrophys.* **403**:1–10.

V. S. Ptuskin & V. N. Zirakashvili (2005). 'On the spectrum of high-energy cosmic rays produced by supernova remnants in the presence of strong cosmic-ray streaming instability and wave dissipation'. *Astron. Astrophys.* **429**:755–765.

W. Reich, et al. (2003). '35 cm observations of a sample of large supernova remnants'. *Astronomy and Astrophysics* **408**:961–969.

S. P. Reynolds, et al. (2012). 'Magnetic fields in supernova remnants and pulsar-wind nebulae'. *Space Sci. Rev.* **166**:231–261.

S. Ritt, et al. (2010). 'Application of the DRS chip for fast waveform digitizing'. *Nucl. Instrum. Meth. A* **623**:486–488.

R. S. Roger, et al. (1999). 'The radio emission from the Galaxy at 22 MHz'. *Astronomy and Astrophysics Supplement Series* **137**:7–19.

H. Sano et al. (2019). 'Possible Evidence for Cosmic-Ray Acceleration in the Type Ia SNR RCW 86: Spatial Correlation between TeV Gamma rays and Interstellar Atomic Protons'. *Astrophys. J.* **876**(1):37.

K. M. Schure & A. R. Bell (2013). 'Cosmic ray acceleration in young supernova remnants'. *Mon. Not. Roy. Astron. Soc.* **435**:1174.

T. Schweizer, et al. (2002). 'The optical calibration of the MAGIC telescope camera'. *IEEE Trans. Nucl. Sci.* **49**:2497–2503.

A. Sezer, et al. (2019). 'Discovery of recombining plasma inside the extended gamma-ray supernova remnant HB9'. *Mon. Not. Roy. Astron. Soc.* **489**(3):4300–4310.

Y. Shikaze et al. (2007). 'Measurements of 0.2 to 20-GeV/n cosmic-ray proton and helium spectra from 1997 through 2002 with the BESS spectrometer'. *Astropart. Phys.* **28**:154–167.

J. Sitarek, et al. (2013). 'Analysis techniques and performance of the Domino Ring Sampler version 4 based readout for the MAGIC telescopes'. *Nucl. Instrum. Meth. A* **723**:109–120.

H. Suzuki, et al. (2020). 'Study on the escape timescale of high-energy particles from supernova remnants through thermal X-ray properties'. *Publ. Astron. Soc. Jap.* **72**(5):Publications of the Astronomical Society of Japan, Volume 72, Issue 5, October 2020, 72, https://doi.org/10.1093/pasj/psaa061.

H. Suzuki, et al. (2022). 'Observational Constraints on the Maximum Energies of Accelerated Particles in Supernova Remnants: Low Maximum Energies and a Large Variety'. *Astrophys. J.* **924**(2):45.

G. A. Tammann, et al. (1994). 'The Galactic Supernova Rate'. *The Astrophysical Journal Supplement Series* **92**:487.

T. Tanaka, et al. (2020). 'Shock-Cloud Interaction in the Southwestern Rim of RX J1713.7−3946 Evidenced by Chandra X-ray Observations'. *Astrophys. J. Lett.* **900**(1):L5.

T. Tanimori et al. (1994). 'Observation of 7-TeV gamma-rays from the Crab using the large zenith angle air Cherenkov imaging technique'. *Astrophys. J. Lett.* **429**:L61–L64.

A. R. Taylor, et al. (2003). 'The Canadian Galactic Plane Survey'. *The Astronomical Journal* **125**(6):3145–3164.

S. Thoudam, et al. (2016). 'Cosmic-ray energy spectrum and composition up to the ankle: the case for a second Galactic component'. *Astron. Astrophys.* **595**:A33.

M. Tluczykont, et al. (2014). 'The HiSCORE concept for gamma-ray and cosmic-ray astrophysics beyond 10 TeV'. *Astropart. Phys.* **56**:42–53.

N. Tsuji, et al. (2021). 'Systematic Study of Acceleration Efficiency in Young Supernova Remnants with Nonthermal X-ray Observations'. *Astrophys. J.* **907**(2):117.

Y. Uchiyama, et al. (2010). 'Gamma-ray Emission from Crushed Clouds in Supernova Remnants'. *Astrophys. J. Lett.* **723**(1):L122.

Y. Uchiyama, et al. (2012). 'Fermi-LAT Discovery of GeV Gamma-ray Emission from the Vicinity of SNR W44'. *Astrophys. J. Lett.* **749**:L35.

V. P. Utrobin & N. N. Chugai (2017). 'Luminous Type IIP SN 2013ej with high-velocity ^{56}Ni ejecta'. *Mon. Not. Roy. Astron. Soc.* **472**(4):5004–5010.

V. Verzi (2020). 'Measurement of the energy spectrum of ultra-high energy cosmic rays using the Pierre Auger Observatory'. *PoS* **ICRC2019**:450.

I. Vovk, et al. (2018). 'Spatial likelihood analysis for MAGIC telescope data - From instrument response modelling to spectral extraction'. *Astron. Astrophys.* **619**:A7.

T. C. Weekes et al. (1989). 'Observation of TeV gamma rays from the Crab nebula using the atmospheric Cerenkov imaging technique'. *Astrophys. J.* **342**:379–395.

D. G. Wentzel (1974). 'Cosmic-ray propagation in the galaxy: collective effects'. *Ann. Rev. Astron. Astrophys.* **12**:71–96.

J. B. Z. Whiteoak & A. J. Green (1996). 'The MOST supernova remnant catalogue (MSC).'. *Astronomy and Astrophysics Supplement Series* **118**:329–380.

Y. Xin, et al. (2019). 'VER J2227+608: A Hadronic PeVatron Pulsar Wind Nebula?'. *The Astrophysical Journal* **885**(2):162.

S. Yanagita & K. Nomoto (1999). 'Nucleosynthetic View of Supernovae Origin of the Galactic Cosmic Rays'. *Astrophysical Letters and Communications* **38**:461.

S. Yanagita, et al. (1990). 'Supernovae Origin of Cosmic Rays'. In *International Cosmic Ray Conference*, vol. 4 of *International Cosmic Ray Conference*, p. 44.

H. Yasuda & S.-H. Lee (2019). 'Time Evolution of Broadband Nonthermal Emission from Supernova Remnants in Different Circumstellar Environments'. *Astrophys. J.* **876**(1):27.

Y. S. Yoon et al. (2017). 'Proton and Helium Spectra from the CREAM-III Flight'. *Astrophys. J.* **839**(1):5.

Q. Yuan, et al. (2017). 'Propagation of cosmic rays in the AMS-02 era'. *Phys. Rev. D* **95**(8):083007.

V. Zabalza (2015). 'naima: a Python package for inference of relativistic particle energy distributions from observed nonthermal spectra'. *Proc. of International Cosmic Ray Conference 2015* p. 922.

R. Zanin (2013). 'MARS, the MAGIC analysis and reconstruction software'. In *33rd International Cosmic Ray Conference*, p. 0773.